

**The Development of Smart Reactors for Flow
Chemistry: The Role of Additive
Manufacturing and Online Analysis for
Automated Optimisation**

Matthew James Harding

A doctoral thesis submitted in partial fulfilment of the requirements for the
award of Doctor of Philosophy



**Loughborough
University**

Supervisor: Dr S.D.R. Christie

© Matthew James Harding 2017

Acknowledgements

Thank you, Steve Christie, for allowing me this opportunity, I am grateful you decided I was worth the risk despite all evidence to the contrary. Thanks also to Andrew Capel for introducing me to the wonderful world of CAD and the joys of unconstrained sketch dimensions, and to Tom Monaghan - your designs make mine look like crayon drawings, it was a privilege to work with you.

Many thanks to Rob Lee, any improvement in my chemistry abilities are due in no small part to you, Colum Breen for tolerating the mess that was my bench, and thanks also to everyone else in F001 for not blowing me up. Special thanks also to Yuqi Li and Shuqi Yang for making the lab such a nice place to be. My most sincere thanks go to Tony New; your encouragement has got me through an MSc and now a PhD, I would not have got this far without your help.

Apologies to my family for not being around much but thank you for your understanding.

Abstract

This thesis investigates the application of online monitoring for the optimisation of flow chemistry, as well as how additive manufacturing can aid the integration of analysis and confer new functionality to flow reactors. The additive manufacturing (AM) processes used were stereolithography (SL) and the metal printing techniques selective laser melting (SLM) and ultrasonic consolidation (UC).

Chapter 1 contains a short literature review, intended to give a clear background to the work contained herein. The literature reported gives a brief introduction to flow chemistry and some of the instrumentation used to perform it. Additionally, the evolution of reactor design is investigated leading to an overview of the use of AM for custom reactors. The subsequent use of online analytical technologies and how they relate to the enhancement of flow chemistry is discussed, as well as some of the protocols that have been employed to date to facilitate automated reaction optimisation.

Chapter 2 investigates the design and manufacture of flow cells capable of online spectroscopy, as well as the integration of spectroscopic monitoring capability directly into reactors. In addition, the use of AM to produce accessories, not necessarily part of the wetted flow path, was investigated and showed that many useful parts such as fibre optic holders and screws could be produced. The capability of these flow cells was assessed through standard material analysis as well as through the online analysis of flow chemistry. In particular, the use of SL has enabled the production of flow cells with features smaller than 100 microns. This allowed *in situ* spectroscopy to be performed by embedding fibre optics directly adjacent to the flow channel, offering a new way for reaction monitoring by ultraviolet (UV) spectroscopy to be performed cheaply, and with full user control over the flow cell specification. No additional quartz features were required for these cheap and highly customisable parts. Flow cells of larger path lengths were also produced, and their performance tested, identifying designs and materials suitable for the inline analysis of flow chemistry. These designs were then successfully incorporated directly within the flow channels of larger scale reactors, tailored specifically to commercial flow equipment, for true inline analysis of flow chemistry.

Chapter 3 examines the use of metal reactors formed through more expensive printing processes, SLM and UC. As the parts these techniques produce are fully dense, chemically resistant and thermally stable, they were used to perform high temperature chemistry, taking solvents substantially above their boiling points to accelerate reactions and perform them in a fraction of the time of the batch process. UC was also used to produce a reactor with a copper flow path and the possibility of reaction catalysis performed with 'active' metal sections was investigated, revealing that chemical modification of the reactor surface greatly improved the reaction yield. UC was also utilised to produce a flow reactor incorporating a thermocouple in the main body, close to the flow channel to enable accurate reaction temperatures to be measured, a significant improvement over the temperature control offered through the flow

instrument. This represents the first use of UC for the production of complicated geometry flow reactors and this work has shown that many more applications of the technique for flow chemistry should be investigated. The ability to perform light mediated coupling reactions in AM produced reactors was also demonstrated successfully for the first time, and further to this that the extended UV curing of SL reactors is crucial for improved robustness of these parts.

Chapter 4 centres on the use of online analytical methods to provide rapid, selective, and quantitative online analysis of flow chemistry. This chapter also outlines some of the steps required for automation to be possible, including equipment specifications and the coding approach undertaken to integrate multiple different instruments. A combination of online nuclear magnetic resonance (NMR) spectroscopy analysis and automated experiment selection was then used to optimise a pharmaceutically relevant, photoredox catalysed, C-N coupling reaction between amines and aryl halides, performed under continuous flow conditions for the first time. This optimisation required minimal user input, operating completely unattended, and revealed that lower concentrations of catalyst could be employed than previously identified, reducing the amount of toxic and expensive metal salts required, while achieving high conversion of the starting material.

In summary, this thesis has demonstrated that AM, in particular SL, can be used for the production of new high resolution microfluidic flow cells, as well as larger scale flow cell designs which can be integrated into the body of large reactors, not easily performed with other manufacturing methods. SL has also been used to produce reactors capable of performing light catalysed reactions directly, with no further modifications. The use of metal printing AM techniques has allowed *in situ* catalysis and high temperature, high pressure reactions to be carried out with ease. Finally, the use of online NMR with computer control and experiment automation has allowed the rapid optimisation of a pharmaceutically important C-N coupling reaction.

Contents

Acknowledgements.....	v
Abstract.....	vi
Collaborations.....	1
Glossary and Abbreviations.....	1
1. Literature review.....	4
1.1 Flow chemistry.....	4
1.1.1 Flow photochemistry.....	7
1.2 Reactor design.....	10
1.2.1 Additive manufacturing for reactor design.....	14
1.2.1.1 Fused Deposition Modelling.....	15
1.2.1.3 Selective laser sintering / selective laser melting.....	18
1.2.1.4 Ultrasonic consolidation.....	19
1.2.2 Applications of AM for the chemical sciences.....	21
1.3 Online analysis for reaction control and optimisation.....	22
1.3.1 Online monitoring through mass spectrometry.....	23
1.3.4 NMR spectroscopy.....	29
1.4 Reaction optimisation - DOE and global optimisation algorithms.....	30
2 3D printing for molecular spectroscopy.....	34
2.1 Introduction.....	34
2.2 Results and discussion.....	34
2.2.1 Straight channel transmission flow cell design.....	34
2.2.2 Z-path flow cell design.....	35
2.2.3 Comparison of flow cells.....	36
2.2.4 Integration of analytical measurement capability directly into reactors.....	39
2.2.4.1 Integrated spectroscopy into SL reactors.....	39
2.2.4.2 Integration of thermocouples into SL reactors.....	40

2.2.5 Use of 3DP flow cells for reaction monitoring through multivariate calibration	41
2.2.6 UV PLSR calibration for 3 components	43
2.2.7 Microfluidic flow cell for online analysis and optimisation	45
2.2.8 Integration of fibre optics.....	46
2.2.9 Use of microfluidic flow cell for reaction monitoring	50
2.2.11 3D printing for fibre optic waveguides	55
2.2.11.1 Visible spectroscopic monitoring for S _N Ar reaction.....	56
2.2.11.2 Use of 3D printed waveguide for the optimisation of the formal [3+3] cycloaddition to give 2H-benzopyrans	59
2.2.11.3 Replacement of EDDA and the use of an ionic liquid catalyst.....	59
2.2.11.4 Optimisation of formal [3+3] cycloaddition under flow conditions	59
2.2.11.5 Ionic liquid promoted synthesis of 2H-benzopyrans	61
2.2.12 3D printing for ATR flow cells.....	63
2.3 Chapter summary	66
2.4 Further work.....	66
3 The use of additive manufacturing for chemical reactors	68
3.1 Introduction.....	68
3.2 Results and Discussion	69
3.2.1 Optimisation of benzopyridoxazine synthesis	69
3.2.1.1 SLM reactor design.....	69
3.2.2 3D printing of functional reactors through ultrasonic consolidation	74
3.2.3 Ullmann coupling.....	76
3.2.4 Copper catalysed azide alkyne cycloaddition (CuAAC) - click chemistry in flow	76
3.2.5 Stephens-Castro Coupling.....	84
3.2.6 Design of reactors for photo-catalysed reactions	84
3.3 Chapter summary	89
3.4 Further Work.....	90
4. Online Analysis and Automated Optimisation Using Flow NMR.....	91

4.1 Introduction.....	91
4.2 Results and Discussion	91
4.2.1 Flow NMR monitoring for the bromination of 1, 3-dimethoxybenzene with N-bromosuccinimide.....	91
4.2.2 Automated optimisation through flow NMR and design of experiments and application to photochemistry.....	93
4.2.3 Trifluoromethylation of heterocycles.....	94
4.2.4 C-N coupling of aniline and 2-fluoro-iodobenzene	97
4.2.5 C-N coupling of aniline and 4-bromo-benzotrifluoride	99
4.2.6 C-N coupling of aniline and 4-bromo-benzotrifluoride: factor level extension to lower nickel equivalents - 2.5 mol. %	104
4.2.7 C-N coupling of aniline and 4-bromo-benzotrifluoride: factor level extension to lower nickel equivalents - 0.1 mol. %	104
4.2.8 C-N coupling of aniline and 4-bromo-benzotrifluoride: automated 3 factor optimisation	106
4.2.9 Automated spectrum acquisition.....	110
4.3 Chapter summary	111
4.4 Further work.....	112
5. Conclusion	113
6. Experimental.....	115
6.1 Instrumentation	115
6.1.1 IR	115
6.1.2 Melting points	115
6.1.3 NMR Spectroscopy.....	115
6.1.4 Column chromatography	115
6.1.5 Flow chemistry equipment.....	115
6.1.6 Mass spectrometry	116
6.1.7 UV/Vis spectroscopy	116
6.1.8 HPLC analysis	116
6.1.9 Automated optimisation.....	116

6.1.10 DOE model generation and coefficient selection.....	116
6.1.11 CAD sketches.....	117
6.1.12 SL part printing	117
6.2 Laboratory procedures	117
6.2.1 General considerations.....	117
6.2.2 Flow bromination of 1,3-dimethoxybenzene in SL reactor (R1) with in-built spectroscopic monitoring port	117
6.2.3 Flow synthesis and online analysis of S _N Ar reaction between 2,4-difluoronitrobenzene and pyrrolidine.....	118
6.2.4 Flow synthesis of (S,E)-2-(2-methyl-5-(prop-1-en-2-yl)cyclohex-2-en-1-ylidene)hydrazine-1-carboxamide.....	121
6.2.5 Formal [3+3] cycloaddition under flow conditions - ionic liquid preparation.....	123
6.2.5.1 Formal [3+3] cycloaddition under flow conditions - optimisation through box Behnken design	124
6.2.5.2 General procedure for the synthesis of 2H-benzopyrans	127
6.2.6 Simplex optimisation for the synthesis of 1,3,4-Trifluoro-5-methyl-5H-benzo[b]pyrido[4,3-e][1,4]oxazine	128
6.2.7 Synthesis of 1, 3, 4-trifluoro-5-methyl-5H-benzo[b]pyrido[4,3-e][1,4]oxazine using DBU.....	131
6.2.8 General procedure for the synthesis of 1-Ethyl-4-phenyl-1 <i>H</i> -1,2,3-triazole through flow CuAAC - DOE study	132
6.2.9 General procedure for the synthesis of 1,4-disubstituted-1,2,3-triazoles.....	134
6.2.10 Synthesis of N-benzylaniline through a modified Ullmann coupling.....	138
6.2.11 Synthesis of 1-(4-Nitrophenyl)pyrrolidine through a modified Ullmann coupling	138
6.2.12 Synthesis of 1-Nitro-4-(phenylethynyl)-benzene through a Castro-Stephens coupling	139
6.2.13 Procedure for the synthesis of 1-(tert-butyl) 3-methyl 4-(trifluoromethyl)-1 <i>H</i> -pyrrole-1,3-dicarboxylate through flow photochemistry - automated DOE	140
6.2.14 General procedure for the synthesis of 2-fluoro-N-phenylaniline through flow photochemistry	141
6.2.15 Automated optimisation of the flow photochemical synthesis of N-phenyl-4-(trifluoromethyl)aniline; residence time and nickel concentration as factors	143

6.2.16 Automated optimisation of the flow photochemical synthesis of N-phenyl-4-(trifluoromethyl); residence time, nickel concentration and photo initiator concentration as factors.....	146
7. References.....	150
8. Appendix 1.....	161
8.1 MATLAB code written for instrument control and optimisations.....	161
8.1.1 Code for creating serial objects to connect RS-232 controlled syringe pumps	161
8.1.2 Code for the optimisation of one reagent factor and residence time - two pumps.....	162
8.1.3 Code for the optimisation of one reagent factor and residence time - three pumps.....	163
8.1.4 Code for the control of four pumps for optimisation of residence time and two stoichiometry factors.....	164
8.1.5 Code for automated NMR acquisition scripts executable in Spinsolve	166
9 Appendix 2. Publication list.....	168

Collaborations

Tom Monaghan; Wolfson School of Mechanical, Electrical and Manufacturing Engineering, Loughborough University.

Nicolas Cheval, Astra Zeneca, Cambridge, UK.

Glossary and Abbreviations

3DP	Three-dimensional printing
4CzIPN	1,2,3,5-Tetrakis(carbazol-9-yl)-4,6-dicyano-benzene
ABS	Acrylonitrile butadiene styrene
AM	Additive manufacturing
API	Active pharmaceutical ingredient
API-MS	Atmospheric pressure ionisation mass spectrometry
ASA	Acrylonitrile styrene acrylate
ATR	Attenuated total reflectance
Boc	Tert-butyloxycarbonyl
BPR	Back pressure regulator
CAD	Computer aided design
CCF	Central composite faced
CFL	Compact fluorescent light
d	Doublet (NMR spectroscopy)
dd	Doublet of doublets (NMR spectroscopy)
ddd	Doublet of doublets of doublets (NMR spectroscopy)
DAD	Diode array detection
DMF	N,N-dimethylformamide
DOE	Design of experiments
dt	Doublet of triplets (NMR spectroscopy)
EI	Electron ionisation
ESI	Electrospray ionisation

FDM	Fused deposition modelling
FEP	Fluorinated ethylene propylene
FFMR	Falling film micro reactor
GC	Gas chromatography
HPLC	High pressure liquid chromatography
Hz	Hertz
IR	Infrared
<i>J</i>	Coupling constant (NMR spectroscopy)
M	Moles per litre
m	Multiplet (NMR spectroscopy)
MBC	Micro bubble column
MIR	Mid infrared
MLR	Multiple linear regression
MRA	Mass rate attenuator
MS	Mass spectrometry
NBS	N-bromosuccinimide
NIR	Near infrared
NMR	Nuclear magnetic resonance
PAT	Process analytical technology
PC	Polycarbonate
PCA	Principal component analysis
PCR	Principal component regression
PDMS	Polydimethylsiloxane
PEEK	Polyether ether ketone
PFA	Perfluoroalky
PLS	Partial least squares
PLSR	Partial least squares regression
PPSF	Polyphenyl sulfone

PEI	Polyetherimide
PTFE	Polytetrafluoroethylene
q	Quartet (NMR spectroscopy)
RS232	Recommended standard 232
RP	Rapid prototyping
s	Singlet (NMR spectroscopy)
SL	Stereolithography
SLM	Selective laser melting
SLS	Selective laser sintering
SNV	Standard normal variate
t	Triplet (NMR spectroscopy)
TEA	Triethylamine
TIR	Total internal reflectance
TLC	Thin layer chromatography
t _R	Retention time
UC/UAM	Ultrasonic consolidation/ultrasonic additive manufacturing
UNF	United Fine Thread
UV	Ultraviolet
Vis	Visible
v:v	Volume : volume

1. Literature review

1.1 Flow chemistry

Organic research in academia, and larger scale manufacturing within the pharmaceutical and fine chemical industries, is still predominantly based on batch reactors and methods that would be familiar to chemists from the turn of the 20th century. An early flow apparatus was described by Philpot in 1940,¹ having gravity fed capillaries whose flow rates were variable depending on the volume of reservoir they were attached to. Things have progressed a little further since and in recent years performing chemical reactions under flowing conditions, either continuously or as discrete aliquots, has become a valuable addition to the toolbox of organic chemistry.²

The lab scale reagent feed can be from any suitable source. Reciprocating piston high pressure liquid chromatography (HPLC) pumps afford precise flow rates, but are susceptible to blockage and wear due to the nature of their operation. Peristaltic pumps, which are more robust due to no contact between reagents and the pump mechanism, offer an excellent option. However, the flow precision, while improving, is not as high as the HPLC type pump. Syringe pumps offer a precise, and often much cheaper, way to perform flow chemistry. The greatest drawback is the inability to flow continuously for extended lengths of time, as syringes have a finite volume. In addition, they cannot pump at high pressures unless the most expensive models are used, raising the cost considerably. However, syringe pumps are often the first step for those looking to set up a cheap and capable flow chemistry system.

Flow reactors can be defined as micro or meso for anything that would be appropriate in a laboratory setting, suitable for up to $\mu\text{g-g}$ per day scale synthesis. Micro reactors will typically have channel diameters from 50-1000 μm ; meso scale reactors will have channel diameters of approximately 1-10 mm. There are many options for the reactor itself, discussed in more detail later, but the simplest is a coil of polytetrafluoroethylene (PTFE) tubing, which will provide a chemically and thermally robust reactor that can also perform some photochemistry.

Flow chemistry has been identified as valuable in early drug discovery for process intensification.³ This is primarily due to the expected advantages⁴ that flow chemistry has over traditional batch chemistry, namely precise control over reaction conditions, ease of scalability and improved heat transfer and mixing. The Jensen group⁵ have further identified areas where flow reactors may provide benefits, including accelerated reaction rates due to the ability to use higher temperatures and pressures,⁶ increased selectivity for the desired products from rapid mixing⁷ and increased control of the reaction due to laminar flow of reagent streams.⁸ The ability to perform cryogenic reactions in flow has also been shown where the high heat transfer properties of micro flow reactors allowed excellent control of the reaction conditions.⁹

Flow chemistry has also been shown to be useful for the safer handling of dangerous reagents such as diethylaminosulfur trifluoride. This compound is explosive under heating¹⁰ and reacts violently with water, in addition the fluorination by-products are also highly reactive. The Ley group showed that careful material choice and close control over reaction temperature allowed facile and safe flow fluorinations of alcohols and carbonyls.¹¹ Flow chemistry has also been used for the *in situ* generation of hazardous reagents such as diazomethane,¹² avoiding any isolation of potentially explosive compounds.

There are also specific disadvantages to flow chemistry that mean it is not always a suitable methodology. One major issue is the difficulty with handling solids, either in starting solutions or formed during the reaction in the residence volume. Due to the small channels there can often be a risk of blockage, potentially destroying a micro reactor, although droplet based chemistry may be employed in some situations to overcome these issues.¹³ They are also primarily best suited to fast reactions, a conversion requiring a 48 h reflux in xylene is not appropriate for flow conditions. However the ability to superheat solvents may accelerate reaction rates to bring them into the realm of flow chemistry, Palmieri *et al.*¹⁴ showed that the Hoffmann rearrangement of aromatic amides to the methyl carbamate product was significantly faster due to superheating the methanol above its usual boiling point.

The ability to superheat while operating under high pressures has therefore allowed the use of solvents in their supercritical state. Yan and coworkers¹⁵ were able to achieve yields of 90 % for the conversion of 6-aminocapronitrile to ϵ -caprolactam, an important industrial feedstock. This was performed by heating the starting material in water at a temperature of 400 °C and a pressure of 400 bars to give supercritical water. The residence time was short at less than 2 minutes, and this work demonstrated the benefits of flow chemistry clearly, offering a high throughput, high yielding and green synthetic route.

Although perfectly able to perform single step transformations, flow chemistry is perhaps most promisingly able to be used for multistep continuous reactions. Webb and Jamison¹⁶ reviewed the use of multistep synthesis in flow, covering such diverse methods as continuous liquid phase reactions, solid supported reactions and continuous separation and distillation.¹⁷ Varying approaches have been used for in flow separation with the Jensen group employing a fluoropolymer membrane that was selectively wetted by the organic phase, preventing the aqueous phase from passing through.¹⁸ The Ley group employed a heated stream of N₂ to evaporate dichloromethane from a mixture with dimethylformamide as it was collected.¹⁹

A continuous flow multi step strategy has several flow reactors and mixers connected, uninterrupted, in series. This approach differs from a batch process in that there is no isolation and work up between each step (Figure 1). Yoshida *et al.*^{20,21} used sequential micro reactors with static micro mixers to substitute two electrophiles into *o*-dibromobenzene, treating with *n*-butyl lithium at -78 °C before each

electrophile addition was carried out at different temperatures (-78 °C for the first, 0 °C for the second). This further demonstrates the flexibility of flow reactors, with two residence volumes easily maintained at a temperature difference of 78 °C by simply submerging each half in a separate bath.

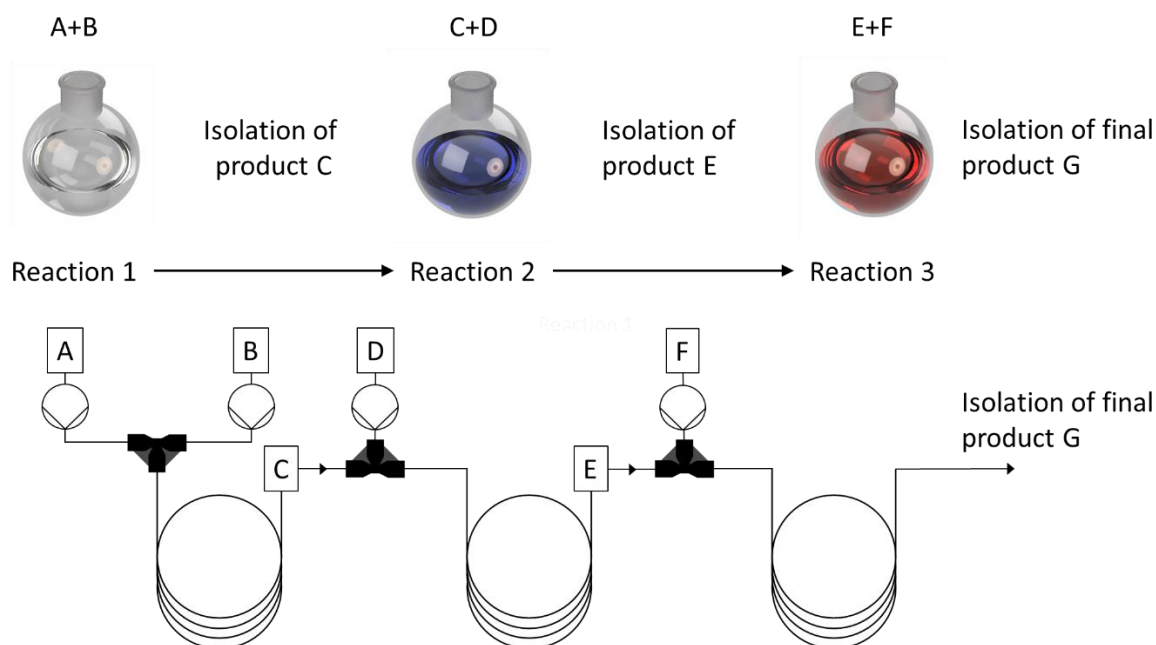


Figure 1. Illustration showing the differing approaches between (Top) batch and (Bottom) continuous flow chemistry.

The continuous flow synthesis of artemisinin was demonstrated by Lévesque *et al.*²² with 3 continuous steps employed to convert artemisinic acid to artemisinin *via* dihydroartemisinic acid with an overall yield of 39 % after purification, and an estimated 200 g maximum production capacity per day of an important active pharmaceutical ingredient (API). This process used mixed phase liquid-gas singlet and triplet oxygen reactions, as well as a same phase liquid-liquid Hock cleavage, showing the versatility of flow chemistry apparatus. Other important reactions such as the Hoffmann rearrangement, known to be useful for the total synthesis of the antiviral medicine Tamiflu, have similarly been shown to be possible in flow¹⁴ as have numerous other natural product syntheses.^{23, 24}

The synthesis of the anti-seizure medication rufinamide in overall 92 % yield over three steps was reported by the Jamison group,²⁵ utilising three reactions overall and two telescoped steps. The reaction conditions were investigated fully which revealed that the use of copper tubing led to a 20:1 excess of the 1,4-disubstituted triazole versus the 1,2-disubstituted species. Use of perfluoroalkyl (PFA) or stainless steel tubing led to 3:1 ratios in each case.

1.1.1 Flow photochemistry

The use of photo-excited oxygen reactants by the Ley group in the synthesis of artemisinin also demonstrates that flow chemistry platforms are well suited to performing photochemistry. The Brooker-Milburn group has published extensively on flow photochemistry, first reporting the use of a custom reactor, based on standard immersion well batch reactors, to carry out the photocycloaddition of maleimide and 1-hexyne to form a cyclobutene.²⁶ Their modification was to incorporate a coil of fluoroethylene polymer (FEP) tubing around a central ultraviolet (UV) emission lamp, temperature controlled through active water cooling (Figure 2). A similar set up has been employed subsequently by other groups.²⁷

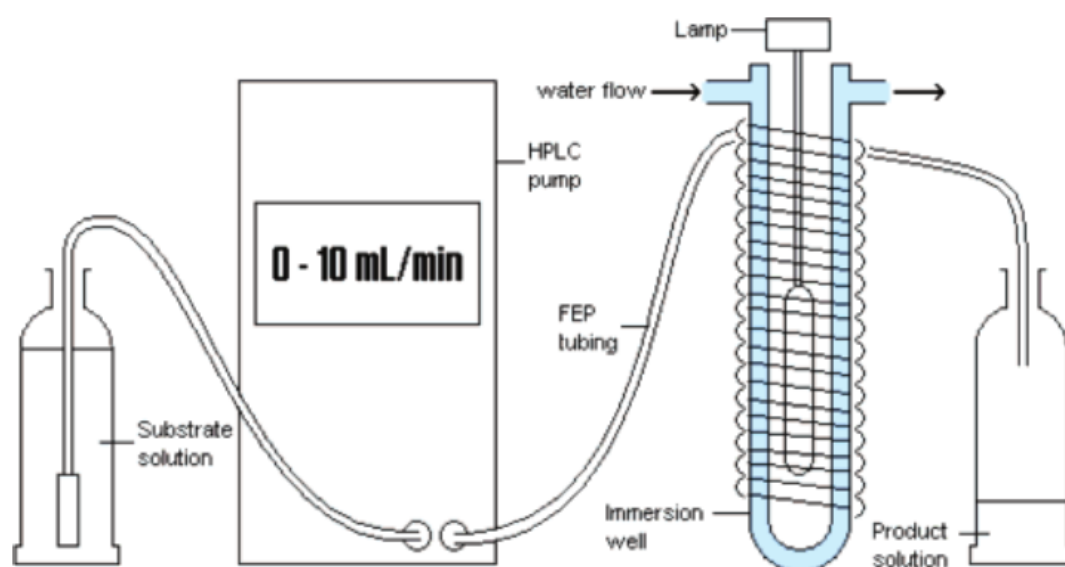


Figure 2. Custom flow through photoreactor designed and built by the Brooker-Milburn group. Figure reproduced from reference.²⁶

This flow reactor, which used FEP tubing wrapped around an immersion well containing a mercury discharge lamp, was customisable in both the number of tubing layers, length of tubing (and so residence time), and the power of the irradiating source. In addition, some further refinement was available for the transmitted wavelength - using a Pyrex well gave transmission only above 280 nm, whereas using a Vycor immersion well allowed transmission at 220 nm and upwards, showing significantly higher conversions than the Pyrex reactor.

The Poliakoff group have published numerous examples of flow photochemistry in supercritical solvents^{28,29,30} as far back as 1993, and have advanced the design of flow photochemical reactors somewhat further, recently utilising an impressive vortex reactor to perform the continuous flow synthesis of artemisinin.³¹ This reactor drew air in from the laboratory, when combined with high efficiency vortex mixing, the rapid mass transfer was great enough that pressurised oxygen was not

required. A flow photoreactor with user selectable UV wavelengths was also developed and used as part of a three stage telescoped reaction.³² Other designs have included a semi continuous flow reactor incorporating a rotary evaporator (Figure 3).³³ This was used to generate a thin film on the inside of a round bottom flask in the absence of a vacuum, which was then irradiated by light emitting diodes (LEDs), maximising transmission efficiency. The use of the rotary evaporator also afforded exceptionally easy temperature control.

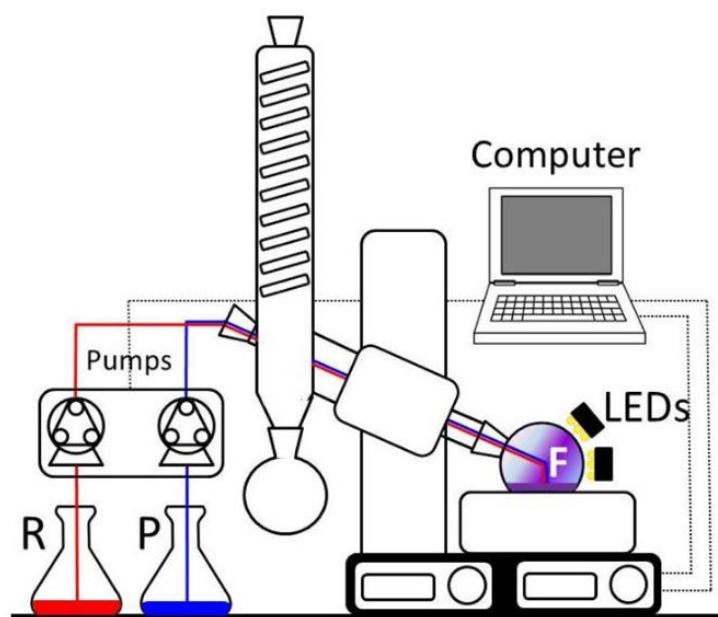
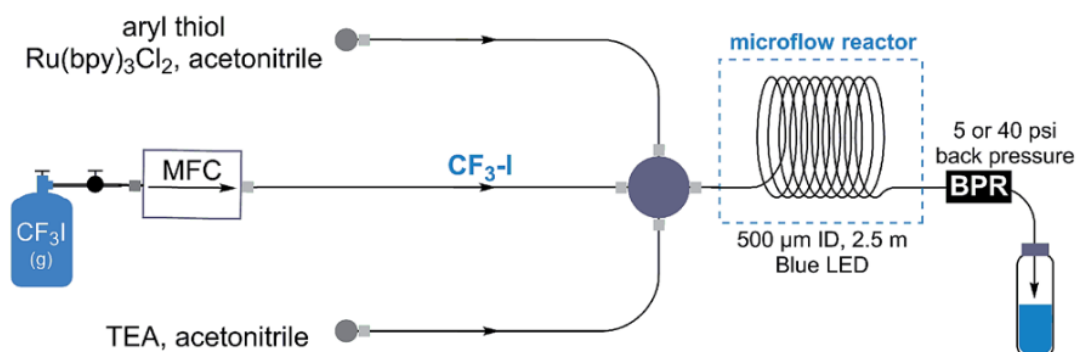


Figure 3. 'PhotoVap' semi continuous photochemistry reactor. Figure reproduced from reference.³³

Commercial photochemical flow reactors are now available from Vapourtec for visible range illumination and Peschl for UV range reactions, to name but a few. Luzchem produce closed illumination cabinets which allow the reactor tubing to be placed inside, but this is essentially a box containing the required lamps. Such a system was used by Caron *et al.*³⁴ to synthesise a number of carbazole skeletons, in good yields, using UV irradiation and residence times from 30 minutes to 3 hours.

Many useful photochemical reactions have been demonstrated in flow, including continuous flow radical benzylic brominations³⁵ in very high selectivity and yields, singlet oxygen oxidation of natural terpenes,³⁶ as well as further cycloaddition reactions.³⁷ A comprehensive review highlighted numerous other reactions, many with yields and selectivity comparable or better than the batch process.³⁸ The insertion of the pharmaceutically important trifluoromethyl group into a number of substrates was demonstrated by Straathof and co-workers in the Noel group.³⁹ They utilised household compact fluorescent lights (CFLs) and a radical CF₃ source for a number of batch reactions and were able to successfully convert the synthesis to a continuous flow system utilising blue LEDs and the dangerous and environmentally unsound trifluoro-iodomethane under pressure (Scheme 1). The Stephenson group

at Princeton have shown that other, safer, radical CF_3 sources such as trifluoroacetic anhydride or sodium trifluoroacetate, can be used with excellent yields,⁴⁰ also demonstrating the chemistry in continuous flow.⁴¹



Scheme 1. Continuous flow trifluoromethylation of thiols. Scheme reproduced from reference.³⁹

Many of these examples have employed expensive metal catalysts such as Ir and Ru.⁴² However, recently the use of an organic photocatalyst, 1,2,3,5-Tetrakis(carbazol-9-yl)-4,6-dicyano-benzene (4CzIPN),⁴³ in place of these metal compounds has been demonstrated with comparable yields.⁴⁴ The synthesis of this photosensitiser is relatively straightforward and offers a cheaper catalytic option. The absorption and emission characteristics of this type of photosensitiser can also be tuned by altering the degree and nature of the substituted groups, offering a wide variety of potential photosensitisers (Figure 4).

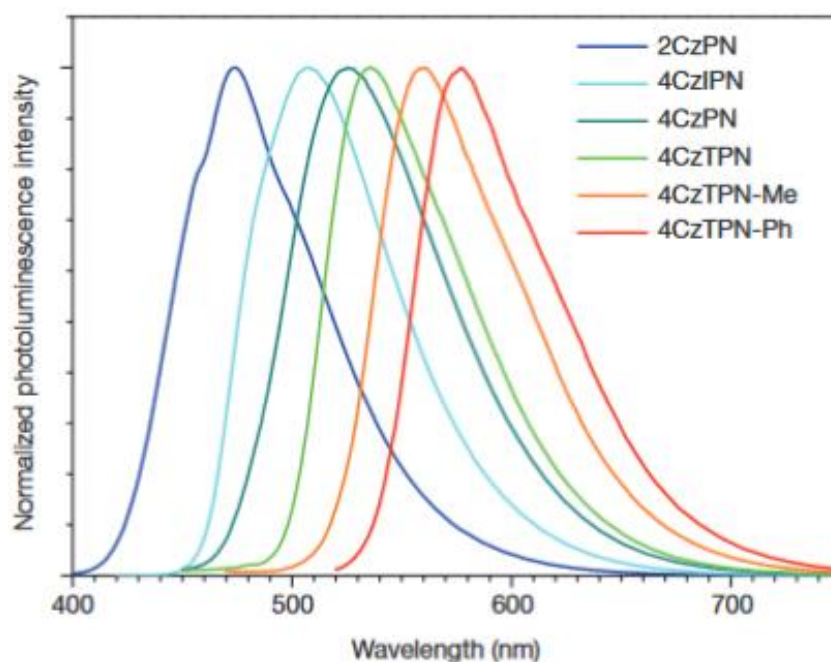


Figure 4. (Bottom left) Emission spectra for cyanobenzene photosensitisers. Figure reproduced from reference.⁴³

Another benefit to the use of a flow photo reactor is more control over the ratio between conversion and starting material degradation. This was demonstrated by Lainchbury *et al.* with 63 % conversion of starting material to the desired product, and then recovery of 20 % unreacted reagent.⁴⁵ This contrasted to the equivalent batch synthesis where no starting material would be expected to be recovered and up to 42 separate runs would have been required to get the same amount of product as a single flow experiment.

While initially the benefits of a flow process seemed clear, a recent in depth comparison by the Brooker-Millburn group between flow reactors and batch reactors suggested that the effective yields and productivities from each were almost identical,⁴⁶ although they did not factor in the ease of scale up for flow. Some benefits were still clear from the flow processes, most importantly single run productivity and the flow process was also less prone to foul up, presumably due to the constant transfer of liquid.

1.2 Reactor design

At its simplest a flow reactor is a tube of defined volume fed by one or more reagent flows at controlled rates. Other features can involve localised heating and mixing elements.⁴⁷ The use of micro reactors, that is micro engineered structures from tens to thousands of microns, was initially pioneered in industry, with early comparisons between micro reactors and running processes being made by Burns and Ramshaw.⁴⁸ They showed that a simple coil reactor of 0.1-0.25 mm internal diameter channels could be used to perform the flow nitration of benzene with good output and selectivity, and that simple parallelisation was an easy way to scale up to industrially useful throughput.

The manufacturing of micro structures builds on the advances made in micro electromechanical systems (MEMS) and is performed by various techniques. These include chemical etching of glass or steel and photo lithography of surfaces such as polydimethylsiloxane (PDMS) or silicon wafers.⁴⁹

The benefits of flow synthesis in micro scale reactors were quickly realised and numerous research groups set about investigating the possible applications.⁴⁹ An early laboratory application was the direct gas-liquid fluorination of toluene in both a falling film micro reactor (FFMR) and micro bubble column (MBC) was demonstrated, and suffered none of the explosive tendencies that had been unfortunately observed in direct fluorinations before.⁵⁰ FFMRs are elegant devices that generate thin films of flowing liquid in numerous micro channels through gravity, initially fed from an HPLC pump or similar. A gas phase reagent is passed over the surface of the film, achieving high levels of mass transfer, before the liquid reaches the exit (Figure 5).

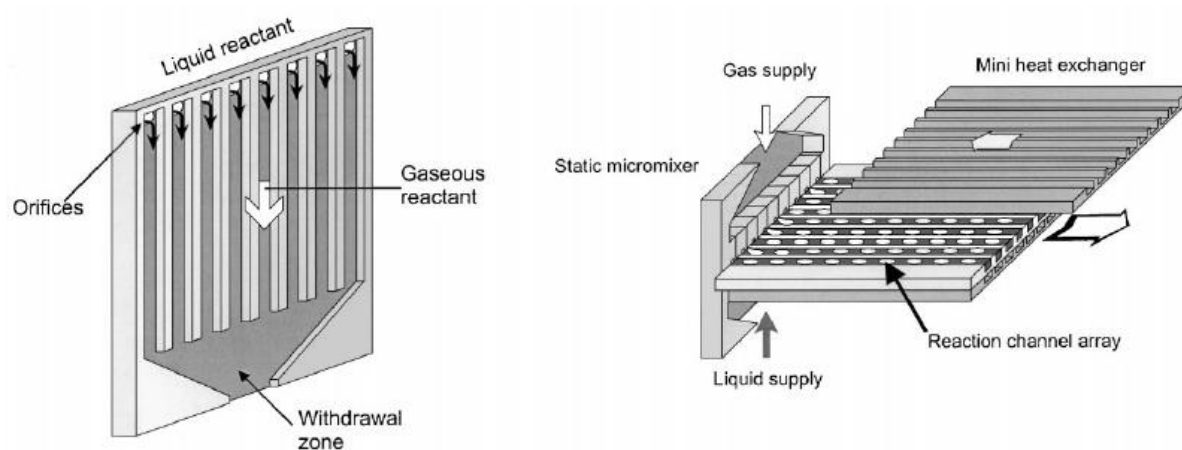


Figure 5. (Left) Falling film micro reactor (Right) Micro bubble column. Figure reproduced from reference⁵⁰

Much of the early micro reactor design innovation was around the development of ever more elaborate micro mixers. These tended to focus on generating narrower and narrower laminae for non-miscible systems,⁵¹ this would then be translated into rapid mixing for miscible systems. The main advantages to micro mixers are shorter mixing times which can become important where extremely short residence times are being used.

Temperature control of microfluidic devices can also be achieved. The addition of aluminium blocks with equipped resistive heaters to PDMS chips, as well as water cooled channels, allowed for the production of reactors with different temperature zones.⁵² This was then used to perform flow through polymerase chain reaction, a DNA amplification process often slowed down by long temperature ramping times.

Several companies started to develop turnkey systems in the 1990s and 2000s, incorporating micro reactor technology and also flow chemistry at larger scales. Syrris, a company established in 2001 specialising in micro reactor systems, introduced the AFRICA system in 2005 which incorporates pumps, temperature control and etched glass reactor chips, up to 1 mL in volume, into one system. A system using larger volume coil reactors (4-6 mL) and higher flow rate HPLC pumps is also available.

Similar etched glass reactor systems are available from Chemtrix, a 2005 spinoff from the University of Hull. Their reactor chips, supplied by Lionix BV, are more complicated than the Syrris chips with the addition of quench inlets after the residence volume (Figure 6) and are aimed towards larger scale operations.

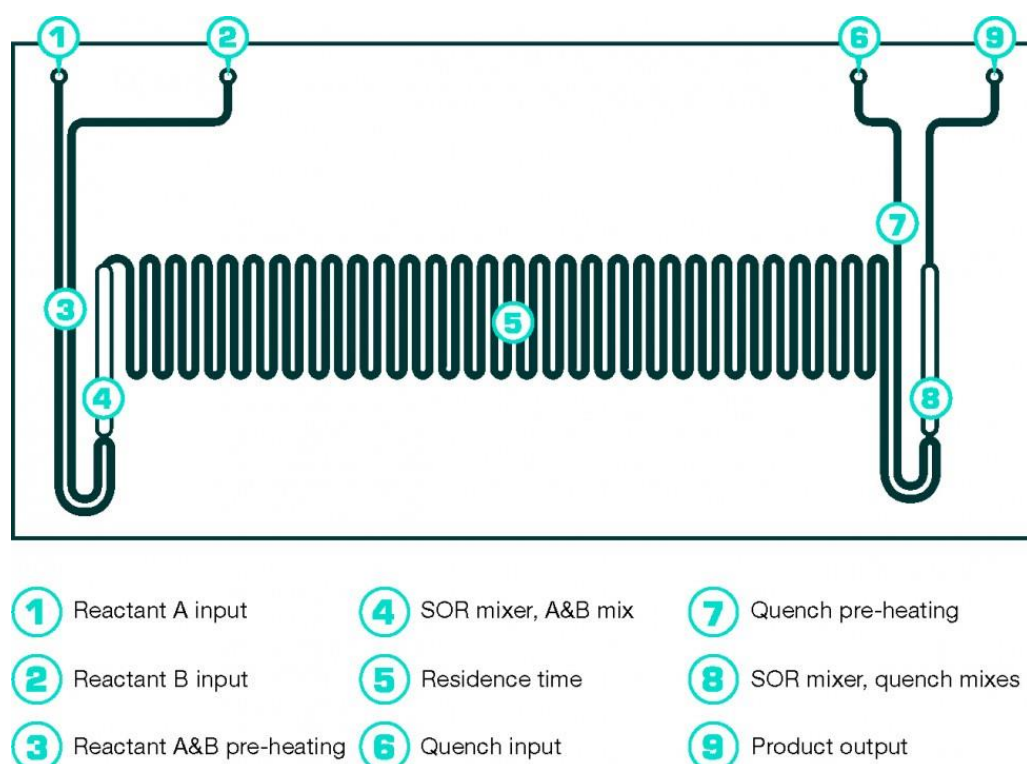


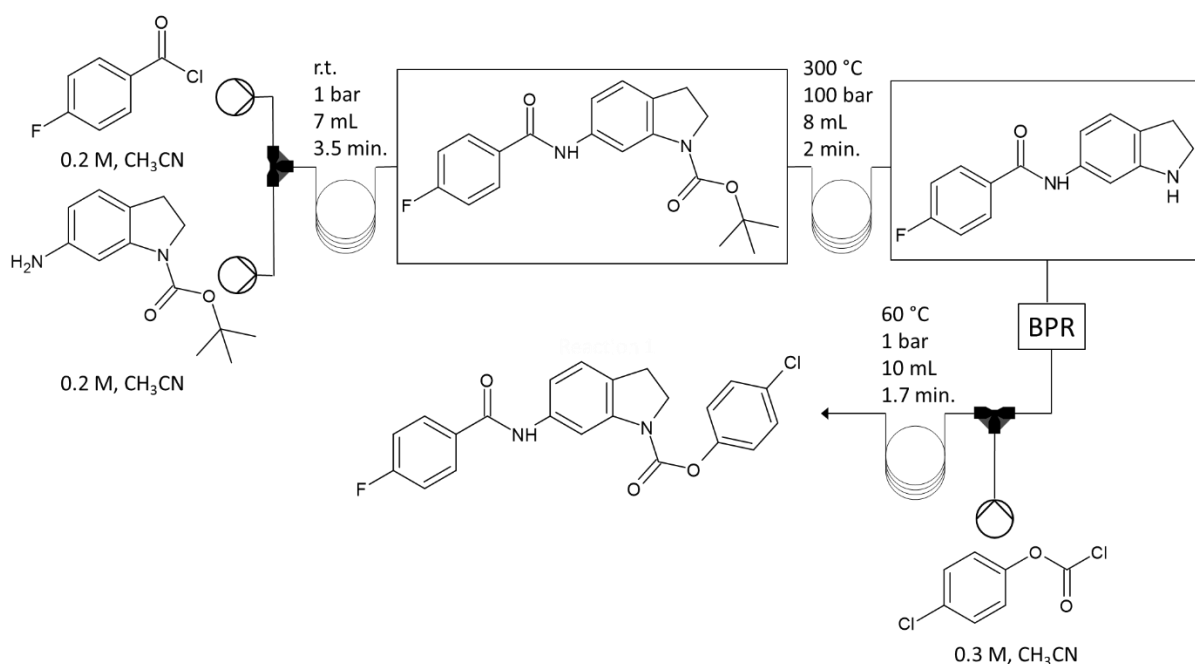
Figure 6. Chemtrix reactor schematic, staggered oriented ridge (SOR) mixer, for reactions of the type $A+B = P1 + Q = P$. Figure reproduced from reference.⁵³

Larger reactor volumes with this system are achieved through stacking of reactor chips. In this manner volumes from 0.8 to 6.5 mL are possible still using micro channel glass reactors. Larger volume systems with larger diameter channels are available with the AFRICA coil reactor, mentioned earlier, or dedicated meso scale instruments. Two meso scale systems of note are the Uniqsis flowsyn (Figure 7) and the Vapourtec E series (Figure 7), both use coil reactors in FEP or stainless steel for wide ranging reagent compatibility, with more specialised copper coils available for *in situ* catalysis. Quenching inlets are fitted using additional tubing and simple T-mixers. These systems have no special geometry, they are simply coils that can be heated or cooled.



Figure 7. (Left) Uniqsis Flowsyn Figure reproduced from reference.⁵⁴ (Right) Vapourtec E series with photochemistry reactor. Figure reproduced from reference.⁵⁵

ThalesNano produce commercial flow reactors with more specific applications in mind such as the H-cube flow hydrogenator, which generates H_2 *in situ* from the electrolysis of water, and combines it with consumable catalyst cartridges; the Icecube, which allows continuous flow reactions at temperatures down to -70 °C; and the Phoenix flow reactor which allows operation up to 450 °C. The latter of these has been recently employed by Bogdan *et al.*⁵⁶ for Boc deprotections in continuous flow; requiring no additional reagents to be added and followed by acylation of the deprotected amine (Scheme 2).



Scheme 2. Multistep synthesis of carbamates with Boc deprotection carried out in the Phoenix flow reactor.⁵⁶

The Flowsyn also contains the option for a flat profiled chip heater, allowing the use of glass mixing chips, or with the additional column holder, packed columns with scavenging resins or solid supported reagents can be used. Vapourtec have further distinguished their system in the market by offering fitted photochemical reactor modules with several high intensity LED lamps of narrow wavelength range, allowing a wide choice of photosensitisers. Bannock and others with the de Mello group have somewhat punctured the vendor hype surrounding flow chemistry and pointed out that chemists can still enjoy the benefits of flow reactions without using these highly engineered systems.²

The heating of reactors in these commercial systems takes place either by physical contact with a plate heated in turn by a resistive coil, or by circulated air heating. Adeyemi *et al.*⁵⁷ simplified the set up to achieve direct resistive heating of the reactor coil itself. By using a steel coil and applying an electric potential across it, controllable heating could be achieved, at up to 400 °C. The heating was also extremely fast, reaching 400 °C within 5 minutes, far quicker than any commercial flow system. Combined with a water cooled back pressure regulator the system was capable of maintaining these temperatures at up to 200 bar, coming very close to the performance of the commercial Phoenix reactor system.

1.2.1 Additive manufacturing for reactor design

Additive manufacturing (AM), colloquially known as 3D printing (3DP) or rapid prototyping (RP), is a technique that builds objects layer by layer using a computer aided design (CAD) model converted to a tessellating network of triangles. The use of CAD software for the sketch allows almost complete

freedom in the design of an object; microstructures such as serpentine reactor volumes can be designed with precision and repeatability for extremely accurate layouts.

The freedom in design means that any geometry can be utilised, most traditional manufacturing techniques for meso and micro reactors are limited to two dimensions or simple tubes, AM offers the potential to incorporate more complicated features with ease. In addition many glass etching techniques are isotropic,⁵⁸ meaning that a curved profile develops and channels can never be deeper than they are wide. AM does not suffer from this limitation - indeed this profile (Figure 8) can be designed if desired as long as it is within the build resolution of the instrument (up to 25-50 μm for the most advanced AM instruments). There are numerous processes under the umbrella term of AM,⁵⁹ some of the more common ones are described briefly below.

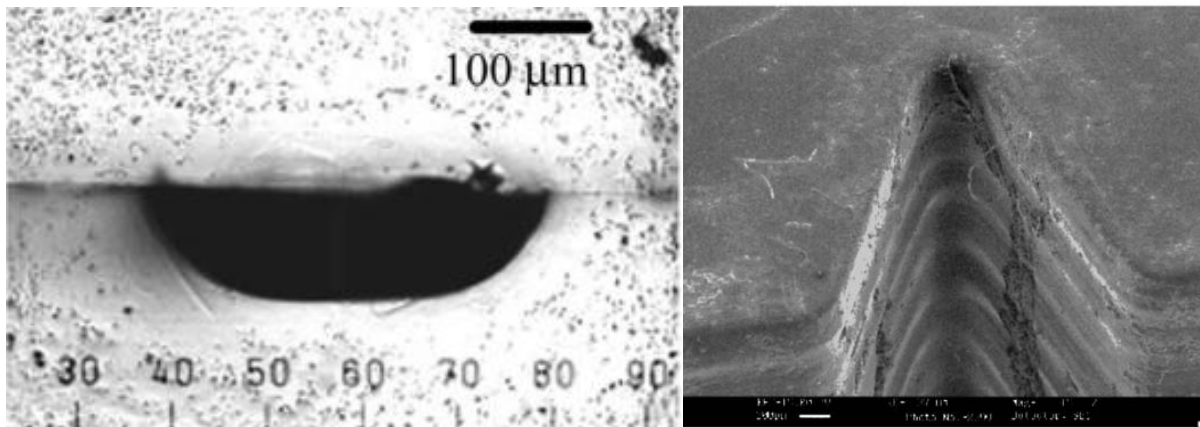


Figure 8. (Left) End on view showing typical channel profile as a result of glass etching⁵⁸ (Right) CAD designed notch built into SL object. Figure reproduced from reference.⁶⁰

1.2.1.1 Fused Deposition Modelling

Fused deposition modelling (FDM, Figure 9) operates by extruding a thermoplastic filament through a nozzle heated to a temperature above the glass transition temperature of the plastic chosen. The nozzle then traces out the object onto a platform slice by slice within two dimensions, before moving upwards by a predetermined layer height, claimed to be as low as 20 μm for high end instruments but typically a minimum of 100 μm , and beginning the next layer on the now solidified first layer.

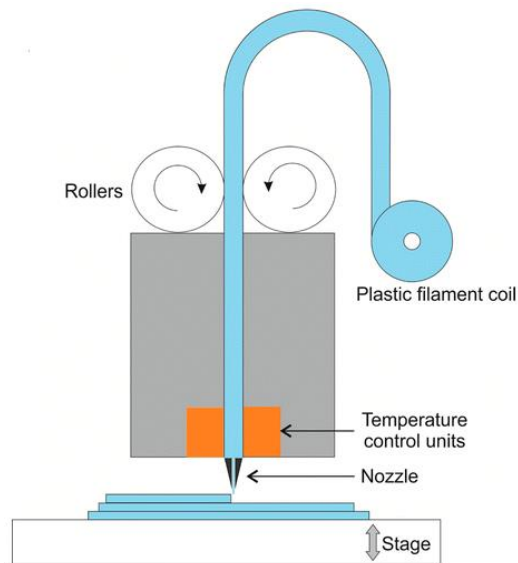


Figure 9. Schematic of an FDM 3D printer. Figure reproduced from reference.⁶¹

Acrylonitrile butadiene styrene (ABS) is the most common material used in FDM, however there are now numerous others with much greater chemical compatibility and thermal resistivity such as polycarbonate (PC), acrylonitrile styrene acrylate (ASA), polyphenyl sulfone (PPSF) and polyetherimide (PEI).

1.2.1.2 Stereolithography

Stereolithography (SL) builds objects *via* the photo polymerisation of acrylate monomer resins with a UV laser (Figure 10). The object is formed layer by layer from a vat of liquid resin with a stage dropping by a specified distance to provide a new supply of fresh resin.

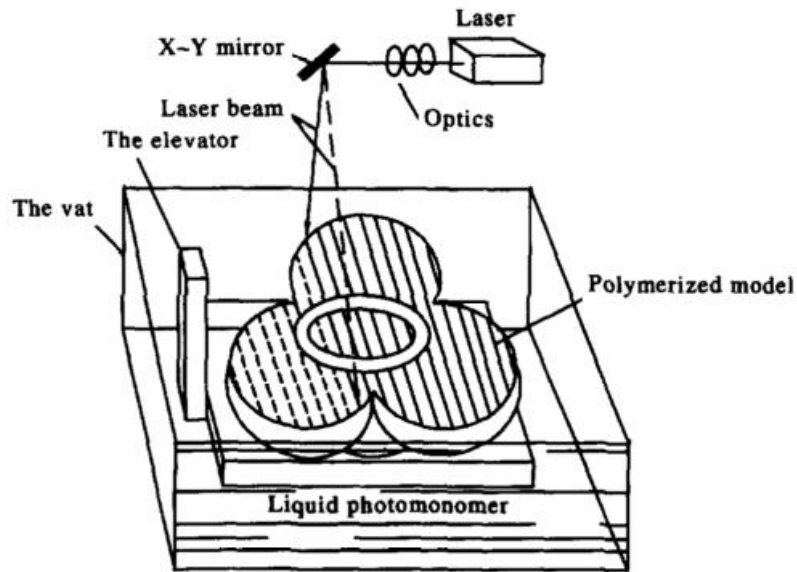


Figure 10. Schematic of an SL 3D printer. Figure reproduced from reference.⁵⁹

As most of the resins are acrylate based they have issues with chemical compatibility and thermal resistivity, yet are mechanically robust.⁶⁰ Ketones or chlorinated solvents will cause destructive swelling to occur but solvents such as ethanol and hexane can be used. Nevertheless it is one of the most popular AM techniques as the build resolution is very high, features as small as 20 μm (Figure 11) have been produced through a micro SL process developed by Zhang and coworkers.⁶² These parts were prepared from a UV curable ceramic powder - a blend of ceramic, resin monomer and photoinitiator, and sintered at high temperature to burn off the resin.

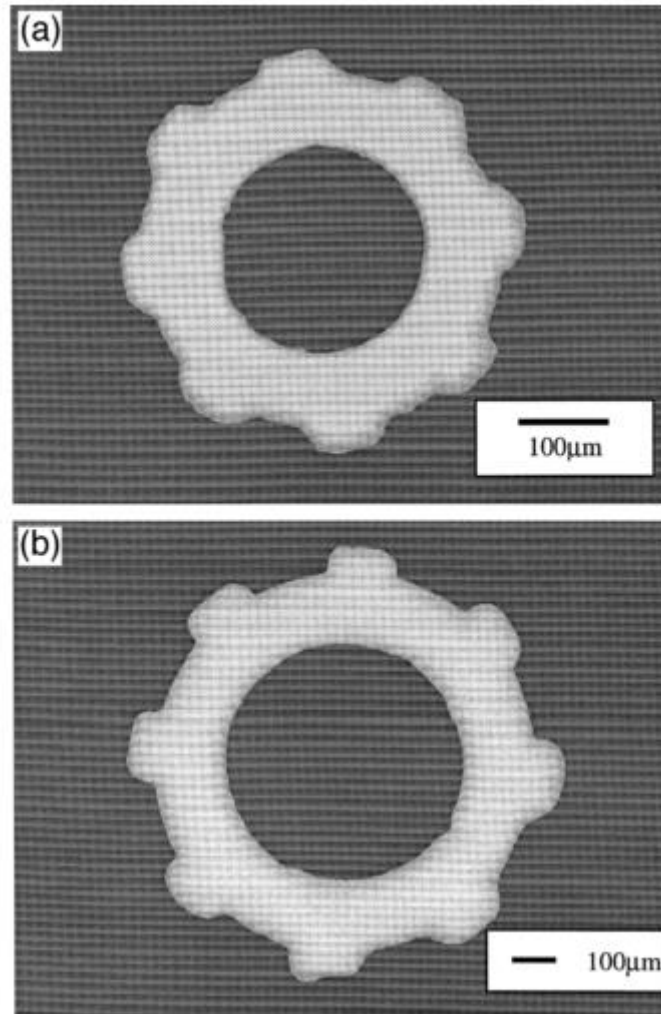


Figure 11. SL printed objects with features as small as 20 μm . Figure reproduced from reference.⁶²

Some care must be taken with the build orientation of the part. Diagonal and curved surfaces in particular can exhibit a large degree of stair stepping or staircase effects, and to minimise this effect, and ensure that resolution is not lost, as many surfaces as possible should be aligned with the vertical plane. A comprehensive computational approach to optimising the build orientation of parts was derived by Cheng *et al.*,⁶³ allowing the best build manner for complicated parts to be determined.

1.2.1.3 Selective laser sintering / selective laser melting

Selective laser sintering (SLS) is used to generate non-fully dense parts from a powder bed of powdered material. Typical materials have included nylon or metals and metal alloys, however as the parts are not fully dense they are of little practicality for the bodies of flow reactors. Other pieces of a composite part may be produced using this technique.⁶⁴

Selective laser melting (SLM) is related to SLS, however it is capable of producing near fully dense parts from beds of powdered material. As a layer is completed a stage drops to expose a new layer of

powder. As a high temperature laser is used for the production some high levels of stress can be built up in the parts, with deformations occurring if care is not taken. SLM allows the use of metal powders such as iron, titanium and aluminium and various elements such as carbon, silicon and phosphorus can be added to aid processability.^{65,66}

Both SLM and SLS suffer from residual metal powder remaining inside the fluidic channels after printing. This powder may exhibit a degree of partial melting, making it extremely hard to remove. This difficulty is increased by longer tubes, becoming all but impossible for reactors of any substantial length. SLM has been used for 0.9 mm I.D. channels,⁶⁷ although the reactor tubing was only 60 cm, equating to a volume of approximately 1.2 mL. As this piece was intended for use as a packed HPLC column the group did test the part to pressures greater than 400 bar, illustrating the potential for high pressure chemistry within SLM parts. The final finish on the internal channels was also visibly rough (Figure 12), and while this was not a problem for a packed column it could inhibit laminar flow and cause flow impingement for chemical reactions.

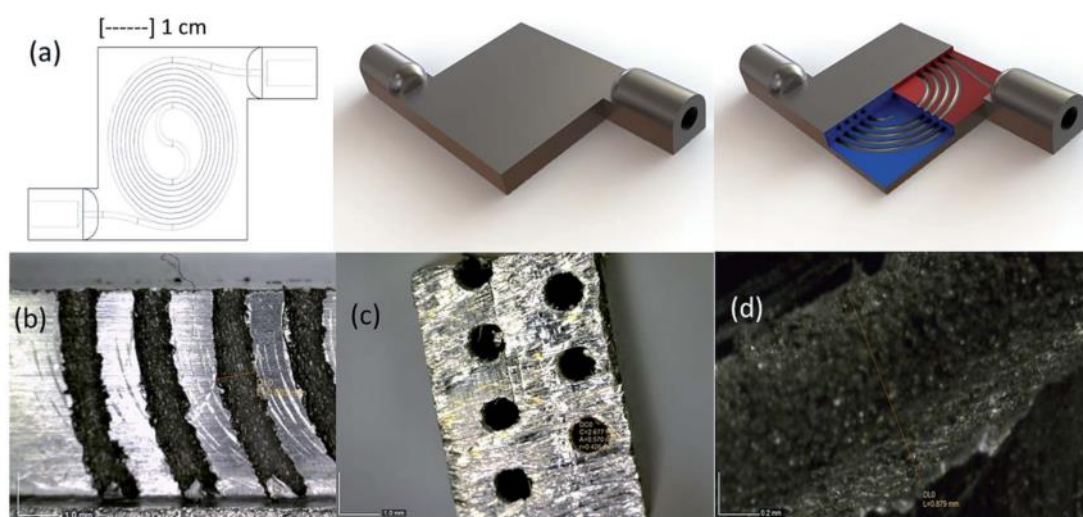


Figure 12. (a) CAD model for SLM column body (b) Resulting surface from SLM process on 0.9 mm I.D. channels. Figure reproduced from reference.⁶⁷

1.2.1.4 Ultrasonic consolidation

Ultrasonic consolidation (UC) is a relatively new AM technique that can be used to bond or weld metal foils of around 100 μm thickness, typically aluminium or iron alloys, together sequentially to form 3-D objects.⁶⁸ The bond is formed through rapid oscillation of the metal foils combined with compression (Figure 13) which disrupts metal oxide layer. UC incorporates computer numerical control (CNC) machining to remove unwanted material and generate the 3D structure, and for this reason is often referred to as a hybrid AM technique. As there is no melting of the materials as there is with SLM the

material finish is often superior, however the parts are typically smaller in scope with lower build heights currently achievable than in SLM.

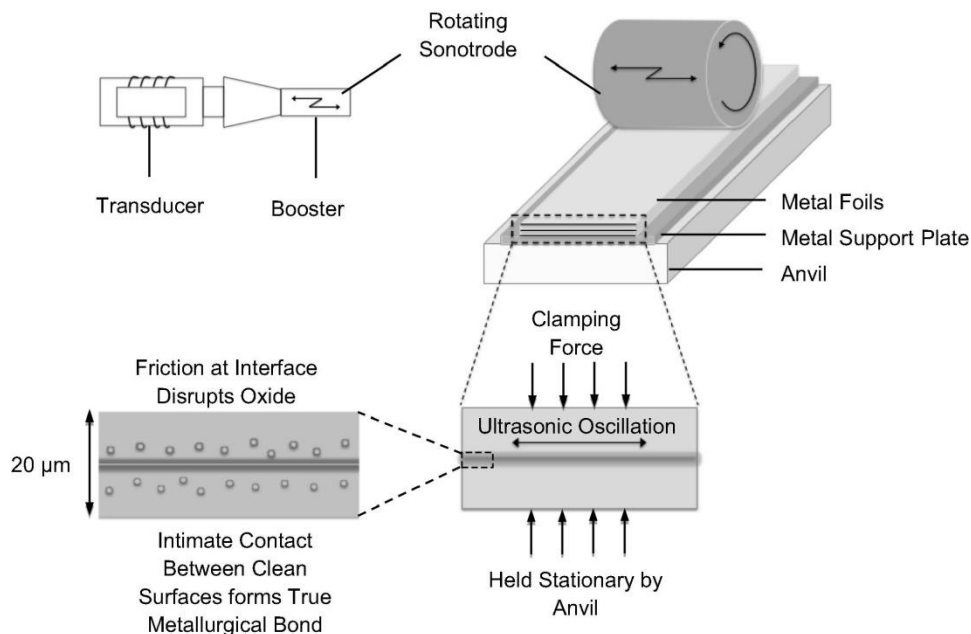


Figure 13. Schematic showing the UAM bonding process. Figure reproduced from reference.⁶⁹

There are currently no published applications of UAM for flow chemistry, however there are instances of heat exchangers being produced by the company Fabrisonics.⁷⁰ As these are nothing more than repeated structures of hollow pipe work (Figure 14) there is no barrier whatsoever to UAM being utilised for the production of flow reactors. Further to this, the finished part specification of UAM heat exchangers indicates burst pressures in excess of 3000 PSI, making them suitable for high pressure and high temperature chemistry applications.

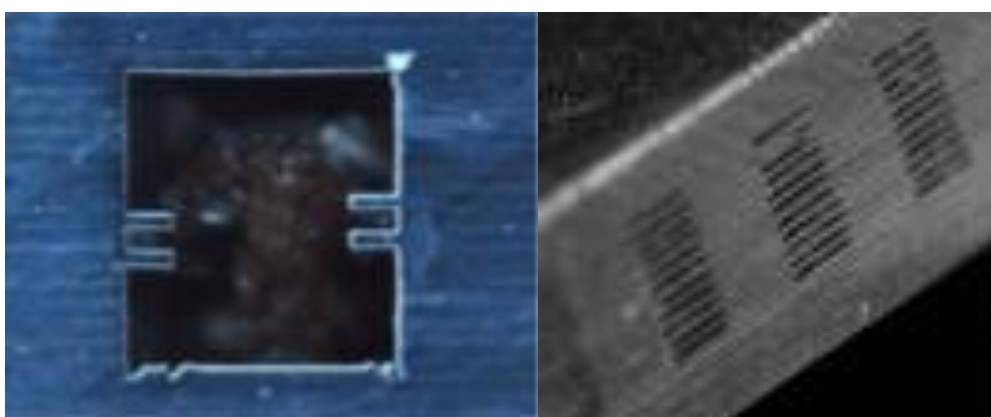


Figure 14. (Left) 1.27×1.27 mm channels produced by UAM. (Right) Layered channels produced by UAM of 0.76×0.15 mm dimensions. Figure reproduced from reference.⁷⁰

1.2.2 Applications of AM for the chemical sciences

While there have been many applications for the use of additive manufacturing in analytical chemistry, biological applications and even for the production of teaching aids,^{71–74} in recent years steps have been made towards the use of additive manufacturing for chemical reactors in both flow and batch applications. An FDM system was one of the first reported examples, used by the Cronin group to make low volume reactors out of polypropylene (PP), these were then used to carry out an imine formation from benzaldehyde and benzylamine in flow.⁷⁵ They also used a less sophisticated printing procedure to prepare reusable batch reactors designed to add reagents in a controlled manner. The reactors could be printed with variable volumes for an internal mixing chamber (Figure 15), and as the reagent wells were kept the same volumes the authors claimed control over the reaction outcome, with a smaller mixing chamber effectively lowering the equivalents of one reactant. More interesting was the use of pauses during the manufacturing step that allowed them to integrate a microscope slide and glass frit to allow basic spectroscopic monitoring of the reactions.⁷⁶

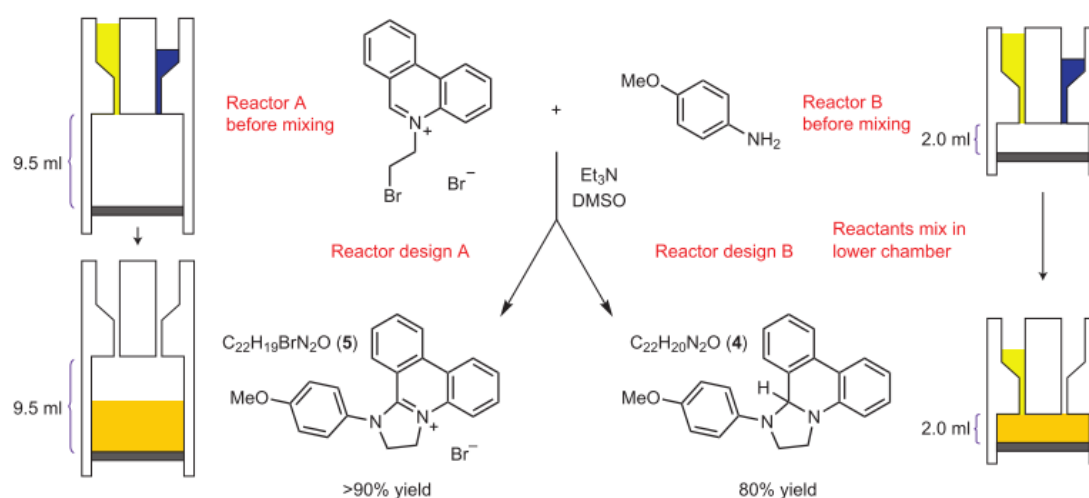


Figure 15. 3D printed reactionware with easily configurable volume for reaction control. Figure reproduced from reference.⁷⁶

Capel *et al.*⁷⁷ showed that some of the AM techniques could produce useful parts for flow chemistry, with several highly intricate objects being designed and made. Importantly this work identified that FDM and non-metal SLS did not typically produce fully dense parts and so had a tendency to leak under the elevated pressures that would be expected in flow chemistry. SL and SLM did produce dense parts and could be used for practical reactors. These included an SL reactor with 3 mm diameter channels and a total volume of 23 mL (Figure 16) that was used to oxidise aldehydes to their corresponding methyl esters. In all cases the yields were comparable to those achieved in a standard tubular flow reactor following the methodology given by Leduc *et al.*⁷⁸ A complicated geometry SLM reactor was constructed from titanium which had excellent solvent compatibility and thermal resistivity (Figure 14).

In the same work a comprehensive investigation into solvent compatibility of SL parts was performed, producing a valuable reference table for chemists using these AM techniques for reactor production.



Figure 16. SL coil reactor with split and recombine mixer. Figure reproduced from reference.⁷⁷

Recent work carried out by the Hilton group at University College London has utilised FDM to print polypropylene reactors.⁷⁹ By cleverly altering the instrument settings to give overlapping layers of printed material, they found the reactors to be leak tight and capable of performing flow chemistry. By further designing the reactors to fit into the column heater module of the Uniqsis Flowsyn a number of S_NAr reaction were performed at temperatures up to 150 °C. This represents a significant advantage for 3D printed reaction ware as the cost of FDM printing is typically the lowest of all mainstream techniques. Other techniques for improving the profile of FDM parts, such as exposure to acetone vapour, have been tried with some success by other groups.⁷²

SL has also been used to produce microfluidic scale pieces as its build resolution is high enough for the small geometries required. Bhargava *et al.*⁸⁰ produced a series of individual elements that can be combined in any manner to give the required functionality for whatever reaction is being performed, which they likened to the modular building toy Lego. These units included straight and right-angled channels, T-junctions, mixers and even IR sensors.

Taking full advantage of the high build resolutions Okafor *et al.* used SL to produce continuous flow reactors for the production of silver nano particles.⁸¹ A tubular reactor with baffles was produced, and taking the concept further they managed to build a continuous oscillatory baffle reactor (COBR) through SL, utilising a syringe pump to oscillate the baffles.

1.3 Online analysis for reaction control and optimisation

The nature of flow chemistry means that integration of analysis is potentially easier than for batch reactions. Although online monitoring is possible with batch chemistry it usually requires numerous dilution steps to prepare samples. Integration of online analysis that can provide information on the

progress of a reaction can then be used to make changes to parameters as required. Analyses that provide high levels of structural information, such as mass spectrometry (MS), nuclear magnetic resonance (NMR), or vibrational spectroscopy, are obvious candidates.⁸²

1.3.1 Online monitoring through mass spectrometry

The use of mass spectrometry for online analysis of flow chemistry is obviously desirable due to the high degree of structural specificity that it offers. An application of electrospray ionisation (ESI) has been rapid reaction acceleration in ES droplets to predict the outcome of subsequent flow experiments, allowing rapid solvent and reagent screening.⁸³ For an N-acylation reaction, a step in the synthesis of diazepam, ESI droplets offered an acceleration factor of 35 versus 25 for Leidenfrost droplet experiments performed on a standard hotplate.

Until recently the instruments available were those used for analytical work, often large instruments requiring separate high vacuum pumps. The onset of small footprint instruments, particularly the Advion compact mass spectrometer (CMS) and Microsaic's prosaically named molecular ion detector (MID), has opened the possibility of online MS without the need for large analytical systems. The Advion system resembles an analytical system and still requires a separate vacuum pump, but the advantage is that its operation is almost the same as any other ESI mass spectrometer; therefore the knowledge base built for widespread ESI instrumentation is applicable to the compact system. The Microsaic system relies on a micro spray chip, requiring a high level of flow splitting for any flow rate into the instrument above 5 μLmin^{-1} . The large benefit to this is that no external vacuum pump is required, allowing the instrument to be highly portable as it requires only a nitrogen supply to function; however, the spray chip is susceptible to blockage due to the narrow capillaries within.

A relatively large number of approaches have been taken to apply mass spectrometry to batch reaction monitoring. Perhaps the simplest of these is contactless atmospheric pressure ionisation/electrospray ionisation (C-API/ESI) mass spectrometry, where one end of a tapered capillary is placed into the reaction and the other end located near to a spectrometer inlet, allowing the analysis of volatile analytes present in the headspace of the reaction flask (Figure 17). Addition of a positive pressure of inert gas to the reaction flask increased the signal to noise and this method has been used to monitor ester deprotection *via* the Zemplén reaction as well as acetylations, and in the work of Yan *et al.* an entire synthetic route of 4 steps was monitored.⁸⁴⁻⁸⁶ A similar batch monitoring method was performed by McCullough *et al.*⁸⁷ where a small amount of reaction mixture was withdrawn and nebulised back into the reaction flask where it was then aspirated *via* a Venturi pump into an ESI source for analysis. This showed very clearly the hydrolysis of ethyl salicylate to salicylic acid.

A more complicated system for batch analysis by MS was demonstrated by Pulliam *et al.*,⁸⁸ using pressurised air to extract volatile analytes of interest into a custom ion trap mass spectrometer. This

system also included a rotary sample selector, printed by FDM and actuated with a stepper motor, with automation and control through an Arduino computer. Integration of all these components allowed monitoring of up to 6 batch reactions continuously over several hours, applied to both different reactions and to variations of reaction conditions. While applied predominantly to monitoring different reactions, this system could also be used to decrease the time required for a systematic reaction optimisation, as well as perform online derivatisations prior to analytes entering the mass spectrometer.

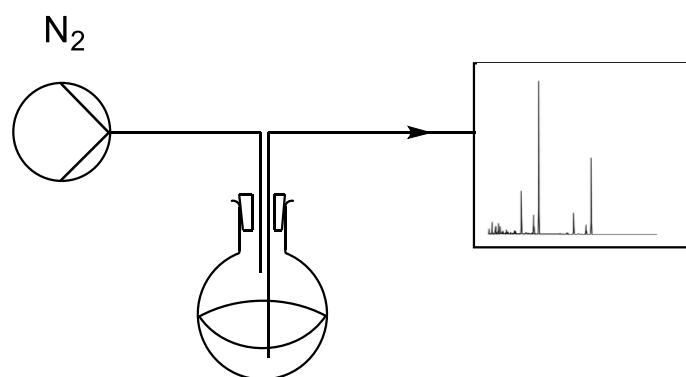


Figure 17. Schematic for the contactless atmospheric pressure electrospray ionisation analysis of batch reactions

It is simple to divert portions of flowing reactions through valves to supply instruments, and as flow chemistry typically requires that no solids be present the reaction is already in a state amenable to chromatography or mass spectrometry. At line API-MS was used to monitor a batch Knoevenagel condensation⁸⁹ but required no fewer than four HPLC pumps to dilute and modify the sample ready for analysis, in addition the generated traces were noisy. A similar system for the monitoring of flow chemistry was realised by Browne *et al.*⁹⁰ as part of the Ley group, using a 5 μL loop to periodically transfer aliquots of flowing reaction mixture to a compact mass spectrometer after two dilution steps.

It is recent work by Holmes *et al.*⁹¹ where the need for such extensive dilution, which adds to both system complexity and reagent wastage, has been minimised. By using a 60 nL loop as the sampling valve, rather than the 5 μL loop used by the Ley group, only one pump delivering make up flow to the ESI-MS was required, a significant improvement on the previous reported work.

MS for continuous analysis of flow chemistry was utilised by Bristow *et al.*⁹² at AstraZeneca who interfaced a miniaturised ESI-MS instrument into a Hofmann rearrangement performed in a 100 μL micro flow reactor using a mass rate attenuator (MRA) to quantitatively split the reaction flow, using a make-up flow to ionise the analytes (Figure 18). The precise and high rate of flow splitting afforded by the MRA meant that again only one pump was needed to supply make up flow to the MS inlet. The $[\text{M}+\text{H}]^+$ ions for the amide starting material, isocyanate intermediate and the amine product were monitored and trends for abundance against reaction temperature plotted, from which they were able to

show that 80 °C gave optimum conversion. Some issues were encountered with detector saturation, meaning levels of the isocyanate appeared constant at all temperatures; in addition, some ionisation suppression was observed when results were compared to offline LC/MS.

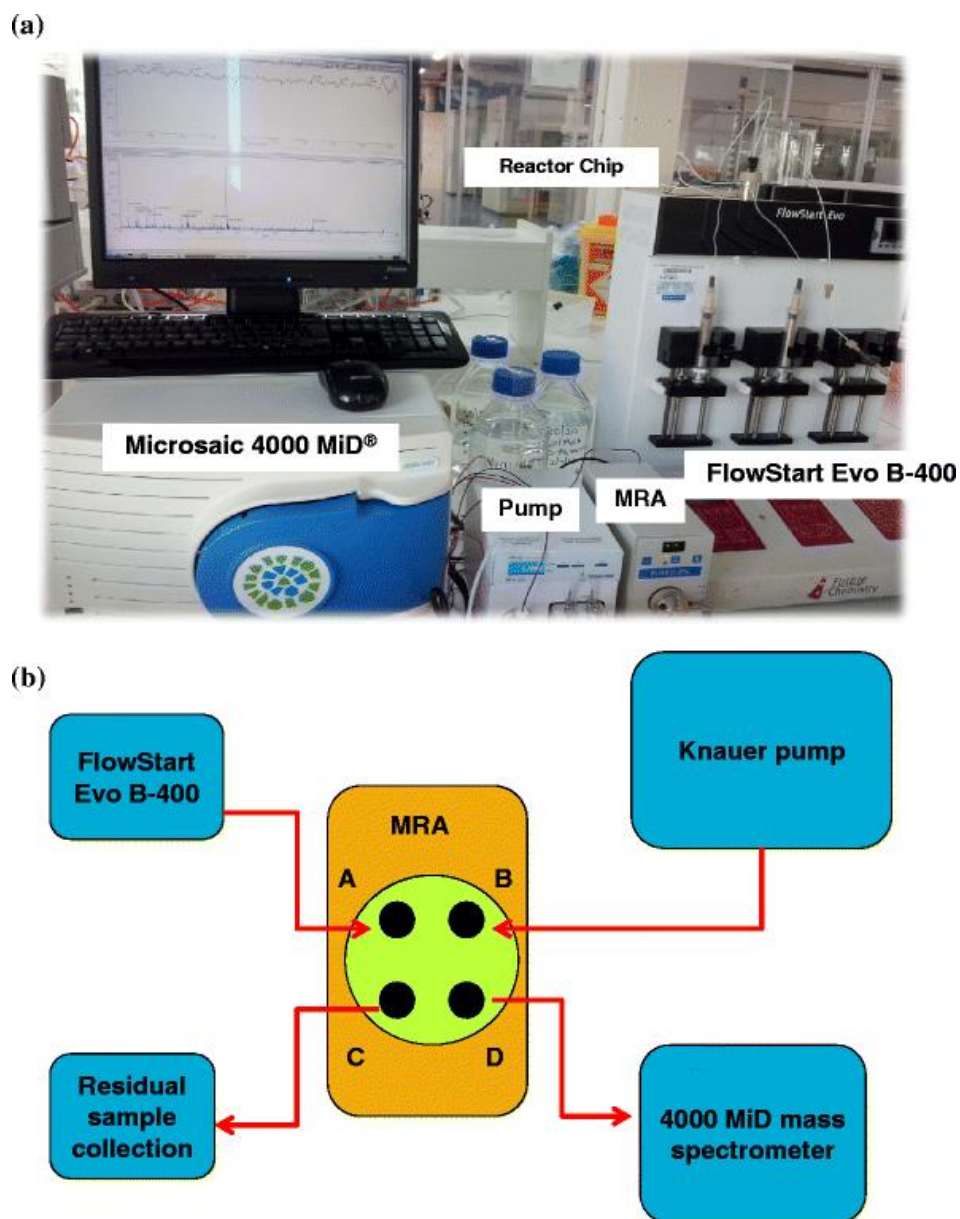


Figure 18. Image and schematic for the online monitoring of flow reactions using a miniature mass spectrometer. Figure reproduced from reference.⁹²

1.3.2 Online monitoring through chromatography

Integration of online HPLC for continuous reaction monitoring was performed by Kittiwachana *et al.*⁹³ at GlaxoSmithKline. An aliquot of reaction mix was removed and diluted automatically approximately three times per hour for an 83-hour reaction. After a simple separation the chromatograms were normalised and analysed in MATLAB without the need for user intervention, and statistical data on the

process performance was generated for inspection. Integration of chromatography offers a large amount of information, especially if diode array detection (DAD) is also used.

1.3.3 Online monitoring through spectroscopy

Other than simple probes such as pH and temperature loggers, spectroscopic monitoring is the easiest technique to integrate into flow chemistry, either by probes or flow cells. Multivariate spectroscopic monitoring⁹⁴ has been a crucial part of Process Analytical Technology (PAT) for continuous process monitoring since 2004 guidance from the US Food and Drug Administration (US FDA).⁹⁵ The use of spectroscopy in this manner has not been at all widespread in lab based organic synthesis, remaining skewed towards analytical methods;⁹⁶ the ease of scalability in flow chemistry - in this case down from an industrial or pilot plant, could allow the use of multivariate methods with many of the common spectroscopy techniques employed in a typical organic research lab. A high temperature and pressure flow cell was utilised by the Poliakoff group in 2004 to monitor the hydrolysis of acetonitrile in near critical water with Raman spectroscopy,⁹⁷ and *in-situ* IR was used to minimise residual hydrazine in a pharmaceutical intermediate,⁹⁸ either of the techniques can be easily combined with multivariate calibration methods which allow more detailed information to be obtained from single spectral measurements.

The use of IR for reaction analysis is widespread, partially due to the availability of the Mettler Toledo ReactIR and FlowIR instruments as turnkey analysis systems which use attenuated total reflectance (ATR) diamonds housed in probe tips or flow cells. These systems have been used by the Ley group⁹⁹ to monitor fluorinations with diethylaminosulfur trifluoride, oxazole formation and hydrogenations with impressive results. The Flow IR system further was used by Brodmann *et al.* to continuously monitor the previously unreported generation of Grignard reagents in flow.¹⁰⁰

However, the use of ATR diamond cells does introduce a 'dead spot' in the spectrum from 2300 to 1850 cm^{-1} due to the diamond absorbance. The use of a transmission flow cell with CaF_2 windows either side of a 25 μm pathlength to monitor the two step hydrolysis of 4-hydroxy-methylbenzoate and diethyl phthalate has been reported.^{101, 102} CaF_2 shows no significant absorbance in the region 3500-800 cm^{-1} so does not suffer the losses that a diamond ATR cell can suffer from. In addition, the use of microfluidic dimensions means that the path length is almost of the same order of magnitude as that found for ATR evanescent wave penetration, so excessive attenuation of the light is reduced. Combined with band target entropy minimisation (BTEM), kinetic data for the reaction could be extracted from multi component infrared (IR) spectra collected throughout the reaction, giving rise to the kinetic profiles for the reaction (Figure 19).

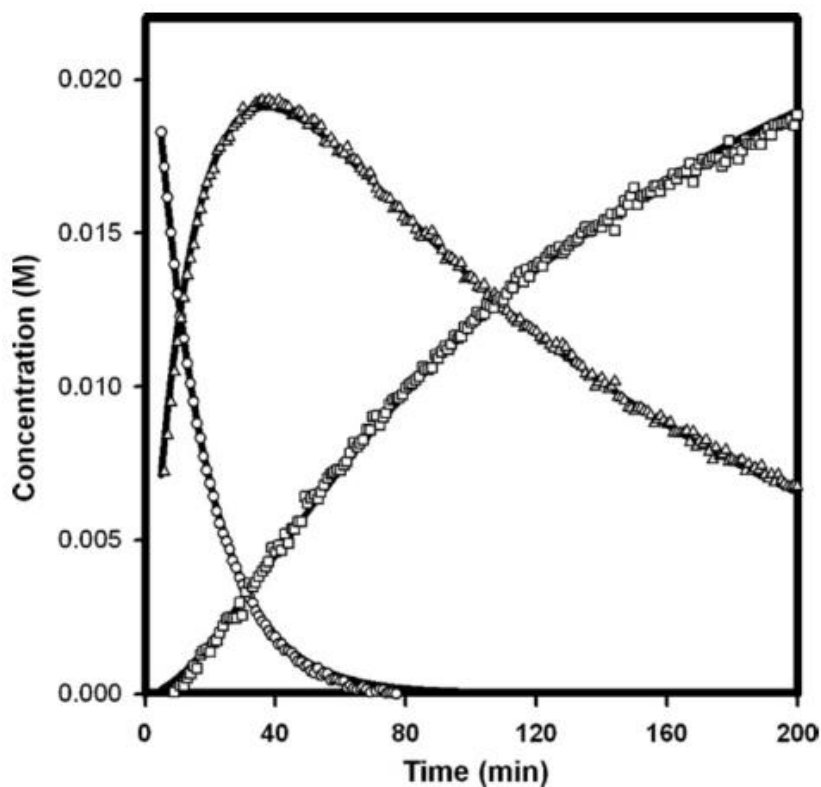


Figure 19. Reaction concentration profiles after BTEM deconvolution. Figure reproduced from reference.¹⁰²

While diamond can marginally limit the useful wavelength range of mid-IR spectra numerous material choices are available for ATR prisms including ZnSe, fused silica, quartz, sapphire and Ge. A particularly interesting application was the integration of an ATR prism onto the surface of a microfluidic chip (Figure 20).¹⁰³ By expanding the field of view of the light source and using a focal plane array detector a region of microfluidic channels could be imaged and the channels discerned from the rest of the chip, offering a powerful means to monitor reactions *in situ* and at numerous residence times.

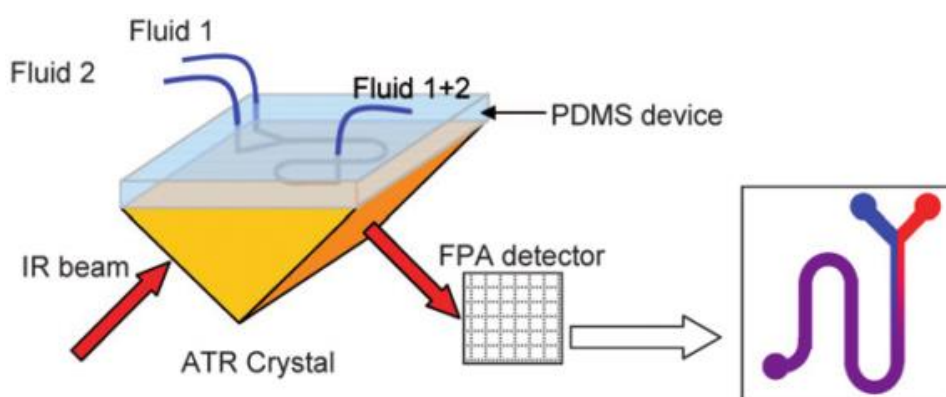


Figure 20. Integration of ATR prism with microfluidic chip for channel imaging of flowing reagents. Figure reproduced from reference.¹⁰³

Similarly, although it carries less structural data than Raman or IR, UV/Vis spectroscopy has been integrated into microfluidic devices for online process analysis. Under segmented flow conditions the synthesis of gold nanoparticles was monitored. Changes in light intensity could be related to aqueous/organic phases separated by N_2 travelling past the light source, as well as changes in UV/Vis spectra for gold nanoparticles synthesised under different conditions.¹⁰⁴

One of the potential advantages of AM processes is the ability to design optics ports in the reactors at any desired point. This can be halfway through residence times to allow monitoring of reaction progression or allow irradiation ports for inline photochemistry with lower intensity losses than observed for the flow photochemistry systems previously seen, as distances from source to reagent flows would be of the order of microns. The integration of optical fibres has been shown for UC, but it was demonstrated that the fibres were prone to transmission losses due to the stresses encountered by the fibres during incorporation.^{105,106} However, work by Monaghan *et al.*⁶⁹ at Loughborough showed that metallized optical fibres could be integrated into solid UC objects with no loss of light transmission, potentially allowing integrated spectroscopic monitoring at any point within a UC reactor.

In a related publication the ability to additively manufacture microfluidic devices in SL with features as small as 50 μm was recently shown by the Christie group at Loughborough University¹⁰⁷ and allowed fibre optics to be embedded directly into flow channels for *in-situ* spectroscopy with no need for waveguides or additional optics. This represents a significant advance in the path lengths that can be achieved without using etching methods or advanced SL instruments. Previous flow cells such as those employed by Ferstl and others^{108, 109} were 2 mm path lengths (Figure 21), limiting the range of wavelengths where useful information could be obtained with total absorption below approximately 650 nm for the highest yield.

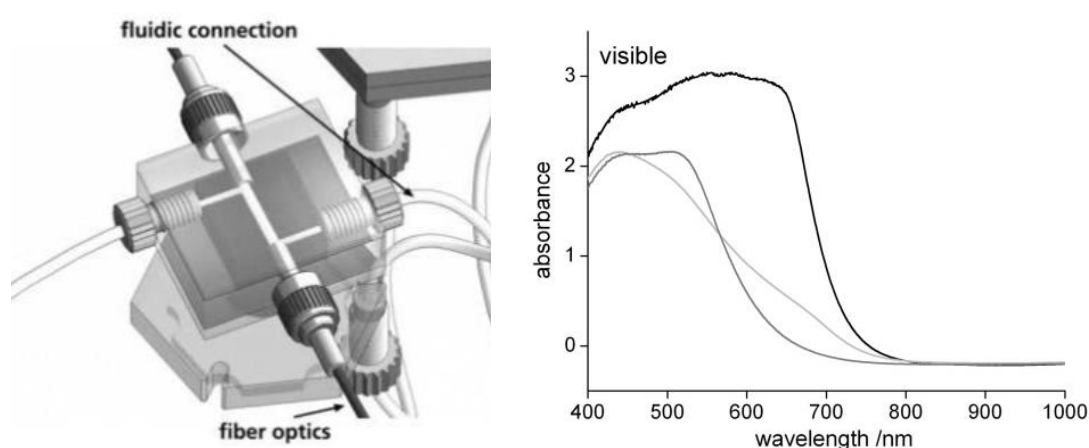


Figure 21. (Left) Online UV/Vis cell employed as part of FAMOS¹⁰⁸ (Right) Acquired spectra showing changes in visible spectrum due to nitration of toluene in a microreactor. Figure reproduced from reference.¹⁰⁹

In an elegant piece of work by Benito-Lopez¹¹⁰ and co-workers the UV/Vis spectra for the amination of p-halonnitrobenzenes¹¹¹ were acquired online, and under high pressure conditions. This was achieved by performing the reaction inside a fused silica capillary; passing it through a steel microfluidic cross with fibres aligned either side for the light source and the detector. As fused silica is transparent to UV light to around 190 nm this could allow a relatively large degree of structural information to be discerned. No detail on the effective path length was given in the work, and the reaction progress was monitored at 391 nm, an off-peak absorbance, but the working concentrations of 0.125 M indicate a path length in the region of 0.5 mm.

A comparison of NIR, FTIR, Raman and UV-vis spectrometry, carried out by McGill *et al.*¹¹² on an acid catalysed esterification under batch conditions revealed that each of the techniques performed well at predicting concentration, though accurate determination of the rate constant could not be achieved with the UV method. Both the Raman and UV techniques suffered from solvent signals dominating the spectra, though careful selection of the analytical region overcame this.

1.3.4 NMR spectroscopy

NMR would appear to be the ideal online monitoring technique given its high degree of selectivity compared to fluorescence and UV/Vis; and far simpler sample preparation when compared to mass spectrometry. Despite this it suffers from a lack of sensitivity compared to other spectroscopies, unless multiple scans are acquired. It is also vastly more expensive than UV/Vis or FTIR instrumentation, meaning that the barriers to its integration into online reaction monitoring are perhaps higher than for simpler, easier to repair, instruments.

As hyphenated LC/NMR analytical techniques have been available for some time, with continuous flow coupling of LC to ¹H NMR being first reported in 1980 by Haw and co-workers to analyse jet fuels after separation by HPLC,¹¹³ it is perhaps surprising that the development of flow chemistry did not coincide with the integration of NMR as a monitoring technique, even though the removal of the dilution effect caused by HPLC solves one of the main disadvantages of LC/NMR. Presumably this is because of the assumption that the use of non-deuterated solvents would obscure too much information, and that running experiments in deuterated solvents would be too expensive. The flow NMR techniques and equipment that were developed therefore often relied on the design of complicated and highly engineered micro flow probes^{114,115} with integrated transmission and receiver coils and solvent suppression pulse methods, instead of simply placing some tubing through the magnet bore and acquiring data for regions not affected by the solvent resonance.

Benchtop NMR spectrometers with stable permanent magnets that remove the need for cryogenics, have been utilised for online analysis and self-optimisation of several simple organic reactions by the Cronin group.¹¹⁶ Though the instrument used in their work had a magnet of relatively low field strength, the

benchtop instrument was able to perform 2D experiments and show reaction progression to give real time yield estimations for a range of reaction classes. Later work by the Ley group¹¹⁷ with an instrument of similar field strength demonstrated inline monitoring for a number of cyclopropanation reactions and the ability to perform J-RES and COSY experiments on flowing reagents, all performed in deuterated solvents.

Typically some line broadening has been observed for flow NMR work conducted in high field instruments. Dalitz and co-workers demonstrated that through determination of the T_1 relaxation times for nuclei of interest a reliable flow rate window can be used if this broadening effect prevents the collection of good quality data.¹¹⁸

1.4 Reaction optimisation - DOE and global optimisation algorithms

Optimisation of chemical processes has traditionally been performed by varying one factor at a time. The disadvantages to this approach are manifest, chief amongst them is the inability to discern combination effects to find true optimal conditions and separate run to run variation. Design of experiments (DOE) is a statistical, systematic method for exploring reaction space; the surface, volume or higher order shape defined by the number of discrete variables, each of which gives rise to a dimension¹¹⁹ i.e. temperature and flow rate gives a 2D region, where the optimal conditions can then be found by varying factors simultaneously. The methods of relating to DOE, originally referred to as the factorial method, were first described by Yates, Tippett and Fisher in the 1930's as a way to carry out agricultural trials with large numbers of variables.¹²⁰⁻¹²²

For a full factorial design, the minimum number of experiments required is given by n^k , where k is the number of factors and n is the number of levels. For 2 factors, 2 levels and 3 factors, 2 levels the following experiment designs would be obtained (Figure 22). Typically, additional replicate samples at the centre of the design would be performed to enable an estimate of the reproducibility of the experiments to be made as well as to determine non-linear effects.

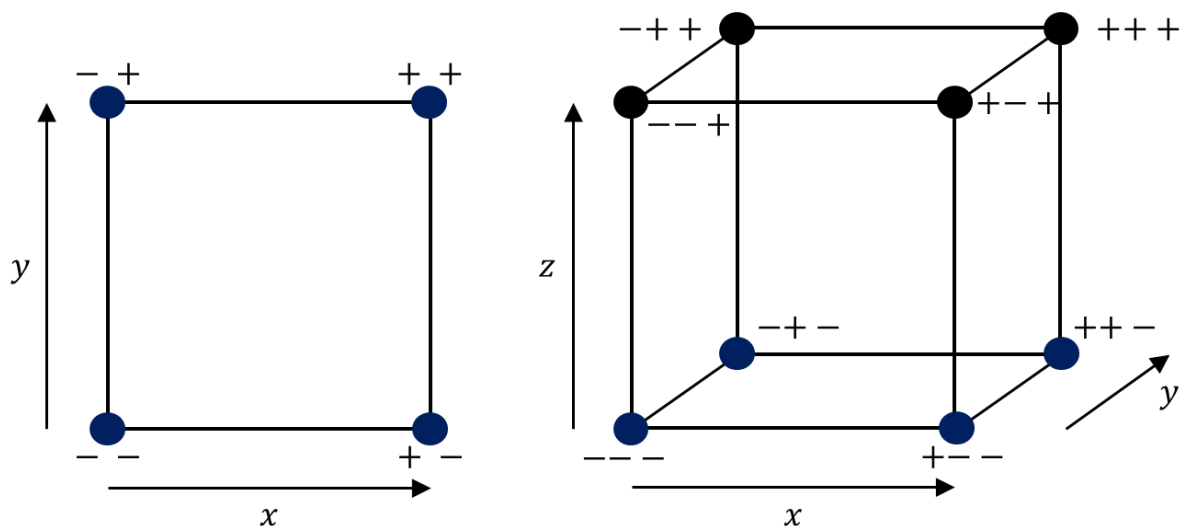


Figure 22. Full factorial design of experiment plots (no centre points).

Examination of responses, such as yield or absorbance, for each experiment in the design would then allow the ideal conditions to be determined - within the space under investigation. DOE is not a global optimisation tool as it can only be used to investigate a defined area and this will be limited by practical considerations in many cases, requiring relatively large numbers of experiments. Nevertheless it can be very useful where some prior knowledge of a system is available and has been employed in numerous, predominantly industrial scale, reactions.¹²³ Where large numbers of factors are required for an investigation other designs are available that reduce the number of experiments, while still maintaining predictive ability such as fractional factorial designs where some of the full factorial vertices are omitted (Figure 23). An extensive investigation into the Willgerodt-Kindler reaction using DOE was published by Carlson *et al.*¹²⁴ more than three decades ago. DOE has also been adopted as part of standard methodology for optimising reaction scale up at Lonza Ltd.^{125,126}

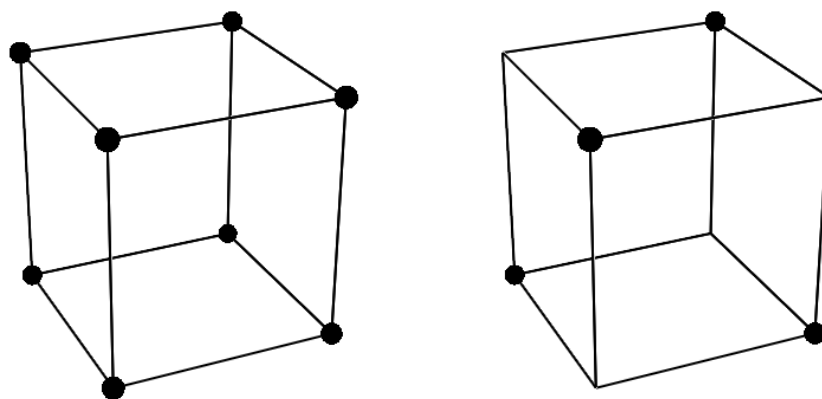


Figure 23. Schematic illustrating the difference between full factorial and fractional factorial designs (Left) 3 factor, 2 level full factorial design. (Right) 3 factor, 2 level, 2^{3-1} fractional factorial design.

Reizman,¹²⁷ as part of the Jensen group at M.I.T., utilised a D-optimal design to estimate the reaction kinetics for a simple S_NAr reaction. This was carried out in an automated manner with full control of the system through LabVIEW and MATLAB.

Automated DOE for reaction optimisation has been demonstrated in micro reactors by Koch *et al.*¹²⁸ who investigated stoichiometry, residence time and temperature for a deprotection step. The optimised conditions were then applied to a preparative scale continuous flow reactor. More recently Holmes *et al.*⁹¹ utilised DOE with online mass spectrometry to optimise a simple organic transformation rapidly and with minimal wasted reagent. They also found that the randomisation often employed in DOE studies was found to have no significant benefit when used for small scale laboratory trials. This allowed the experiments to be run in the most efficient order possible, avoiding the lengthy reactor cool down that adds significant time cost into optimisations, as well as reagent costs, as flowing solvent must be maintained during the equilibration stages.

The high level of control inherent to flow chemistry combined with the ability to integrate numerous analytical techniques allows for fine adjustments to reaction conditions based upon the monitoring data and subsequent global optimisation over the reaction space. Early applications have been in the field of nanoparticle synthesis¹²⁹ where the low reactor volumes and flow rates make reagent wastage low. An in-line spectrometer was used to monitor the production of CdSe nanoparticles,¹³⁰ relying on the relationship of the ratio of Cd/Se and the resulting spectral shifts. Coupled with the stable noisy optimisation by branch and fit (SNOBFIT) algorithm, maximisation of an arbitrary emission wavelength was achieved in 2 and 3 reaction dimensions (Cd and Se flow rates and temperature changeable respectively). In related work computer control of an integrated heater within a micro reactor was used to control the syntheses of similar CdSe nanocrystals.¹³¹

McMullen *et al.*¹³² employed the simplex algorithm to optimise a Heck coupling in a continuous flow micro reactor, allowing variation in residence time and alkene molar equivalents. An online HPLC

system was used to provide the response in the simplex method and the total time per experiment, from injection of reagents to HPLC results, was around twenty minutes.

Pioneering work in this field has been performed by the Poliakoff group who have utilised global optimisation algorithms in a variety of applications. Two dimensional correlation GC was used for the analysis and optimisation of a continuous flow catalytic Friedel-Crafts alkylation in supercritical CO₂.¹³³ Automated optimisation was demonstrated by Bourne *et al.*^{134,135} using the super modified simplex algorithm (SMSIM) to locate an optimum set of reaction conditions for the methylation of alcohols with dimethyl carbonate, relating experimental yield by GC to reaction conditions. Importantly the next set of conditions was determined from the online analysis, and a feedback protocol set the flow system up and ran the next experiment starting from an initial tetrahedron of conditions, while remaining within a defined set of 'safe' values.

An interesting potential application for online optimisation procedures has been proposed by Skilton *et al.*,¹³⁶ namely the possibility of 'cloud' chemistry. This is the running of continuous flow reactor systems by researchers in less well-equipped laboratories but could be extended to general remote chemistry to allow access to specialised flow chemistry apparatus/online analysis equipment.

As previously discussed spectroscopy is a key technology for online analysis and optimisation, primarily due to the speed of measurements and the structural information that can be obtained. Skilton *et al.*¹³⁷ built on the work of the Ley group and used online ATR-FTIR with the stable noisy optimisation by branch and fit (SNOBFIT) algorithm to optimise the methylation of 1-pentanol.

2 3D printing for molecular spectroscopy

2.1 Introduction

This chapter will address the 3D printing of flow cells and optics ports for molecular spectroscopy, focussing on UV/Vis applications, with the overall aim of using them for reaction monitoring. The same approach would be applicable to fluorescence spectroscopy with the use of more sensitive detectors, however mid-infrared methods (MIR) would typically require path lengths an order of magnitude lower. While there are many commercial options for online analysis by spectroscopy, including immersion probes,¹³⁸ transmission flow cells¹³⁹ and reflectance probes,¹⁴⁰ they are all relatively expensive. In addition, commercial flow transmission cells typically require expensive quartz or sapphire optics for UV transmission and additional cell holders for fibre alignment. For online analysis the reactor must be modified to accommodate them as an external flow loop or a large diameter probe insert which is not practical or desirable for laboratory scale reactor systems.

The integration of sensors and optics directly into the reactor body reduces the added volume and simplifies the system. Although commercial transmission flow cells for UV/Vis analysis can have path lengths as low as 100 μm they are typically restricted to 1 mm and greater. Even custom parts have mostly been greater than 1 mm path length, in previous work by Ferstl *et al.*¹⁰⁸ a 2 mm path length flow-through cell was used to collect online spectra for the nitration of toluene in a microreactor. However, due to the high molar extinction coefficient of the substrate and products the observed peaks were limited to broad absorbances above 500 nm. Due to the relatively large pathlength. By coating part of the microreactor with gold, and equipping it with sapphire windows, reflectance IR measurements could be obtained and these were able to show the formation of the mono-nitrated product clearly.¹⁰⁹

To be of practical use therefore in direct monitoring of organic synthesis, 3DP flow cells must be able to contain path lengths of 0.1-5.0 mm or smaller, otherwise throughput rates and reaction rates will be limited by the low concentrations required. Because of the need for small build resolutions the AM technique chosen for most parts was SL.

2.2 Results and discussion

2.2.1 Straight channel transmission flow cell design

A transmission flow cell (C1) was designed in CAD software with a 6 mm path length and a channel diameter of 1 mm, widening to 2 mm shortly before the optics port (Figure 24). Quartz windows, originally designed for use in HPLC DAD detectors, were compressed against o-rings to create a leak tight fit using screws. A receiving thread for the compressing screw was manually cut into the part using a pre-designed opening, slightly narrower than the minor thread diameter.

Originally the compressing screws were simply steel screws with a central, manually drilled, hole; a redesigned compressing screw was made with the SMA 905 standard dimensions added to the reverse side, allowing SMA 905 fibre optic fittings to attach easily. This therefore achieved very close alignment with the internal waveguides perpendicular to the flow channel. The compressing screws were made by both selective laser sintering (SLS) using nylon as the material, and stereo lithography using a photo cured acrylate/epoxy resin. These parts do not encounter any reagents so do not have to be chemically resistant. They do however encounter physical forces through the unscrewing of fibres and removal from the part, so material hardness and durability must be reasonable if they are to be anything but disposable items.

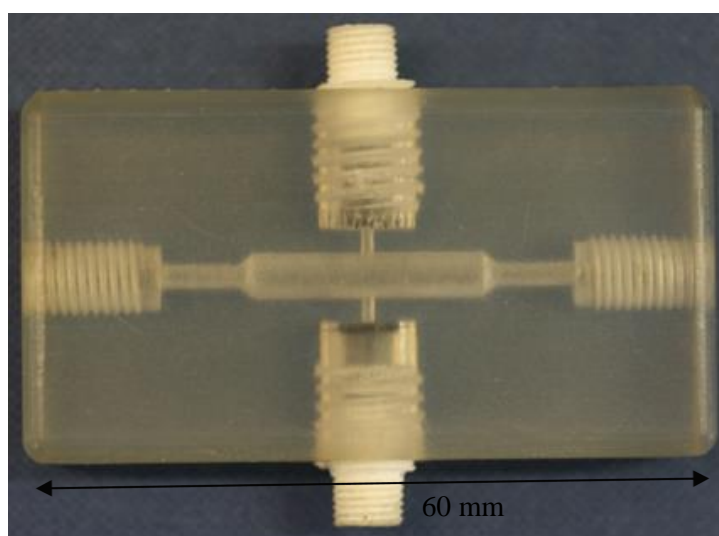


Figure 24. Top down view of the straight channel transmission flow cell (C1). The nylon, SLS manufactured, SMA 905 fibre adapters are shown at the top and bottom of the part.

2.2.2 Z-path flow cell design

A flow cell (C2) with a ‘Z’ shaped flow path geometry was designed in CAD software with a 6 mm path length and channel diameter of 1 mm (Figure 25). This design was chosen as it is commonly employed in HPLC detectors and it was thought it might be more compact, allowing easier integration into reactors, and also avoid the potential for poor flow at the flow channel/waveguide interface of the straight pass flow cell. DAD windows were inserted in a similar manner to those used in the flow cell C1 described in section 3.2.1.

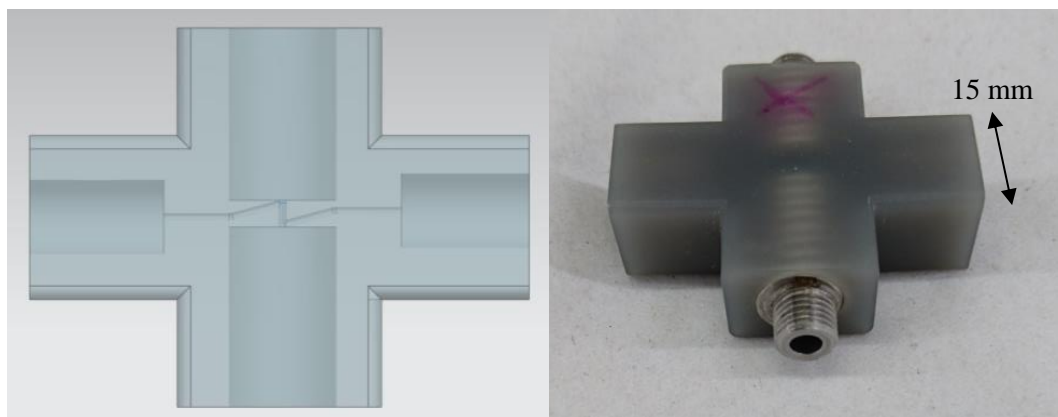


Figure 25. (Left) CAD model for Z-path flow cell (C2) (Right) Cell shown fitted with SMA 905 fibre optic connector.

A later modification to this flow cell design removed the need for expensive DAD windows by embedding fused silica windows instead. These have a similar range of UV transmission and are a fraction of the price of the DAD parts. Unfortunately, these could not always be reliably sealed and suffered from leakages more often than cells using the DAD windows.

Of significant importance is that for this part that the internal screw threads required for both the compression screws, and the 1/4"-28 threads per inch (TPI) fluidics fittings, were printed as part of the design rather than being added as post processing *via* manual tapping. As the tapping process generates large amounts of powdered resin it would often lead to blockages within the parts and the incorporation of the threads into designs greatly reduces this potential for failure. The settings used for the screw thread are standard unified fine thread (UNF) values of; 0.25 " / 6.35 mm major diameter, 28 TPI, 0.035714 " / 0.9071 mm pitch, which represent a slightly larger fluidic fitting, but which is still perfectly suitable to hold 1/16" I.D. tubing.

2.2.3 Comparison of flow cells

The quality of the spectra acquired in the respective flow cells described in 2.2.1 and 2.2.2 was assessed by using nicotinamide solutions and comparing them to spectra acquired in a commercial Ocean Optics flow cell of 10 mm path length (Figure 26). Nicotinamide is freely soluble in water and many polar organic solvents and possesses a maximum absorbance at 263 nm with a molar attenuation coefficient of approximately 2600 L.mol⁻¹.cm⁻¹. This makes it a suitable test compound for aromatics and other UV absorbing compounds commonly utilised in organic synthesis.

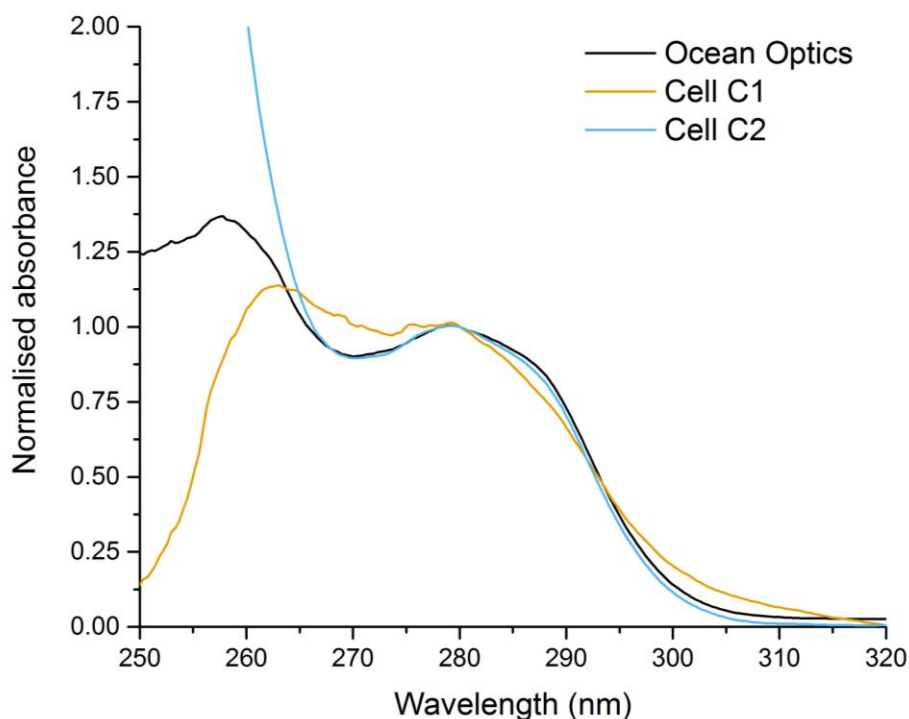


Figure 26. Overlaid spectra normalised by absorbance at 263 nm.

The spectrum obtained in the Z path cell is substantially closer to the commercial cell spectra. This is predominantly due to this cell being made from an opaque resin while the straight cell was made from transparent material which allowed background light through. This transparent resin has its advantages for reactors, allowing reactions to be monitored visually, but for flow cells it allows a large degree of stray light into the cell (Figure 27) and impacts on the resultant linear dynamic range of the spectrometer. Therefore, for the best spectroscopic performance, flow cells should be made from opaque materials or blacked out after production.

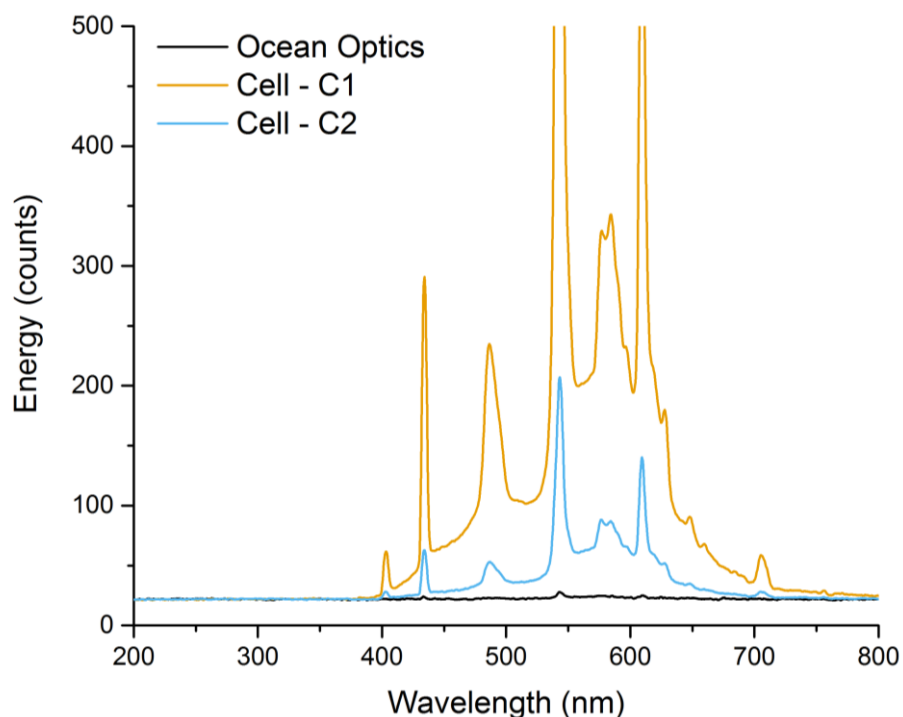


Figure 27. Comparison of stray light recorded by 3DP flow cells.

A calibration series was also constructed for each cell to test linearity at 263 nm (Table 1). Each cell produced a linear calibration with very little difference between the AM cells and the commercial example. The commercial cell should have an absorbance approximately twice that of the AM cells, though the actual value was less than this due to shrinking of the SL polymer when cured, resulting in a subsequent deviation from the path length specified in the CAD model. A standardisation of the cell with a compound of known molar attenuation coefficient and concentration allows an accurate value for the final path length of any part to be determined.

Table 1. Calibration data for commercial and AM flow cells

Nicotinamide concentration / μM	Ocean Optics cell A_{263}	AM Straight SLA cell A_{263}	AM Z path SLA cell A_{263}
0	0	0	0
0.11	0.402	0.125	0.236
0.22	0.825	0.256	0.337
0.44	1.427	0.495	0.699
0.66	2.122	0.717	1.035
R²	0.997	0.999	0.996

The Z shaped cell seemed more reliable in operation, with fewer bubbles observed to form within the channel (qualitatively assessed by the loss of light transmission to the spectrometer). A cell with this geometry was built with a 2 mm path length, due to the requirement for a wall thickness inside parts of no less than approximately 1 mm; this is the smallest possible path length practically achievable with this configuration.

2.2.4 Integration of analytical measurement capability directly into reactors

2.2.4.1 Integrated spectroscopy into SL reactors

An SL reactor (R1) was designed with a Z geometry flow cell integrated half way along the volume (Figure 28). The additional volume to the reactor was negligible overall and allowed true inline monitoring of reactions. A model reaction, the bromination of electron rich aromatics with N-bromosuccinimide (Scheme 3), was chosen to test R1, first pumping starting material with solvent before introducing the brominating reagent.

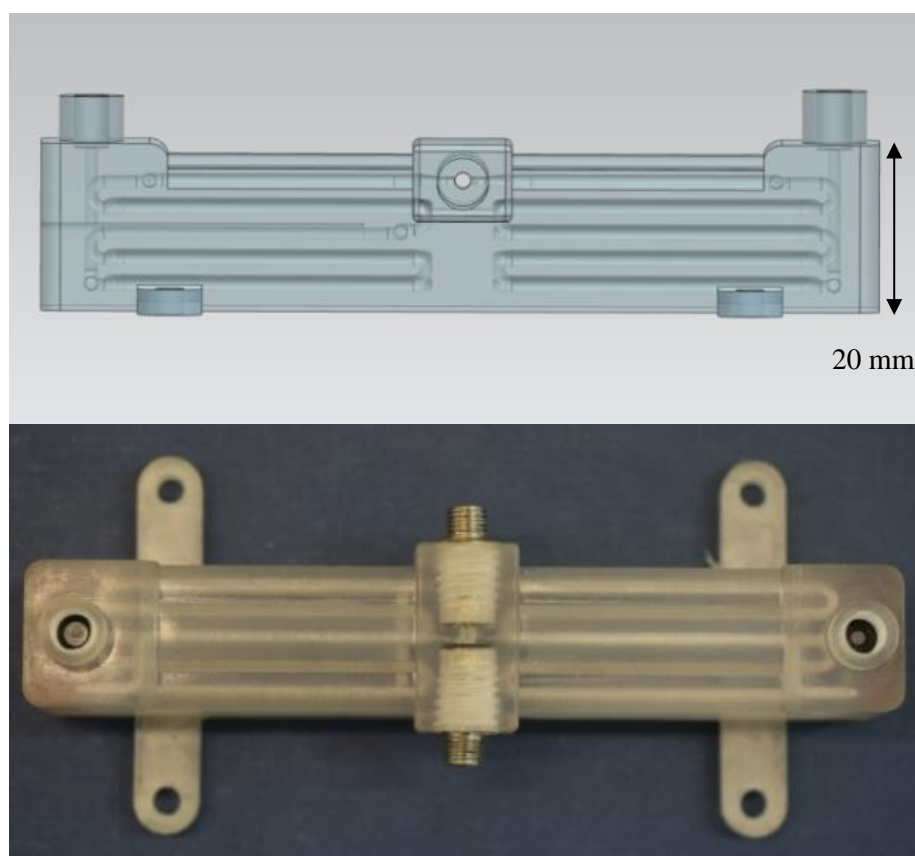
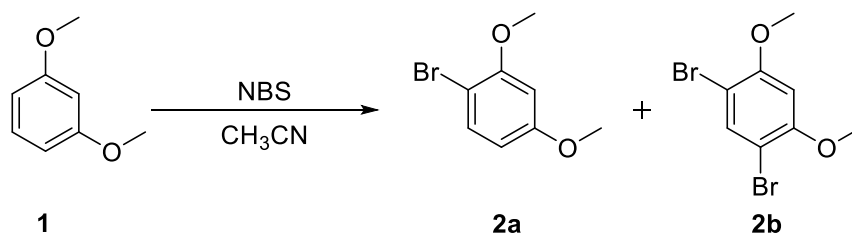


Figure 28. (Top) CAD model for reactor with integrated optics (Bottom) SL 3DP part with fibre optic alignment tools.



Scheme 3. Bromination of 1,3-dimethoxybenzene using N-bromosuccinimide (NBS).

The limitation of the 2 mm path length is clear; even reactions attempted with only moderate concentrations led to complete absorbance at wavelengths < 300 nm. However, despite this, useful information about the reaction could still be inferred by examining the shift in the absorbance cut off (Figure 29). When compared to spectra of the starting material and the products the formation of the brominated compounds is clearly indicated, and while no information can be obtained regarding the ratio of the mono versus di substituted products, the value of integrated spectroscopy, here a truly in-line measurement, is apparent.

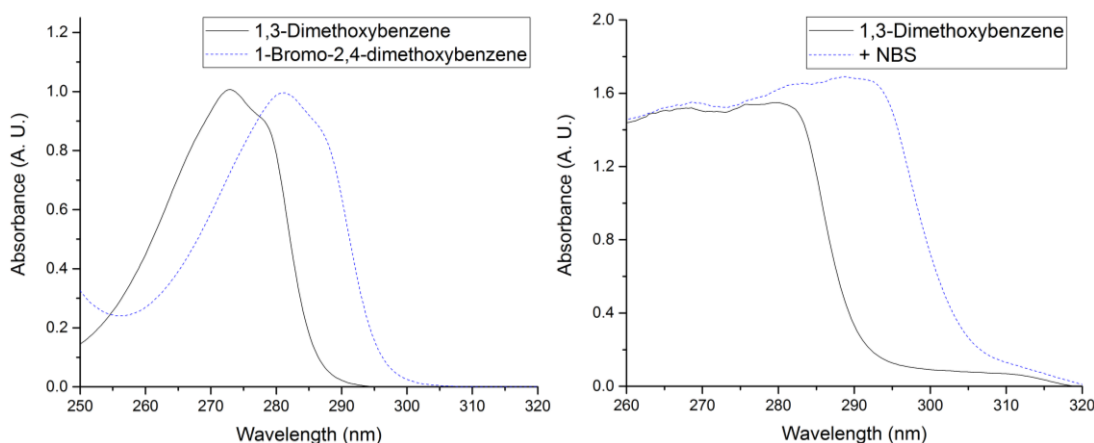


Figure 29. (Left) Reference UV spectra of dilute solutions (Right) Spectra obtained in-situ by the integrated optics port.

2.2.4.2 Integration of thermocouples into SL reactors

An SL reactor (R2, Figure 30) was designed to have a large internal volume but also have a predesigned cavity that would allow the insertion of a thermocouple in the centre of the flow path, allowing the measurement of the internal reactor temperature. While SL resin is not significantly thermally conductive the part serves to illustrate how sensors can be integrated into reactors through the use of AM.

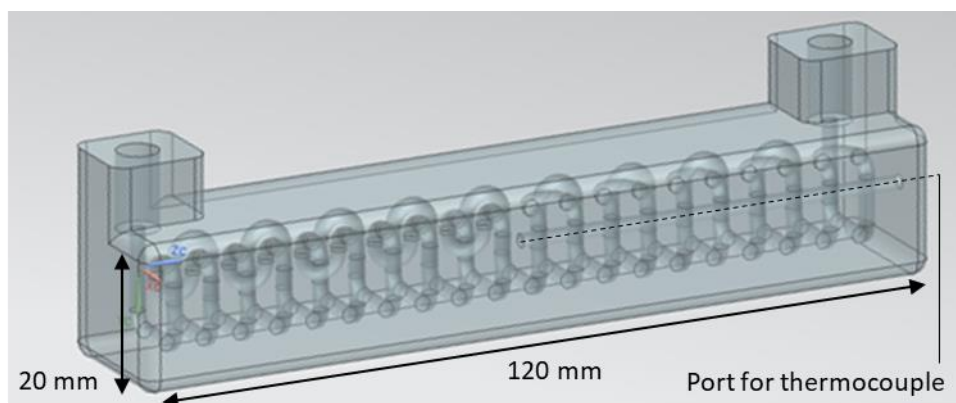


Figure 30. CAD sketch for helical flow path reactor with thermocouple port (visible at right hand side)

The part was tested to determine whether any change in reactor temperature could be detected when the part was heated. To this end, the reactor was placed onto a hotplate with a 2 mm thermocouple inserted. The hotplate was very slowly increased in temperature up to around 60 °C, at which temperature the reactor began to show signs of failure with layers of cured resin separating. Unfortunately no thermocouple data could be collected before this occurred. The failure in the part was observed to occur along the layers of cured resin (Figure 31), while in FDM parts the separation between each printed layer is enough to cause leakages, with SL this is not typically the case. However it would appear that the layers remain the weak point in the part, perhaps unsurprising, but any activity to strengthen this aspect of AM reactors could lead to more robust parts.

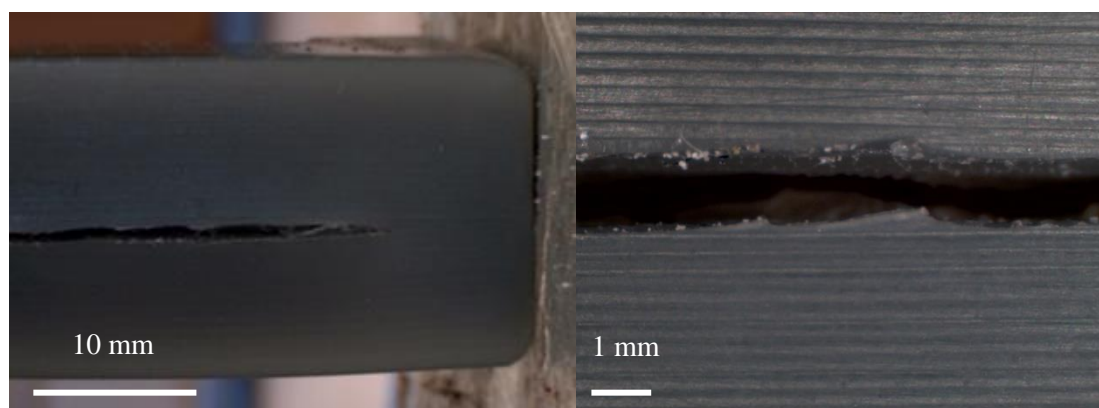


Figure 31. (Left) Failure of SL reactor due to thermally initiated delamination (Right) Magnified view showing failure along resin layers

2.2.5 Use of 3DP flow cells for reaction monitoring through multivariate calibration

While the acquisition of UV/Vis spectra is usually rapid (< 1 s) in comparison to IR, it lacks structural specificity. Mixtures of compounds or low level impurities can give rise to subtle changes in the spectra that are often not clear when visually examined or when univariate calibrations are used. The use of multivariate calibrations has been embraced in the pharmaceutical industry and other areas of chemical

manufacturing for process control and for online reaction monitoring. These calibrations enable predictions to be made from the complicated spectra that arise from reaction mixtures. Publications in the field have typically focussed on the use of NIR, Raman and FTIR as the spectroscopic tool of choice.¹⁴¹⁻¹⁴³ There have been fewer well developed examples of UV spectroscopy reported,^{133, 139-141} although the multivariate methods required for NIR spectra are typically also suitable for resolving the broad overlapping absorbance bands observed for reaction UV/Vis spectra.

The suitability of 3DP flow cells for reaction monitoring through PLS was shown by using a 6 mm variant of the flow cell C2 to analyse a flowing mixture of benzaldehyde and nicotinamide. These compounds have absorbance maxima at 280 nm and 260 nm respectively, and mixtures of them give rise to general, broad absorbance bands between 260 - 290 nm, making it difficult to obtain specific structural information. To extract information on the ratio of the two compounds partial least squares regression (PLSR) was used to construct a regression equation which relied on the differences in spectra as the ratios changed. Non-reproducible spectra or spectral aberrations would impact the ability of this technique to work in 3DP flow cells.

The solutions used for the PLS regression were chosen to cover a range of concentrations (Table 2). They were also chosen to have a low correlation, meaning that all combinations between low and high levels were analysed.

Table 2. Analysed solutions for PLS regression analysis.

Solution	Benzaldehyde concentration (mM)	Nicotinamide concentration (mM)
1	0.000	0.000
2	1.000	0.200
3	0.200	0.200
4	1.000	0.050
5	0.200	0.050
6 (centre point)	0.600	0.125
7	1.000	0.000
8	0.000	0.200

Using the wavelength range of 265 - 290 nm, with 5 and 4 factors for benzaldehyde and nicotinamide respectively, seemed to give the best result. No spectral processing was applied, and indeed the use of SNV or mean centring seemed to produce models with good R^2 values but very poor predictability when applied to a real data set. The models were tested by acquiring spectra of benzaldehyde (2 mM) and

nicotinamide (0.1 mM) solutions in methanol. The order of reagents was; 1) pump A - nicotinamide, pump B - methanol; 2) pump A - nicotinamide, pump B - methanol; 3) pump A - methanol, pump B - benzaldehyde; 4) pump A - methanol, pump B - methanol.

When processed through the PLS model the spectra show the expected trends with some minor deviations (Figure 32). These occur mainly when the two components are present together, showing as an underestimate of the nicotinamide when benzaldehyde is also present, and would be resolved with a more extensive calibration. A spike in the trend is also visible, corresponding to an air bubble passing through the flow cell. This would not typically be resolvable with a more extensive calibration set, although robustness to bubbles could be introduced to a certain extent, but can also be removed through the use of median smoothing (Figure 32). If a relatively small number of adjacent points are utilised then the trends are not obscured, this smoothing approach is of use in process control allowing incorrect process changes to be minimised.¹⁴⁷

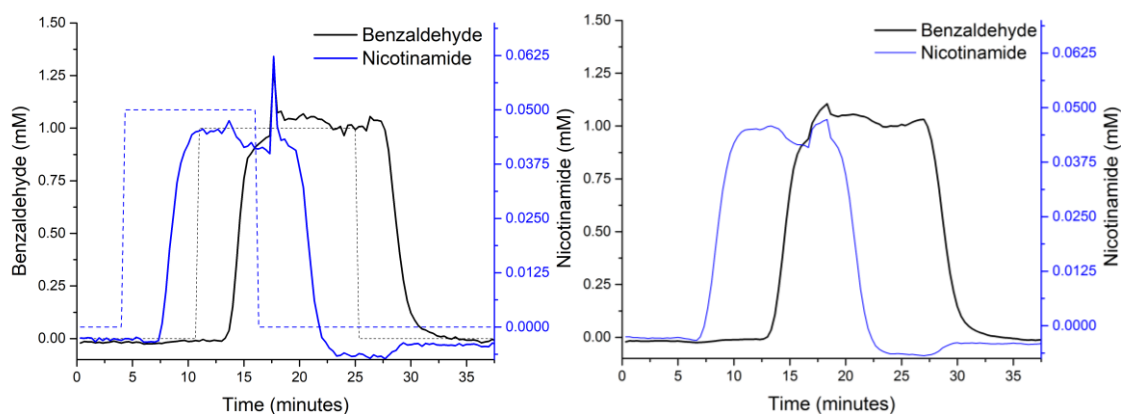


Figure 32. (Left) Trends from PLS model. Dashed lines represent the system set points. (Right) Median smoothing applied to data.

2.2.6 UV PLSR calibration for 3 components

The electrophilic bromination of 1,3-dimethoxybenzene using N-bromosuccinimide in acetonitrile¹⁴⁸ was again chosen as a suitable model reaction to determine whether PLSR in 3DP cells for reaction monitoring was feasible. This is a more complicated spectral system than that seen in section 2.2.5 due to more than one product being possible as well as the absorbance of any unreacted starting material.

To ensure low correlation between the reaction components a full factorial design was used. As the reaction should proceed smoothly the residual starting material concentration was assumed to be low compared to the products. The NBS, as well as the succinimide by-product, were analysed and found to have insignificant contributions to absorbance above 240 nm for this system.

While UV spectroscopy does not typically provide the level of structural information obtained with Raman or mid-IR spectroscopy, it can be used to build PLSR models from reference data containing

this information. In this manner a model was built from concentration data for three components; 1,3-dimethoxybenzene, 2,4-dimethoxy-bromobenzene and 1,5-dibromo-2,4-dimethoxybenzene. UV spectra were collected in an SLM flow cell of 2 mm path length. The exact ratios were determined with a full factorial DOE approach. Building a model in this way allows full interactions between the components to be modelled, improving the model and future prediction capability.

The increasing degree of bromination causes a bathochromic shift in the spectrum with each substitution providing small changes in spectra when the ratios are altered. PLSR was applied with 3-5 factors, all spectra were processed with mean centring before PLSR was performed in MATLAB (Mathworks, Massachusetts, U.S.A.), and all models were built over the region 245 - 325 nm. The results show that mean centring of the data with no other processing gave the best R^2 value for the data (Table 3).

Table 3. Model R^2 values

Component	No. of factors	R^2		
		Mean centring	Mean centring + SNV	Mean centring + Min Max
1,3-dimethoxybenzene	3	0.8568	0.3882	0.3796
	4	0.9771	0.5764	0.5034
	5	0.9882	0.6503	0.5832
1-bromo-2,4-dimethoxybenzene	3	0.9731	0.7361	0.7421
	4	0.9911	0.8678	0.8395
	5	0.9966	0.9301	0.9285
1,5-dibromo-2,4-dimethoxybenzene	3	0.9983	0.7888	0.7826
	4	0.9991	0.9517	0.9477
	5	0.9993	0.9833	0.9849

Applying this model to the bromination reaction used previously (Scheme 3) yielded estimates of each component concentration from a single spectroscopic measurement. The data acquisition was performed in a fully automated manner, using MATLAB to drive pumps and trigger the spectrometer to acquire data at the end of each experiment.

The automated experiment worked as intended, varying stoichiometry and residence time with an automatically acquired spectrum at the end of each experiment. Unfortunately the estimates derived from the model were poor, presumably due to the low concentrations demanded by the flowcell path length. As no heating was applied to this reaction the formation of products was minimal if at all, therefore the calibration was poorly set up to estimate any of the components - the 1,3-

dimethoxybenzene level was too high and the mono and di brominated species were too low in concentration. This reinforces the need for small pathlengths and also illustrates the degree of work required for such multivariate calibrations, which can then be next to useless if substantially away from the experimental space the reaction is found to be operating in.

2.2.7 Microfluidic flow cell for online analysis and optimisation

For online monitoring of organic reactions with transmission type flow cells it is clear that the path length must be decreased. ATR cells typically exhibit path lengths of $<10\ \mu\text{m}$ but are relatively expensive.

To try and approach path lengths near this range a microfluidic flow cell (C3) with a path length of 0.5 mm was designed in collaboration with Thomas Monaghan (Wolfson School of Materials Engineering, Loughborough University). The reduction in path length was achieved by routing the flow channel to the surface of the part allowing narrower channels and a higher build precision compared to fully encapsulated channels. The sealing of the part built in this work was achieved through the use of double sided sealing tape which could be backed with poly carbonate film, glass cover slips, or any other flat material. After this work was carried out the use of other AM techniques for printing simple open microfluidic channels has been further demonstrated for capillary flow, with mixed results due to surface roughness effects and no attempt to seal the channels.¹⁴⁹

The tape was tested at pressure by blanking the part outlet and pumping water into it while monitoring the reading on the pressure sensor built into the Flowsyn flow chemistry platform. The tapes typically withstood approximately 200 psi, above this pressure the sealing tape would delaminate from the surface. Tests on solvent compatibility showed that the tapes could tolerate a number of polar organic solvents (alcohols, acetonitrile) but that ethyl acetate would cause the dissolution of the adhesive and then tape failure.

Without the plastic backing the design of the flow channels could be felt as a slightly raised surface when solvent was pumped under low pressure into a $500\ \mu\text{m}$ channel built at the surface of a part. Introduction of ethyl acetate to the cell caused rapid peeling from the edges of the channel and blistering under the surface of the tape (Figure 33).

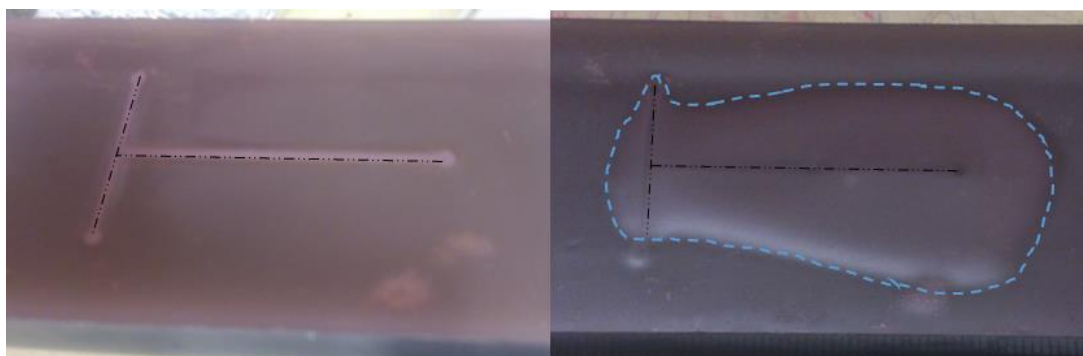


Figure 33. (Left) Image of T-junction, shown with methanol flowing, which led to slight lifting of the tape over the flow channel (marked with black dashed line). (Right) Same T-junction shown with ethyl acetate flowing, resulting in blistering over channel (extent of swelling indicated by blue dashed line).

For situations where greater solvent resistance was required this could be achieved using glass plates to seal the cells if it was combined with a thin layer of PTFE or Viton gasket to cover the fluid channels. Cells such as these could also withstand much higher pressures and be installed in line for telescoped reactions that ran with significant back pressure.

2.2.8 Integration of fibre optics

Due to the small channel size and the location of the fluidics at the surface the only way to obtain spectral data from the flow cells was to embed fibre optics directly adjacent to the flow channel. This approach requires no quartz windows or additional wave guides and allows wavelengths in the far UV or NIR to be collected depending on the installed fibres. The channels for the fibres were of a similar dimension to the flow channels, with cladding and coating layers over the silica core increasing fibre diameters to approximately 300-500 μm depending on type.

The optimal orientation of the fibres was investigated first to ensure that any reaction monitoring part gave the best performance. A part with a 500 μm path length and three guide channels for fibre optics was created (Figure 34).

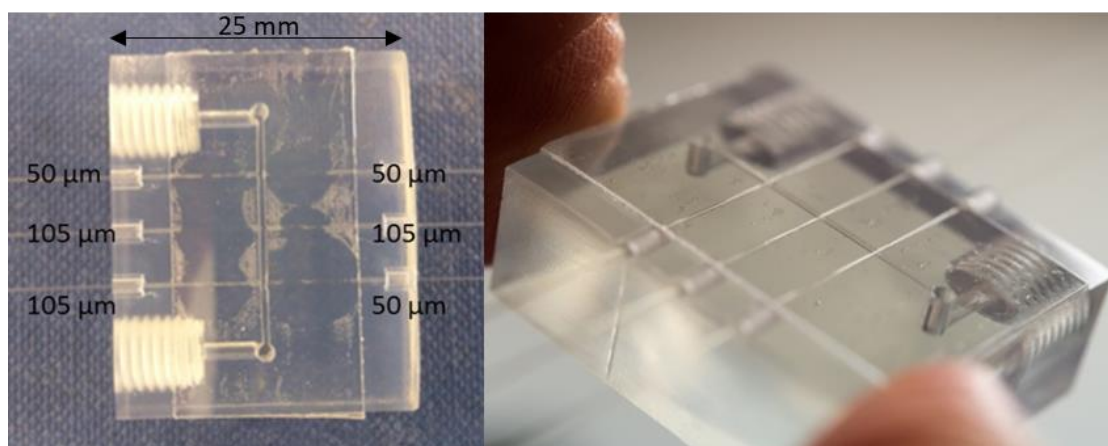


Figure 34. (Left) Microfluidic flow cell with various fibre core diameters labelled (Right) Perspective view of flow cell.

The available fibre cores were 50 and 105 μm and couplings of 50 - 50, 50 - 105, 105 - 50 and 105 - 105 were investigated by measuring the transmitted light through each pairing for a fixed acquisition time of 10 ms (Figure 35).

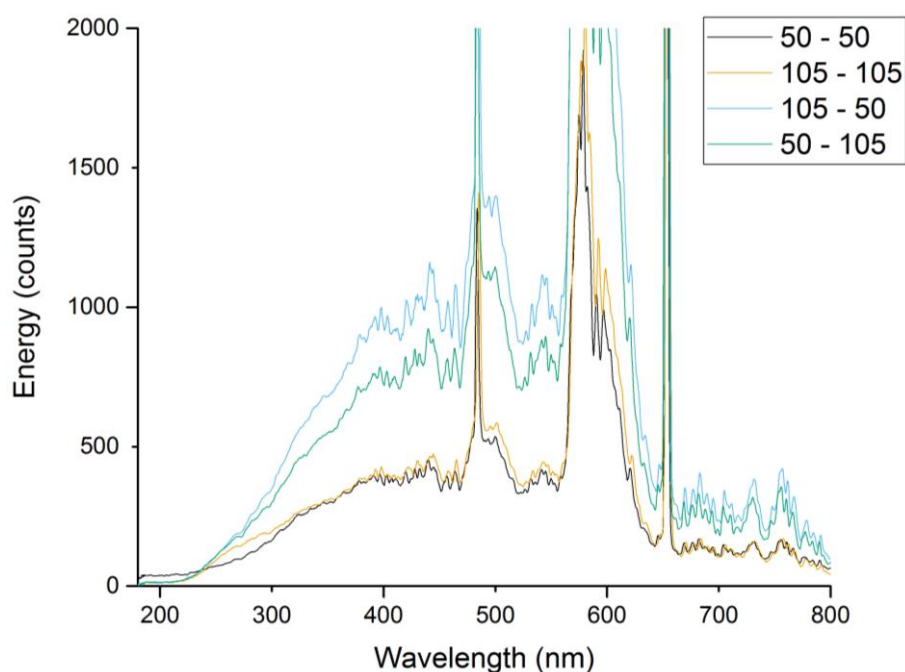


Figure 35. Energy spectra for different fibre combinations in a microfluidic cell.

It was immediately clear that light transmission was maximised when mismatched fibres were used, so that the light was projected from a larger fibre onto a smaller or *vice versa*. This arrangement ensures that light is incident on the entire face of a fibre, or that the light is accurately ‘targeted’ onto the receiving fibre (Figure 36). Alignment of matching diameters is difficult for objects which are little wider than a human hair, leading to transmission losses, and this explains the lower transmissions for

fibres of equal diameter, and the 50 - 50 μm pairing having the lowest transmission efficiency of all. While the transmission losses can often be mitigated by extending the acquisition times, by keeping transmission efficiency high shorter acquisition times are possible for spectral measurement, allowing multiple spectra every minute and therefore giving greater control over continuous processes.



Figure 36. (Left) Light transmission from 105 μm fibre to 50 μm fibre (Right) 50 μm to 105 μm .

The optimal fibre combination was then used in a number of cells with path lengths ranging from 100 to 500 μm . To determine the analytical performance of these parts a series of solutions were infused. The first was a solution of nicotinamide, used to determine the upper working concentration limit for the cells, which with a maximum molar attenuation coefficient of approximately $2600 \text{ L}\cdot\text{mol}^{-1}\cdot\text{cm}^{-1}$ provides a reasonable approximation for aromatics and other organic molecules with chromophores that may be used for reactions. The second solution was fluorescein, an organic dye with a molar attenuation coefficient of approximately $77000 \text{ L}\cdot\text{mol}^{-1}\cdot\text{cm}^{-1}$, which was used to simulate the detection of fluorescently labelled molecules such as proteins or oligonucleotides¹⁵⁰ and was used to determine the limit of detection.

As the nicotinamide concentration increased each cell in turn began to show complete absorbance by the solutions leading to curvature in the calibrations graphs (Figure 37). The only cell able to acquire a spectrum for each nicotinamide solution was the 100 μm cell which had an absorbance value of < 1 for all solutions. The other cells reached an upper limit in the order expected. To calculate a lower working limit for these cells only results with an absorbance < 1 were used to build linear calibrations. The limits of detection (LOD) were then calculated from the $y = mx + c$ regression slopes (Equation 1) with the assumption that $S_B = S_{y/x}$. The calculated linearity for all solutions, and the upper and lower working limits of each path length were calculated (Table 4).

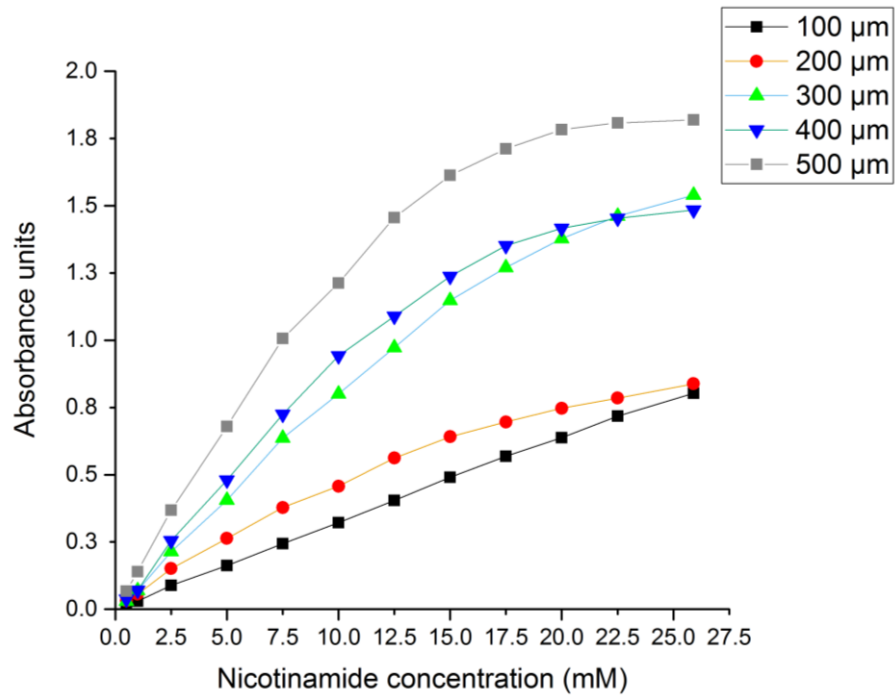


Figure 37. Calibration graphs for microfluidic flow cells

$$\text{LOD} = \text{regression intercept} + 3S_B \quad (1)$$

Where;

$$S_B = \sqrt{\sum_i \frac{(y_i - \hat{y}_i)^2}{n - 2}} \quad (2)$$

S_B = Standard deviation of the blank/y-residuals

y_i = Absorbance (A.U.)

\hat{y}_i = Calculated absorbance value from regression equation

n = number of samples

Table 4. Results for cell calibration series

Path length / μm	Fluorescein limit of detection / μM	Nicotinamide upper working concentration / mM
100	47	26*
200	23	15
300	16	13
400	12	10
500	9	7.5

*Upper limit not reached - estimated to be 38 mM of nicotinamide by the Beer Lambert law

Only the 100 μm path length flow cell was able to acquire a good quality spectrum for all solutions, and the plot of absorbance values versus nicotinamide concentration exhibits very little curvature as a result. The transmission efficiency for the fibres installed in the 100 μm cell was very good. This is a physical effect arising from the small separation between the cores, resulting in very little collimation loss between the fibres - essentially the cone of light emerging from the fibre tip has very little chance to diverge before encountering the receiving fibre.

2.2.9 Use of microfluidic flow cell for reaction monitoring

To demonstrate the application of an additively manufactured microfluidic cell a 100 μm version was used to spectroscopically monitor the synthesis of carvone semicarbazone from carvone and semicarbazide (Scheme 4). While a simple path length only cell was used for most of the work a more complicated cell with a mixing flow path was also designed and produced (Figure 38) to demonstrate the large degree of design freedom available with these cells.

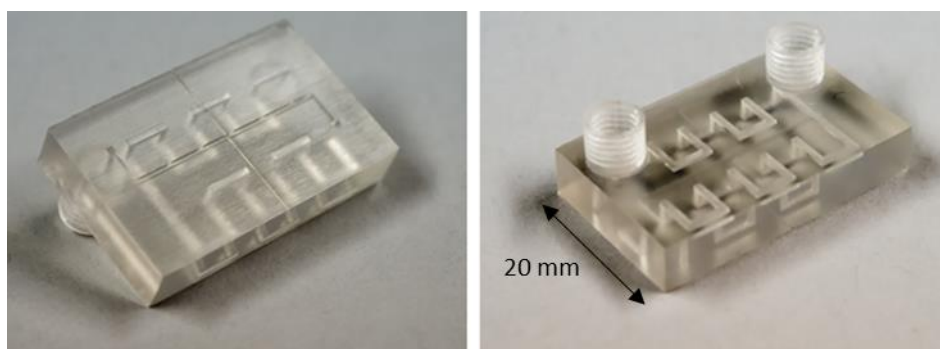
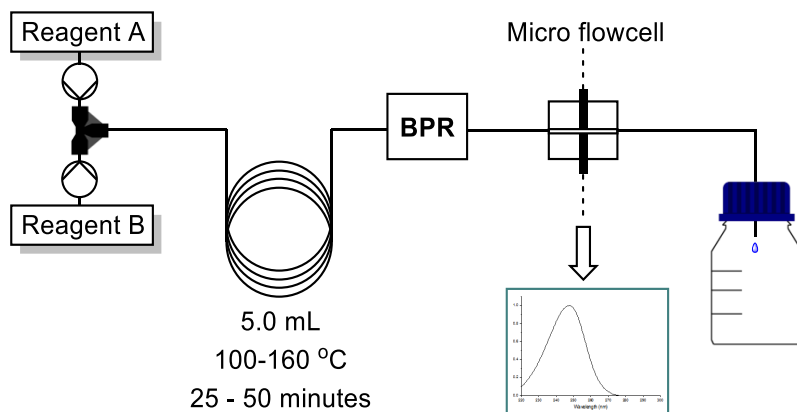
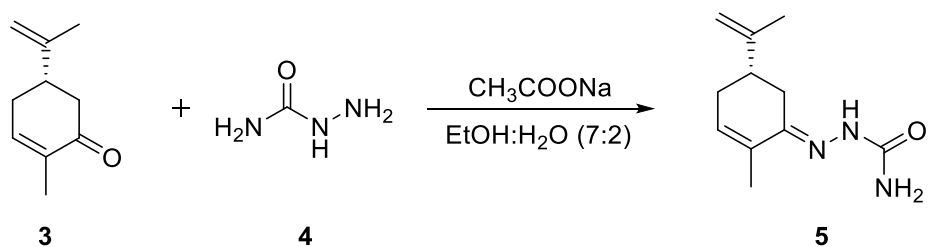


Figure 38. (Left) Topside of part showing fibre alignment channels (Right) Underside showing fluidic inlets



Scheme 4. (Top) Synthesis for carvone semicarbazone (Bottom) Schematic for flow synthesis with online analysis.

The carvone semicarbazone product shows a red shift in absorbance maxima compared to the carvone starting material (Figure 39). This spectral shift was used to perform a DOE optimisation for the reaction, treating temperature and residence time as factors, and taking the absorbance at the higher wavelength as the response. The most forcing conditions were assumed to be high temperature and long residence times and least forcing to be the converse of these.

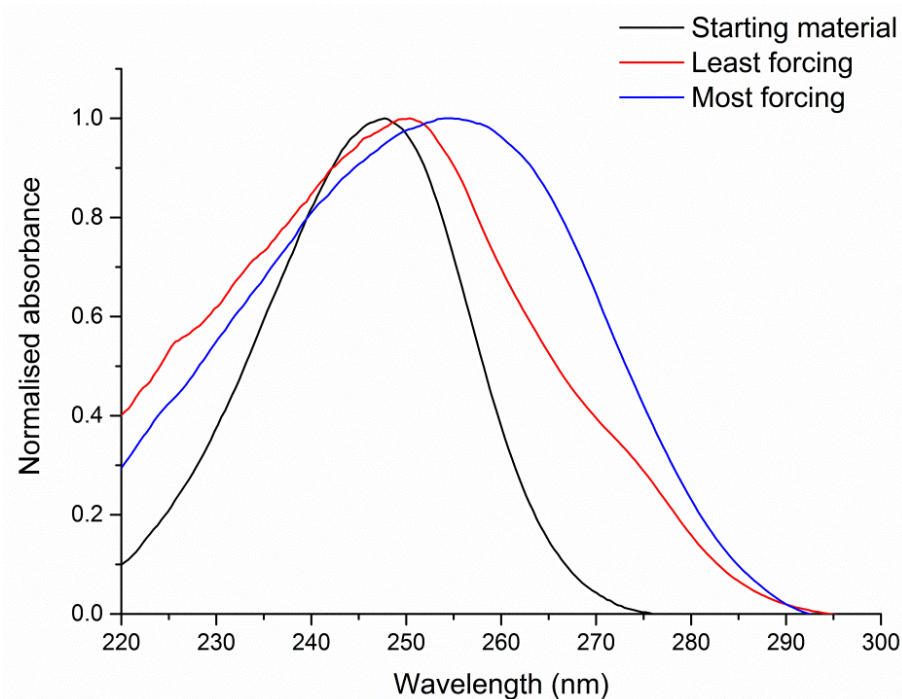


Figure 39. UV spectra showing change in λ_{\max} for semicarbazone product formation compared to (R)-(-)-carvone

The DOE experiments were performed (Table 5) using a full factorial design and 2 extra centre points; the full list of experiments is located in the experimental section for this chapter. In addition, a K type thermocouple was attached to the reactor coil to more accurately monitor the temperature of the reaction, as the internal flow system thermocouple does not accurately reflect the reaction temperature. These measured temperatures were used as the points in the design space, and due to a linear heat loss, not a constant heat loss, greater differences were observed at higher temperatures resulting in a slight offset being introduced into the design.

Table 5. Reaction conditions for DOE. Measured temperature value in brackets.

Parameter	Low value	High value	Centre point
Temperature (°C)	120 (108)	160 (140)	140 (120)
Residence time (minutes)	25	50	33.3

To remove the unwanted effects of air bubbles and pump pulsation all spectra were processed with min-max normalisation over the range 210 to 290 nm (Equation 3). After this processing the absorbance value at 265 nm was taken as the response. It should be noted that model building through MLR without this treatment led to a much poorer model result and underlies the importance for spectral processing for online analysis.

$$A_j = \frac{A_i - A_{\min.}}{A_{\max.} - A_{\min.}} \quad (3)$$

Where:

A_j = min. max. normalised absorbance value

A_i = original absorbance value

A_{\min} = minimum absorbance value in normalised range

A_{\max} = maximum value in normalised range

The model was fitted with multiple linear regression (MLR) using MODDE software using terms for temperature, residence time, quadratic terms and an interaction term. Of these only the temperature x residence time interaction term appeared to be insignificant, removal from the model led to a modest gain in the Q^2 value indicating a reduction in overfitting. The summary of fit statistics were: $R^2 = 0.99$, $Q^2 = 0.98$, validity = 0.93 and reproducibility = 0.98.

The model statistics indicate an excellent model with strong predictive ability. The response contour plot for the model (Figure 40) identifies the optimum conditions as being high temperature and longest residence time. It should be noted that this corresponds to the best conditions only within this design space. The global optimum could very well lie elsewhere and an optimisation over a larger space would be required to identify it. The model predicts that a residence time slightly lower than 50 minutes would be optimal, due to decomposition of the semicarbazide when held at a higher temperature for an extended time.

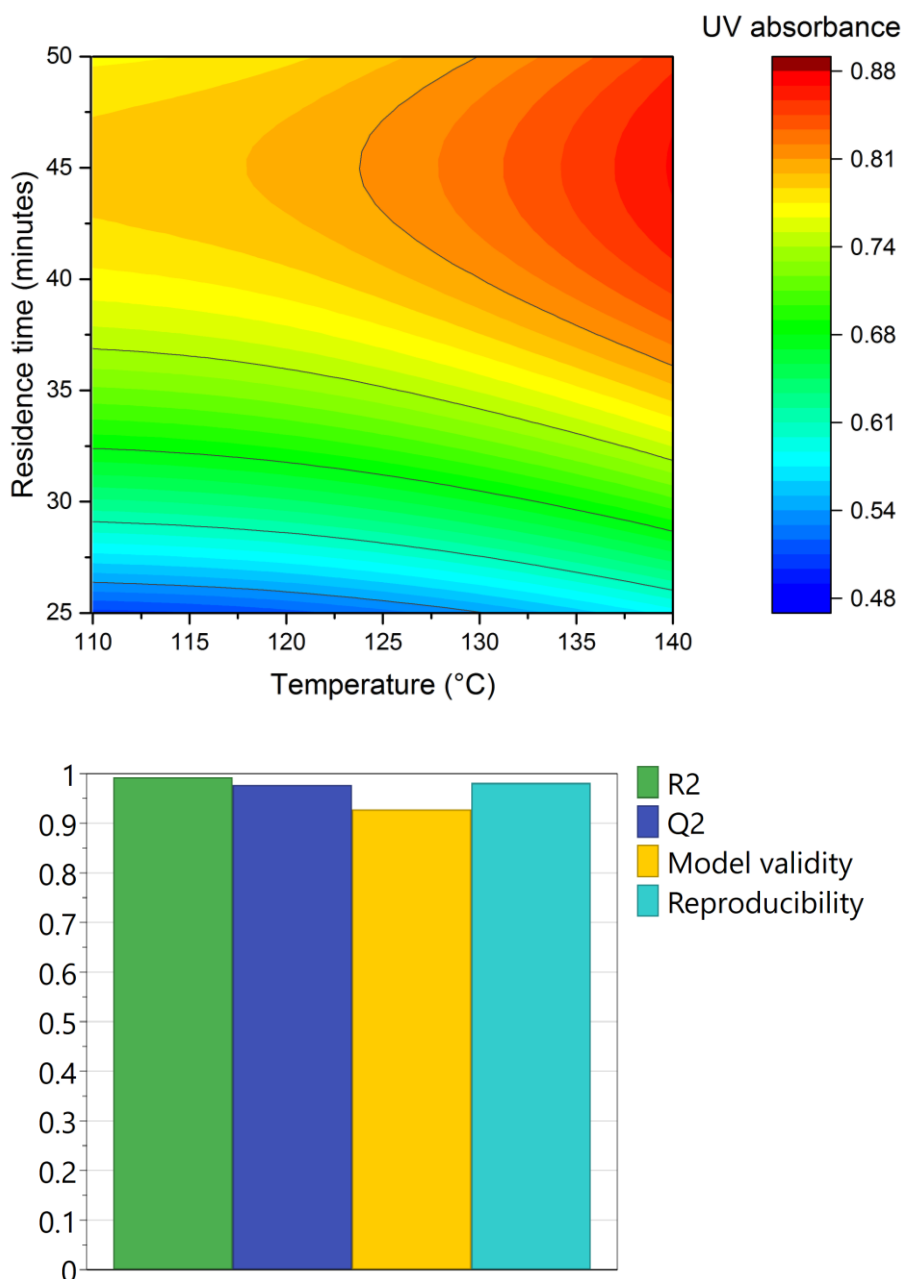


Figure 40. (Top) Response surface for DOE optimisation of carvone semicarbazone synthesis (Bottom) Model statistics calculated using MODDE.

The cell was used for over 10 hours of inline monitoring with so signs of degradation to the resin body, although the sealing tape was replaced. Having the cell installed as part of the system meant that identifying the onset of steady state conditions was extremely simple, all that was required was to examine the real time spectra, observing the absorbance value at 265 nm increasing and then plateauing as the steady state conditions are achieved (Figure 41). This is useful for continuous process control; if a standard deviation threshold was met for an absorbance of certain magnitude, then it can be safely assumed that the reaction was at steady conditions and collection then triggered.

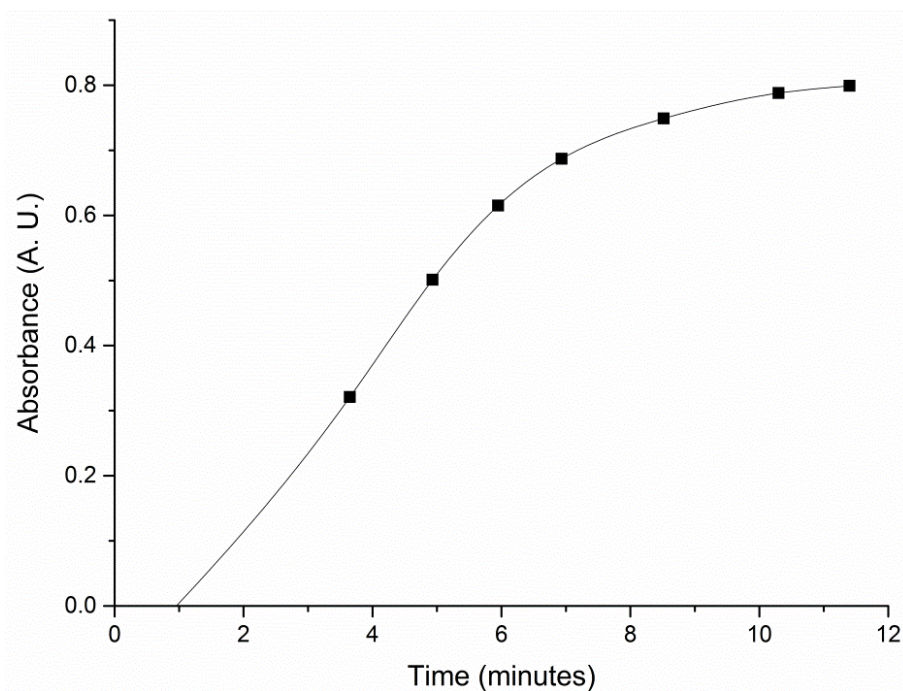


Figure 41. Change in reaction absorbance showing onset of steady state conditions

2.2.11 3D printing for fibre optic waveguides

In addition to the printing of parts that can house the reaction mixture directly it was imagined that 3D printing could also act to hold reactor coils. PTFE and PFA are common choices for reactor coils and have the benefit of transmitting light in the visible and ultraviolet wavelength regions. If fibre optics could be accurately aligned either side of the hollow core, spectroscopic monitoring could then be performed on solutions within the tubing, allowing reactions to be monitored.

As a test of the concept a short length of PTFE tubing was aligned between two collimating lenses (Figure 42) connected to a halogen light source and a visible range spectrometer. The test was successful, but while the visible absorption spectrum of fluorescein could be measured, the sensitivity was low due to the high amount of stray light reaching the detector.

The 3DP cell subsequently used to align the fibre optics either side of the tubing was the straight channel transmission flow cell C1, which serendipitously/due to excellent foresight, had all the characteristics required. The 1/4"-28 TPI connectors could then be used to keep the tubing taut and fixed in position - an important refinement that kept spectra reproducible. Larger core fibre optics (600 μm) were used to ensure that the entire hollow core of the tubing was irradiated. If smaller fibre cores were used then a poorly aligned fibre could merely cross the top of the cavity, producing a path length smaller than the internal diameter of the tubing.

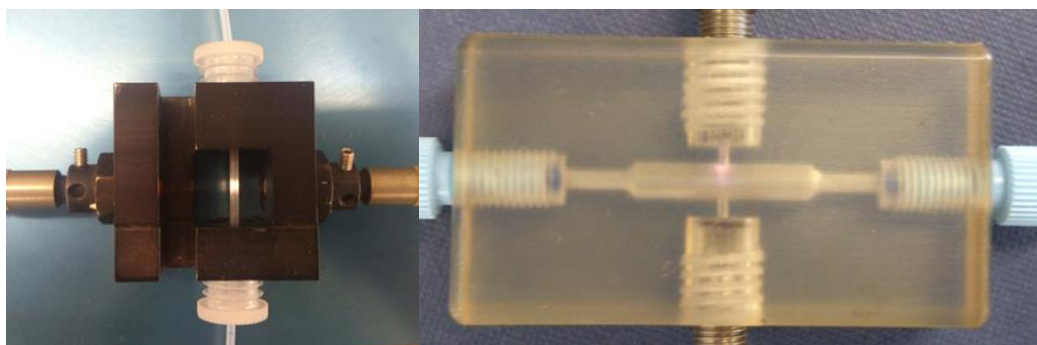


Figure 42. (Left) Use of collimated lenses for in tube spectroscopy (Right) Use of 3D printed waveguide

The 3DP waveguide was successful and allowed the acquisition of good quality spectra, predominantly due to the large reduction in stray light. As most tubing used in laboratory scale flow chemistry is approximately 0.1-1.0 mm I.D. this provides a suitable range of path lengths for absorption spectroscopy, although naturally for standard 1/16 " tubing the wall thickness becomes larger as the I.D. decreases, potentially leading to attenuation of the signal. Analysis of fluorescein solutions in PTFE tubing of different internal diameters demonstrated a linear relationship (Figure 43), allowing customisable analysis by changing the tubing used.

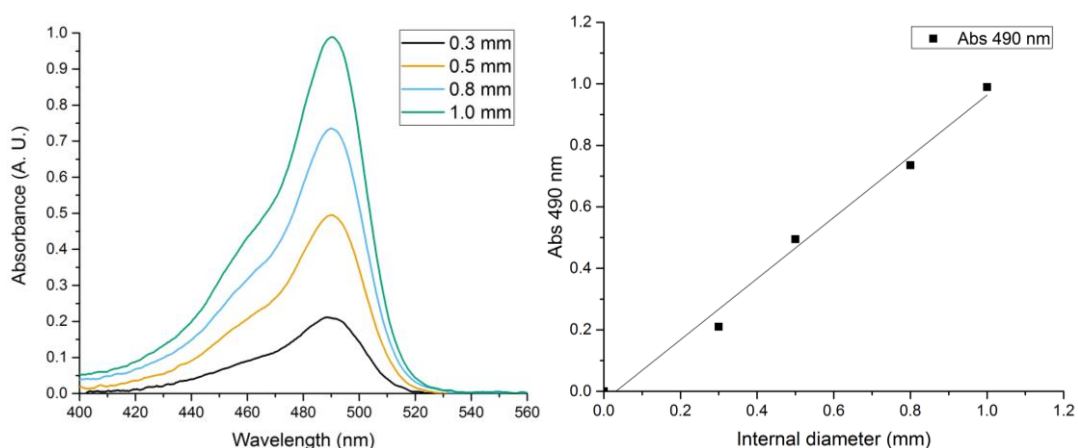


Figure 43. (Left) Spectra acquired for fluorescein inside PTFE tubing (Right) Change in absorbance at 490 nm for tubing of varying internal diameter.

2.2.11.1 Visible spectroscopic monitoring for S_NAr reaction

As a test reaction for the ‘in-tube’ spectroscopy the aromatic substitution reaction between a nucleophilic base and an aryl halide was carried out (Scheme 5). This reaction has been utilised for flow chemistry many times before, most recently and notably by Hone *et al.*¹⁵¹ who utilised an automated reactor system with online HPLC analysis to determine kinetic models for the products.

Initial use of morpholine as the base led to precipitation and near blockage of tubing due to the formation of morpholinium fluoride, as a result it was decided to switch to pyrrolidine. The aromatic substitution

products of this reaction exhibit an absorbance at approximately 400 nm and above (Figure 44) which will be visible through the PTFE tubing. A DOE optimisation was carried out using a central composite faced (CCF) design, taking the absorbance at 480 nm as the response. A full list of experiments is in the experimental section. Data was collected by an MChem student, Richard Carrington, under supervision, as part of a final year undergraduate research project.

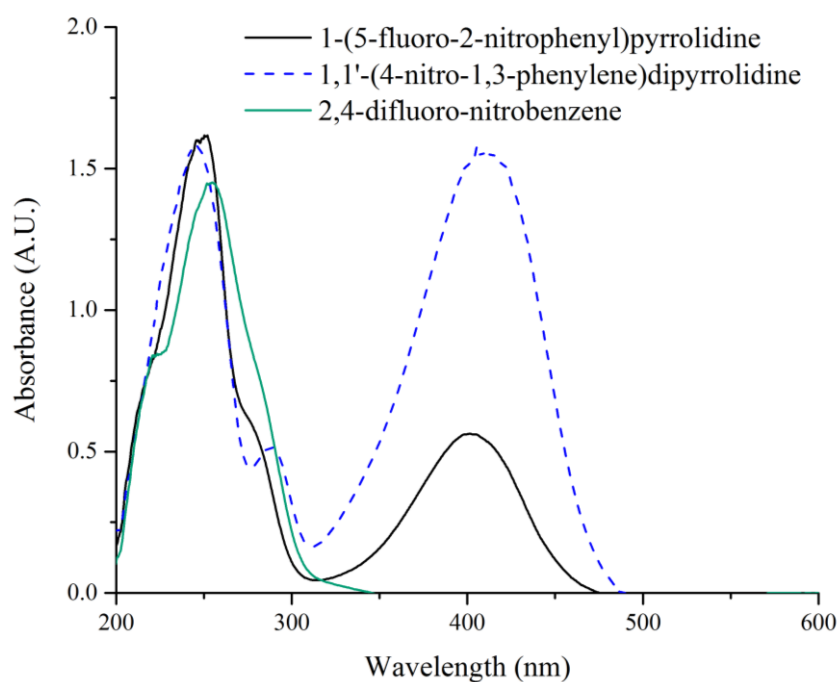
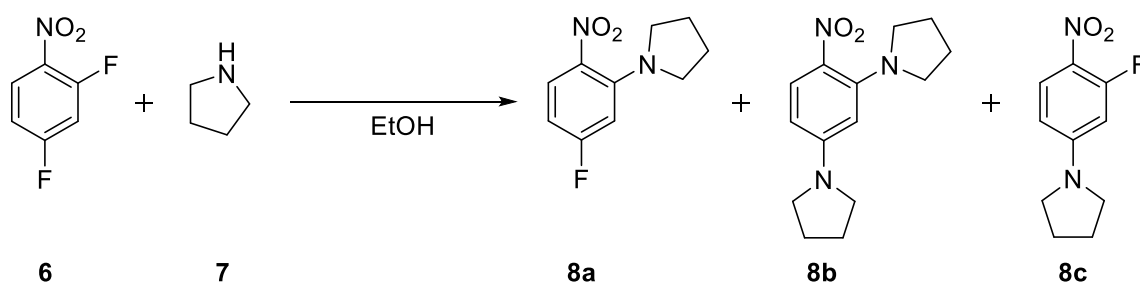


Figure 44. UV/Vis spectra for the main products of the S_NAr reaction between pyrrolidine and 2,4-difluoro-nitrobenzene



Scheme 5. S_NAr reaction between pyrrolidine and 2,4-difluoronitrobenzene

The model was built in MODDE software using MLR, using the coefficients for temperature, equivalents, residence time and the residence time squared term. The temperature squared coefficient, equivalents squared coefficient, and the interaction term were excluded as they were deemed to be insignificant. This gave an R^2 value of 0.904 and a Q^2 of 0.784. The reproducibility was high at 0.989, this led to a low validity score of 0.343 as the error in the model was inevitably higher than that for the extremely close replicates - this does not affect the model quality. A contour plot generated from the

model shows that the highest response at 480 nm is achieved at high temperatures, long residence times and a high equivalent of base (Figure 45).

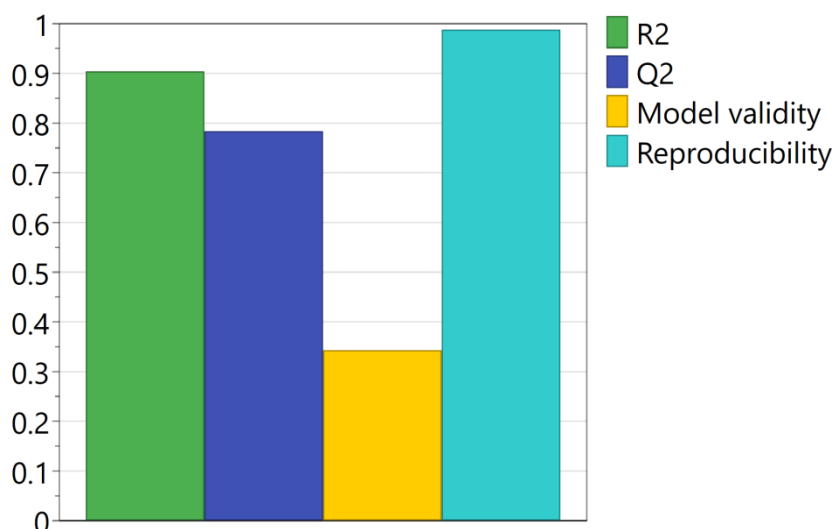
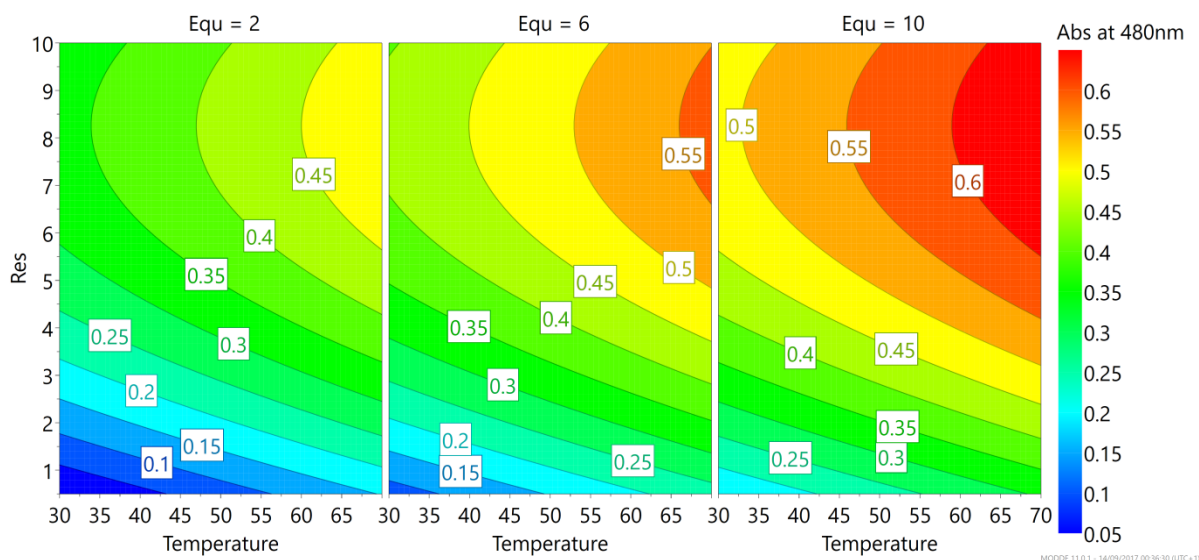


Figure 45. (Top) Contour plot for DOE optimisation showing increasing absorbance as conditions reach higher levels (Bottom) Model statistics calculated using MODDE.

The absorbance response here is unable to differentiate between the mono and di substituted product as both show an absorbance at 480 nm. If a more selective analytical technique, such as HPLC, were employed then this effect would be discernible. Nevertheless, the 3DP waveguide allows a very simple and customisable flow cell to be easily installed into almost any flow chemistry equipment.

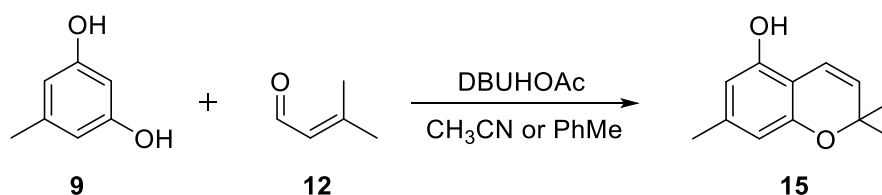
2.2.11.2 Use of 3D printed waveguide for the optimisation of the formal [3+3] cycloaddition to give 2H-benzopyrans

The 3D printed waveguide in section 2.3.1 was next applied to the synthesis of 2H-1-benzopyrans, an important structure found in a wide range of applications. The work of Lee *et al.*¹⁵² has shown that the simple [3+3] cycloaddition of substituted 1,3-dihydroxybenzenes with α,β -unsaturated aldehydes gives the 2H-1-benzopyrans under catalysis by ethylenediamine diacetate (EDDA), an acid-base conjugate salt, in moderate yields and with long reaction times in refluxing xylene. It was thought that the ability to superheat the reaction using flow chemistry would allow a more rapid synthesis.

2.2.11.3 Replacement of EDDA and the use of an ionic liquid catalyst

EDDA was found to be insoluble in most organic solvents except alcohols, limiting the potential for flow synthesis using the [3+3] approach with this catalyst. Tests with up to 5 % added water into acetonitrile allowed dissolution of the EDDA and showed a small amount of conversion to the product, however the yields were very low at < 5 %. This is presumably due to the inability of the ring closing condensation step between the carbonyl and the aromatic ring to proceed with a high mole percent of water present.

It was hypothesised that an acid-base conjugate ionic liquid would be miscible with a wide range of organic solvents and would therefore represent a good option for flow synthesis. The ionic liquid was prepared from DBU and acetic acid to give DBU acetate [DBUHOAc]. A test performed in batch for the reaction between 5-methyl-1,3-dihydroxybenzene and 1 equivalent of 3-methyl-2-butenal, using 10 mol. % DBUHOAc (Scheme 6), gave a 25 % yield of the 2H-benzopyran **15** when refluxed for 14 hours in acetonitrile, increasing to 37 % when the reaction was performed in refluxing toluene.



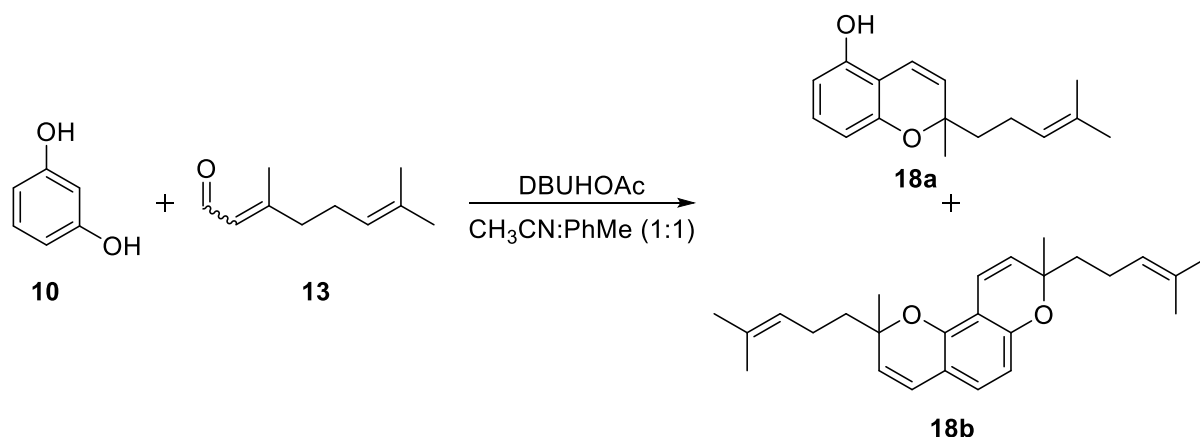
Scheme 6. Synthesis of 2,2,7-trimethyl-2H-1-benzopyran-5-ol

The product of this reaction is lightly coloured and would absorb light in the near visible region, therefore it was decided to use the AM waveguide from section 2.2.11 to try and optimise the reaction.

2.2.11.4 Optimisation of formal [3+3] cycloaddition under flow conditions

An alteration was made to the reaction (Scheme 7) such that 1,3-dihydroxybenzene was used in place of the methyl substituted dihydroxybenzene used for the batch test. The methyl substituent would be

expected to increase the reaction rate, so a non-optimal starting material would give a wider range of substrates that can be used with the optimised conditions. The unsaturated aldehyde was switched to two equivalents of 3,7-dimethyl-2,6-octadienal instead of the single equivalent of 3-methyl-2-butenal as the product is slightly deeper in colour due to the extra unsaturated moiety, enhancing the spectroscopic response.



Scheme 7. Synthesis of 2H-benzopyran and 2H,8H-benzodipyran

The AM waveguide was fitted with a 0.8 mm ID tube to maximise the absorbance, optimisation was performed for temperature residence time and loading of the DBU-acetate. This was performed through a Box Behnken design, allowing the generation of a response surface model while reducing the number of required experiments. Samples were taken at steady state for each experiment and further analysed offline with HPLC to determine if the absorbance measurement was selective for the formation of the 2H-benzopyran **18a** rather than side products such as self-condensation of the unsaturated carbonyl.

MODDE software was used to generate a DOE model for the experiments; this identified a positive skewness to the distribution of the results so a logarithmic transformation of the response, Y , with the form $\log(a \times Y)$ was applied. The online spectroscopic data was fitted with a model containing terms for each of the factors only, giving a good model (Table 6). The HPLC data for the experiments was similarly treated and MLR models also built in MODDE. The model for the 2H, 8H-benzodipyran **18b** required the addition of a quadratic term for DBU acetate loading and the interaction term for the DBU acetate loading and temperature, again demonstrating that the use of UV absorbance as a response can lead to non-specific reaction information.

Table 6. Model statistics for different responses

Response	log factor	R ²	Q ²	Reproducibility
420 nm absorbance	1	0.88	0.80	0.94
2H-benzopyran peak area	1.3	0.86	0.74	0.99
2H, 8H-benzopyran peak area	1.3	0.96	0.90	0.99

All the models predicted higher product formation at high temperatures, catalyst loadings and residence times. Very low responses were observed at catalyst loadings of 10 mol. % for all analysis techniques with an increase in responses expected as the loading increased, although the effect of increasing catalyst is predicted to plateau for the 2H,8H-benzopyran **18b** at around 80 mol. %.

2.2.11.5 Ionic liquid promoted synthesis of 2H-benzopyrans

With a catalyst that was now miscible with organic solvents, a small number of 2H-benzopyrans were synthesised under flow conditions (Scheme 8) with poor to moderate yields. 1 equivalent of aldehyde was used to try and selectively produce the 2H-benzopyrans rather than the 2H-8H-benzopyrans (Table 7).

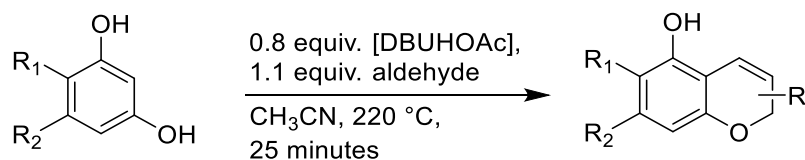
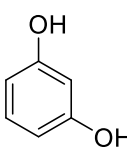
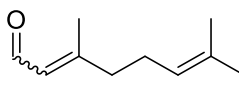
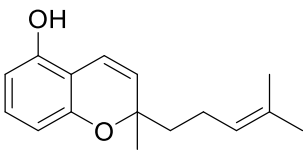
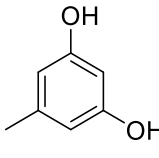
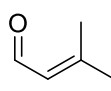
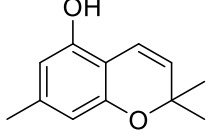
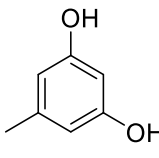
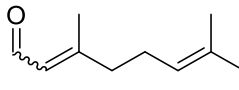
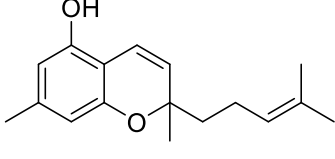
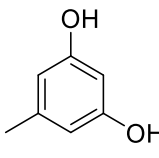
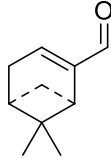
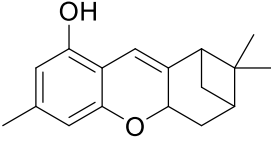
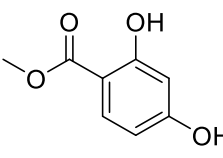
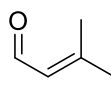
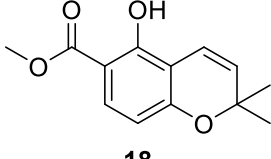
**Scheme 8.** General synthesis of 2H-benzopyrans

Table 7. Reaction of benzene-1,3-diols with α,β -unsaturated aldehydes under flow conditions

Entry	R ₁ , R ₂	α,β -unsaturated aldehydes	Product (yield)
1	 10	 13	 18a (27 %*)
2	 9	 12	 15 (49 %)
3	 9	 13	 17 (38 %)
4	 9	 14	 16 (Trace)
5	 11	 9	 18 (Trace)

*Additional 12.5 % yield of the 2H,8H-benzopyran

While the yields for some are comparable to the batch reactions in the literature, usually requiring > 10 hours reaction time in refluxing xylene, the yield for the methyl-2,4-dihydroxybenzoate was poor, due to the presence of the electron withdrawing ester on the aromatic ring. This is further confirmed by the lowered reactivity of the benzene-1,3-diol compared to the 5-methylbenzene-1,3-diol, but higher than the methylbenzoate suggesting that the electron rich aromatic has an enhanced ability for completing the ring closing dehydration and a more nucleophilic character for the hydroxyl groups.

2.2.12 3D printing for ATR flow cells

Earlier work in this thesis has demonstrated that the lowest achievable path length with in tube spectroscopy is approximately 0.2 mm, essentially the smallest size commercially available tubing. This approach could also be applied to capillaries, and if quartz were to be used the full UV range would be available. The microfluidic cell can theoretically achieve path lengths down to 50 μm , however path lengths smaller than this size would significantly increase the chances of blockages forming within the part, and lead to an increase in the back pressure generated. While some of the backpressure increase could be addressed through design changes it is still likely that the risk of sealing failure would increase to an unacceptable degree.

To produce cells with path lengths lower than this therefore requires the use of ATR. It was conceived that an AM device could be designed to hold a prism such that fibre optics could be angled onto the surface as well as a fluidic channel. If the angle is shallow enough then it would be possible to achieve total internal reflectance (TIR) within the prism and collect the spectrum for any liquid in contact with the prism surface. Excellent work utilising a similar approach was used to image flowing reagents by Chan *et al.*¹⁰³ by placing an ATR prism over network of micro channels.

A part was designed (C4) whereby a prism would be held in place to form one wall of a fluidic channel. Fused silica was the material chosen for the prism, mainly due to its excellent transmission of wavelengths from UV to IR, but also because fused silica is significantly cheaper than quartz or sapphire. The first CAD model aimed to use a double bounce of incident UV light (Figure 46) and used an AM compression ring, designed to tighten against the prism to form a seal against a rectangular Viton gasket and the flow channel was cut into the gasket. The light was collected *via* fibre optics and routed to a UV/Vis spectrophotometer. However, this design did not achieve a sufficient angle between the light and the surface of the prism, being only 45 ° meaning TIR could not be achieved and only a small amount of light was transmitted to the spectrometer. In addition, the part was found to be prone to liquid leaks as the compression ring could not exert enough force to seal the prism against the gasket without damaging the contact points.

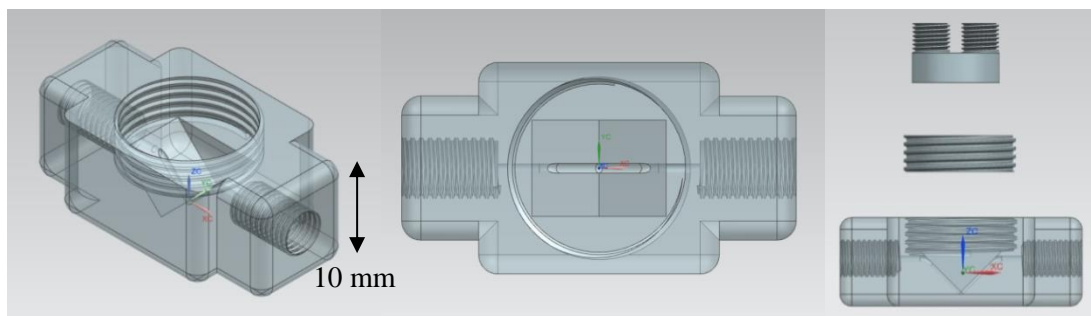


Figure 46. (Left) First iteration, C4 (centre) Top down view showing prism cavity (right) Separated view showing main body, compression ring and fibre optic alignment tool.

The part was redesigned so that the flow path was in contact with the base of the prism rather than the angled sides. While now only a single bounce, this allowed an improved fit with the Viton gasket and gave a part (C5) that was leak tight. This also enabled a shallower angle between the fibre optics and the prism plane (Figure 47), achieving TIR for water, ethanol and solvents with similar refractive indices to these.

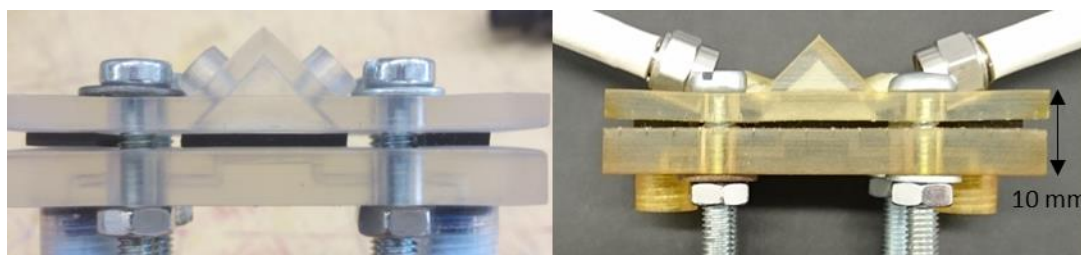


Figure 47. (Left) Original 45 ° alignment cell. (Right) Redesigned AM ATR flow cell, C5, with fibre optics in place.

The ability to perform spectroscopy in the part was demonstrated by infusing solutions of fluorescein in water and ethanol. The aqueous solution was prepared at 0.032 M which by the Beer Lambert law would give a (theoretical) absorbance of 25 at 490 nm in a 100 μm path length flow cell. The spectrum demonstrates both the visible absorbance and those in the UV (Figure 48) and gave an absorbance of 0.483 at 490 nm, equating to an effective path length of approximately 2 μm .

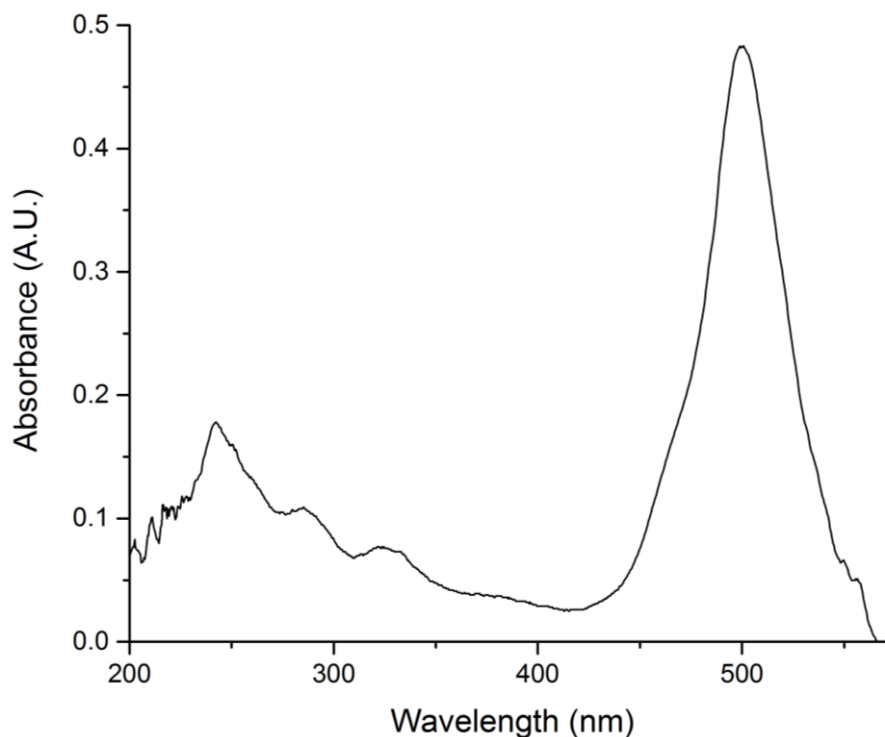


Figure 48. Absorbance spectrum for fluorescein in AM ATR flow cell.

While the spectrum for fluorescein was of good quality, with only minor distortion due to the ATR, it was found that trying to analyse concentrated solutions (> 1 M) of compounds with lower molar extinction coefficients was problematic, particularly at wavelengths < 300 nm, leading to broad spectra with large lambda max deviations. This is presumably due to the change in refractive index of more concentrated solutions relative to water and could be overcome through a move to a material of higher refractive index.

Experiments using a cylindrical sapphire window to conduct ATR spectroscopic measurements did show reasonable wavelength accuracy when used to analyse fluorescein, rose bengal and methylene blue, but the shape of these windows was not as amenable as the fused silica prism to integrate into a flow cell. Attempts to fit the window into a flow cell with an integrated flow path (Figure 49) led to leaks at the edges and spectra could not be acquired with the system.

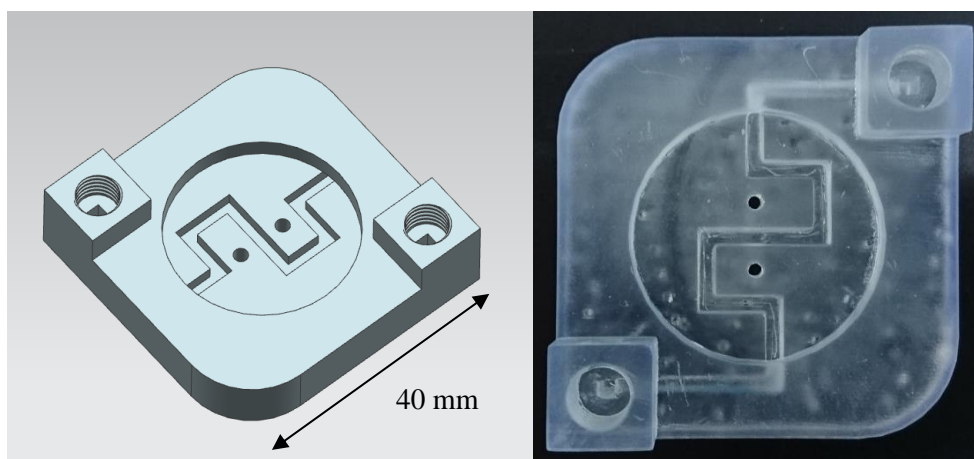


Figure 49. (Left) CAD model for sapphire prism holder (Right) SL printed prism holder with integrated flow path for sapphire ATR flow cell

2.3 Chapter summary

The use of additive manufacturing to produce parts capable of spectroscopic monitoring of flow chemistry has been clearly demonstrated. Due to the high level of customisation possible through AM numerous designs have been produced, all of which were able to record spectra. Of particular note is the production of microfluidic scale channels with embedded fibre optics. These units are cheap, simple to prepare and capable of high quality analysis, both for flow chemistry and as parts for analytical chemistry.

Where the chemical compatibility of the SL parts is not sufficient a cheap design for the printing of waveguide has been devised. This part allows the collection of spectra inside commercial PTFE tubing, with control over the analysis pathlength possible simply by changing to tubing with a different internal diameter.

The issues with AM parts regarding part porosity and solvent compatibility have directed efforts towards the use of SL but ideally metal printing techniques should be utilised whenever inline monitoring is the aim for maximum robustness. The use of AM techniques has also been realised where non-wetted accessories are to be produced.

2.4 Further work

Further work in this area will focus on the development of the ATR cells further, as they offer the most practical way to monitor flow chemistry with no inline dilution or reduction in reagent concentration. Parts exploiting multiple bounces within a prism would allow the desired path length to be selected simply by moving the receiving fibre up or down a prism face to collect light from 1 bounce, 2 bounces and so on.

Another area of focus should be the use of heavy walled quartz tubes with internal diameters of 100 microns or lower in the 3D printed waveguide. Short lengths of tubing with such small diameters would not unduly increase back pressure, and the use of quartz allows access to UV wavelengths down to 190 nm, and additionally provides an extremely robust material where temperature and chemical resistance are concerned. Combined with the printed waveguides introduced in this thesis a powerful, and simple, reaction monitoring method would be possible.

3 The use of additive manufacturing for chemical reactors

3.1 Introduction

In earlier work by Capel *et al.*⁷⁷ AM reactors were shown to be viable alternatives to commercial tubing, with more design freedom allowing the integration of mixers and other features. While SLM reactors were also featured in this work¹⁵³ the reaction conditions used with them were relatively mild with all reactions being performed below the boiling point of the water:methanol solvent mixture.¹⁵⁴ The use of these SLM reactors under more extreme conditions was investigated by incorporating them into a commercial flow chemistry platform, a Uniqsis Flowsyn, to perform chemistry with superheated reagents and under high pressures.

SLM printed reactors do unfortunately have significant drawbacks surrounding the clearance of channels post printing. The work by Capel and co-workers⁷⁷ found that removal of powder from flow channels was extremely difficult, and had to be performed through repeated cycles of nitrogen flushing, tapping and sonication to loosen the material. In addition the surface of the internal channels is often not smooth, and this can have negative effects for parts built where laminar flow is the goal, such as for the synthesis of nanoparticles.¹⁵⁵

To this end, the use of ultrasonic consolidation/ultrasonic additive manufacturing (UC/UAM) was investigated to produce metal reactors, capable of heating to the same extent as the SLM reactors and with good chemical compatibility, without the drawbacks of a powder bed system. Parts built through UC/UAM are smaller in scope, but this is a limitation of the build platforms of current machinery, not inherent to the technique itself, and will be overcome through technological improvements in the near future.

Finally, the ability to produce transparent parts through SL led to the design of reactors for photochemistry. Two designs were tested to ascertain the limiting factors on reaction efficiency as well as the optimal flow channel geometry. The bonding of quartz cover slips to etched silicon was shown by Lu and co-workers as early as 2001¹⁵⁶ and this allowed both the photochemical reaction of benzophenone and isopropanol to synthesise benzopinacol, and online/inline analysis of the product by UV/Vis spectroscopy, to be performed in the same reactor. The reactor was of very small volume and therefore the product throughput was low, by using SL printing techniques it should be possible to produce larger scale reactors capable of performing photochemical transformations.

3.2 Results and Discussion

3.2.1 Optimisation of benzopyridoxazine synthesis

3.2.1.1 SLM reactor design

A metal reactor (R2) had been previously designed and printed with SLM by Andrew Capel (Chemistry Department, Loughborough University) and used for flow chemistry within the wider group. R2 was fabricated from stainless steel and after removal of non-melted powder was found to have a volume of 8.6 mL (Figure 50). The flow channel was a serpentine design, with numerous hairpins to aid mixing, and the inlets were manually tapped to have 1/4" 28 t.p.i. inlet ports.

The reactor R2 was designed to fit into the column oven of an Agilent 1100 HPLC system and had a rectangular cuboid shape with a flat base, helpfully enabling the part to also be easily installed onto the chip heater of the Uniqsis Flowsyn (Figure 50).

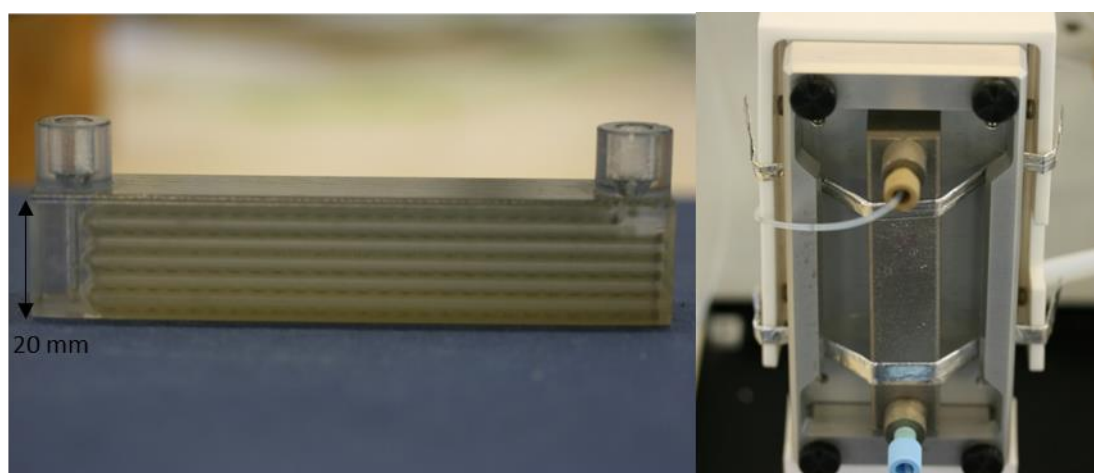
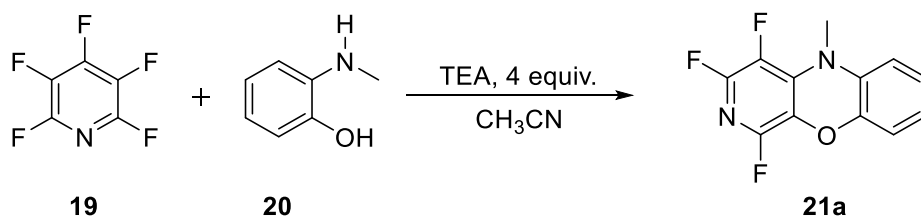


Figure 50. (Left) SL printed version of R2 (Right) SLM R2 installed carefully on Uniqsis Flowsyn chip heater.

This afforded precise temperature control up to 200 °C and the reactor was then used for the flow synthesis of a benzopyridoxazine (Scheme 9), compounds potentially with promise as a treatment for trypanosoma brucei, previously synthesised by the Weaver group at Loughborough University who recently published the synthesis of benzothiophenes through similar chemistry.¹⁵⁷



Scheme 9. (Top) Synthesis of 1, 3, 4-Trifluoro-5-methyl-5H-benzo[b]pyrido[4,3-e][1,4]oxazine.

Early scoping experiments were performed using a 100 μm path length UV/Vis flow cell installed after the BPR. Once the reaction had exited the reactor the temperature was increased to 150 $^{\circ}\text{C}$ from 50 $^{\circ}\text{C}$ and spectra were acquired regularly. The product exhibits a new absorbance at 330 nm not seen in the starting materials and monitoring the spectra at this wavelength allowed a measure of the reaction progress to be obtained (Figure 51). This revealed a relatively rapid increase in absorbance, showing that temperature was the most significant factor in improving the absorbance at 330 nm. Once the temperature had reached 150 $^{\circ}\text{C}$ there was an approximately 20-minute delay before the rate of absorbance increase had decreased to almost zero, revealing that residence time also had a contribution to improved absorbance.

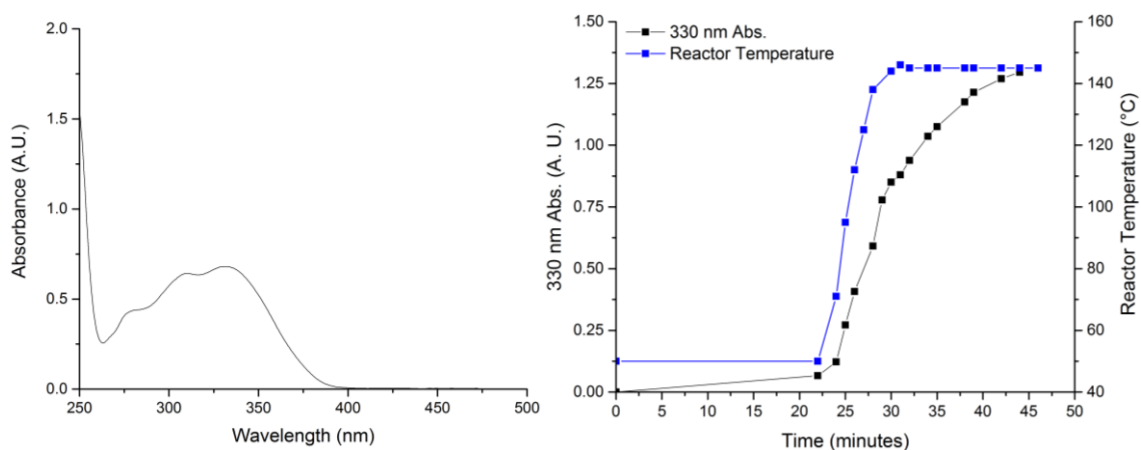


Figure 51. (Left) UV absorption spectrum for 1, 3, 4-Trifluoro-5-methyl-5H-benzo[b]pyrido[4,3-e][1,4]oxazine showing a maximum at 330 nm (Right) Trend showing increasing absorbance at 330 nm as the reactor temperature is increased.

Optimisation of the reaction was then carried out through the use of a fixed step simplex algorithm, which is capable of locating local maxima on an n -dimensional surface by building a simplex of $n+1$ vertices. The boundaries of the surface were set as residence times of 8.6 to 86 minutes and temperatures of 100 to 180 $^{\circ}\text{C}$. As the reaction solvent was acetonitrile all reactions would be above boiling point, so were performed using a 250 psi back pressure regulator. An initial simplex was carried out (Table 8), allowing steps of 14 $^{\circ}\text{C}$ and 0.16 mLmin^{-1} . Samples were taken at steady state conditions, diluted 1 in 100 with acetonitrile and analysed by UV/Vis spectroscopy.

Table 8. Initial simplex points.

Simplex point	Flow rate (mLmin ⁻¹)	Temperature (°C)
S1	0.72	107
S2	0.72	121
S3	0.88	114

The responses were ranked from low to high and the two initial simplex points with the highest absorbance were used to generate a new point within the design space (Equation 3). This point corresponds to a reflection of the lowest ranked response in the line passing through the two highest ranked points and results in all factors being changed at once.

$$(x_1 + x_2, y_1 + y_2) - (x_3, y_3) \quad (4)$$

Where:

x_1, x_2 = Flow rates of the highest and second highest response points respectively

y_1, y_2 = Temperatures of the highest and second highest response points respectively

x_3, y_3 = Flow rate and temperature respectively of the lowest response point

This process was then repeated until the absorbance stopped increasing, or, circling around a point began. In this manner a total of 16 experiments were carried out until a local maximum was found (Figure 52). At the boundary some conditions were placed on the simplex to try and re-enter the reaction space. When a new vertex point was generated outside the boundary the worst and middle points from the previous vertex were reflected in the line through the best point and the adjacent axis. So; if a temperature boundary was encountered the flow rates of the lowest and next lowest ranked points would be reflected in the line equal to the flow rate of the best point. In this way the simplex kept exploring space and also moved in the direction of travel previously undertaken. The stop criteria were then set so that when a stable absorbance value was reached the simplex would cease.

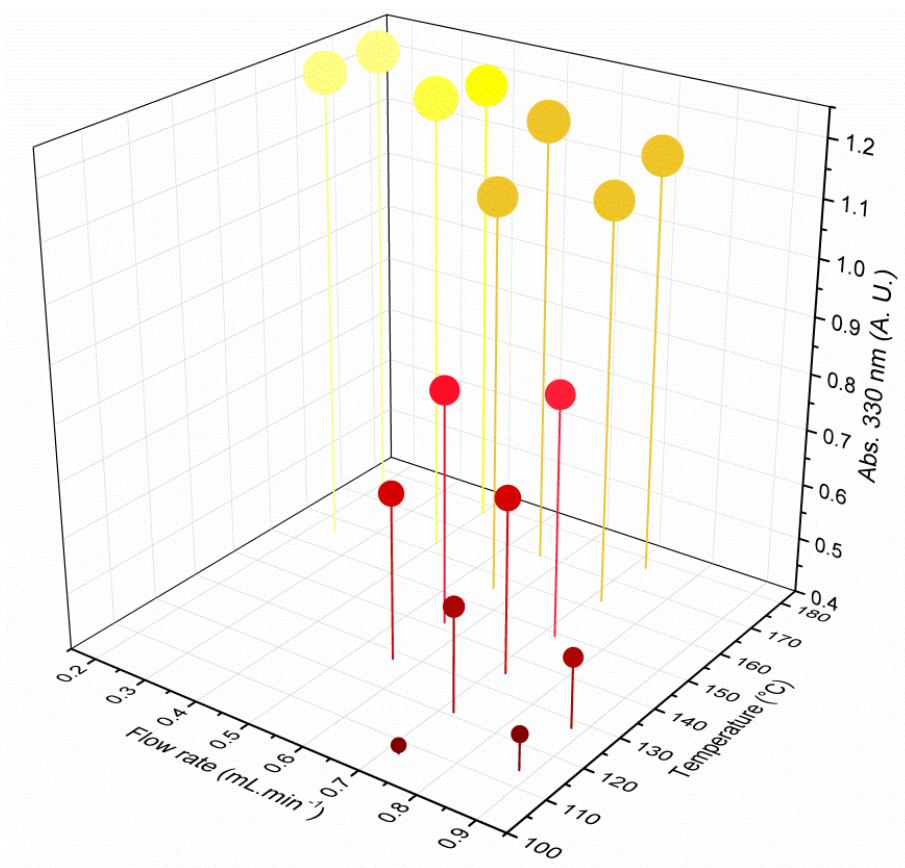


Figure 52. Progression of simplex optimisation function

The highest absorbance was found at a flow rate of 0.24 mL/min and a temperature of at least 156 °C (156 and 170 °C gave the same absorbance of 1.24 A. U.). The data was entered into MODDE for modelling ($R^2 = 0.96$, $Q^2 = 0.94$), which simply revealed that longer residence times and higher temperatures were both positive effects for increased absorbance at 330 nm, as would be expected given the direction of travel observed for the simplex. No interaction term for temperature and residence time was significant, a result that was not obvious by simple inspection of the collected data. Further analysis by HPLC was performed on simplex points S1, S7 and S15 (Figure 53) to estimate yield by comparison to a reference standard of the desired benzopyridoxazine (Table 9). Caution should be exercised regarding the generated model from the simplex data, as it does not cover the reaction space in as systematic a manner as a formal DOE would.

Table 9. Yield calculation for simplex points.

Injection	Sample Peak Area (m.A.U.minute)	Concentration (mg.mL ⁻¹)	Yield (%)
Standard	1854.34	0.1020	NA
Simplex 1	89.54	0.0049	2.55
Simplex 7	772.45	0.0425	22.0
Simplex15	878.55	0.0483	25.0

The desired product peak (retention time approximately 24 minutes) increases in area from simplex 1 to simplex 15. Concurrently there is a decrease in peak area for impurities (retention times of approximately 10 and 16 minutes) as the simplex experiment number increases. The impurity was identified through ¹⁹F NMR and is the result of nucleophilic attack by both the hydroxyl and amine groups of 2-(methylamino)-phenol on separate pyridines.

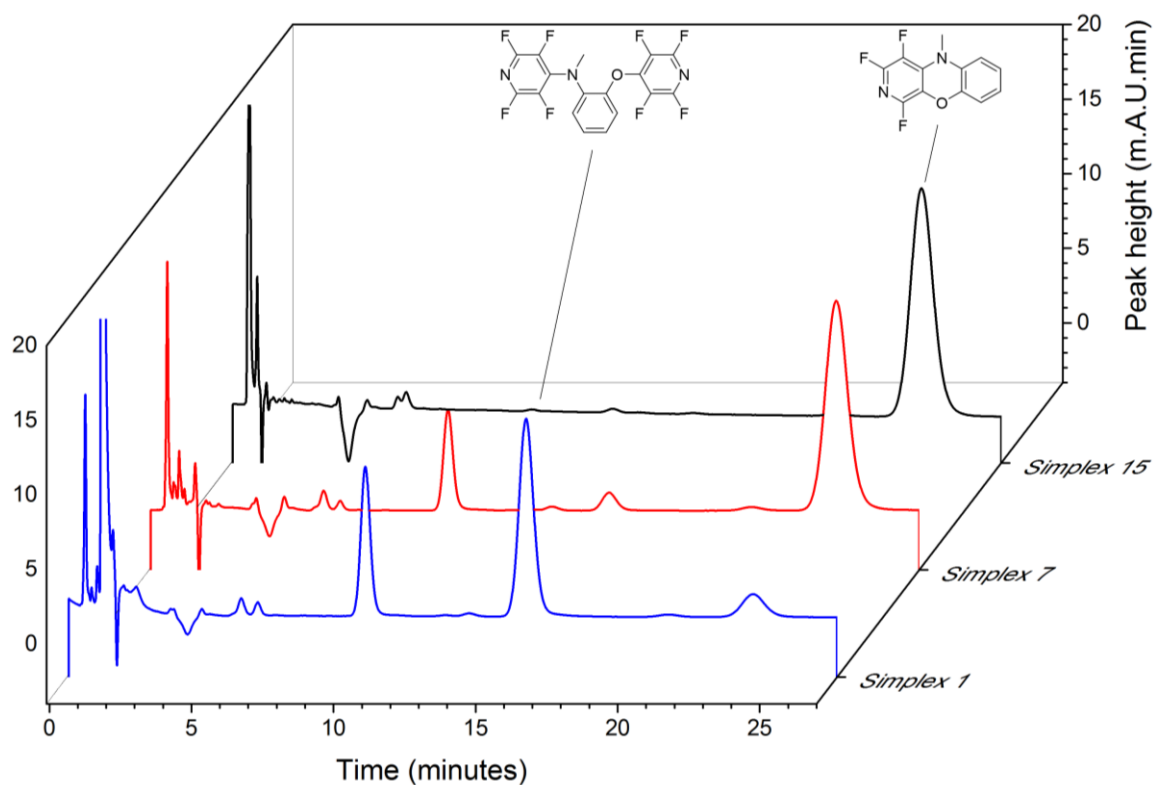
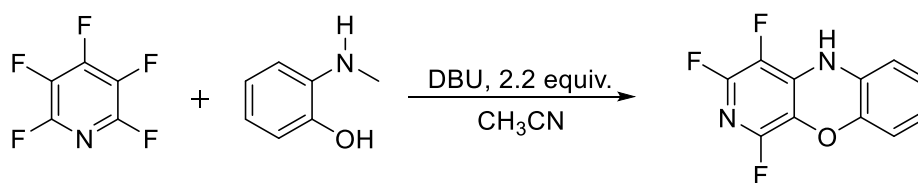


Figure 53. Chromatograms for the analysis of simplex runs 1, 7 and 15

The simplex improved the outcome of the reaction by a factor of 10 within a relatively small number of experiments, the temperature limit of the heater being used is 200 °C so some further gain could be achieved if the simplex were extended slightly further. The use of UV/Vis spectroscopy for the optimisation would be limited for any further increase, for the spectrometer used for this work an absorbance value of approximately 2 A.U. is the highest that is practical. Due to the dynamic linear range of UV/Vis spectroscopy this would only allow an increase over the starting conditions of around 10 - 20-fold, and if starting from a low initial value this may not be enough to optimise the reaction yield close to 100 %. This would have to be overcome through the choice of a different starting simplex as well as a different path length or dilution factor for analysed samples.

It was hypothesised that the deprotonation of the amino group after nucleophilic attack on the pyridine was slow with triethylamine and was limiting the yield of the reaction. To improve this it was decided to use 1,8-diazabicyclo [5.4.0] undec-7-ene (DBU) in place of TEA as the higher pKa of DBU versus TEA (12 vs. 10.8, values in water for conjugate acids¹⁵⁸ would allow a greater yield to be achieved in flow and potentially use a lower stoichiometry.

The maximum scoring vertex from the simplex optimisation was selected and the reaction carried out (Scheme 10).



Scheme 10. Synthesis of 1,3,4-Trifluoro-5-methyl-5H-benzo[b]pyrido[4,3-e][1,4]oxazine using DBU to replace TEA.

The absorbance was significantly higher than previously observed for reactions using triethylamine giving a value of 1.54 A.U. compared to the previous maximum of 1.24 A.U. The reactor (R2) tolerated the use of DBU easily, with no signs of degradation at the inlets.

3.2.2 3D printing of functional reactors through ultrasonic consolidation

A UC/UAM flow reactor (R3) was designed by Tom Monaghan (Wolfson School of Mechanical, Electrical and Manufacturing Engineering, Loughborough University) and printed by Fabrisonics LLC (Columbus, OH, USA). The design featured a 1 mL internal volume and additional inlets at the start of the flow path to allow A + B = C type chemistry, and a further inlet at 0.5 mL to allow the addition of a quench feed or a further reagent feed to be used. The main body was manufactured in aluminium to minimise cost, while the reactor path was formed from copper, integrating a catalytic surface (Figure 54). As UC/UAM allows the embedding of optical fibres and similar sensors⁶⁹ a K-type thermocouple

was fitted between the copper layers to enable the measurement of a ‘true’ reaction temperature rather than the estimated reaction temperature from a thermocouple located in the heater block of the flow chemistry instrument.

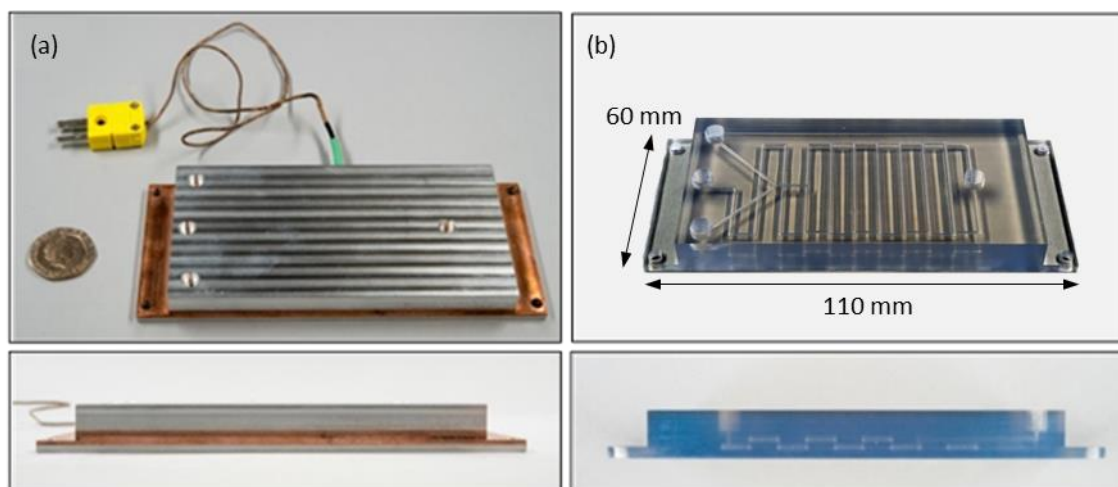


Figure 54. (a) UAM reactor (b) SL prototype of reactor showing internal structure

As with the R2 this reactor was designed through CAD to be used on the chip heater unit of the Flowsyn system (Figure 55), allowing reactor temperatures of up to 200 °C. M6 mounting screws were used to ensure good contact between the reactor base and the surface of the heating plate.

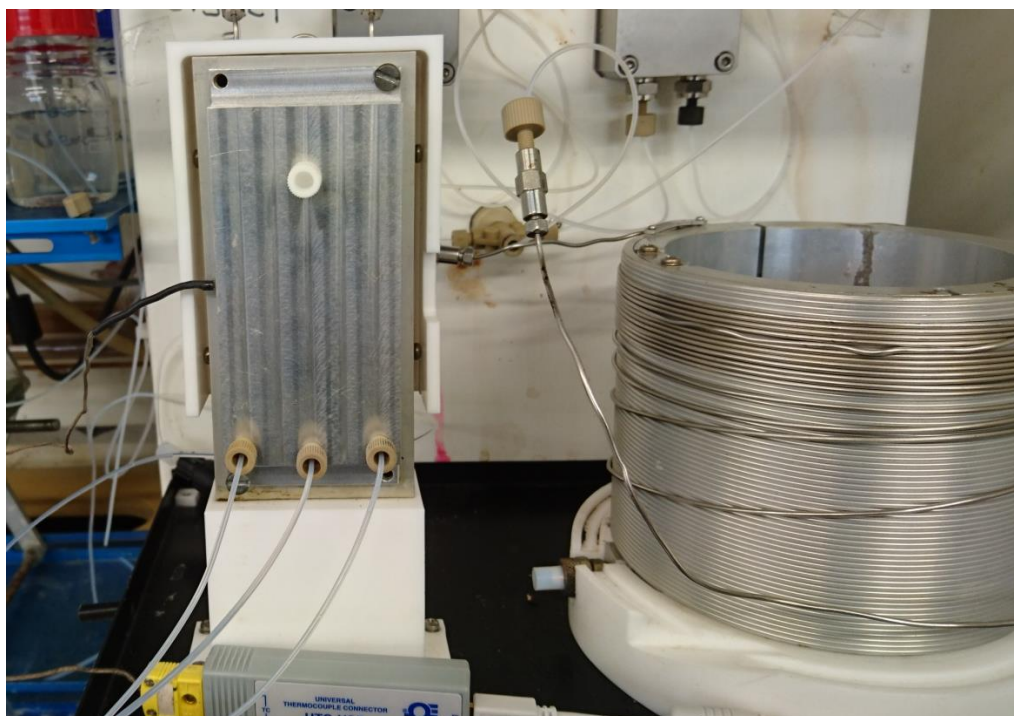
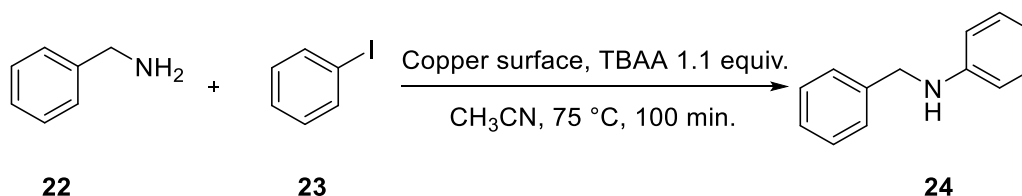


Figure 55. UAM flow reactor mounted to Uniqsis Flowsyn system. Setup as an A+B reaction system.

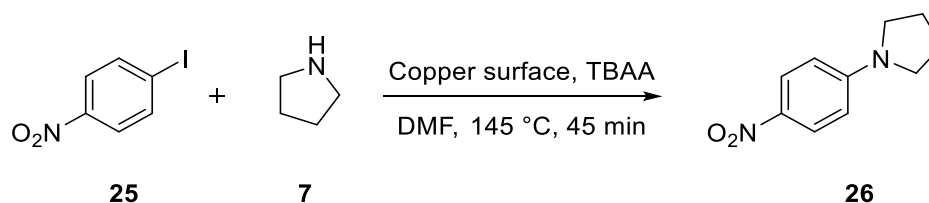
3.2.3 Ullmann coupling

As an initial test of the reactor the flow synthesis of N-benzylaniline, *via* an Ullmann like coupling (Scheme 11), was performed in a ‘one pot’ methodology. The reactor outlet stream was pale green in colour, strongly implying the removal of copper from the surface of the reactor and suggesting that the copper catalysis was occurring through removed copper rather than at the surface only. The product was not isolated but analysis of the reaction by $^1\text{H NMR}$ showed a conversion of 40 % to the product, confirming that copper was available to the reaction from the reactor.



Scheme 11. Ullmann like coupling of benzylamine and iodobenzene

Due to the seemingly large amount of copper removed by the cyano group of the solvent a modification of the synthesis was attempted, switching the solvent to DMF to avoid excessive leaching of copper from the surface of the reactor and instead performing the coupling of 4-nitro-iodobenzene with pyrrolidine (Scheme 12). This reaction also proceeded smoothly with good conversion of the starting material, determined by HPLC to be 66 %.



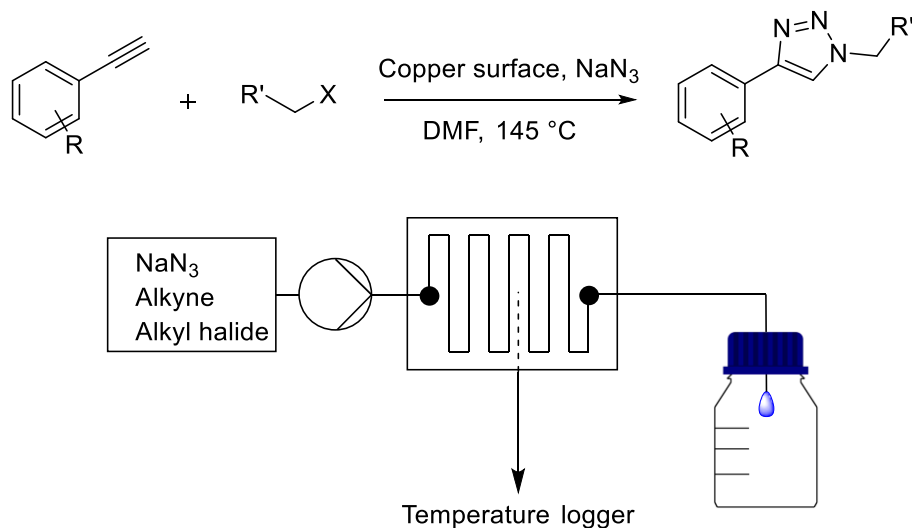
Scheme 12. Modified Ullmann coupling of pyrrolidine and 4-nitro-iodobenzene

3.2.4 Copper catalysed azide alkyne cycloaddition (CuAAC) - click chemistry in flow

The UAM reactor was next used to perform a series of copper catalysed alkyne azide cycloadditions (CuAAC) (Scheme 13). An initial optimisation for the substrates phenylacetylene and iodoethane was carried out through a full factorial DOE design, using temperature and residence as parameters. The reagents were delivered by syringe pump to ensure accuracy; due to the small build volumes inherent to UC/UAM the reactor volume was only 1 mL, requiring a flow rate in the region of μLmin^{-1} for longer residence times.

The alkyne:azide ratio was fixed at 1:2. The reaction would again be performed as a ‘one pot’ synthesis, generating the organic azide *in situ* and allowing it to react with the alkyne straight away, rather than

isolating potentially unstable compounds, therefore allowing access to small organic azides in a safer manner. The optimisation was performed for phenylacetylene and iodoethane and the response was taken as the peak area ratio of the triazole product to the phenyl acetylene starting material, determined by HPLC. The parameters varied for the optimisation were temperature and residence time (Table 10).



Scheme 13. (Top) CuAAC flow synthesis (Bottom) Flow schematic for synthesis using copper UC/UAM reactor.

Table 10. DOE parameters

Variable	Low	Centre point	High
Temperature (°C)	100	125	150
Residence Time (min.)	5	10	15

To ensure that the formation of the product was not simply due to the elevated reactor temperature the reagents were also passed through an aluminium reactor (R5) with identical dimensions to the copper reactor. No conversion of the starting material was observed for this, confirming that the product formation was due to the presence of the copper surface rather than the thermally initiated Huisgen 1,3-dipolar cycloaddition. When only the phenyl acetylene was pumped through the copper reactor the formation of a bright yellow solid was observed corresponding to copper phenyl acetylide and confirming again that the reactor acts as a source of Cu(I).

The reaction temperature was measured from the embedded thermocouple rather than relying on the Flowsyn temperature reading. A linear offset was observed for all of the temperature settings used for the DOE study (Figure 56). The embedded thermocouple allowed much greater control over the reaction temperature as expected, and the design of the reactor also gave rapid heating compared to a coil reactor.

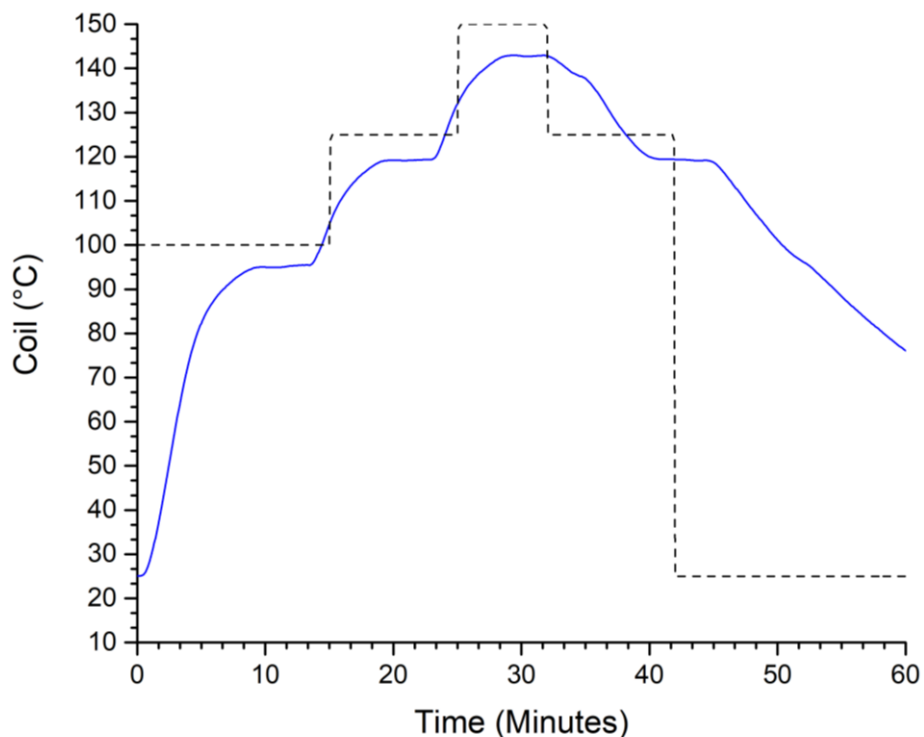


Figure 56. Measured reactor temperature (blue steady line) compared to the set reactor temperature (dashed black line).

A reasonable model was obtained, utilising the temperature, residence time and residence time squared terms, with values of 0.81, 0.53, 0.86 and 0.73 for the R^2 , Q^2 , validity and reproducibility respectively. The p value for the residence time squared term was greater than 0.05 at 0.072, however removal of this term led to a significant reduction in R^2 and Q^2 . The best conditions were estimated to be 13.3 minutes residence time and 150 °C set temperature; a subsequent confirmation run gave a peak area ratio of 53.9% compared to a predicted 55.3%. A decrease in response was noted for longer retention times (Figure 57) and this is due to decomposition of the organic azide formed through the S_N2 reaction between the alkyl halide and sodium azide. Although generated here in small amounts organic azides of carbon chain length < 4 are typically considered to be relatively unstable and this accounts for the non-linear effect of residence time on product yield identified through the model.

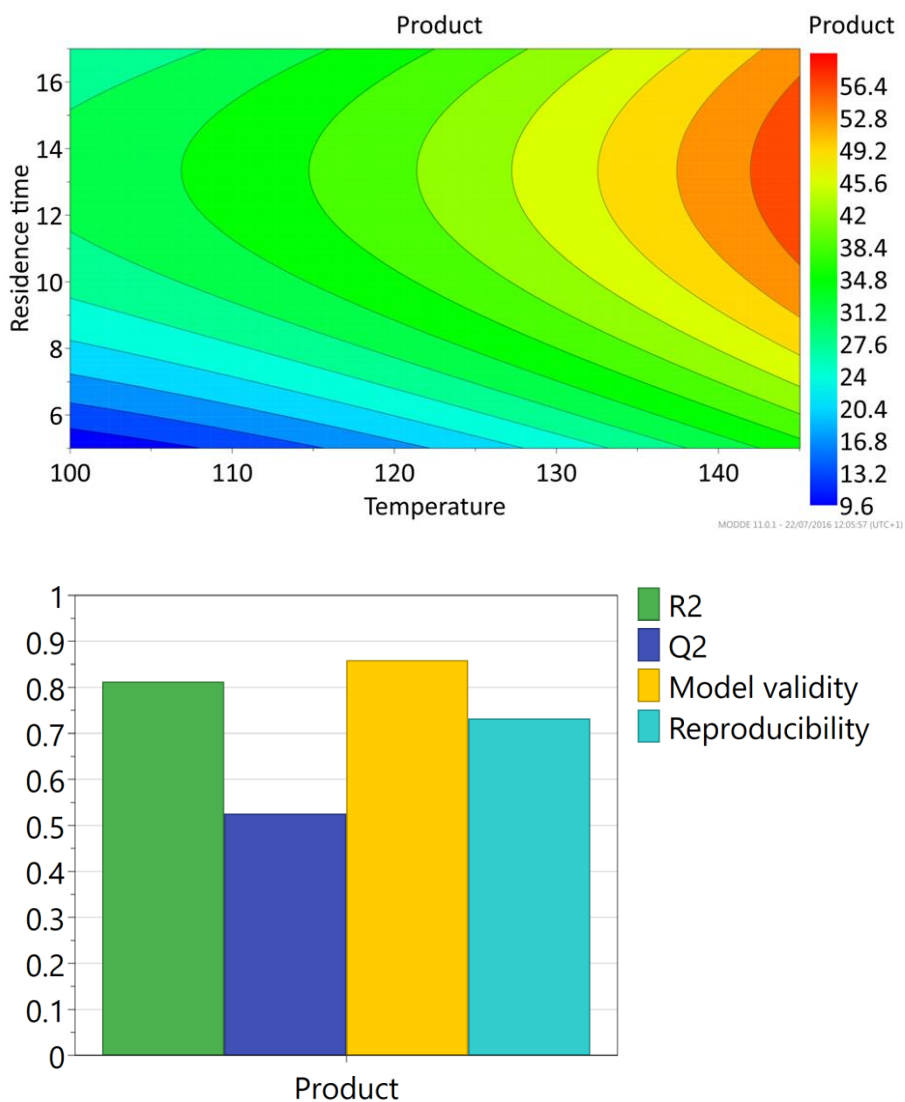


Figure 57. (Top) Response contour plot for CuAAC optimisation (Bottom) Model statistics calculated using MODDE.

Some variability in early results was noted, with early sampling for the first experiment in a set of runs often giving unusually high conversion of the alkyne starting material, subsequently analysis for the DOE was always performed on samples taken at the same time point, allowing steady state conditions to evolve, despite this the reproducibility of the repeated centre point experiments is higher than would be ideal.

As the reaction proceeds *via* a Cu(I) species it was hypothesised that increasing the amount of Cu(I) present on the reactor surface would lead to an improved yield. The reactor was therefore ‘activated’ with a 36% aqueous solution of H₂O₂ to oxidise the Cu(0) surface to Cu(I). To confirm this had indeed converted the copper surface the CuAAC reaction between phenyl acetylene and iodoethane was run again using the best conditions from the DOE and the reaction crude analysed by HPLC. A substantial increase in conversion was observed (Figure 58) with no phenyl acetylene visible in the chromatogram

and a large increase in the product peak. The surface oxidation of a copper reactor was commented on in the work by Ceylan *et al.*,¹⁵⁹ who observed that the heating profile of their reactor, where thermal control was achieved through inductive heating, would plateau at 180 °C, which they attributed to surface oxidation due to air in solvents. They did not associate oxidation with a change in the subsequent ability to catalyse CuAAC reactions. Fuchs *et al.*,¹⁶⁰ in a piece of impressive work, have shown that it is surface Cu(I) that is responsible for catalytic activity in Cu(0) systems, using HCl and H₂O₂ to repeatedly raise and lower conversion rates for a batch microwave assisted triazole synthesis, corresponding to surface oxidation and reduction of the copper metal respectively.

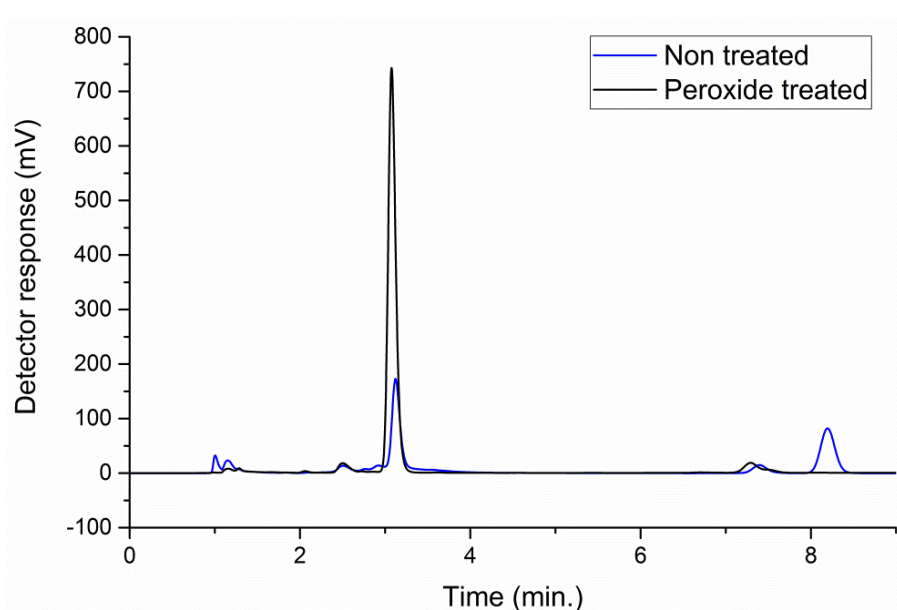
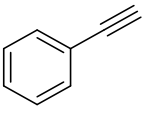
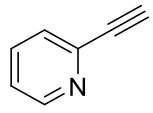
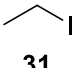
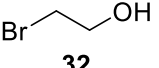
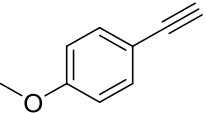
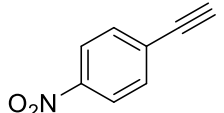
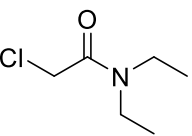
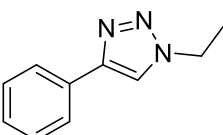
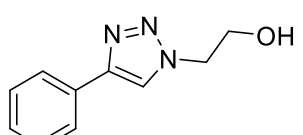
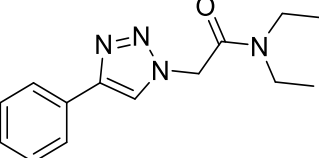
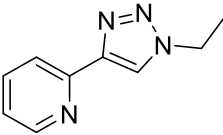
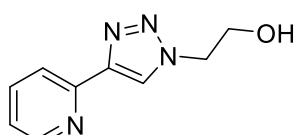
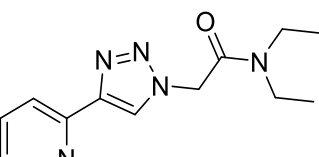
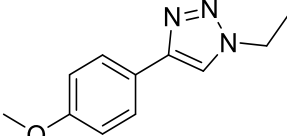
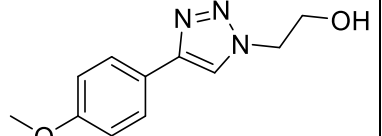
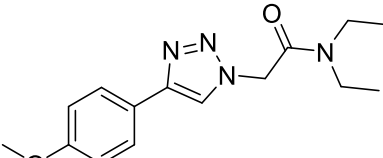
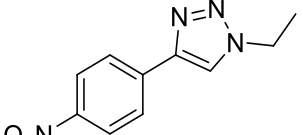
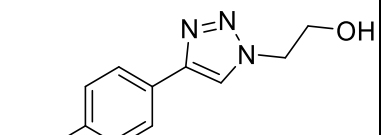
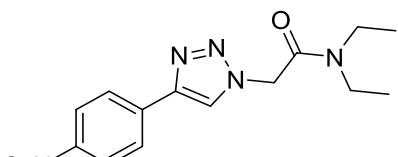


Figure 58. Overlaid chromatograms showing the increase in conversion after peroxide treatment, product at 3.1 minutes, phenylacetylene at 8.2 minutes.

The optimum conditions from the DOE study, combined with reactor pre-treatment with H₂O₂, were then used to synthesise a number of 1,4-disubstituted-1,2,3-triazoles (Table 11). Conversions were determined by comparison to a standard injection of alkyne starting material, analysed by HPLC.

Table 11. Synthesised 1,4-disubstituted-1,2,3-triazoles. Alkyne conversion percentages in parentheses.

Acetylenes		Halides	
 27	 28	 31	 32
 29	 30	 33	
Synthesised 1,4-disubstituted-1,2,3-triazoles			
 34 (> 99 %)	 35 (38 %)	 36 (93 %)	
 37 (> 99 %)	 38 (> 99 %)	 39 (> 99 %)	
 40 (76 %)	 41 (44 %)	 42 (> 99 %)	
 43 (> 99 %)	 44 (> 99 %)	 45 (> 99 %)	

Of the alkyne substrates tested the 4-ethynyl anisole demonstrated the lowest overall reactivity, while for the alkyl halides the 2-bromoethanol was markedly lower than the others, due to bromine being a poorer leaving group than iodine. The 2-chloro-N,N-diethylacetamide exhibits greater reactivity due to the presence of the electron withdrawing amide group nearby activating the chlorine bearing carbon towards nucleophilic attack by the N_3^- species.

As it was known that the reactor had a lower activity when not activated by peroxide a short study to determine the lifetime of the reactor enhancement was undertaken. Samples of the reaction between phenyl acetylene and iodoethane were taken periodically as product exited the peroxide treated reactor, starting at 1 reactor volume and continuing until 6 reactor volumes had passed through. These samples were then analysed by HPLC and the peak area ratio between the product and phenyl acetylene calculated. The result of this was a clear downward trend after approximately 2 reactor volumes (Figure 59) towards a baseline activity consistent with that observed in the DOE study, which was performed with no peroxide treatment.

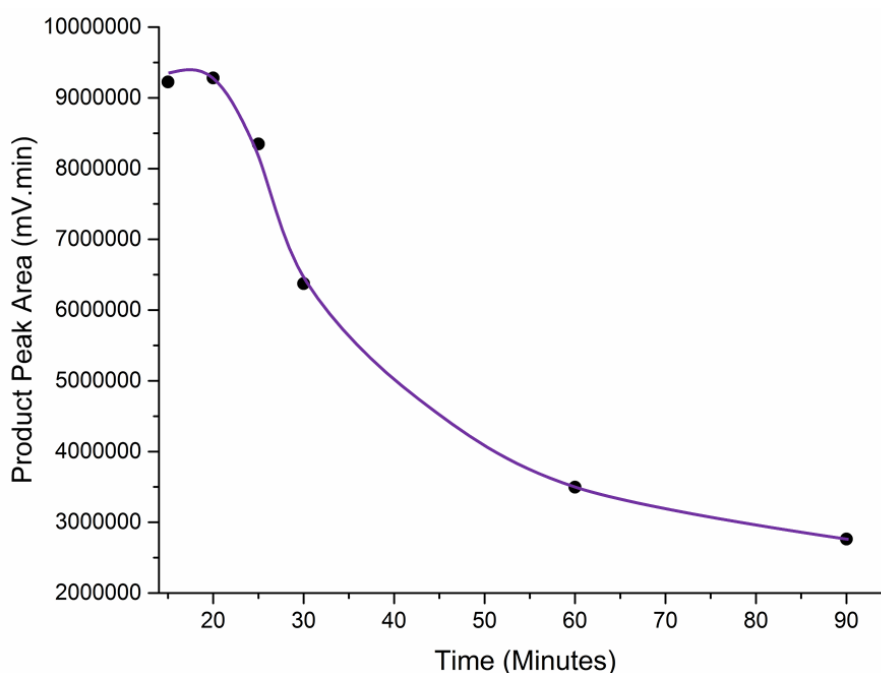


Figure 59. Downward trend observed in catalytic activity for UAM copper reactor

Obviously, the need to continually ‘refresh’ surface Cu(I) poses an issue for continuous processes, particularly if H_2O_2 were to be used following organic solvents due to the possible generation of explosive compounds. An investigation into organic oxidants, such as pyridine N-oxide or benzoyl peroxide, which could be added into the reaction to provide constant oxidation of the copper, would be worthwhile. Alternatively, a continuous segmented flow approach where the oxidant and solvent were separated could be explored. The early variability in conversions was a result of overnight oxidation of

the copper surface by air alone; a liquid/gas biphasic reaction mixture could therefore give continuous oxidation.

Further to this, work was performed to determine the minimum exposure time required for formation of the Cu(I). H₂O₂ was infused and left to stand for increasing lengths of time followed by a reaction between phenyl acetylene and iodoethane after each period to deplete the Cu(I). The triazole product peak area percentage was calculated for each exposure time (Table 12).

Table 12. Change in product peak area with varying peroxide exposure times

Peroxide exposure time (minutes)	Product peak area %
0.5	90.7
2.5	99.7
5	99.0
10	97.5
15	96.1
30	99.5

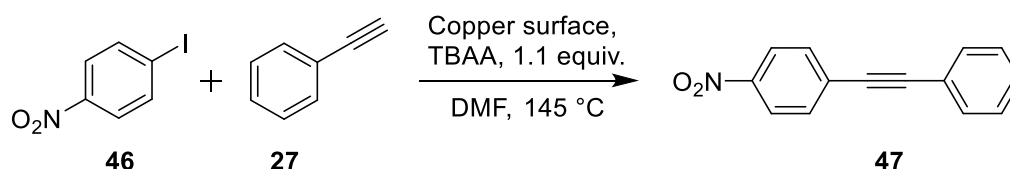
Only 2.5 minutes was required for a very high level of conversion. This is useful from a process development aspect as the downtime between reactions can be minimised with such short exposure times.

The amount of leached copper in the DOE samples was quantified by ICP-OES and found to be 208 mg/L on average with a standard deviation of 74 mg/L. No clear trend could be discerned from the DOE samples in relation to the copper content. The average concentration of leached copper equates to approximately 2 mol. % based on the phenylacetylene concentration of 0.125 M and is in line with that seen in literature for batch reactions.¹⁶¹

At the time of writing approximately 250 mL of reaction solution has been run through the reactor with no loss in catalytic ability, equating to around 40 mg of copper removed from the surface, therefore indicating a substantial reactor lifetime. As the solvent acts as the ligand in this flow reaction it could be found that a switch to a non-ligating solvent such as water or alcohol, and the use of a separate ligand such as di-tert-butyl-bipyridyl, allows the amount of leached copper to be reduced and the reactor lifetime to be extended even further. As full conversion was observed for several compounds the copper concentration is not a limiting factor in the reaction, therefore there is scope to reduce the effective copper concentration.

3.2.5 Stephens-Castro Coupling

The Stephens-Castro coupling of a terminal alkyne and an aryl halide (Scheme 14) was also attempted to demonstrate further the variety of reactions that could be performed using the copper functionalised reactor. As with the modified Ullmann couplings and the CuAAC reactions the presence of Cu(I) species on the surface of the reactor was able to catalyse the reaction. Full conversion of the iodo-nitrobenzene starting material was observed, but the yield of the desired product was low at only 33 %.



Scheme 14. Stephens-Castro coupling of 4-nitro-iodobenzene and phenylacetylene.

3.2.6 Design of reactors for photo-catalysed reactions

The use of metal reactors allows access to a wide range of chemistry through improved thermal resistance and chemical compatibility. In addition, through newer manufacturing methods, specifically designed catalytic sections can be added by the chemist into a bespoke reactor. A newer field of chemistry, which these reactors do not access, is that of photocatalysis; for example, iridium catalysed photoredox reactions or the initiation of free radical halogenations through visible light. While it is possible to embed light sources into the bodies of metal reactors, the illuminated portion can never be the whole flow channel limiting the potential reactor efficiency.

As previously noted however, with resins of high optical clarity SL can produce transparent reactors that allow the transmission of visible light wavelengths. A 2 mm thick section of SL resin will attenuate light at the lower visible wavelengths to quite a large extent, but if the levels of incident light remain high enough the reactions will proceed. Tests with 2 cm² pieces, 2 mm thick, determined that the cut off wavelength for cured SL resin (specifically Accura 60) was 350 nm with an attenuation of approximately 85 - 90% over the range 400 - 550 nm (Figure 60). This resin was not polished or treated in any way and so represents a worst-case scenario for light transmission, the use of fine grit polishing paper or ZnO suspended in propan-2-ol would be expected to reduce scatter of the incident light and improve the intensity of the light reaching the channels.

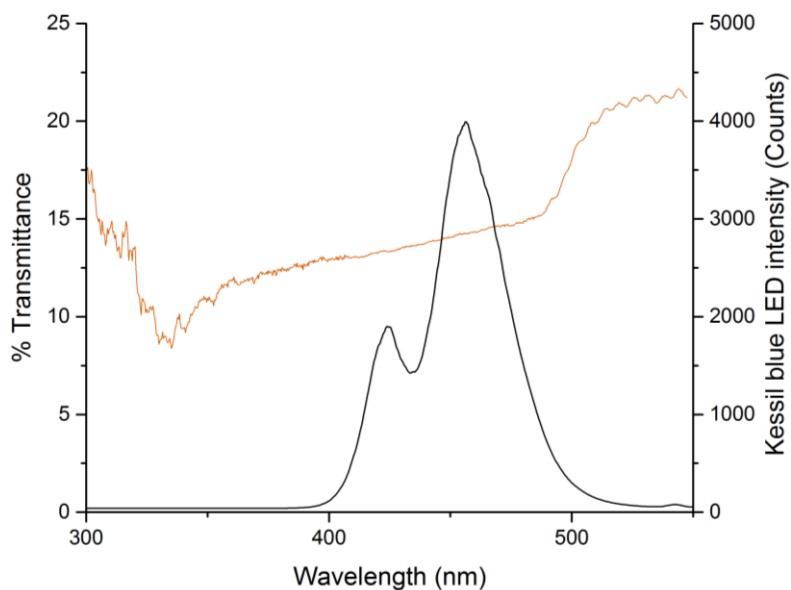


Figure 60. Visible light transmission spectrum for 2 mm thick piece of cured Accura 60 resin (red line) overlaid with the emission spectrum of a Kessil A160WE LED lamp.¹⁶²

As a moderate amount of light was still observed to be transmitted two SL reactors were tested which would potentially allow photochemical reactions to be performed. The first design was a simple flat coil of 0.5 mL volume and 2 mm channel diameter (R5, Figure 61), to be irradiated on the reverse face to that with the fluidic fittings. This reactor was kindly printed from a design supplied from Loughborough by the Hilton group at UCL and subjected to an extended post print UV cure to minimise the un-crosslinked resin monomer that remained. The second reactor (R6, Figure 62), previously designed and printed by Andrew Capel (Chemistry Department, Loughborough University) as a simple residence time reactor, that could also monitor reactions through a built in optics port,¹⁵⁴ had a similar planar layout, but with a second tier of channels stacked directly beneath the first set. This reactor was given only a standard post print UV cure of 1-2 hours.

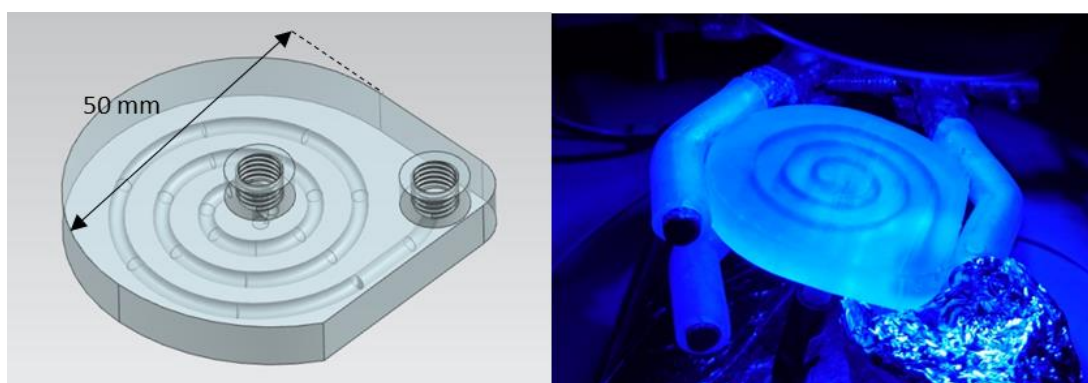
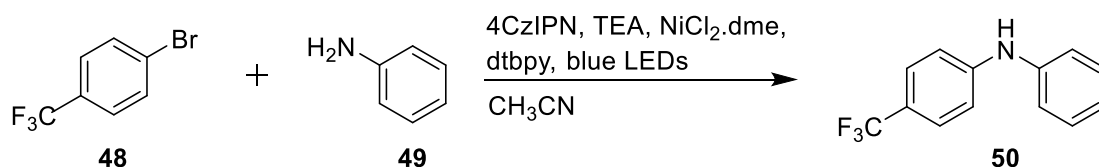


Figure 61. (Left) CAD sketch for the simple coil photo reactor, R5, non-irradiated surface visible (Right) Reactor under irradiation by blue LEDs.

The reactors were tested by performing a dual catalysed cross coupling of aniline with an aryl halide (Scheme 15) in a 'one pot' manner; flowing the reaction mix *via* syringe pump through the reactor. The solutions were analysed with ^{19}F NMR to determine the conversion of the starting material.



Scheme 15. Dual catalysis C-N coupling reaction

A residence time of 30 minutes in the coil reactor R5 gave a conversion of 43 %, clearly showing that the light is not completely attenuated by the cured polymer and can initiate the reaction. The same residence time of 30 minutes in the double layer reactor R6 gave a conversion of only 20 % initially, when the residence time was increased to 60 minutes an increase in conversion to 74 % was observed. The double stack reactor demonstrates that very little light passes through the extra layers of resin, in addition to the 1 mm of reagent, so the reaction effectively proceeds in the directly irradiated tier only.

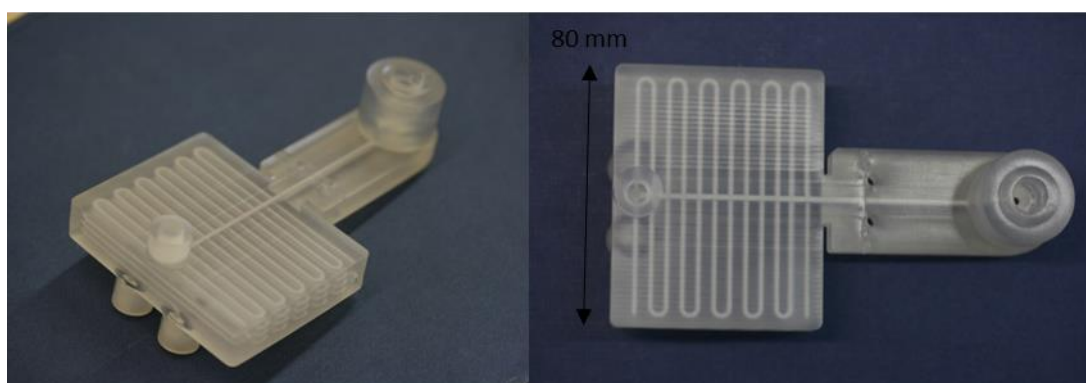


Figure 62. Double stack SL reactor used for photoredox catalysed C-N coupling.

The reactor could be easily operated with lights on both sides, doubling the effective irradiation, however it was noticed that the reactor became noticeably warm to the touch, therefore prolonged operation would require active cooling due to the large thermal bulk of the cured resin. Although external heatsinks could be engineered as part of the reactor design the thermal conductivity of the resin is poor and the use of fans would be recommended. As the reactor is fully leak tight it would be no impediment to safe operation to immerse the entire body into a cooling bath. Water would continue to transmit the light from the LED lamp and would act as an excellent heat sink due to its high specific heat capacity. In a similar way the part could be engineered with a cooling jacket by building the flow channel inside a larger cavity equipped with fluidic fittings. A test part was designed and worked entirely as expected, with a separate cooling flow running around a contained channel. To prevent the

'ceiling' of the part from collapsing as it was printed the fluidic channel had buttresses added above and below, with cut outs for coolant flow (Figure 63).

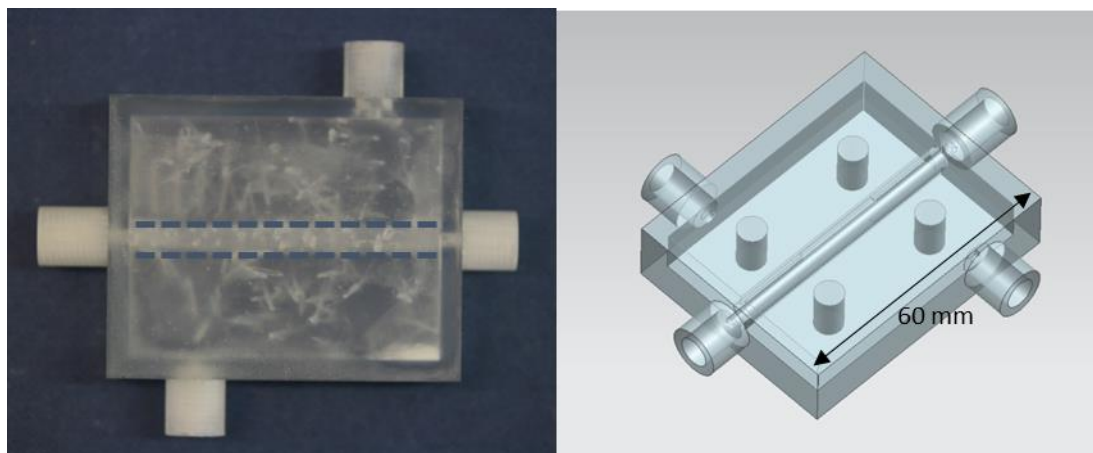


Figure 63. (Left) Part showing fluidic channel surrounded by a 'cooling' channel. Dashed lines added to illustrate channel direction (Right) CAD design for cooling jacket part.

A double layered reactor of 8.9 mL designed volume (6 mL measured volume after curing, R#) was designed (Figure 64) with offset layers to maximise the transmitted light, whether illuminated from one or both sides, and this was supplied to Nicolas Cheval (AstraZeneca) for testing. The reactor was able to perform the C-N coupling for aniline with 2-methoxy-iodobenzene and 4-methyl-iodobenzene, with moderate yields after 40 minutes residence time, of 40 % and 52 % respectively. The addition of a second light gave an increase in the reaction yield of 7 % for the 2-methoxy-iodobenzene coupling partner, which while moderate shows that reactor design was able to offer a route to better reaction efficiency with no change in the chemistry or reaction conditions.

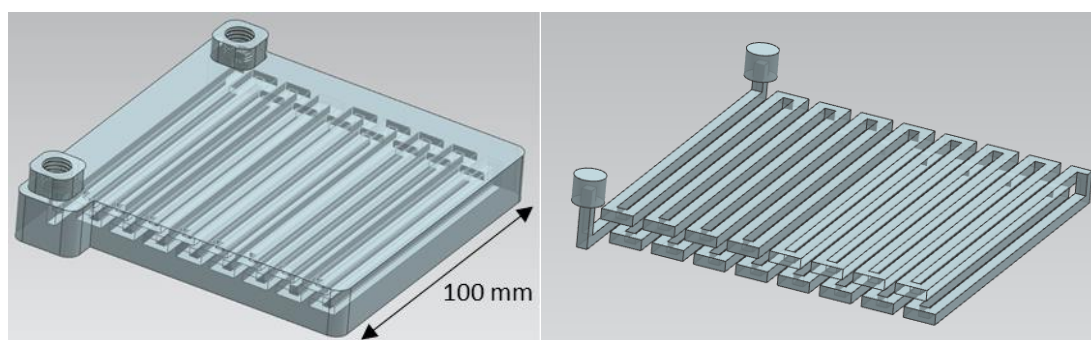


Figure 64. (Left) CAD sketch for the double layered photochip with 2 mm width channels (Right) Flow channel only to illustrate the offset stacking approach.

The reactor was used for more than five hours under irradiation, however eventually the reactor failed due to the development of a crack between the surface and a channel. This is unlikely to be due to the solvent, squares of the cured SL resin immersed in acetonitrile for 1 week show no degradation. However, TEA is known to affect the resin and a ~0.4 M concentration could be enough to have a

weakening effect when combined with the increased temperature. The poor thermal conductivity of the SL resin is the most probable cause of failure as the irradiated surface gets noticeably hotter than the underside. With this in mind, active cooling, or evenly distributed heating, could allow for even longer operation of the SL photo reactors.

Examination of the reactors used for the C-N coupling reaction showed that the without the extended curing procedure the reactors seemed to be slightly porous to the reaction mixture, with a faint ‘halo’ appearing around the channels (Figure 65).

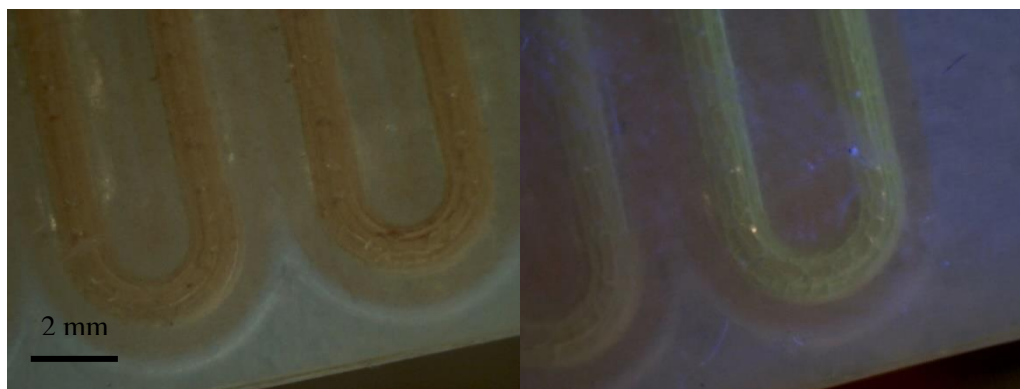


Figure 65. (Top) End on view of channels under normal and 400 nm lighting, showing reagent ingress to polymer (Bottom) Top down view of channels under normal and 400 nm lighting clearly showing the halo and green colouration.

This could have been due to the original printing method as the laser spot is not completely uniform and leads to a lower degree of curing slight distance from the desired location. However, it was observed that under 400 nm illumination some of the halo glowed green due to photosensitiser that had leached into the walls (Figure 66), therefore suggesting the reaction as the source of the halo. Neither the halo effect, nor the leaching of photosensitiser, was apparent for the spiral reactor subjected to the extended curing.

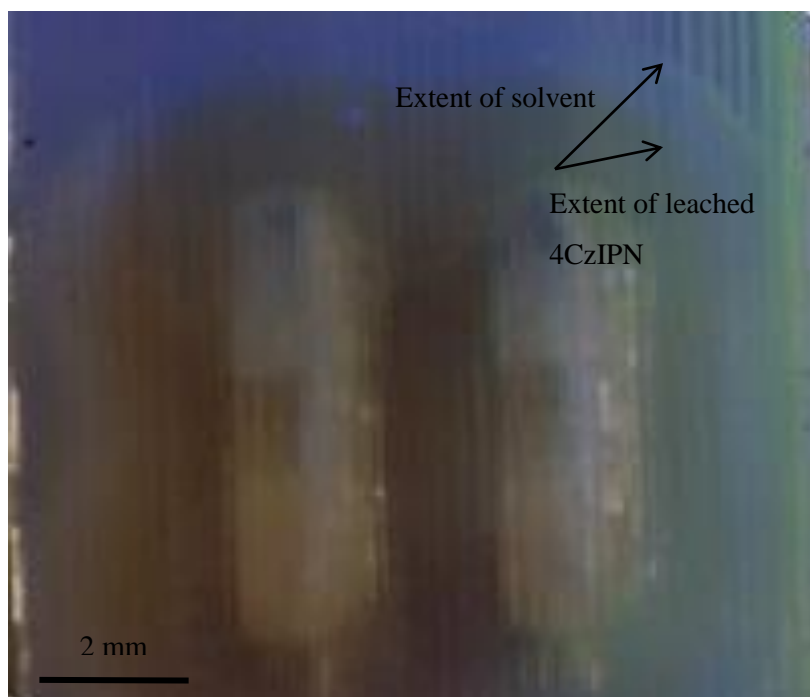


Figure 66. Reactor under 400 nm illumination showing extent of solvent penetration and photosensitiser leaching

The reagent leaching effect could potentially be used to modify the reactor walls to give some degree of functionality. If the photoinitiator could be infused rapidly into an SL reactor at sufficient concentration before full curing of the part had taken place, then the ability to conduct photoredox reactions may be present without the need to add the photo catalyst into the reagent mixture later on. To prevent the leaching and minimise solvent impact on the SL reactors it is clear that an extended post cure is advisable to crosslink as much of the resin monomer as possible. A similar result was reported by Hague *et al.*⁶⁰ who showed that moderately UV cured samples underwent further thermal curing when analysed by direct scanning calorimetry (DSC).

3.3 Chapter summary

The use of metal printing techniques has been shown to be crucial in the development of flow reactors through AM. No other technique is able to offer the robustness required for high temperature operation, as well as the ability to tolerate a wide range of solvents and reagents. Additionally, UC is a versatile technique, allowing the easy integration of sensors and the same freedom of design as other AM processes, and is therefore deserving of far greater attention in future research.

The inclusion of copper metal into the reactor did allow metal catalysed reactions to be performed, and further to this it was identified that the oxidation state of the surface could be easily modified to increase productivity. This effect has been reported before for batch reactions only, this work represents the first instance of a flow reactor being chemically treated to boost yields.

The leaching of copper from the surface into the reaction solvent means that the reactor potentially has a shortened life time, however this is no different to the copper tubing marketed by commercial flow chemistry companies. As previously discussed, for the reactions carried out using the copper reactor, the amount of leached copper could be reduced by using a non-ligating solvent and using only the base and ligand required for the reaction to proceed.

3.4 Further Work

Further work on the development of a continuous process using the surface oxidation method would be worthwhile; this could be achieved through the use of a mild organic oxidant such as benzoyl peroxide, or perhaps through a gas liquid biphasic mixture using additional air flow.

It is clear that further investigation into the use of palladium and other transition metal catalysts should be undertaken, the actual amount of these expensive metals required for the flow path is relatively small, as seen with the copper reactor utilised for this work which was predominantly aluminium. No other technique allows the hybrid approach of differing metals, built with extremely high precision, to be used.

Where high temperature operation is not needed SL offers the ability to produce reactors with multiple inlets and integrated mixing. Future work to improve the heat transfer away from the reactor, and also to improve the light transmission through material choice or part post processing, would be required for robust and high efficiency reactors for photochemistry.

4. Online Analysis and Automated Optimisation Using Flow NMR

4.1 Introduction

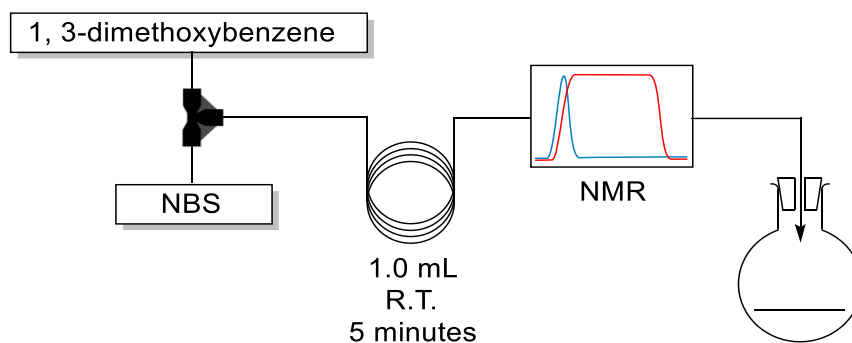
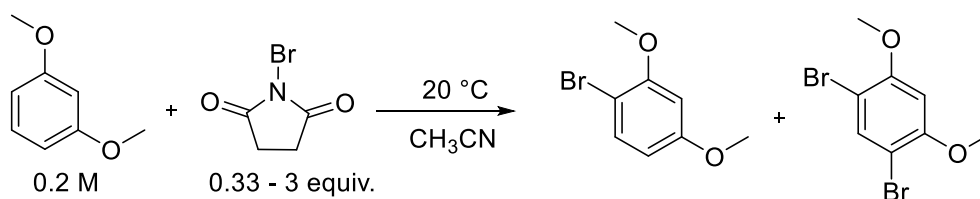
While UV/Vis spectroscopy had been previously demonstrated as a suitable method for online analysis it lacks selectivity unless significant effort is expended on multivariate calibration building. In addition to this the linear dynamic range of UV/Vis spectroscopy is relatively small compared to techniques such as HPLC, MS or NMR. The high degree of structural information inherent to NMR makes it an attractive choice for online monitoring and advancements in the field stability of permanent magnets have allowed several 'benchtop' NMR spectrometers to become affordable.¹⁶³⁻¹⁶⁶

While the resolution of these benchtop spectrometers is not at the level of high field instruments, they do allow the monitoring of peaks relating unequivocally to functional groups, either involved in reactions or close to reaction sites, when they are well isolated. As NMR is also a quantitative technique, lengthy multivariate calibrations become unnecessary. The focus for successful online monitoring should be on peaks with ideally zero or only minimal coupling. Extensive splitting reduces the signal to noise ratio for a peak significantly and requires that long acquisition times must be implemented; a disadvantage when rapid data collection can reveal much about the kinetics and progress of a reaction.

4.2 Results and Discussion

4.2.1 Flow NMR monitoring for the bromination of 1, 3-dimethoxybenzene with N-bromosuccinimide

As a test of a benchtop NMR system for flow reaction monitoring the bromination of 1,3-dimethoxybenzene using N-bromosuccinimide (NBS) in acetonitrile was again carried out (Scheme 16), using a 5-minute residence time. The stoichiometry of NBS to 1, 3-DMB was varied from 1:3, 1:1 and 3:1 by altering the ratio of the reagent streams while the overall flow rate was kept constant. The reactor coil was connected to a 0.5 mL glass flow cell, carefully aligned within the shimmed region of the NMR, using 1/4" - 28 connectors. This effectively added an additional 0.5 mL to the reactor volume, but as the flow rate was kept constant this had no effect on the reaction.



Scheme 16. (Top) Reaction scheme for bromination of 1,3-dimethoxybenzene (Bottom) Schematic for flow reaction with online NMR monitoring.

The reaction proceeded easily giving a mixture of products at the lower NBS equivalents and exclusively the di-brominated product at high equivalents of NBS. The formation of the different products is clear in the 1H spectra due to the well separated methoxy singlets (Figure 67). The di-brominated product has a single peak at 3.87 ppm of 6 protons, the mono-brominated product has peaks at 3.82 and 3.75 of 3 protons each. The starting material is visible as a single peak at 3.74 ppm, partially resolved from the mono-substituted product. A ^{13}C satellite peak from the CH_3CN solvent is visible at 3.51.

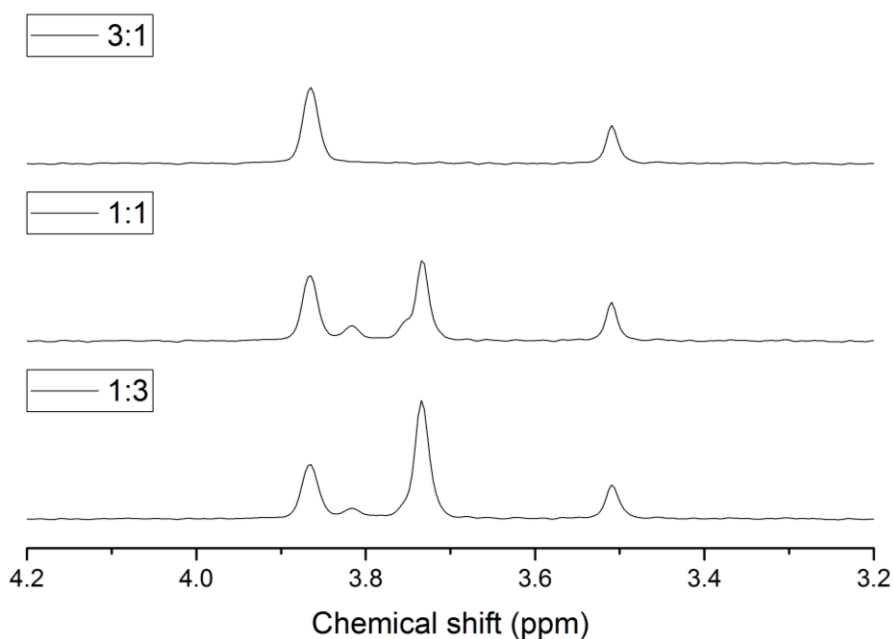


Figure 67. Online ^1H NMR spectra acquired for bromination of 1,3-dimethoxybenzene.

For the 3 to 1 NBS experiment, residual NBS was visible as a peak at 2.77 ppm. This peak was only seen when a large excess was used, confirming that all NBS had reacted in the previous experiments. The ^{13}C satellite peak was used as an internal standard to reference all peak chemical shifts as well as to normalise integrals, as the magnitude of this signal should be constant for a reaction system, unless the solvent is also being utilised as a reagent.

This referencing approach has been used in quantitative NMR,¹⁶⁷ but never before in flow, and should be highly useful for inline, quantitative NMR with no need for additional standards to be added. The solvent must be chosen carefully, but through a chemometrics approach such as that pioneered by Carlson *et al.*¹²⁴ a suitable solvent should be available with peaks located away from functional groups of interest. The online monitoring rapidly revealed that under the flow conditions chosen the regioselective control was poor, with significant amounts of di substituted product being formed for all levels of NBS.

4.2.2 Automated optimisation through flow NMR and design of experiments and application to photochemistry

Automated optimisation methods have clear potential but for reactions that require significant heating to proceed there are disadvantages related to large temperature swings. Changes can require a significant amount of time before a new stable temperature is achieved, potentially leading to wasted reagents. The use of photochemical reactions typically avoids this limitation and allows for more rapid optimisations, as the wait for stable temperatures to be achieved is removed.

Two reactions with importance for pharmaceutical applications were chosen for optimisation, working in collaboration with Nicolas Cheval (Astra Zeneca). The first was the trifluoromethylation of arenes and heteroarenes through ruthenium redox catalysis, developed by the Stephenson group,¹⁶⁸ using trifluoroacetic anhydride (TFAA) as the CF_3 source. The second reaction was the C-N coupling of amines to aryl halides through photochemistry *via* a two-step catalytic cycle involving a photo catalyst and Ni(II) species.⁴⁴

A DOE approach was used for the optimisations, performing several structured experiments and relying on a predictive model to locate optimal conditions. This is contrasted with simplex, or hill climbing, optimisation methods, which may cover the same reaction space as a DOE study but instead actively travel towards a maximum. The implementation of a list of predetermined experiments is also simpler from an automation point of view. Further to this the strength of the model desired can be tailored through several prebuilt DOE matrices with more or fewer factor levels or data points, allowing a more efficient use of chemicals and researcher resources.

For a simple two factor optimisation for residence time and stoichiometry, using two pumps, the first approach taken to automate an optimisation used a DOE list containing the residence time and the equivalents of trifluoromethylation reagent. This information allowed the calculation of the experimental flow rates, using the known volume of the reactor coil. From this, a command list was generated by using the 'num2str' command on the calculated flow rate followed by the 'strcat' command to build the text string of the correct structure for the pumps being used. These commands were used within a 'for' loop which repeated for as many experiments were present in the DOE (Figure 68).

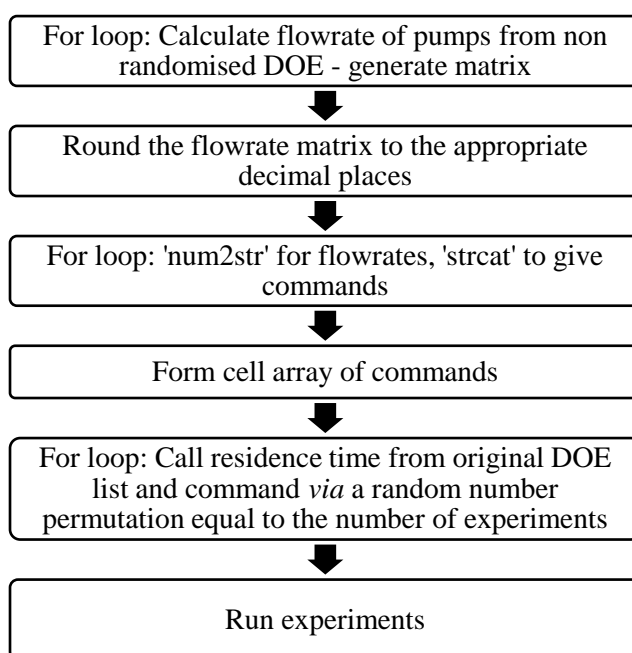
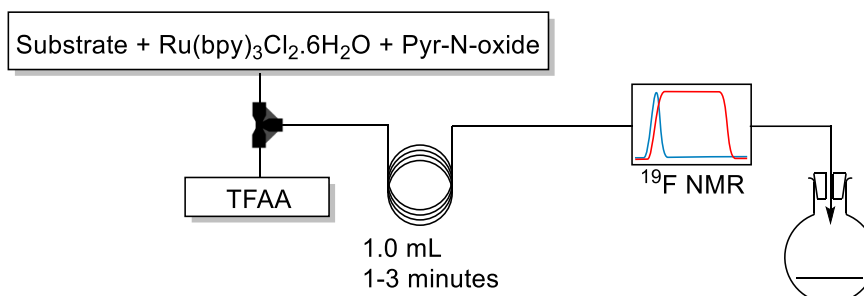
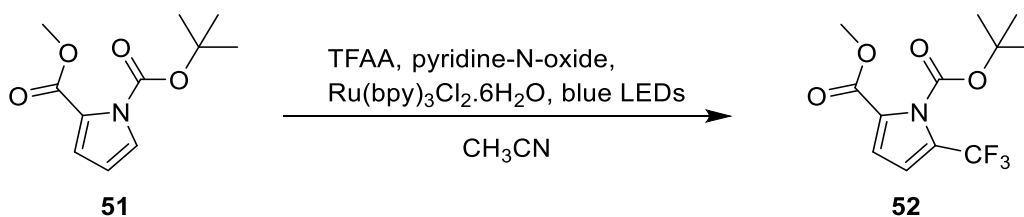


Figure 68. Flowchart showing the methodology for automated optimisation with two pumps.

4.2.3 Trifluoromethylation of heterocycles

The reaction was performed (Scheme 17) and optimisation carried out taking residence time and the equivalents of TFAA as changeable factors. The molar equivalents of all other reagents to the substrate were kept constant. MATLAB was used to produce the DOE list of factor combinations to be run using the inbuilt command 'fullfact(A,B,C,...)' with the number of levels for each factor to be included entered in the parentheses. This basic DOE list does not include any additional centre points.



Scheme 17. (Top) Reaction scheme for trifluoromethylation of N-Boc-pyrroles (Bottom) Flow reactor schematic.

The reagent feeds were from two syringe pumps controlled *via* an RS232 interface through MATLAB. The ratio of TFAA to the pyrrole was varied by altering the flow rates of the individual pumps. This was done automatically with a MATLAB function (Figure 69) that took the desired residence time and molar equivalents of TFAA, specified by the list of experiments, to calculate the correct flow rates for each pump (Equation 4, Equation 5).

$$\text{Substrate flow} = \frac{\text{TFAA equiv.}}{\text{TFAA equiv.} + 1} \times \frac{\text{Reactor vol.}}{\text{residence time}} \quad (4)$$

$$\text{TFAA flow} = \frac{\text{reactor volume}}{\text{residence time}} - \text{substrate flow} \quad (5)$$

This approach did lead to variable substrate concentration depending on whether low or high equivalents of TFAA were to be used. This could have an effect on the kinetics of the reaction, although as all the concentrations were of the same order of magnitude this effect was assumed to be negligible for this experiment. The number of significant figures for the flow rates, calculated by the algorithm, had to be limited as the RS232 communication would not function correctly if too many values were transmitted. This decimal point limit will vary depending on the pumps being utilised, however the rounding of the calculated flow rates will impact the actual residence time and equivalents used, adjustment of the factor values in the DOE to the true values is recommended to ensure as accurate a model as possible.

To allow the calculation of yields from the spectra α,α,α -trifluorotoluene was included as an internal standard in both reagent feeds. This peak was used to reference the chemical shifts and was used to normalise the other peaks by integrating as equal to one in all spectra. All MATLAB scripts employed

are located in the Appendix. As the residence time of this reaction was short, spectra were continuously acquired manually.

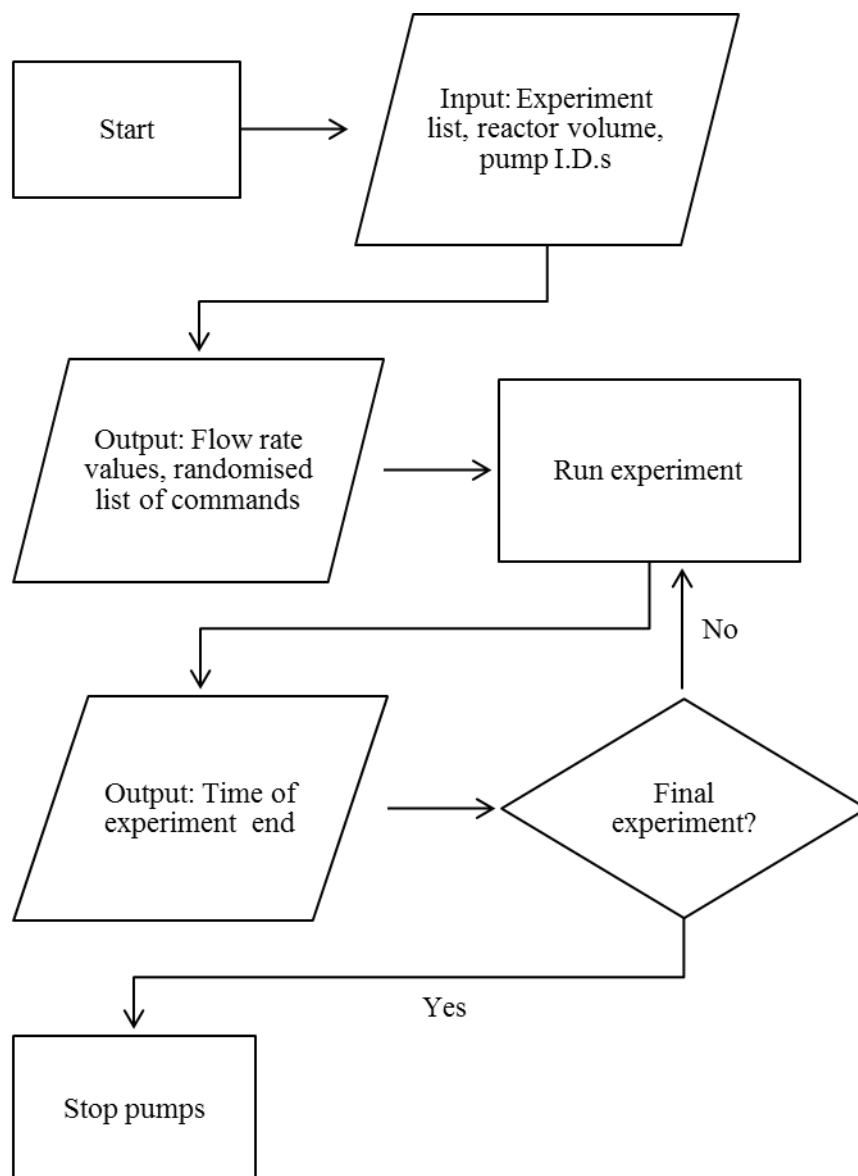


Figure 69. Flowchart for automated optimisation algorithm using two pumps.

At the end of each experiment the optimisation algorithm logged the time in a cell structure, this was then used to find the spectra with the closest acquisition time. As the ratio of TFAA to substrate was variable this was accounted for as a dilution factor and used along with the internal standard concentration to calculate a percentage yield. This was then used to generate a MLR model in MODDE. The model with the highest Q^2 value of 0.88 had an R^2 of 0.98 and contained the terms for TFAA equivalents and residence time as well as the interaction term. The residual probability plot suggested that experiment 8 was an outlier due to its deviation from the normal probability line and was removed from the data set. This greatly improved the model statistics; however, the surface contour plot was broadly the same for a model built with or without this point. (Figure 70).

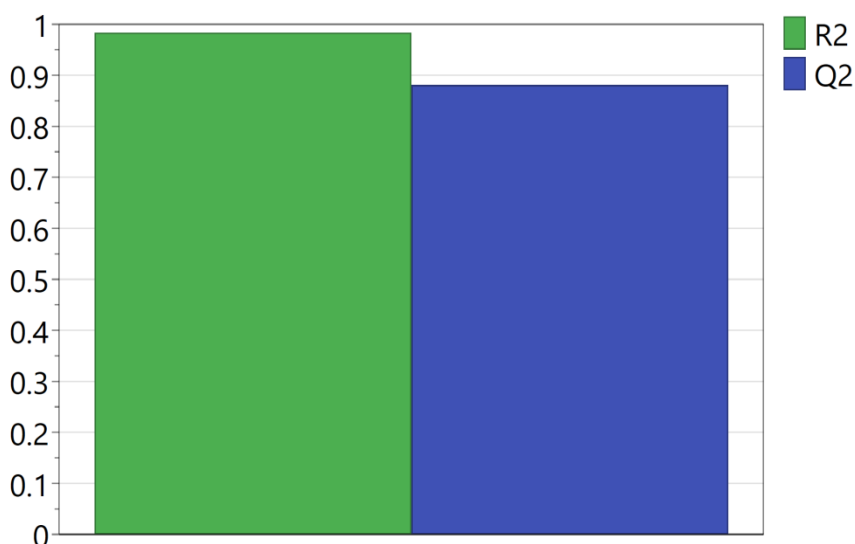
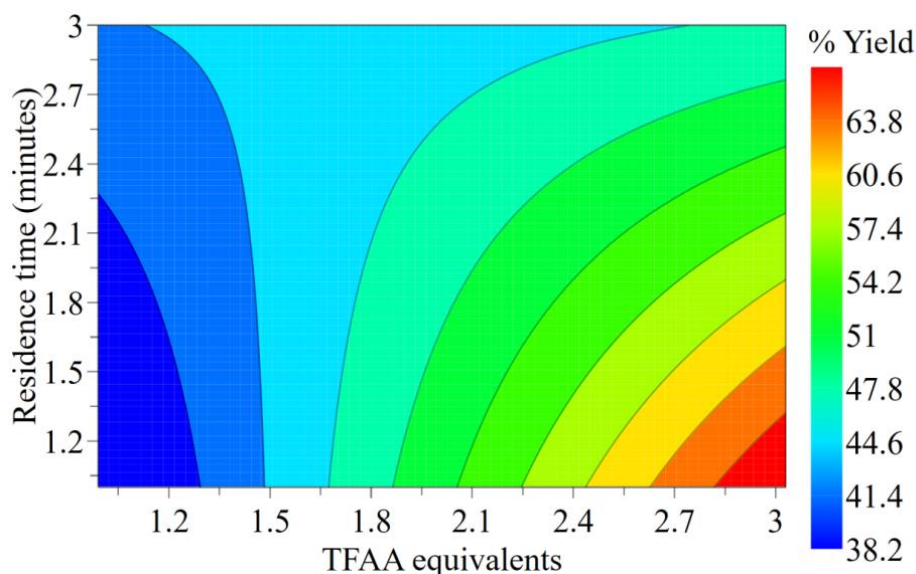


Figure 70. (Top) Response surface contour plot for trifluoromethylation of N-boc-pyrrole (Bottom) Model statistics calculated using MODDE.

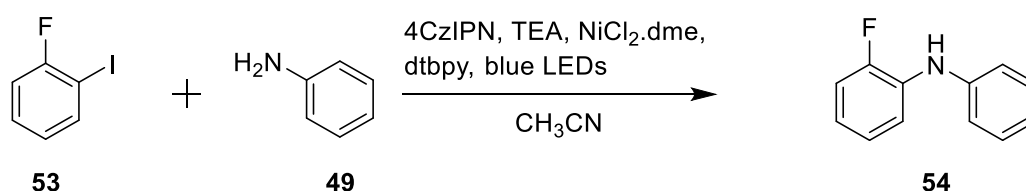
The residence time term and the interaction term for the residence time and the TFAA equivalents were both negative. This is shown in the response surface plot where the highest product yields are achieved in the lower right-hand corner of the experimental space.

4.2.4 C-N coupling of aniline and 2-fluoro-iodobenzene

The automated DOE algorithm was next applied to the photo catalysed C-N coupling. No centre points had been included in the automated optimisation used in section 4.2.3, and to have more robustness in future optimisations the ability to add any number of centre points was added to the ‘fullfact’ command through a custom MATLAB function (Appendix). The ‘fullfact’ function generates a coded matrix of 1, 2 or 3 for the factor’s lower value, centre point and higher value respectively.

For the centre point function to work the number of extra centre point experiments is chosen by the user by specifying an integer; in the case of the 3 level DOE the new code simply adds additional '2' values to the end of the coded experiment matrix. A vector containing the real lower and upper values for the factors was then used to interpolate for all the integer coded experiments, generating a matrix of the true experimental parameters. 3 levels were used for all designs in this work, but the code can be easily modified to automatically add the correct coded integer to the end of the experiment matrix. The flow rates are then calculated, and randomisation applied.

The scope of the reaction conditions was investigated by performing the reaction between aniline and 2-fluoroiodobenzene (Scheme 18) inside a 0.5 mm NMR tube containing a micro stir bar. This gave 21 % peak area percent for the C-N product **54** after 15 minutes reaction, further irradiation did not lead to an increase in yield.



Scheme 18. C-N coupling of aniline and 2-fluoro-iodobenzene.

An initial offline optimisation was then performed to try and determine the effect of the 4CzIPN photo initiator loading and the residence time on the reaction yield. The loading of the 4CzIPN was varied from 1.5 to 2.5 mol. %, while the residence time was varied from 15 to 60 minutes. A randomised full factorial DOE was used to ensure all factor combinations were analysed. 2-fluoro-iodobenzene had been included as part of a substrate screen at Astra Zeneca and it was thought that the change in the fluorine environment would give rise to a chemical shift in the ^{19}F NMR spectrum, and therefore offer a means to monitor the reaction without the need for reaction workup.

The flow reactor setup was the same as that used in section 4.2.3, including the addition of α,α,α -trifluorotoluene as an internal standard. The acquisition time for the NMR spectrum was considerably longer than for the trifluoromethylation study in section 4.2.1 due to the coupling of the fluorine with aromatic protons and subsequent loss of sensitivity. As a result of this coupling, the analysis of this reaction was performed offline by collecting the reactor output into an NMR tube for determination of the product integral.

Analysis of the experiments was performed in MODDE and showed that a MLR model for product peak area %, with coefficients for residence time, 4CzIPN loading and the 4CzIPN squared term gave the best results, with an $R^2 = 0.90$, $Q^2 = 0.70$, validity = 0.83 and reproducibility = 0.92. The linear term for 4CzIPN had a p value of 0.28 and was only included so that the 4CzIPN quadratic term also could be. One of the three centre points was removed from the model due to being greater than 4 residuals from the normal probability line. This was the final experiment to be performed and analysis showed

the excessive formation of an impurity had occurred due to loss of the iodine from the 2-fluoro-iodobenzene.

While the range of peak areas varied only from 28 - 41 % the model did identify a non-linear effect for the 4CzIPN loading, indicating that at higher loadings the peak area of the product would be decreased, and formation of fluorobenzene as an impurity would be promoted. A response surface contour plot was generated and showed an optimal region for the conditions investigated, at longer residence times and approximately 2 mol. % 4CzIPN. (Figure 71).

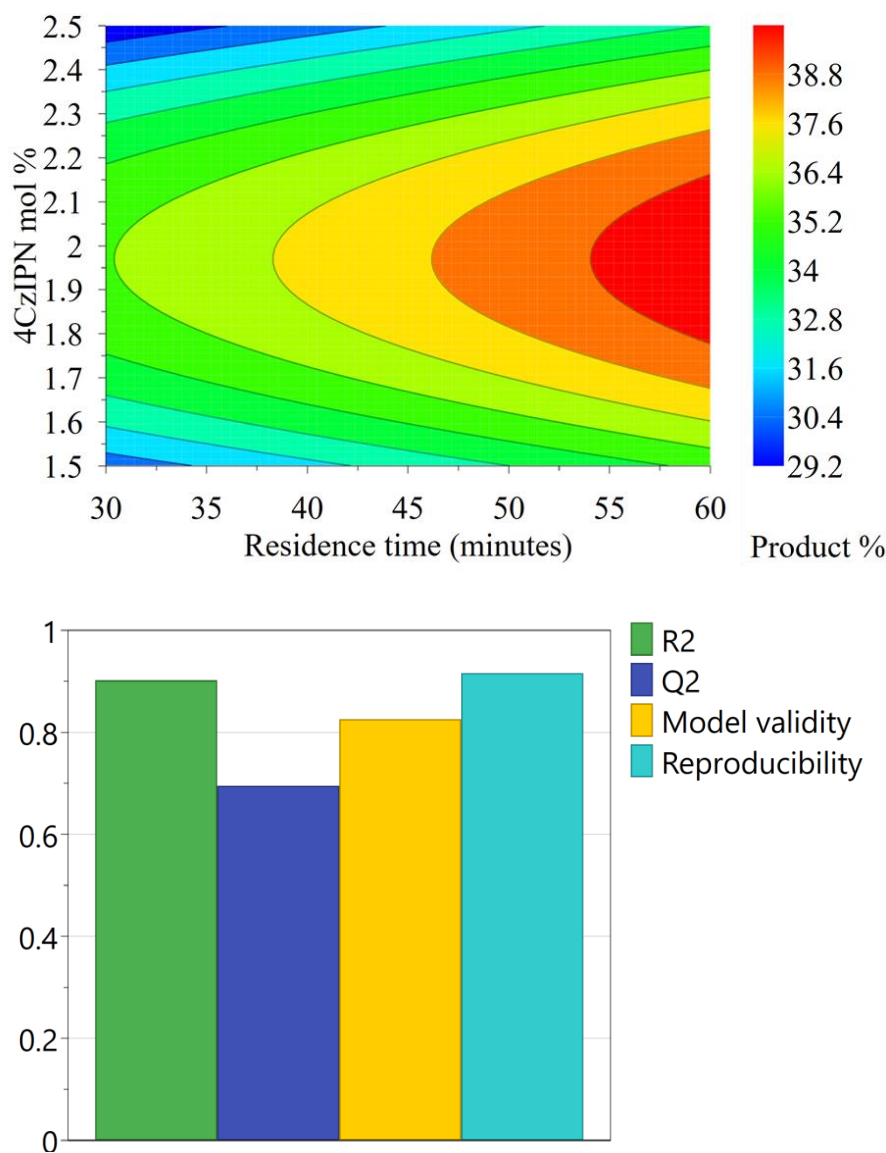


Figure 71. (Top) Response contour plot for C-N coupling of aniline and 2-fluoro-iodobenzene (Bottom) Model statistics calculated using MODDE.

4.2.5 C-N coupling of aniline and 4-bromo-benzotrifluoride

The optimisation performed in section 4.2.4 did allow useful information about the reaction to be obtained. However, the lengthy acquisition times required, due to the extensive nuclide coupling to

nearby protons, limited it as a practical system for online, automated analysis and optimisation. It was therefore hypothesised that switching to an ortho or para-trifluoromethyl substituted aryl halide would provide a much clearer NMR signal that could be monitored (Figure 72). In addition, switching to an aryl bromide instead of an aryl iodide reduces susceptibility to dehalogenation of the substrate. The C-N coupling was therefore performed again, this time with aniline and 4-bromo-benzotrifluoride (Scheme 19). The internal α,α,α -trifluorotoluene was omitted from the reaction this time due to its chemical shift being too near to that of the starting material to allow full resolution. A perfluorinated aromatic could be used instead; however, this has a risk of unwanted S_NAr reactions occurring and it was decided that a peak area ratio would be sufficient to determine the extent of the reaction progress.

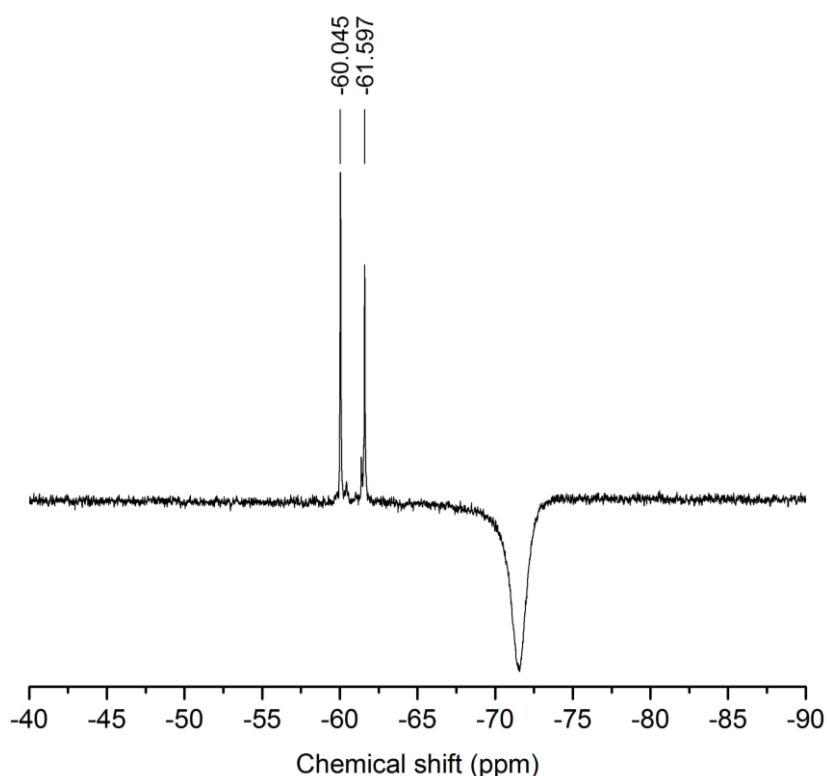
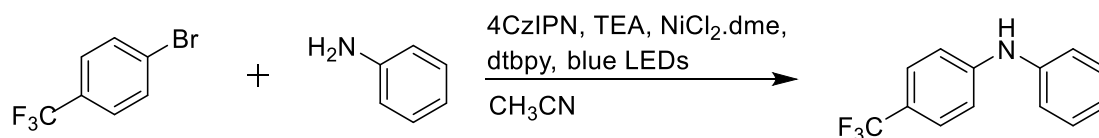


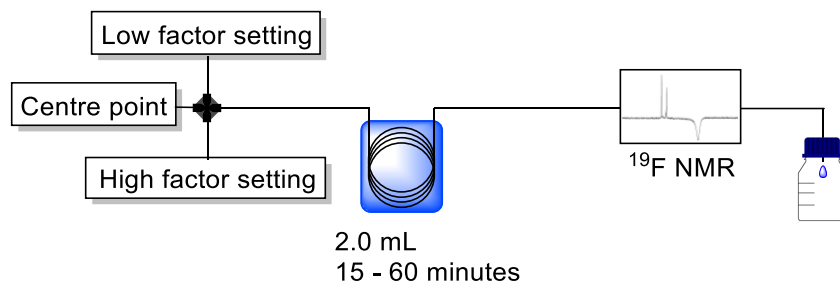
Figure 72. Typical online ^{19}F NMR spectrum for flow C-N coupling reaction with 4-bromo-benzotrifluoride. The starting material is shown at - 61.6 ppm, product at -60.0 ppm, chemical shifts have not been referenced.



Scheme 19. C-N coupling of aniline and 4-bromo-benzotrifluoride.

In addition to the change in substrate the reactor was plumbed into the glass flow cell of a benchtop NMR to allow online monitoring under flow conditions. The scripting ability of the Magritek Spinsolve software was utilised to continually acquire spectra every 5 minutes for a pre-determined number of spectra, allowing unattended operation of the flow reactor. The flow reactor set up (Scheme 20) was

altered from that used in section 4.2.3 to a system using three separate reagent streams, the necessary pump being automatically selected by a MATLAB algorithm through a logic test (Figures 73, 74), depending on the nickel loading of the experiment. While requiring a greater number of pumps than the algorithm used for the trifluoromethylation, there is no variable dilution effect due to the varying of pump flow ratio to reach the required residence time. This avoids any issue surrounding substrate concentration being an uncontrolled factor in the DOE optimisations.



Scheme 20. Three reagent feed flow reactor setup for automated optimisation.

Optimisation was performed for the loading of $\text{NiCl}_2\cdot\text{dme}$ and residence time; initially the experimental limits were set as approximately 5 - 10 mol. % $\text{NiCl}_2\cdot\text{dme}$ and 15 to 60 minutes residence time. The effect of the 4CzIPN, identified in 4.2.3, was considered and used to set the 4CzIPN loading at approximately 1 mol. % that of the aryl halide, reducing the risk of dehalogenation and the formation of impurities.

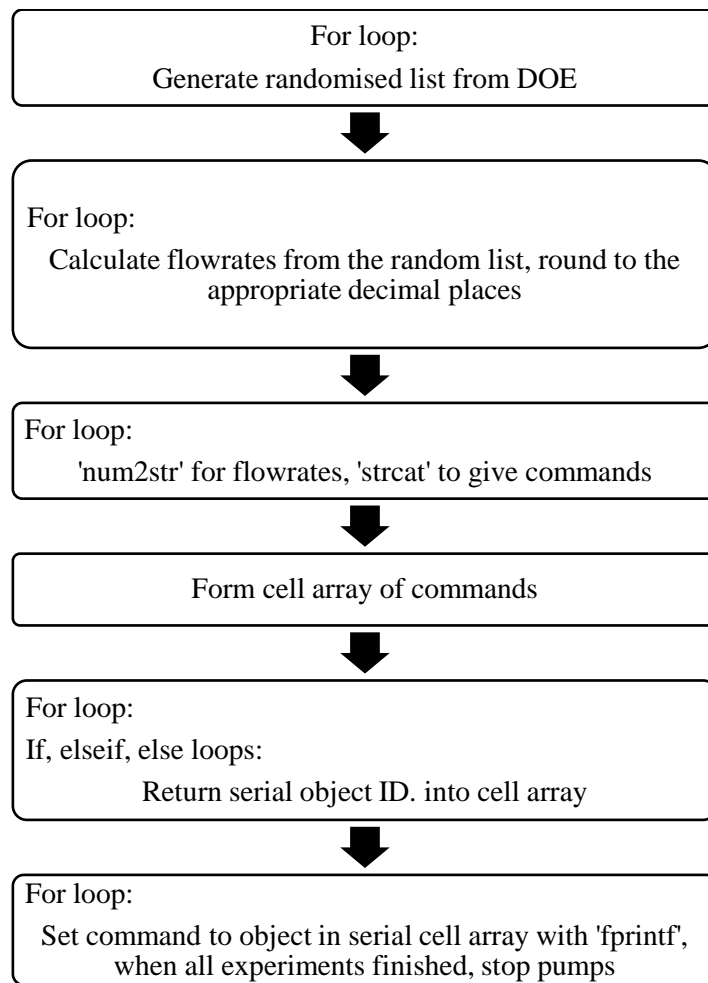


Figure 73. Flowchart for the automated selection of reagent feeds.

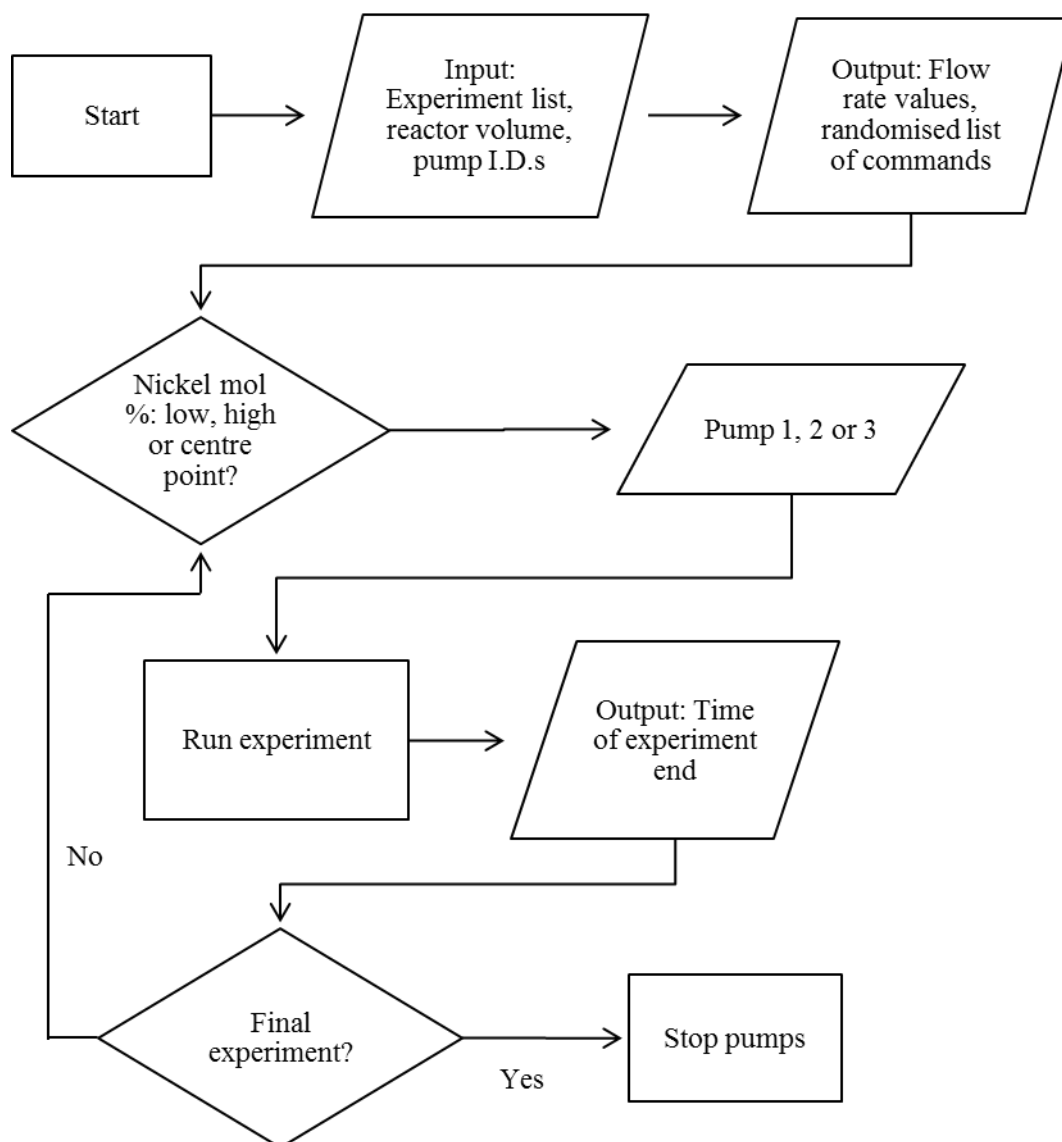


Figure 74. Flowchart for automated optimisation with three reagent feeds.

The building of an MLR model through MODDE revealed that over these factor ranges only the residence time was a significant factor, with a positive contribution to product peak area, and only minimal change due to variation in the nickel loading. The R^2 and Q^2 of a model with only residence time included in addition to the constant term were 0.95 and 0.92 respectively, indicating a strong model. The addition of further terms did not appreciably reduce these values; however, their inclusion would be an example of overfitting, as their removal led to an increase in the Q^2 of the model. A product peak area percentage $> 90\%$ was achieved for all the 60-minute residence time experiments and generally the model predicted that longer residence times would lead to greater product yields.

4.2.6 C-N coupling of aniline and 4-bromo-benzotrifluoride: factor level extension to lower nickel equivalents - 2.5 mol. %

To ascertain the lowest threshold of nickel that would still achieve good yields a further series of experiments were performed to extend the DOE study in 4.2.3.1 to lower nickel loadings. This was achieved by carrying out only 5 further experiments, the new lower factor levels at around 2.5 mol. % and two further centre points at the previous low factor setting of approximately 5 mol. %, to give a new group of centre points. Experiments from the previous study were then included to give a new symmetrical experiment space and the use of experiments from separate studies would overall lead to a more robust model that accounted for the variability of the analysis and synthesis. The acquisition of new data points was automated using the same MATLAB algorithm, except that the unnecessary points were manually deleted from the ‘fullfact’ generated DOE list before the optimisation function was started.

The MLR model built in MODDE with the highest value for Q^2 (0.86), while maintaining a high value for R^2 (0.96), incorporated positive terms for residence time, the squared nickel term and an interaction term for nickel and residence time. The nickel term was included and had a negative contribution to product peak area. This identified that lower nickel loadings were also beneficial to the formation of the product while residence time and the interaction term were positive contributions, but with a greater effect at low nickel loadings.

4.2.7 C-N coupling of aniline and 4-bromo-benzotrifluoride: factor level extension to lower nickel equivalents - 0.1 mol. %

As the previous DOE studies had revealed that lower nickel loadings could be beneficial and improve the efficiency of the reaction, a further extension of the experimental parameters was performed to try and identify the lower limit of nickel that still allowed high product yields. The DOE was extended in the same manner as in 4.2.6, adding only 5 additional experiments to those previously carried out. This extension identified that 0.1 mol. % nickel led to almost zero conversion at all residence times in the design space, and showed a large region of nickel loading at approximately 3-6 mol. % that would give similar, if not higher, yields as a loading of approximately 10 mol. %, with residence times of 50 minutes or longer.

All the data, collected for all ranges, was collected into a single study and a MLR model fitted to them. Due to the repeated changes in the effectiveness of the nickel catalyst the model required a cubic nickel term to accurately describe the data and locate an optimal region (Figure 75). In addition to the constant term the MLR model utilised the linear terms for nickel and residence time, the quadratic and cubic nickel terms, and the interaction terms between residence time and nickel and residence time with the quadratic nickel term. The residence time and quadratic nickel interaction term had a p value of 0.06,

however its removal led to a large decrease in both R^2 and Q^2 . Almost all other literature utilising this catalytic system has opted for 5-10 mol. % of the NiX_2 species. A limited investigation by Basch *et al.*,¹⁶⁹ reported in the supplementary information for the work, resulted in a slight drop in yields (79 - 69 %) when 5 mol. % was used instead of 10 mol. %. The work by Corcoran¹⁷⁰ within the Macmillan group on a ligand free batch protocol also investigated the nickel catalyst loading and other parameters through one factor at a time optimisation, showing a variation in yield with changing nickel concentration. Their work also required a change in solvent to N,N-dimethylacetamide due to the ligand removal.

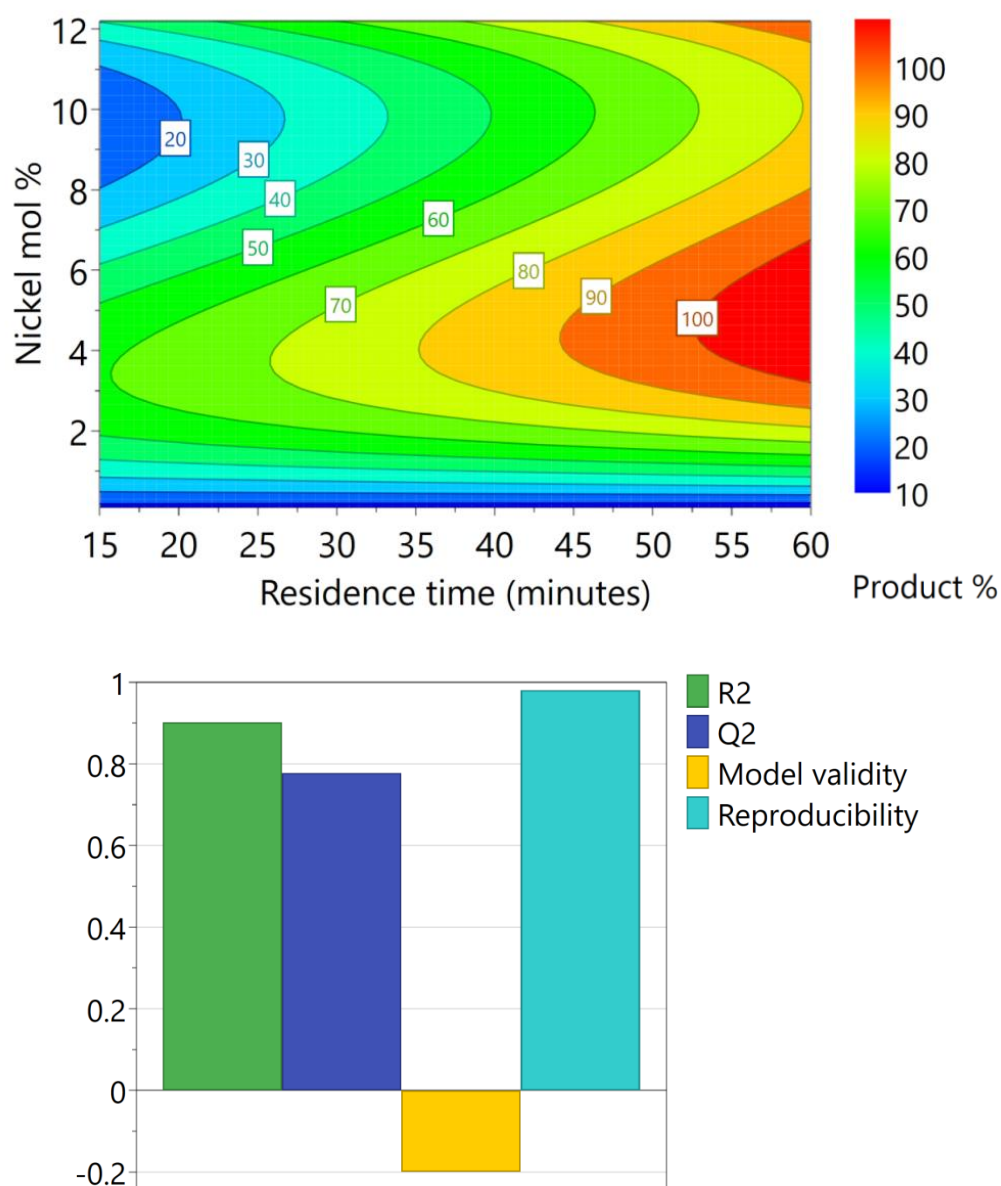


Figure 75. (Top) Response surface contour plot for the full data set collected (Bottom) Model statistics calculated using MODDE.

Comparison of the model with a cubed nickel term with three separate models covering the same 0.1 to 12 mol % nickel loading range provides some justification for the use of the cubic model term (Figure

76), with the same pattern showing that the lower level of nickel is more effective being repeated when separate models are used.

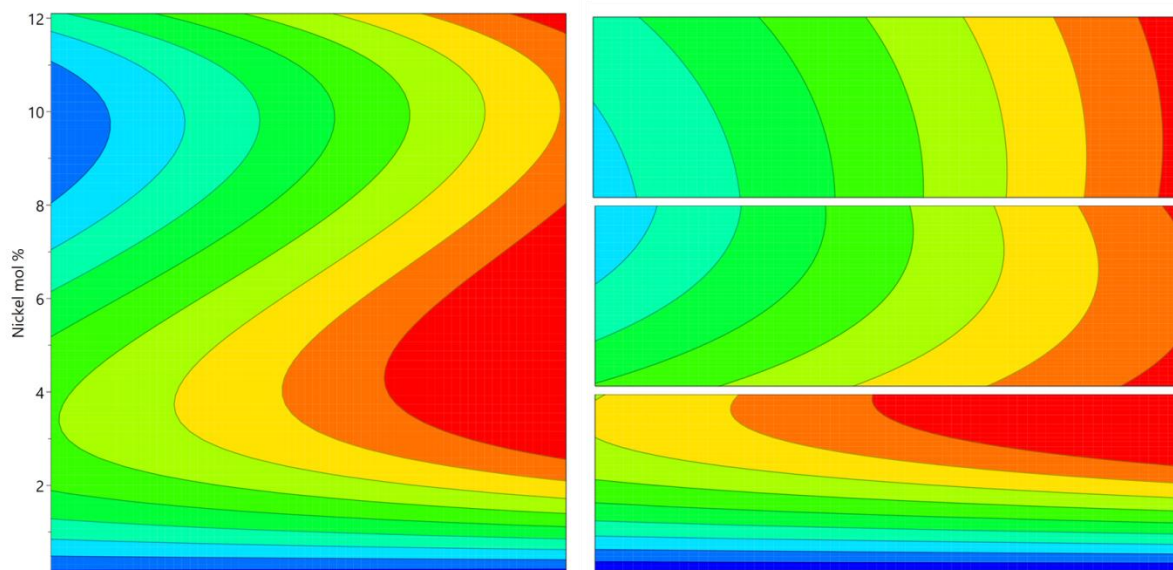


Figure 76. (Left) Contour plot for model over the range 0.1 to 12 mol % nickel. (Right) Contour plot for model over range 12 to 6 mol %, 9 to 3 mol % and 6 to 0.1 mol % at top, middle and bottom respectively.

Due to the poor solubility of both the nickel and the 4CzIPN catalysts the fine suspended particles would have an attenuation effect on the light source and lead to a subsequent reduction in reaction efficiency. The reduction in product peak area is in all likelihood due to light attenuation rather than any chemical effect from the nickel. This could be tested in further work by dosing insoluble glass microbeads into the solution and monitoring the effect on the product yield. Unfortunately, the chemical vendor did not have information on the particle size of the nickel catalyst so this would have to be determined through a light scattering method.

4.2.8 C-N coupling of aniline and 4-bromo-benzotrifluoride: automated 3 factor optimisation

To determine if any interaction between 4CzIPN and the nickel catalyst was significant, an automated protocol was written whereby the centre point of a three level DOE would be generated for the nickel and 4CzIPN from an equal combination of low and high levels for each reagent factor (Figure 77). In this manner only four pumps are required to investigate the effect of 2 additional reagents (Scheme 21) in addition to other variables such as residence time. This code was further modified so that the user needed to only enter the low and high levels for each factor, with the algorithm then generating a randomised, full factorial experiment list, before running each of the experiments.

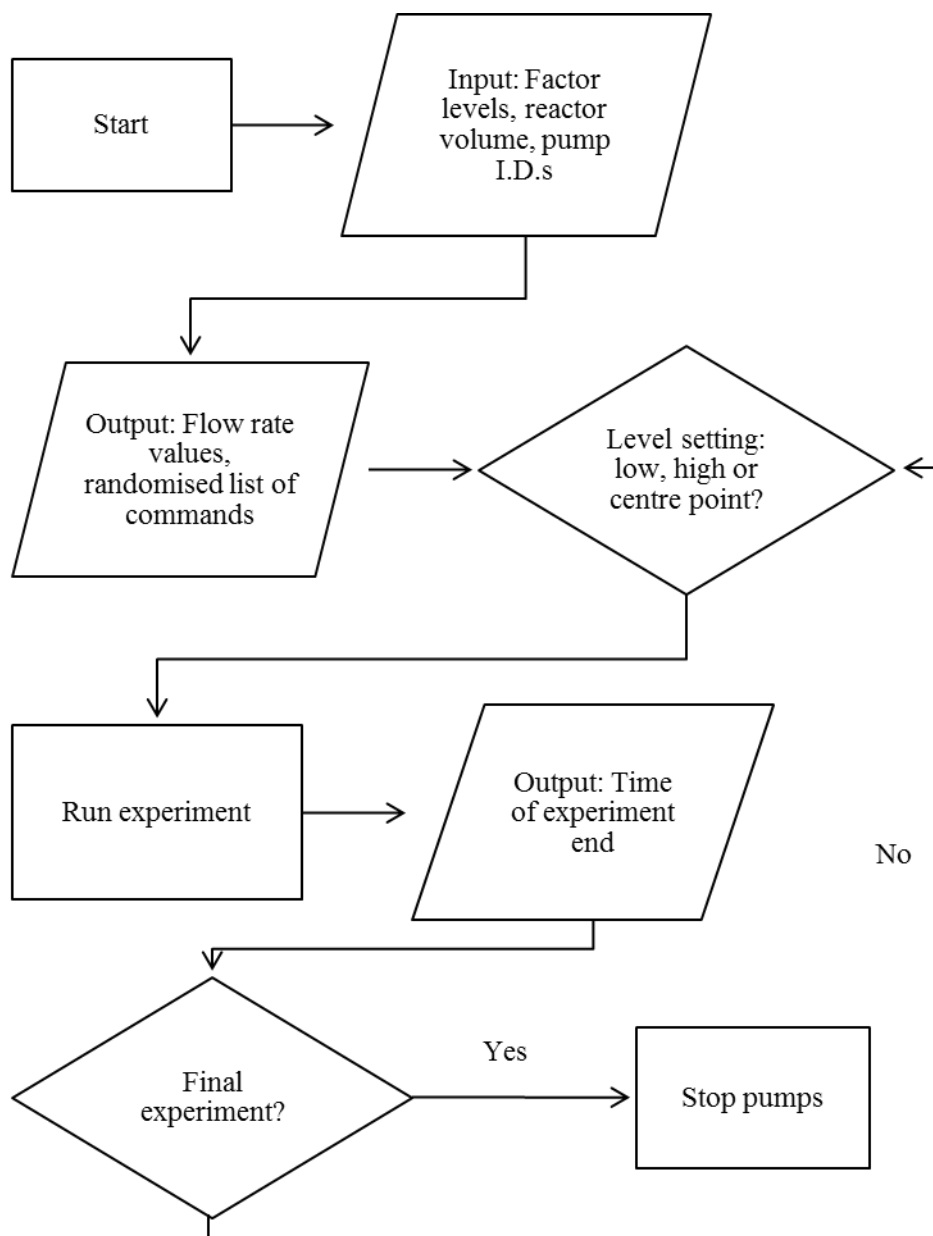
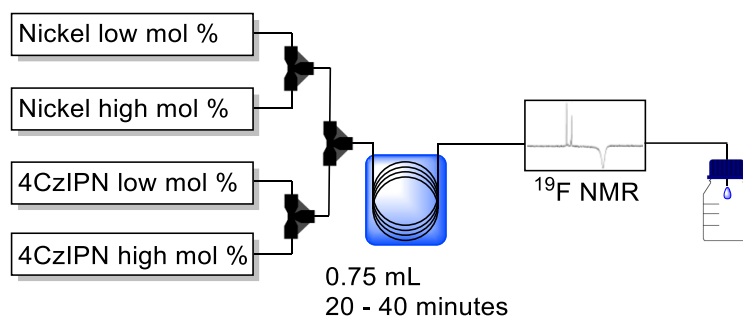


Figure 77. Flowchart for automated 3 factor optimisation through DOE, with two stoichiometric factors.

To include an additional stoichiometric factor with the approach utilised in sections 4.2.3 and 4.2.4 would require no fewer than 6 pumps for three levels and two reagents, and a further pump for each extra level for each factor, rapidly becoming unsustainable to all but the most well-funded research groups. Some compromises are required however, the reagent feeds must be prepared at twice the desired concentration due to the 1:1 dilution effect that will occur, and this can pose an issue for systems where compounds are near their maximum solubility, such as the system under investigation here. Additionally, the total flow rate for each reagent centre point is generated from both feeds, halving the effective flow rate at each pump. This is not a problem when accurate syringe pumps or similar are employed (as here), however for less accurate pumps, such as the Flowsyn system which is most reliable only down to 0.02 mL/min, this could introduce an additional source of variation into the results.



Scheme 21. Four pump optimisation system for 3 factor optimisation, including 2 stoichiometry factors.

The number of experiments was of course much greater than for the two factor optimisations, totalling 29. Because of this some of the experiments exhibited a greater degree of band broadening in the spectra than usual; this is likely due to a reduction in flow rates due to the use of a smaller reactor coil, which was chosen to reduce the reagent consumption for this larger scale optimisation. This led to greater heating of the reagents by the LED lamp than with other automated optimisations performed, and this can have the effect of broadening the NMR signal leading to a loss of sensitivity. Due to this a small number of experiments were removed from the MLR model in MODDE; one of the centre points was significantly different compared to the other two so was excluded, two other points were those farthest out on the residual normal probability plot.

The use of a full factorial design instilled some redundancy into the model, so despite the removal of these data points a reasonable model, though of lower quality than desired, could still be arrived at through MODDE. Using MLR led to a model with an R^2 of 0.76 and a Q^2 of 0.59, this model included linear terms for residence time, nickel and 4CzIPN; quadratic and cubic nickel terms and an interaction term for nickel and 4CzIPN. A response surface plot for the three factors was generated (Figure 78) to identify optimal regions of the experiment space. This model is of rather low quality, and as such there is a high degree of uncertainty in the results, it should be noted that this model could not be relied upon in its current state for high predictive power.

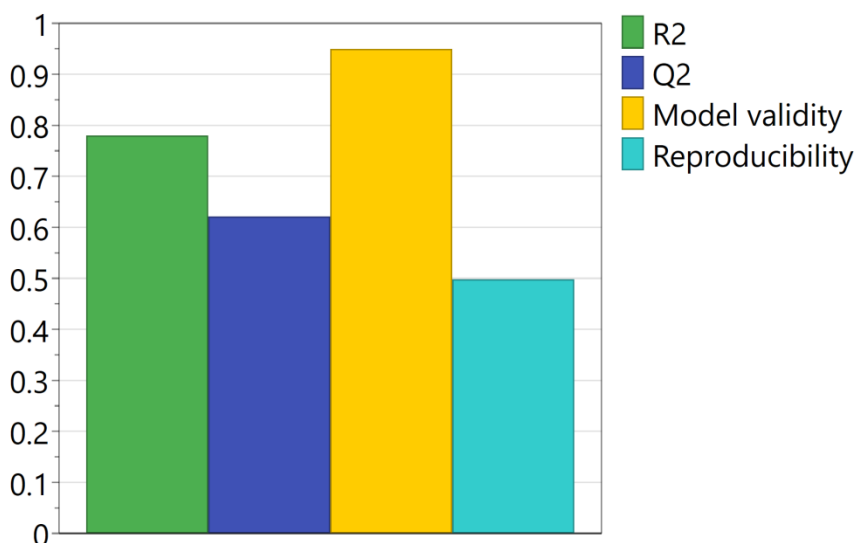
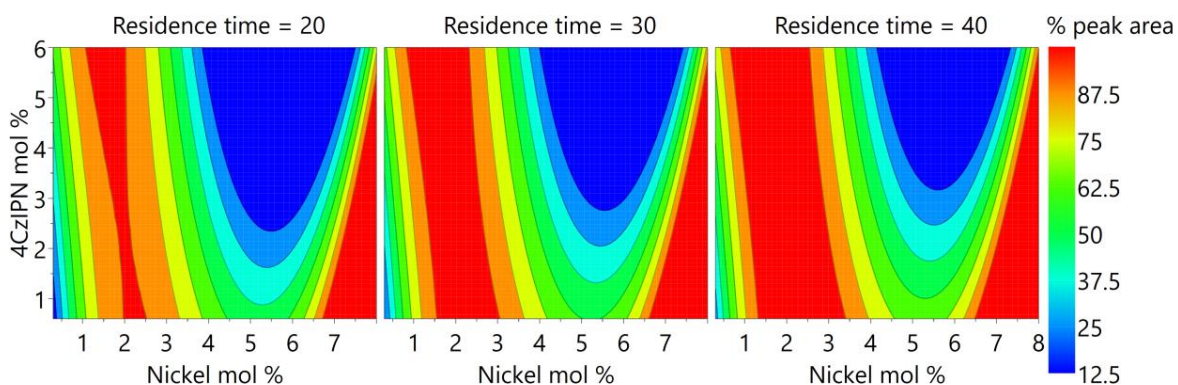


Figure 78. (Top) Contour plot showing the change in product formation with variation in all three factors (Bottom) Model statistics calculated using MODDE.

By varying the loading of the photo initiator in conjunction with the nickel it was revealed that low 4CzIPN levels could be used at high nickel concentrations, at a wide range of residence times, to achieve high yields. However, use of low nickel concentrations with low 4CzIPN loading would also give good yields (> 90 %) at residence times of approximately 30 minutes and longer, beneficial given that nickel salts are generally highly toxic and relatively expensive. These conditions should be applicable to any electron poor aryl bromide or iodide, but more work would be required to determine the scope of substrates that could be coupled with lower nickel loadings.

Further alterations were made to the reaction conditions at this point to determine what other parameters were fundamental to the reaction. The photosensitiser was changed to first riboflavin and then riboflavin tetraacetate at 5 mol. %, keeping all other parameters the same. This led to no visible conversion by ^{19}F NMR. The wavelength of the lamp was then altered to 400 nm, returning to the use of 4CzIPN, and this also showed no conversion by ^{19}F NMR. Finally, the ligand concentration was increased to three times the loading of the $\text{NiCl}_2\cdot\text{dme}$ - this also showed no conversion to the product.

4.2.9 Automated spectrum acquisition

As a further improvement to the automated optimisations performed so far, a piece of MATLAB code was written to allow automated data acquisition with the Spinsolve software, which has a limited scripting ability for reaction monitoring. The function generates a series NMR experiments to be run with variable time delays, based on the input experiment list (Figure 79). In the case of the automated optimisations performed so far this is a DOE list, but any list of experiments would be suitable.

The NMR acquisition is timed for the end of each DOE run, and the acquisition time for the spectrum is also factored into the function. The output of the function is an ASCII encoded script with the file type '.sss', as required by the Spinsolve software. When copied into the reaction monitoring folder of the Spinsolve software it is then user selectable. To begin automated analysis the user simply starts the Spinsolve script and the MATLAB function at the same time.

The actual increase in efficiency by using this bespoke acquisition approach is minimal compared to the experiments run where timestamps were generated. Thankfully the need to preserve computer storage space has passed and excessive data sets can be collected without issues for computer performance. However, for use in industry or for non-expert users a simplified data set would have advantages.

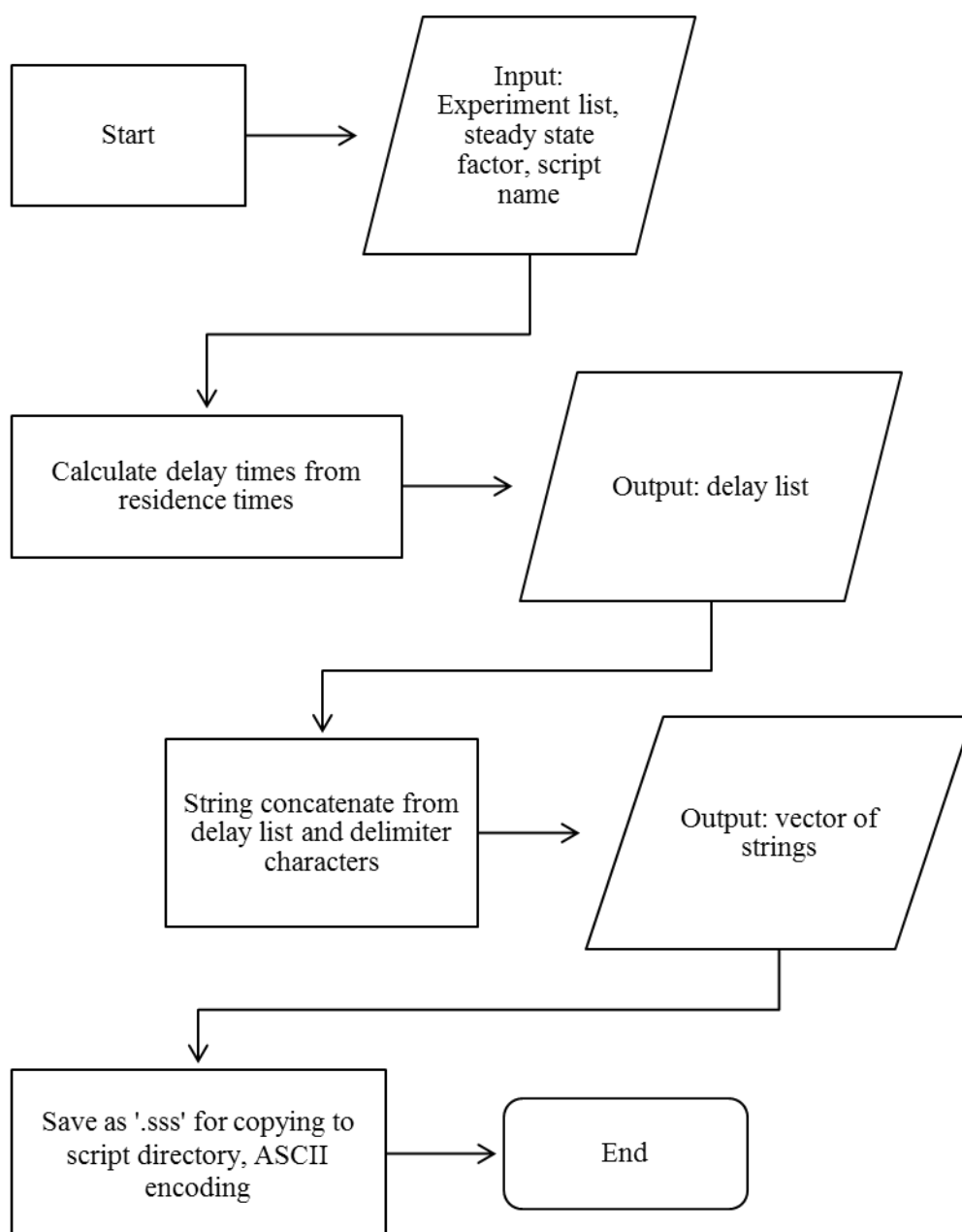


Figure 79. Flowchart for generation of automated acquisition scripts for Spinsolve software.

4.3 Chapter summary

This chapter has shown the usefulness of flow NMR with low field benchtop instruments and identified the experimental conditions necessary for the generation of good quality analytical data. Combined with automated experiments the majority of experimental effort was expended on data analysis, and automation has also allowed this stage to become relatively straightforward through the creation of hardware specific scripts for data acquisition or the generation of timestamps for experiments. The optimisation of the C-N coupling reaction has been simplified to essentially a push button operation and could be easily performed by scientists with relatively little experience.

An overview of the approach taken to write the code required for automated multi-experiment runs shows there are numerous approaches with specific disadvantages and advantages. The optimisation conducted using two syringe pumps can be easily modified so that a third pump dosing a makeup flow of solvent, and internal standard if desired, could be added to avoid the problem of substrate dilution. This would be required for reactions where the substrates were reactive, fortunately not the case with the C-N coupling examined here, but far more likely to be encountered.

Application of the optimisation system to the photoredox C-N coupling of aryl halides with aniline identified an optimal region at lower nickel loading than typically used in other work, reducing the amount of expensive and highly toxic nickel salt that was required. At this stage the effect is thought to be due to light attenuation through scattering of light by non-dissolved material, this is supported by the 3 factor optimisation study which identified the interaction between the photosensitiser and metal catalyst is negative for the product yield.

4.4 Further work

Further work in automation of flow chemistry must address the lack of open communication for modern instrumentation, as relatively few manufacturers are willing to share their protocols, often regarding it as commercially sensitive information. Without an open architecture, researchers must overcome communication barriers through workarounds or be restricted to using the few systems whose manufacturers are admirably willing to share communication protocols, such as Ocean Optics and Uniqsis.

To fully investigate the reason for the variable nickel activity, the use of inert microbeads, which are available as a reference material for light scattering based particle size analysers, is recommended. If such an effect is identified then the use of varying particle sizes would allow the effect to be quantified and controlled, leading to a more robust process.

5. Conclusion

The overall objective of this work was to use AM techniques to develop ‘smart’ reactors - reactor systems with integrated analysis which allows reactions to be optimised quickly and simply. Using AM, reactor modules with tortuous and stacked flow paths and ports for embedded sensors were produced – parts that could not be produced by other manufacturing methods.

The integration of analytical methods into reactors focused on the use of spectroscopy as it is non-destructive. Several designs for flow cells that could be integrated directly into a flow system, or reactors with integrated optics were produced by SL and shown to be successful. The limiting path length for modules with internal flow channels was found to be 2 mm, too large for UV monitoring of typical organic reactions. Using a new approach to printing parts through SL, creating the details at the surface of the part and sealing with film, AM flow cells with microfluidic features < 100 µm were produced for the first time, and, when combined with directly embedded optical fibres, were shown to be suitable for the direct UV spectroscopic monitoring of flow organic chemistry with high quality spectra obtained.

Where chemical compatibility was a concern, given the limitations of epoxy-acrylate resins utilised in SL, a system for spectroscopy to be performed directly within reaction tubing was devised and used to collect online spectra for the optimisation of a [3+3] formal cycloaddition. AM was also used for the design and initial testing of low cost ATR systems, which were shown to be capable of collecting visible spectra with an effective pathlength of < 10 µm. This reduction in pathlength is crucial for online spectroscopic monitoring of organic reactions, and the use of AM allowed a part with minimal dead volume to be made. This is in contrast to the bulky and highly expensive ATR probes available, which require a large disruption to the reactor system if online and inline measurements are to be made rather than measurement of a reaction volume within a potentially non-representative sampling loop.

The use of parts produced through metal printing techniques then allowed a versatile range of chemistry to be performed. High temperature and high-pressure reaction conditions were possible with the use of a SLM printed reactor, and a catalytically active copper reactor was made through the hybrid AM technique ultrasonic consolidation and designed to allow multi-step chemistry within a single reactor. This UC reactor proved to be applicable to several copper catalysed reactions and additionally incorporated an embedded sensor to facilitate online temperature measurement, which was more accurate than the temperature readings available from the flow chemistry equipment.

Photo chemistry was also shown to be possible within SL reactors and demonstrated on a pharmaceutically relevant reaction. This is among the first reported examples of photochemical reactions being performed within a 3D printed reactor and shows that the benefits of reactor design achievable through AM so far discussed can be applied to custom photoreactors. This reaction was then

optimised in a fully automated manner using design of experiment methodology and computer control of the flow equipment combined with online analysis. An efficient optimisation strategy was outlined, requiring fewer pumps than typically needed to generate many discrete levels from only two pumps per experimental factor. The optimisation identified that lower levels of expensive and toxic nickel salt catalyst could be employed than had typically been reported.

The use of online UV/Vis spectroscopy for the early work in this thesis allowed reactions to be optimised, but typically resulted in a non-specific optimisation as they tended to focus on an increased absorbance, which all compounds present may contribute to. By using NMR spectroscopy, a selective method that allows the monitoring of several components at once, the photochemical reactions in this work were easily optimised for the desired product. Further to this some of the desirable parameters for the successful use of online NMR were identified, with singlet peaks corresponding to methyl, methoxy or trifluoromethyl close to the reaction site most likely to be of use because of the inherent lack of sensitivity of NMR.

6. Experimental

6.1 Instrumentation

6.1.1 IR

All IR spectra were acquired using a Perkin-Elmer 65 FTIR spectrometer. Liquid spectra were collected as thin films on sodium chloride discs and solid spectra were collected by dissolving in dichloromethane applying to the disc surface and allowing the solvent to evaporate, leaving a thin layer.

6.1.2 Melting points

All melting points are uncorrected and were acquired using open ended melting point tubes and a Stuart SMP-3 melting point apparatus.

6.1.3 NMR Spectroscopy

All ^1H , ^{19}F and ^{13}C NMR spectra were collected at 400, 376 or 100 MHz respectively with either a Bruker Avance II spectrometer or a Jeol ECS-400 spectrometer. ^1H and ^{13}C signals were referenced to the residual non-deuterated solvent. The solvents used for NMR spectroscopy were CDCl_3 (δ 7.26, ^1H ; 77.0, ^{13}C), CD_3OD (δ 3.31, ^1H ; 49.00, ^{13}C) or $(\text{CD}_3)_2\text{SO}$ (δ 2.50, ^1H ; ^{13}C , 39.52). ^{19}F spectra were collected using α, α, α -trifluorotoluene as the reference (δ -63.7, ^{19}F). Chemical shifts are reported in parts per million (ppm) and J values are reported in Hertz (Hz).

All ^{19}F and ^1H NMR for reaction optimisation studies were collected using a Magritek Spinsolve 40 at 42.5 MHz. Where a reference standard was included this is stated in the experimental section for that investigation and the spectra were collected in non-deuterated reaction solvent.

6.1.4 Column chromatography

Reactions were monitored using thin layer chromatography (TLC) on aluminium backed plates coated with Merck TLC 60 F₂₅₄ silica gel. Visualisation of compounds was by UV light at 254 nm, or by staining with an acidified solution of vanillin in ethanol followed by heating. Purification by column chromatography was performed using 40-63 μm particle size silica gel (Apollo ZEOprep 60).

6.1.5 Flow chemistry equipment

Flow reactions were carried out using a Flowsyn flow chemistry platform (Uniqsis, UK) system with stainless steel reactor tubing or custom 3DP reactors. Further reactions were carried out using AL-1000 syringe pumps (WPI, UK) with PTFE tubing.

6.1.6 Mass spectrometry

High resolution mass spectrometry was performed using a Thermo scientific orbitrap Q Exactive MS in ESI mode (Thermo Fisher Scientific, MA, USA). GC/MS was performed using a Thermo Finnigan Trace Ultra GC (Thermo Fisher Scientific, MA, USA) with a single quadrupole MS detector, or a Shimadzu QP-2020 single quadrupole system (Shimadzu, Kyoto, Japan), equipped with an HP-5ms, 30 m \times 0.25 mm I.D, 0.25 μ m film thickness, using helium as the carrier gas.

6.1.7 UV/Vis spectroscopy

UV/Vis spectroscopy was performed using S2000 or STS-UV fibre optic spectrometers (Ocean Optics, FL, USA) controlled with OceanView software (V1.5.2, Ocean Optics, FL, USA) in Windows 7. Solarisation resistant fibre optic cables were used to transmit at wavelengths below 300 nm. The light source was a DH-2000 (Ocean Optics, FL, USA) with deuterium and halogen bulbs. Acquisition times were generally set so that total counts were as high as possible without saturation occurring in the region of interest.

6.1.8 HPLC analysis

HPLC analysis was performed using a Hitachi Chromaster quaternary pump HPLC system (Hitachi, Tokyo, Japan) with diode array detection and column temperature control. The column used was either an ACE C18 4.6 \times 250 mm, 5 μ m particle size (Advanced Chromatography Technologies, Aberdeen, Scotland), or a Zorbax Eclipse plus C18, 3.0 \times 30 mm, 2.7 μ m particle size (Agilent, Cheshire, UK), specified in the relevant experimental section.

6.1.9 Automated optimisation

Scripts for the control of equipment and automation of experiments and data collection were written in MATLAB (R2012a/R2015b, Mathworks, MA, USA) in Windows 7/10. Simplex optimisation protocols were written in Microsoft Excel 2010 (Microsoft Corporation, WA, USA).

6.1.10 DOE model generation and coefficient selection

The models for DOE optimisations were typically generated in MODDE software (Umetrics, Umeå, Sweden). Models were generally built with MLR, and in addition to the constant term, coefficients for the factors, cross terms and quadratic terms were included by default to begin. Coefficients were removed from the model to focus on obtaining the highest Q^2 result, a strong measure of the prediction strength of the model. Lower order terms were kept in the model when insignificant if required for the inclusion of a higher order term that would result in a higher Q^2 value.

6.1.11 CAD sketches

All CAD drawings were produced in NX versions 7.5, 8.5 and 10, software (Siemens, Bavaria, Germany) in Windows 7. All drawings were converted to .stl files for printing.

6.1.12 SL part printing

Models were produced using a 3D Systems Viper si2 SL instrument (3D systems, SC, USA) using Accura 60 resin. Manufacturing was performed according to manufacturers recommended processing conditions.

6.2 Laboratory procedures

6.2.1 General considerations

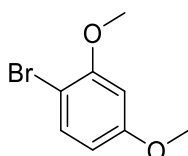
All solvents and reagents were used as supplied by the vendor or purified according to standard literature techniques.

6.2.2 Flow bromination of 1,3-dimethoxybenzene in SL reactor (R1) with in-built spectroscopic monitoring port

Solutions of 1,3-dimethoxybenzene (0.05 M) and N-bromosuccinimide (0.05 M) were prepared in acetonitrile. The reagents were pumped separately, meeting at a T-piece immediately before the SL reactor inlet. The total flow rate was 2 mLmin⁻¹, equating to a residence time of 6 minutes.

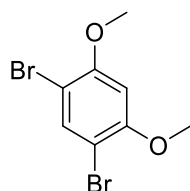
Material for UV spectrum acquisition was produced by mixing 10 mL of 1,3-dimethoxybenzene in acetonitrile (0.2 M) with 10 mL of N-bromosuccinimide in acetonitrile (0.2 M) and allowing to stand for 2 hours at room temperature. The solution was evaporated *in vacuo* before adding diethyl ether (25 mL), followed by washing with water (3 × 20 mL). The aqueous portions were combined and washed with diethyl ether (20 mL), the organic layers were combined, washed with brine (10 mL) and dried over MgSO₄ before filtration. The crude mixture was purified by column chromatography over silica in a mixture of hexane:ethyl acetate (10:1, v:v) to give the mono and di brominated products. The characterisation data is in agreement with the published literature.^{171,172}

1-Bromo-2,4-dimethoxybenzene (2a)



Light brown oil; ^1H NMR (CDCl_3 , 400 MHz), δ 3.79 (s, 3H, CH_3), 3.86 (s, 3H, CH_3), 6.39 (dd, 1H, $J = 8.7, 2.9$ Hz, Ar-H), 6.48 (d, 1H, $J = 2.9$ Hz, Ar-H), 7.40 (d, 1H, $J = 8.7$ Hz, Ar-H); ^{13}C NMR (CDCl_3 , 100 MHz), δ 55.5, 56.1, 99.9, 102.4, 105.8, 133.1, 156.5, 160.2; MS (EI), m/z 218 (95.2 %), 216 (M^+ , 100), 175 (24.5), 173 (27.8), 173 (27.8), 108 (20.3), 107 (31.6), 79 (24.1); IR (film) $\nu_{\text{max}}/\text{cm}^{-1} = 3004\text{m}, 2962\text{m}, 2940\text{m}, 2836\text{m}, 1591\text{s}, 1489\text{s}, 1464\text{s}, 1437\text{s}, 1410\text{m}, 1308\text{s}, 1282\text{s}, 1210\text{s}, 1164\text{s}, 1061\text{s}, 1023\text{s}$.

1,5-Dibromo-2,4-dimethoxybenzene (2b)



White solid; m.p. 140-142 °C (lit. 141 °C)¹⁷²; ^1H NMR (CDCl_3 , 400 MHz), δ 3.91 (s, 6H, CH_3), 6.49 (s, 1H, Ar-H), 7.66 (s, 1H, Ar-H); ^{13}C NMR (CDCl_3 , 100 MHz), δ 56.5, 97.4, 102.4, 135.9, 156.1; MS (EI), m/z 298 (49.9 %), 296 (100), 294 (M^+ , 52.4), 255 (21.1), 253 (43.9), 251 (22.6); IR (film) $\nu_{\text{max}}/\text{cm}^{-1} = 1581\text{s}, 1489\text{s}, 1465\text{s}, 1435\text{s}, 1371\text{s}, 1290\text{s}, 1211\text{s}$.

6.2.3 Flow synthesis and online analysis of $\text{S}_{\text{N}}\text{Ar}$ reaction between 2,4-difluoronitrobenzene and pyrrolidine

A 0.1 M solution of 2,4-difluoronitrobenzene was prepared in ethanol. Further solutions of pyrrolidine (0.2, 0.6 and 1.0 M) were prepared in ethanol. The 2,4-difluoronitrobenzene was pumped *via* syringe pump separately from the required pyrrolidine solution, which was also delivered *via* syringe pump, meeting at a mixing tee immediately before a PTFE reactor coil (1 mL) immersed in a water bath maintained at the temperature specified by the experiment settings. A CCF design was selected to carry out the optimisation, varying temperature, residence time and the equivalents of pyrrolidine (Table 13). The visible absorption was monitored online using a 3D printed waveguide, threaded with 0.8 mm I.D. PTFE tubing and spectra were acquired at steady state conditions of 1.5 reactor volumes.

Table 13. Experiments performed for optimisation using online spectroscopy

Experiment name	Run order	Temperature (°C)	Pyrrolidine equivalents	Residence time (minutes)	480 nm absorbance (A.U.)
1	9	30	2	0.5	0.026
2	16	70	2	0.5	0.199
3	5	30	10	0.5	0.148
4	3	70	10	0.5	0.187
5	6	30	2	10	0.324
6	17	70	2	10	0.461
7	1	30	10	10	0.416
8	4	70	10	10	0.684
9	14	30	6	5.25	0.35
10	8	70	6	5.25	0.5
11	2	50	2	5.25	0.28
12	15	50	10	5.25	0.625
13	11	50	6	0.5	0.204
14	10	50	6	10	0.474
15	13	50	6	5.25	0.446
16	7	50	6	5.25	0.416
17	12	50	6	5.25	0.45

Combined reactions were diluted with ethyl acetate (20 mL) and washed with water (3×20 mL) and brine (3×10 mL). The solvent was evaporated *in vacuo* and the crude purified by column chromatography using a 20 % mixture of ethyl acetate in hexane. The characterisation data is in agreement with the published literature.¹¹¹

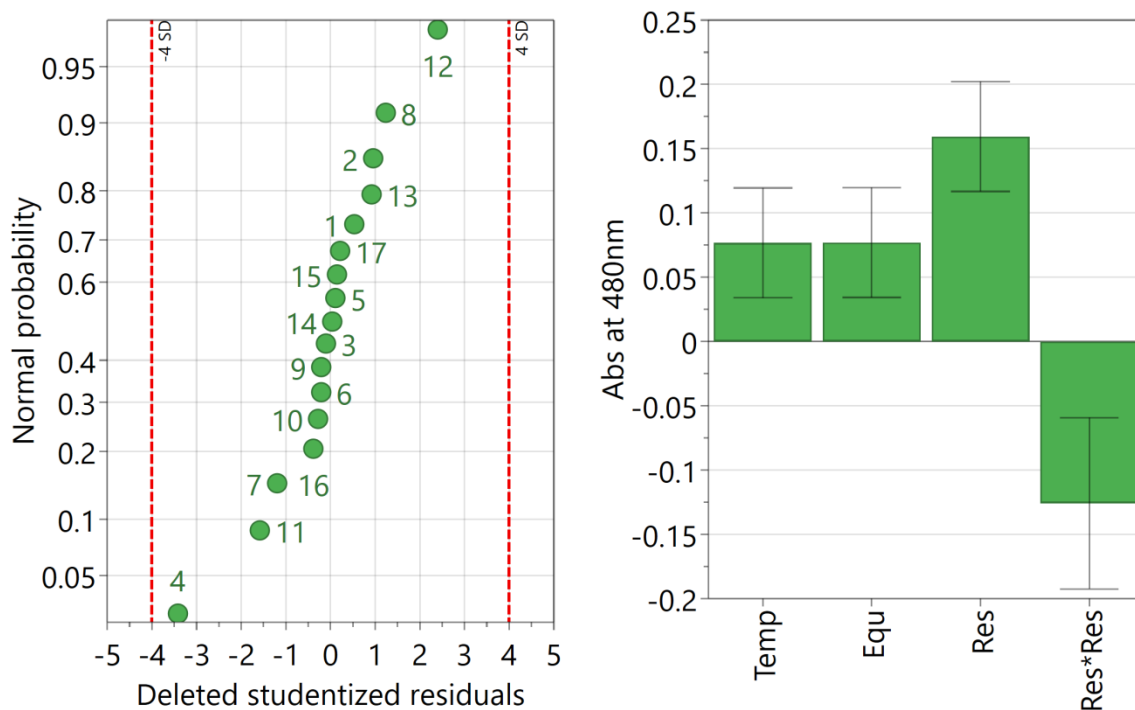
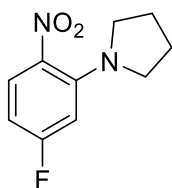


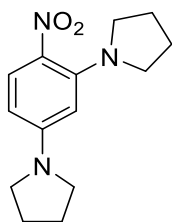
Figure 80. (Left) Residual normal probability plot for S_NAr synthesis MLR model (Right) Coefficient plot.

1-(5-Fluoro-2-nitrophenyl)pyrrolidine (**8a**)



Orange solid; m.p.79-82 °C; 1H NMR ($CDCl_3$, 400 MHz), δ 1.99 (m, 4H, CH_2), 3.19 (m, 4H, CH_2), 6.41 (m, 1H, Ar-H), 6.56 (dd, 1H, $J = 11.9, 2.5$ Hz, Ar-H), 7.77 (dd, 1H, $J = 9.1, 6.2$ Hz, Ar-H); ^{13}C NMR ($CDCl_3$, 100 MHz), δ 25.7, 50.6, 101.8 (d, $J = 27$ Hz), 103.2 (d, $J = 24$ Hz), 129.2 (d, $J = 13$ Hz), 133.7, 144.6 (d, $J = 13$ Hz), 165.1 (d, $J = 252$ Hz); ^{19}F NMR ($CDCl_3$, $C_6H_5CF_3$, 376 MHz), δ -104.25 (m); MS (EI) 210 (M^+ , 35.5 %), 193 (87.8), 163 (95), 162 (100), 149 (20.5), 137 (34.5), 135 (28.8), 122 (62.9), 109 (24.9), 95 (42.5), 75 (20.1); IR (film) $\nu_{max}/cm^{-1} = 2975m, 2876m, 1624s, 1566s, 1510s, 1362m, 1283s, 1204m$.

1,1'-(4-Nitro-1,3-phenylene)dipyrrolidine (8b)

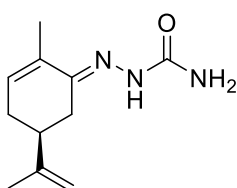


Orange red solid; m.p. 134-137 °C (lit. 140-141 °C)¹¹¹; ¹H NMR (CDCl₃, 400 MHz), δ 1.92 - 1.99 (m, 4H, CH₂), 1.99 - 2.07 (m, 4H, CH₂), 3.19 - 3.30 (m, 4H, CH₂), 3.30 - 3.40 (m, 4H, CH₂), 5.72 (d, 1H, *J* = 2.5 Hz, Ar-H), 6.00 (dd, 1H, *J* = 9.3, 2.3 Hz, Ar-H), 7.90 ppm (d, 1H, *J* = 9.5 Hz, Ar-H); ¹³C NMR (CDCl₃, 100 MHz), δ 25.4, 25.7, 47.7, 50.9, 94.8, 102.2, 127.5, 129.9, 146.4, 151.3; MS (EI), 261 (M⁺, 26.9 %), 244 (100), 229 (22.7), 228 (26.6), 227 (88.9), 226 (87.7), 216 (21.2), 201 (26.3), 200 (30.3), 199 (24.8), 188 (32.2), 186 (26.6); IR (film) $\nu_{\max}/\text{cm}^{-1}$ = 2967m, 2871m, 1606s, 1556s, 1314s, 1264s.

6.2.4 Flow synthesis of (S,E)-2-(2-methyl-5-(prop-1-en-2-yl)cyclohex-2-en-1-ylidene)hydrazine-1-carboxamide

Material for characterisation was prepared by dissolving semicarbazide.HCl (0.9 mmol) and sodium acetate trihydrate (1.2 mmol) in a mixture of 0.8 mL water and 1.4 mL ethanol. Carvone (0.66 mmol) was added and the mixture heated at 60 °C for 1 hour before leaving for 14 hours. The resulting white crystals were filtered and washed with ice cold water before air drying (0.10 g, 74 %). The characterisation data is in agreement with the published literature.¹⁷³

(S,E)-2-(2-methyl-5-(prop-1-en-2-yl)cyclohex-2-en-1-ylidene)hydrazine-1-carboxamide (5)



White solid; m.p. 139-142 °C (lit. 138 °C)¹⁷³; $\lambda_{\max}(\text{EtOH}/\text{H}_2\text{O})/\text{nm}$ 265 (log $\epsilon/\text{L mol}^{-1} \text{cm}^{-1}$ 4.27); ¹H NMR (CDCl₃, 400 MHz), δ 1.76 (s, 3H, CH₃), 1.85 (s, 3H, CH₃), 2.07 (m, 2H, CH₂), 2.34 (m, 2H, CH₂), 2.70 (dd, 1H, *J* = 15.8, 3.8 Hz, CH), 4.79 (d, 2H, *J* = 13.6 Hz, CH₂), 6.07 (m, 1H, CH), 8.34 (s (br), 1H, NH); ¹³C NMR (CDCl₃, 100 MHz), δ 17.7, 20.8, 28.9, 29.9, 40.4, 110.2, 132.3, 132.4, 147.4, 148.1, 157.8; MS (ESI) *m/z* 208 ([M+H]⁺); IR (film) $\nu_{\max}/\text{cm}^{-1}$ = 3583m, sh, 3470m, 3195m, br, 1689s, 1574s, 1474m, 1422m.

For the flow synthesis, solutions of R-(-)-carvone (0.06 M) and semicarbazide.HCl (0.08 M) with sodium acetate (0.11 M) were prepared in EtOH:H₂O (7:4). The solutions were pumped separately,

meeting at a T-piece immediately before the reactor. The reactor was a 5 mL coil of stainless steel tubing (1.0 mm I.D.) preheated to the required temperature and allowed to equilibrate while pumping solvent through both reagent channels. After the coil a 200 PSI backpressure regulator was installed followed by the microfluidic flow cell.

A central composite faced experiment design was used to optimise the reaction for temperature and residence time, while the ratio of semicarbazide to carvone was maintained at 2:1 for all experiments. This required 11 total experiments to be performed, including 3 centre points to allow an estimate of the reaction reproducibility (Table 14). Spectra were acquired throughout each experiment to aid the identification of steady state conditions.

Table 14. Experiments performed for optimisation of carvone semicarbazone synthesis.

Experiment name	Run Order	Temperature (°C)	Residence time (minutes)	Carvone flow rate (mLmin ⁻¹)	Semicarbazide flow rate (mLmin ⁻¹)	UV absorbance (265 nm, min-max)
1	5	108	25	0.08	0.12	0.510
2	11	140	25	0.08	0.12	0.584
3	10	108	50	0.04	0.06	0.772
4	3	140	50	0.04	0.06	0.838
5	6	108	33.3	0.06	0.09	0.690
6	9	140	33.3	0.06	0.09	0.778
7	4	120	25	0.08	0.12	0.514
8	2	120	50	0.04	0.06	0.798
9	8	120	33.3	0.06	0.09	0.698
10	1	120	33.3	0.06	0.09	0.713
11	7	120	33.3	0.06	0.09	0.709

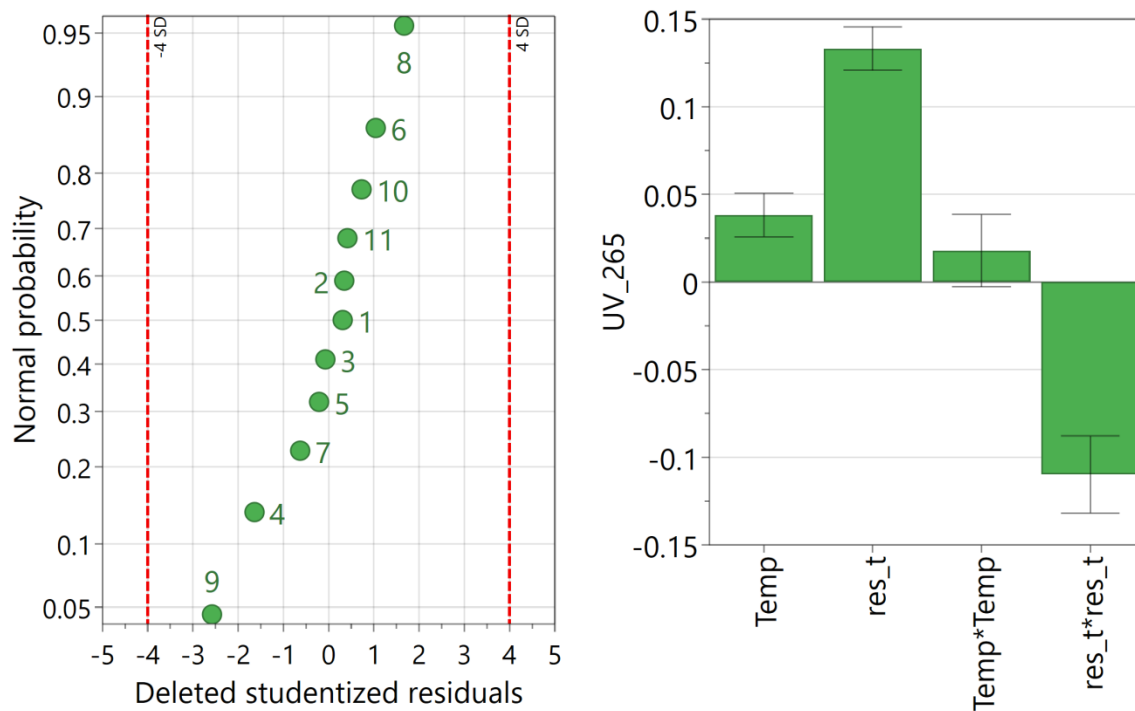
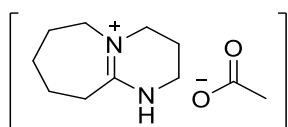


Figure 81. (Left) Residual normal probability plot for carvone semicarbazone synthesis MLR model (Right) Coefficient plot.

6.2.5 Formal [3+3] cycloaddition under flow conditions - ionic liquid preparation

DBU (8.7 mmol) was added to a two-necked round bottom flask, cooled in an ice bath, under N₂. Acetic acid (8.7 mmol) was then slowly added dropwise with stirring, and the mixture finally stirred for 2 hours. The temperature was then increased to 50 °C and the mixture was stirred for 24 hours to give a viscous yellow liquid. The characterisation data is in agreement with the published literature.¹⁷⁴

2,3,4,6,7,8,9,10-Octahydropyrimidol[1,2-a]azepinium-acetate (DBU-acetate)



Pale yellow oil; ¹H NMR ((CD₃)₂SO, 400 MHz), δ 1.53-1.68 (m, 6H, CH₂), 1.62 (s, 3H, CH₃), 1.80-1.90 (m, 2H, CH₂), 2.70-2.77 (m, 2H, CH₂), 3.21 (t, 2H, *J* = 6 Hz, CH₂), 3.41 (t, 2H, *J* = 6 Hz, CH₂), 3.48 (m, 2H, CH₂); ¹³C NMR ((CD₃)₂SO, 100 MHz), δ 19.3, 23.8, 25.1, 26.3, 28.5, 31.0, 37.7, 47.8, 53.1, 165.1, 174.2; IR (film) $\nu_{\max}/\text{cm}^{-1}$ = 1649s, 1406s, 1325s, sh.

6.2.5.1 Formal [3+3] cycloaddition under flow conditions - optimisation through box Behnken design

A solution of benzene-1,3-diol (0.11 M), 3,7-dimethylocta-2,6-dienal (0.2 M), and DBU-acetate of varying concentration, was prepared in a 1:1 (v:v) mixture of acetonitrile and toluene. The solution was pumped into a 5 mL coil of stainless steel tubing (1.0 mm I.D.) preheated to the required temperature and allowed to equilibrate while pumping solvent through. As all the experiment would be performed using temperatures substantially above the boiling points of the solvents a 250 PSI backpressure regulator was installed after the reactor coil. The entire 5 mL aliquot was collected, minus the solution remaining in the tubing before the pump head, which was then evaporated *in vacuo*. The crude mixture was re-dissolved in 5 mL of methanol and a 50 μ L aliquot diluted to 1000 μ L with methanol for analysis by HPLC (Table 15). The column used for the analysis was a 3.0 \times 30 mm, 2.7 μ m particle size poroshell C18.

Table 15. HPLC method parameters for benzopyran analysis

Flow rate (mLmin ⁻¹)	1.0
Injection volume (μ L)	5.0
Column temperature ($^{\circ}$ C)	60
Detection wavelength (nm)	254 (spectra acquired from 200 - 400)
Gradient settings, water : methanol - Initial	95 : 5
2.0 minutes	95 : 5
8.0 minutes	10 : 90
13.0 minutes	10 : 90
13.1 minutes	95 : 5
18.0 minutes	95 : 5

The 2H-benzopyran had a retention time of 8.3 minutes and the 2H,8H-benzopyran eluted at 10.4 minutes. All samples were treated in the same manner and so integrated peak areas were used as the response for the DOE study (Table 16).

Table 16. Experiments carried out for optimisation of formal [3+3] cycloaddition.

Exp. name	Run order	Catalyst (mol. %)	Temp. (°C)	Residence time (minutes)	420 nm abs. (A.U.)	2H-benzopyran peak area (mAUmin)	2H,8H-benzopyran peak area (mAUmin)
1	3	9	160	15	0.029	36.844	36.602
2	12	98	160	15	0.059	223.2	362.571
3	14	9	220	15	0.058	110.619	54.773
4	1	98	220	15	0.293	778.232	3033.98
5	6	9	190	5	0.015	15.044	11.5
6	10	98	190	5	0.062	158.435	197.832
7	7	9	190	25	0.051	136.449	113.995
8	9	98	190	25	0.287	691.283	2841.32
9	13	53	160	5	0.027	9.775	35.808
10	4	53	220	5	0.081	253.599	222.93
11	11	53	160	25	0.061	174.257	252.83
12	2	53	220	25	0.244	589.893	2152.14
13	15	53	190	15	0.092	288.462	458.276
14	5	53	190	15	0.141	242.948	454.515
15	8	53	190	15	0.119	330.09	611.699

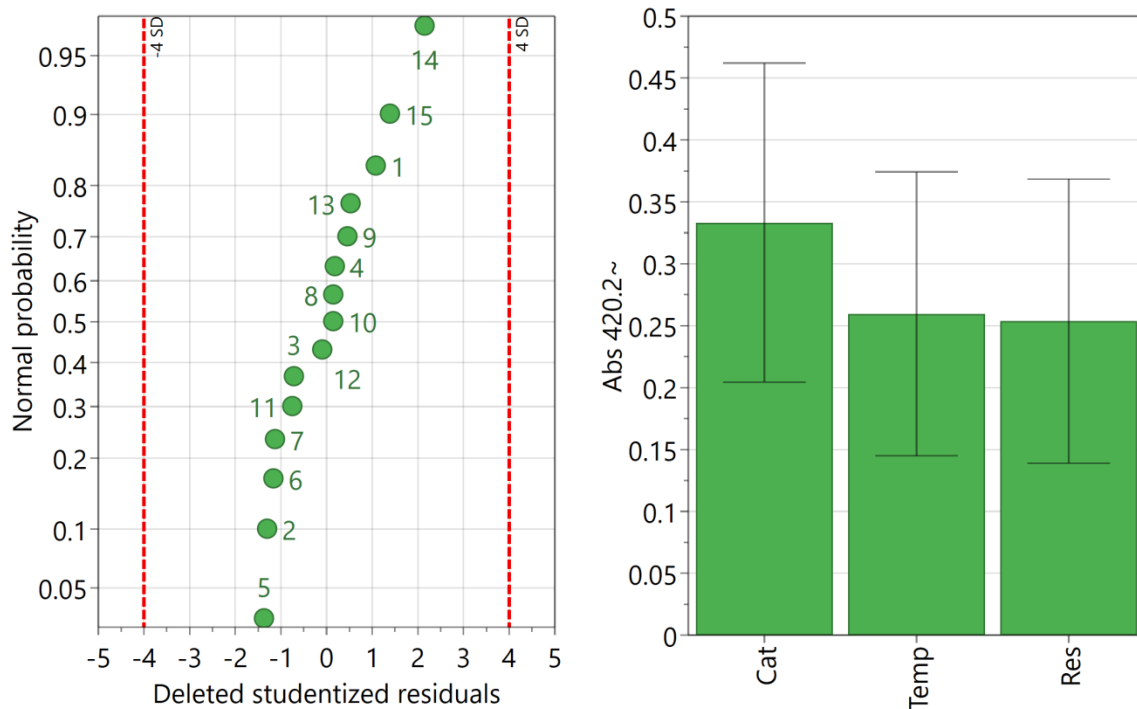


Figure 82. (Left) Residual normal probability plot for formal [3+3] visible absorbance MLR model (Right) Coefficient plot.

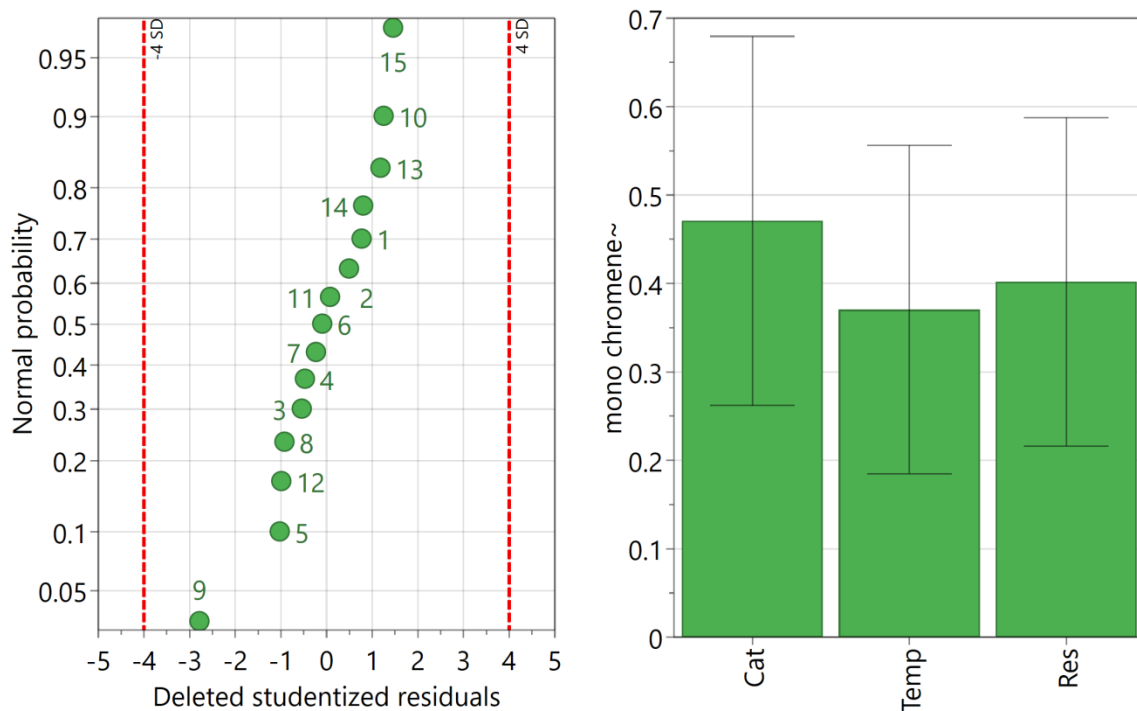


Figure 83. (Left) Residual normal probability plot for formal [3+3] mono-chromene HPLC MLR model (Right) Coefficient plot.

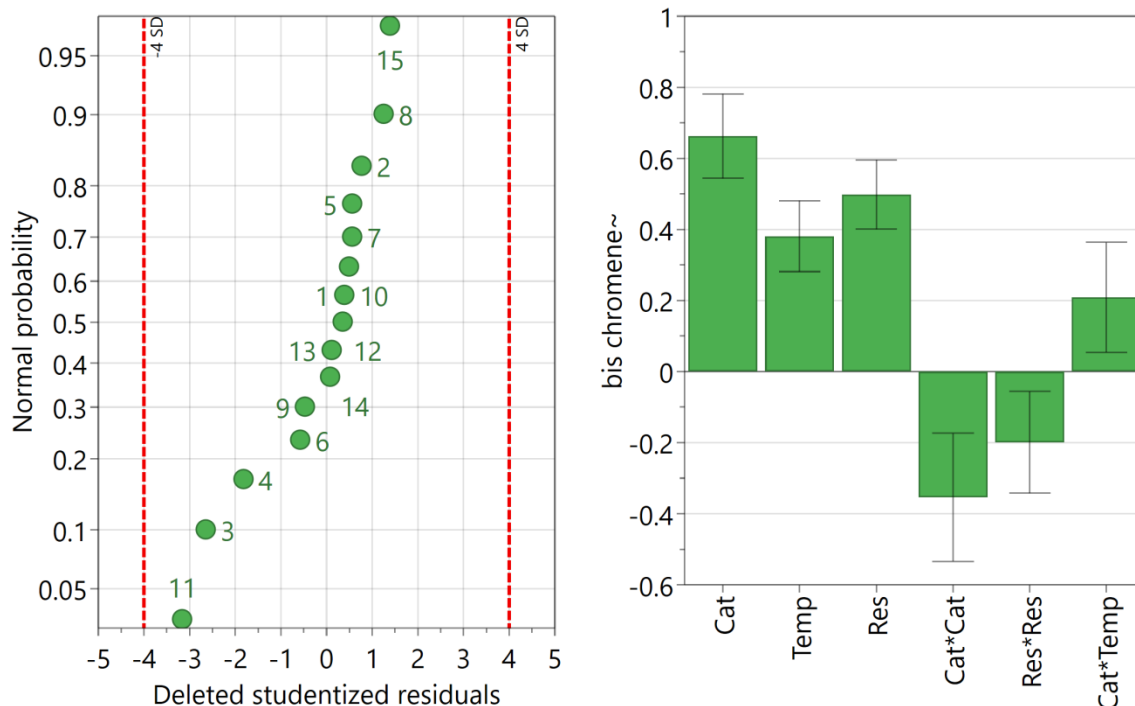
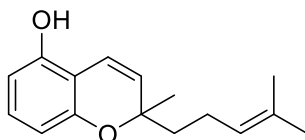


Figure 84. (Left) Residual normal probability plot for formal [3+3] bis-chromene HPLC MLR model (Right) Coefficient plot.

6.2.5.2 General procedure for the synthesis of 2H-benzopyrans

A solution of substituted dihydroxybenzene (0.1 M), an α , β -unsaturated aldehyde (0.11 M), and DBU-acetate (0.08 M), was prepared in a 1:1 (v:v) mixture of acetonitrile and toluene. The solution was pumped at 0.2 mL/min, for a residence time of 25 minutes, into a 5 mL reactor coil of stainless steel tubing (1.0 mm I.D.) preheated to 220 °C. As the synthesis uses temperatures above the boiling points of the solvents a 250 PSI backpressure regulator was installed after the reactor coil. The reactor output was collected and immediately purified by column chromatography using 9 % ethyl acetate in hexane. The characterisation data is in agreement with the published literature.^{152,175,176}

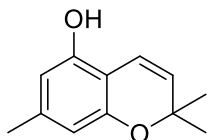
2-Methyl-2-(4-methylpent-3-en-1-yl)-2H-1-benzopyran-5-ol (18a)



Yellow oil; 0.038 g (27 %); ¹H NMR (CDCl₃, 400 MHz), δ 1.39 (s, 3H, CH₃), 1.58 (s, 3H, CH₃), 1.6-1.78 (m, 4H, CH₂), 1.66 (s, 3H, CH₃), 5.06-5.13 (m, 1H, CH), 5.55 (d, 1H, J = 9.9 Hz, CH), 6.28 (d, 1H, J = 7.4 Hz, Ar-H), 6.39 (d, 1H, J = 7.8 Hz, Ar-H), 6.66 (d, 1H, J = 9.9 Hz, CH), 6.93 (t, 1H, J = 8 Hz, Ar-H); ¹³C NMR (CDCl₃, 100 MHz), δ 17.6, 22.7, 25.7, 26.2, 41.0, 78.2, 107.5, 109.1, 109.4, 116.8,

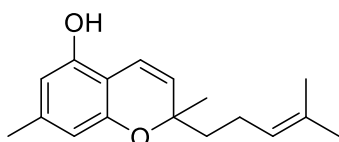
124.1, 128.2, 128.9, 131.7, 151.3, 154.3; MS (EI), m/z 244 (M^+ , 6.1 %), 161 (100); IR (film) $\nu_{\max}/\text{cm}^{-1}$ = 3391s, br, 3583s, 2969s, 2919s, 1614m, 1583m, 1461s.

2,2,7-Trimethyl-2H-1-benzopyran-5-ol (15)



Off white solid; 0.039 g (49 %); mp 109-112 °C (EtOAc); ^1H NMR (CDCl_3 , 400 MHz), δ 1.42 (s, 3H, CH_3), 2.20 (s, 3H), CH_3 , 4.99 (s (br), 1H, OH), 5.53 (d, 1H, $J = 9.9$ Hz, CH), 6.13 (s, 1H, Ar-H), 6.25 (s, 1H, Ar-H), 6.59 (d, 1H, $J = 9.9$ Hz, CH); ^{13}C NMR (CDCl_3 , 100 MHz), δ 21.4, 21.7, 75.9, 106.9, 108.5, 109.9, 116.3, 128.2, 139.6, 151.1, 153.8; MS (EI), m/z 176 (12 %), 175 (100), 41 (7.2); IR (film) $\nu_{\max}/\text{cm}^{-1}$ = 3366s, br, 2980m, 1624s, 1579s, 1454m.

2,7-Dimethyl-2-(4-methylpent-3-en-1-yl)-2H-1-benzopyran-5-ol (17)



Yellow oil; 0.049 g (38 %); ^1H NMR (CDCl_3 , 400 MHz), δ 1.37 (s, 3H, CH_3), 1.58 (s, 3H, CH_3), 1.70-1.77 (m, 2H, CH_2), 2.07-2.13 (m, 2H, CH_2), 2.19 (s, 3H, CH_3), 5.06-5.12 (m, 1H, CH), 5.23 (s (br), 1H, OH), 5.48 (d, 1H, $J = 9.9$ Hz, CH), 6.12 (s, 1H, Ar-H), 6.23 (s, 1H, Ar-H), 6.62 (d, 1H, 9.9 Hz, CH); ^{13}C NMR (CDCl_3 , 100 MHz), δ 17.6, 21.5, 22.7, 25.6, 26.2, 41.0, 78.1, 106.8, 108.3, 109.7, 116.8, 124.2, 127.0, 131.6, 139.5, 151.2, 154.0; MS (EI), m/z 258 (M^+ , 6 %), 175 (100); IR (film) $\nu_{\max}/\text{cm}^{-1}$ = 3391s, br, 2969s, 2923s, 1624s, 1579m, 1450s.

6.2.6 Simplex optimisation for the synthesis of 1,3,4-Trifluoro-5-methyl-5H-benzo[b]pyrido[4,3-e][1,4]oxazine

The synthesis was performed using the Uniqsis Flowsyn fitted with a stainless steel SLM printed reactor with an internal volume of 8.6 mL, secured to the chip heater of the instrument. A solution of 2-(methylamino)-phenol (0.1 M) with triethylamine (0.4 M) was prepared in acetonitrile. A separate solution of pentafluoropyrindine (0.1 M) was prepared in acetonitrile. The solutions were pumped separately at half the total required flow rate each, meeting at a T-piece shortly before the AM reactor. A back pressure regulator of 200 PSI was installed after the AM reactor outlet.

Solutions were allowed to pump until 1.5 reactor volumes had passed through the reactor. At this time a 1 in 100 dilution with acetonitrile was made and the absorbance at 330 nm recorded using a 10 mm

path length flow cell as well as HPLC analysis being performed (Table 15). The absorbance value was used to calculate the next simplex experiment (Table 16) and the new settings entered. The system was allowed to equilibrate at these new values, switching the system to pump solvent only to conserve reagent, then pumping reagents to perform the next experiment.

Table 15. HPLC method for the analysis of simplex experiments.

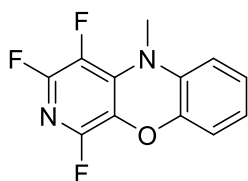
Flow rate (mLmin ⁻¹)	0.7
Injection volume (μL)	5.0
Column temperature (°C)	40
Detection wavelength (nm)	254 (spectra acquired from 200 - 400)
Mobile phase composition (methanol : water)	50 : 50
Stop time	25

Table 16. Simplex experiments performed for benzopyridoxazine optimisation

Simplex reaction	Temperature (°C)	Flow rate (mL.min ⁻¹)	330 nm absorbance (A.U.)
1	107	0.72	0.415
2	121	0.72	0.587
3	114	0.88	0.463
4	128	0.88	0.525
5	135	0.72	0.712
6	128	0.56	0.697
7	142	0.56	0.820
8	149	0.72	0.833
9	156	0.56	1.100
10	163	0.72	1.110
11	170	0.56	1.185
12	177	0.72	1.143
13	177	0.4	1.194
14	163	0.4	1.209
15	170	0.24	1.238
16	156	0.24	1.238

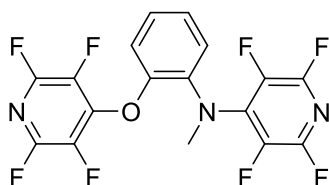
Simplex reaction 9 was run for longer to collect material for characterisation. 44 mL of reactor output was evaporated *in vacuo*, dissolved in 20 mL ethyl acetate, and washed with 2 × 10 mL water. The aqueous portions were combined and washed with 20 mL ethyl acetate. The organic portions were combined, washed with 10 mL brine and dried with MgSO₄ before filtration. The crude mixture was purified by column chromatography on silica using 5 % ethyl acetate in hexane. The characterisation data for **21a** is in agreement with the published literature.¹⁵⁴

1, 3, 4-Trifluoro-5-methyl-5H-benzo[b]pyrido[4,3-e][1,4]oxazine (21a)



Off white solid; m.p. 151-153 °C (lit. 150-152 °)¹⁵⁴; ¹H NMR (CDCl₃, 400 MHz), δ 3.40 (d, 3H, *J* = 4.4 Hz, CH₃), 6.70 (dd, 1H, *J* = 7.9, 1.4 Hz, Ar-H), 6.80 (dd, 1H, *J* = 7.9, 1.6 Hz, Ar-H), 6.87 (td, 1H, *J* = 7.7, 1.5 Hz, Ar-H), 6.96 (td, 1H, *J* = 7.7, 1.5 Hz, Ar-H); ¹³C NMR (CDCl₃, 100 MHz), δ 35.6 (d, *J* = 11.9 Hz), 113.5, 116.1, 124.1, 124.8, 126.3 (dd, *J* = 29.2, 5.3 Hz), 130.6 (ddd, *J* = 213, 31.7, 5.1 Hz), 132.4, 136.5 (m), 142.7 (ddd, *J* = 235.3, 17.0, 1.8 Hz), 145.2 (dt, *J* = 236.9, 16.3 Hz), 145.3; ¹⁹F NMR (CDCl₃, C₆H₅CF₃, 376 MHz), δ -163.20 (m, 1F), -96.07 (dd, 1F, *J* = 22.8, 14.6), -93.99 (dd, 1F, *J* = 23.3, 14.6); MS (EI), *m/z* 253 (10.8 %), 252 (M⁺, 77.8), 238 (12.9), 237 (100), 205 (6.3), 126 (6.7); IR (film) $\nu_{\max}/\text{cm}^{-1}$ = 1650m, 1499s, 1464s, 1289s, 1192s.

2,3,5,6-Tetrafluoro-N-methyl-N-(2-((perfluoropyridin-4-yl)oxy)phenyl)pyridin-4-amine (21b)



Colourless oil; ¹H NMR (CDCl₃, 400 MHz) δ 3.53 (t, 3H, *J* = 2.5 Hz, CH₃), 7.08 (d, 1H, *J* = 7.8 Hz, Ar-H), 7.24 (td, 1H, *J* = 7.4, 2.1, Ar-H), 7.29 (td, 1H, *J* = 7.8, 2.1, Ar-H), 7.5 (dd, 1H, *J* = 7.8, 2.1, Ar-H); ¹⁹F NMR (CD₃OD, C₆H₅CF₃, 376 MHz) δ -158.4 (m, 2F), -154.8 (m, 2F), -96.0 (m, 2F), -91.7 (m, 2F); MS (EI), *m/z* 421 (M⁺, 100 %), 255 (59), 177 (29), 150 (26), 138 (53), 105 (16), 100 (70).

6.2.7 Synthesis of 1, 3, 4-trifluoro-5-methyl-5H-benzo[b]pyrido[4,3-e][1,4]oxazine using DBU

The synthesis was performed using the Uniqsis Flowsyn fitted with a stainless steel SLM printed reactor with an internal volume of 8.6 mL, secured to the chip heater of the instrument. A solution of 2-(methylamino)-phenol (0.1 M) with DBU (0.22 M) was prepared in acetonitrile. A solution of pentafluoropyridine (0.1 M) was prepared in acetonitrile. The solutions were pumped separately at 0.07 mLmin⁻¹ each for a residence time of 36 minutes, meeting at a T-piece shortly before the AM reactor which was held at 170 °C. A back pressure regulator of 200 PSI was installed after the AM reactor outlet. At 1 reactor volume aliquots were collected, diluted 100 fold with acetonitrile and analysed by UV spectroscopy with a 10 mm flow cell.

6.2.8 General procedure for the synthesis of 1-Ethyl-4-phenyl-1*H*-1,2,3-triazole through flow CuAAC - DOE study

Solutions of phenylacetylene (0.125 M) and iodoethane (0.25 M) were prepared in DMF. A solution of sodium azide (0.25 M) was prepared in DMF : H₂O (4 : 1). Equal aliquots of these solutions were then mixed and pumped through the copper reactor (R3) at the required temperature and residence time (Table 17). A syringe pump was used to pump the reagent to ensure accurate flow rates and more reproducible experiments. A sample of the reactor output was sampled at 1.5 reactor volumes and analysed by HPLC (Table 18) to determine the percentage peak area ratio of the product to the phenylacetylene.

Table 17. Experiments performed for the optimisation of the CuAAC synthesis.

Experiment name	Run order	Temperature (°C)	Residence time (minutes)	Product peak area (%)
1	4	100	5	9.7
2	2	125	5	22.4
3	3	145	5	26.3
4	5	100	10	16.3
5	11	125	10	33.2
6	9	145	10	59.6
7	6	100	16.7	30.8
8	1	125	16.7	32.0
9	10	145	16.7	51.0
10	7	125	10	32.7
11	8	125	10	46.2

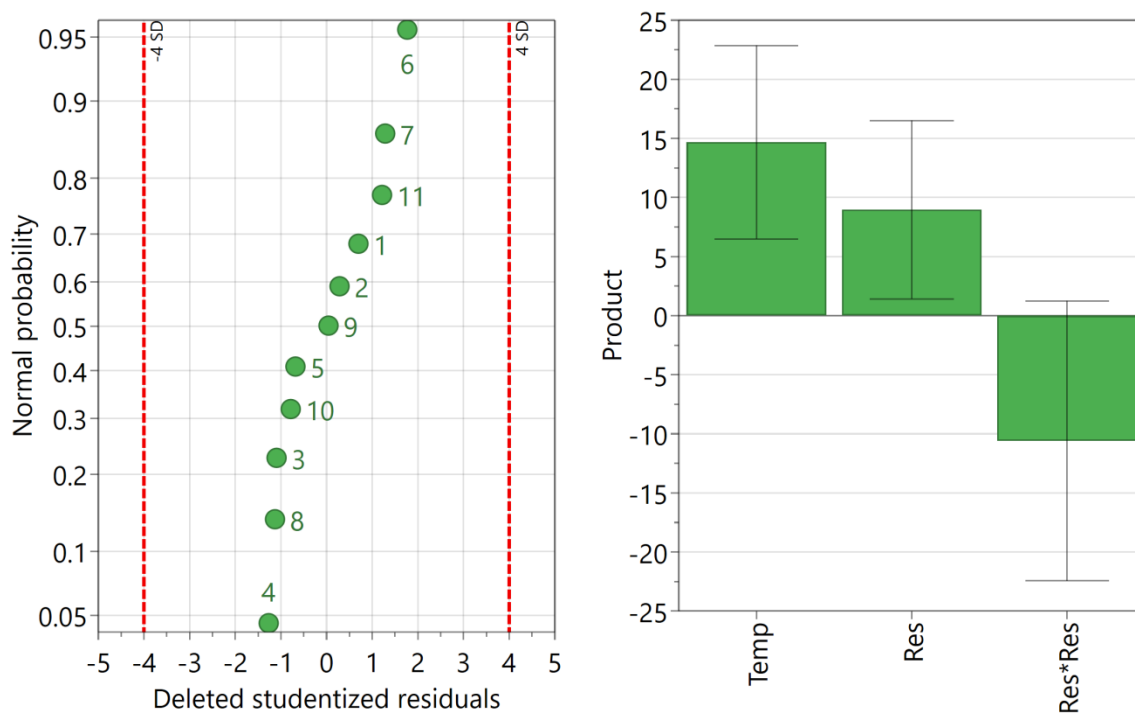


Figure 85. (Left) Residual normal probability plot for CuAAC triazole MLR model (Right) Coefficient plot.

Table 18. HPLC method for the analysis of 1-Ethyl-4-phenyl-1*H*-1,2,3-triazole prepared for optimisation study

Flow rate (mLmin ⁻¹)	1.5
Injection volume (μL)	5.0
Column temperature (°C)	40
Detection wavelength (nm)	254 (spectra acquired from 200 - 400)
Mobile phase composition (methanol : water)	50 : 50
Stop time	10

Analysis of three repeated standard injections of the iodoethane and phenylacetylene starting materials gave a % RSD for the peak areas of 0.15 and 0.20 % respectively, demonstrating excellent reproducibility and confirming the suitability of the method.

ICP-OES analysis of CuAAC solutions

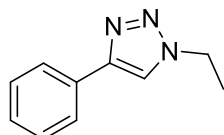
Standard copper solutions were prepared from a Spex Certiprep standard solution (1000 mg/L Cu(I) in 5 % HNO₃) and diluted in a 5 % DMF in 2 % HNO₃ (aq) solution. The calibration samples were prepared from 0.1 to 150 mg/L and the R² value for the calibration was calculated to be 0.9995 over the entire range. Samples were similarly prepared in the 5 % DMF in 2 % HNO₃ (aq) solution used for the standard preparation and diluted 20 fold. Analysis of the solutions was performed with an iCAP 6000 ICP-OES controlled through iTEVA Analyst software (Thermo Scientific).

6.2.9 General procedure for the synthesis of 1,4-disubstituted-1,2,3-triazoles

The copper reactor (R3) was mounted to the chip heater of the Uniqsis Flowsyn. The reactor was washed with water before 36 % (aq.) hydrogen peroxide was infused slowly into the reactor and left to stand for approximately 5 minutes. A second hydrogen peroxide infusion was then carried out and the reactor left to stand for a further 5 minutes before being flushed with water to ensure no peroxide was remaining. DMF was then pumped through the reactor *via* syringe pump while equilibrating at 145 °C, once this was reached the reagent solution was pumped through from a second syringe pump, connected by a mixing tee, and a sample for HPLC was taken at 1.5 reactor volumes. The HPLC method was similar to that used for the analysis of the DOE optimisation samples (Table 18) except for a modification to the mobile phase composition in some cases to 60 : 40, or 70 : 30, methanol : water, to ensure full resolution of the triazole products from residual starting material.

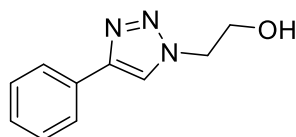
DMF was then pumped through to eject the reagent from the reactor. The reaction solution was diluted with 10 mL ethyl acetate before washing with 10 mL water and brine (3 × 10 mL) to remove residual DMF. The organic phase was dried over MgSO₄ before filtration and evaporated to dryness *in vacuo*. Purification was by column chromatography, using varying mixtures of hexane and ethyl acetate. The characterisation data is in agreement with the published literature.^{177–182}

1-Ethyl-4-phenyl-1H-1,2,3-triazole (34)



Yellow solid, m.p. 58 °C (lit. 61-62 °C)¹⁷⁷; ¹H NMR (CDCl₃, 400 MHz) δ 1.61 (t, 3H, *J* = 7.4 Hz, CH₃), 4.47 (q, 2H, *J* = 7.4 Hz, CH₂), 7.33-7.35 (m, 1H, Ar-H), 7.40-7.44 (m, 2H, Ar-H), 7.76 (s, 1H, Ar-H), 7.82-7.84 (m, 2H, Ar-H); ¹³C NMR (CDCl₃, 100 MHz) δ 15.8, 45.4, 119.0, 125.9, 128.3, 129.0, 130.9, 148.1; HRMS (ESI-orbi): *m/z* calculated for C₁₀H₁₁N₃Na [M+Na]⁺ 196.0851; found: 196.0844; IR (film) ν_{max}/cm⁻¹ = 3122w, 2924w, 1647w, 1466m, 1262m.

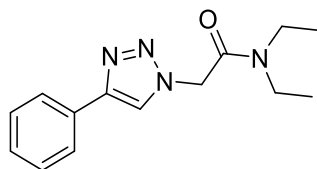
2-(4-Phenyl-1H-1,2,3-triazol-1-yl)ethan-1-ol (35)



Off white solid, m.p. 86-89 °C (lit. 89-92 °C)¹⁷⁸; ¹H NMR (CDCl₃, 400 MHz) δ 4.14 (t, 2H, *J* = 4.9 Hz, CH₂), 4.53 (t, 2H, *J* = 4.9 Hz, CH₂), 7.33 (t, 1H, *J* = 7.4 Hz, Ar-H), 7.40 (t, 2H, *J* = 7.8 Hz, Ar-H), 7.76 (d, 2H, *J* = 7.8 Hz, Ar-H), 7.86 (s, 1H, CH); ¹³C NMR (CDCl₃, 100 MHz) δ 52.9, 61.5, 121.1, 125.8,

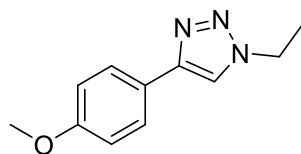
128.4, 129.0, 130.5, 147.8; HRMS (ESI-orbi): m/z calculated for $C_{10}H_{11}N_3ONa$ $[M+Na]^+$ 212.0800; found m/z 212.0792; IR (film) ν_{max}/cm^{-1} = 2962w, 1661s, 1464w, 1265s.

N, N-diethyl-2-(4-phenyl-1H-1,2,3-triazol-1-yl)acetamide (36)



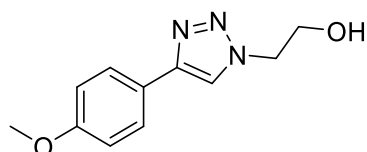
Off white solid, m.p. 124-126 °C; 1H NMR ($CDCl_3$ 400 MHz) δ 1.15 (t, 3H, J = 7.2 Hz, CH_3), 1.26 (t, 3H, J = 7.0 Hz, CH_3), 3.40-3.47 (m, 4H, CH_2), 5.24 (s, 2H, CH_2), 7.30-7.34 (m, 1H, Ar-H), 7.40-7.44 (m, 2H, Ar-H), 7.82-7.86 (m, 2H, Ar-H), 8.04 (s, 1H, CH); ^{13}C NMR ($CDCl_3$ 100 MHz) δ 13.0, 14.6, 41.2, 42.2, 51.1, 121.6, 125.9, 128.3, 129.0, 130.7, 148.2, 164.2; HRMS (ESI-orbi): m/z calculated for $C_{14}H_{18}N_4ONa$ $[M+Na]^+$ 281.1378; found m/z 281.1369; IR (film) ν_{max}/cm^{-1} = 3129w, 2971m, 2922m, 1651s, 1474sm 1263s, 1082s.

1-Ethyl-4-(4-methoxyphenyl)-1H-1,2,3-triazole (40)



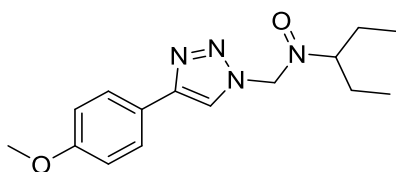
Off white solid, m.p. 96-100 °C; 1H NMR ($CDCl_3$ 400 MHz) δ 1.59 (t, 3H, J = 7.4 Hz, CH_3), 3.84 (s, 3H, CH_3), 4.44 (q, 2H, J = 7.4 Hz, CH_2), 6.95 (d, 2H, J = 8.8 Hz, Ar-H), 7.67 (s, 1H, CH), 7.75 (d, 2H, J = 8.8 Hz, Ar-H); ^{13}C NMR ($CDCl_3$ 100 MHz) δ 15.8, 45.5, 55.5, 114.4, 118.3, 127.2, 147.9, 159.7; IR (film) ν_{max}/cm^{-1} = 1033 (s), 1251 (s), 1461 (s), HRMS (ESI-orbi): m/z calculated for $C_{11}H_{13}N_3ONa$ $[M+Na]^+$ 226.0956; found m/z 226.0949; IR (film) ν_{max}/cm^{-1} = 3133m, 2942m, 2840m, 1619s, 1561s, 1501s, 1462s, 1251s.

2-(4-(Methoxyphenol)-1H-1,2,3-triazol-1-yl)ethan-1-ol (41)



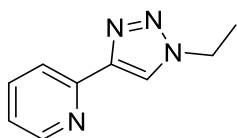
Off white solid, m.p. 107-110 °C (lit. 112-113 °C)¹⁷⁸; 1H NMR ($CDCl_3$ 400 MHz) δ 3.84 (s, 3H, CH_3), 4.13 (t, 2H, J = 4.9 Hz, CH_2), 4.50 (t, 2H, J = 4.9 Hz, CH_2), 6.93 (d, 2H, J = 8.7 Hz, Ar-H), 7.67 (d, 2H, J = 8.7 Hz, Ar-H), 7.74 (s, 1H, CH); ^{13}C NMR ($CDCl_3$ 100 MHz) δ 52.9, 55.5, 61.5, 114.4, 120.3, 123.2, 127.1, 147.6, 159.8; HRMS (ESI-orbi): m/z calculated for $C_{11}H_{13}N_3O_2Na$ $[M+Na]^+$ 242.0905; found m/z 242.0897; IR (film) ν_{max}/cm^{-1} = 1641m, 1459w, 1263m.

N, N-diethyl-2-(4-(4-methoxyphenyl)-1H-1,2,3-triazol-1-yl)acetamide (42)



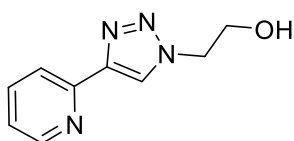
Off white solid, m.p. 101-102 °C; ¹H NMR (CDCl₃ 400 MHz) δ 1.15 (t, 3H, *J* = 7.1 Hz, CH₃), 1.25 (t, 3H, *J* = 7.2 Hz, CH₃), 3.43 (q, 4H, *J* = 7.0 Hz, CH₂), 3.83 (s, 3H, CH₃), 5.22 (s, 2H, CH₂), 6.95 (d, 2H, *J* = 8.8 Hz, Ar-H), 7.76 (d, 2H, *J* = 8.8 Hz, Ar-H), 7.92 (s, 1H, CH); ¹³C NMR (CDCl₃ 100 MHz) δ 13.0, 14.6, 41.2, 42.2, 51.2, 55.5, 114.4, 120.8, 123.4, 127.3, 148.0, 159.8, 164.2; HRMS (ESI-orbi): *m/z* calculated for C₁₅H₂₀N₄O₃Na [M+Na]⁺ 311.1484; found *m/z* 311.1474; IR (film) ν_{max}/cm⁻¹ = 3135w, 3040w, 1654m, 1467m.

2-(1-Ethyl-1H-1,2,3-triazol-4-yl)pyridine (37)



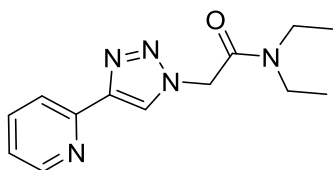
Pale yellow oil, ¹H NMR (CDCl₃ 400 MHz) δ 1.60 (t, 3H, *J* = 7.4 Hz, CH₃), 4.48 (q, 2H, *J* = 7.4 Hz, CH₂), 7.20-7.24 (m, 1H, Ar-H), 7.75-7.80 (m, 1H, Ar-H), 8.15 (s, 1H, CH) 8.15-8.20 (m, 1H, Ar-H), 8.55-8.59 (m, 1H, Ar-H); ¹³C NMR (CDCl₃ 100 MHz) δ 15.6, 45.7, 12.4, 121.5, 123.0, 137.2, 148.6, 149.5, 150.5; HRMS (ESI-orbi): *m/z* calculated for C₉H₁₀N₄Na [M+Na]⁺ 197.0803; found *m/z* 197.0797; IR (film) ν_{max}/cm⁻¹ = 2987w, 1602m, 1475w, 1422m.

2-(4-(Pyridine-2-yl)-1H-1,2,3-triazol-1-yl)ethan-1-ol (38)



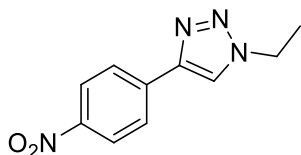
Off white solid, m.p. 102-103 °C (lit. 103°C)¹⁸¹; ¹H NMR (CDCl₃ 400 MHz) δ 4.13 (t, 2H, *J* = 4.9 Hz, CH₂), 4.56 (t, 2H, *J* = 4.9 Hz, CH₂), 7.21 (m, 1H, Ar-H), 7.75 (m, 1H, Ar-H), 8.07 (m, 1H, Ar-H), 8.30 (s, 1H, CH), 8.46 (m, 1H, Ar-H); ¹³C NMR (CDCl₃ 100 MHz) δ 53.2, 61.3, 120.5, 123.1, 123.7, 137.4, 147.8, 149.2, 150.1; HRMS (ESI-orbi): *m/z* calculated for C₉H₁₀N₄ONa [M+Na]⁺ 213.0752; found *m/z* 213.0745; IR (film) ν_{max}/cm⁻¹ = 3133w, 2925m, 2856m, 1602s, 1420m, 1363m.

N, N-diethyl-2-(4-(pyridine-2-yl)-1H-1,2,3-triazol-1-yl)acetamide (39)



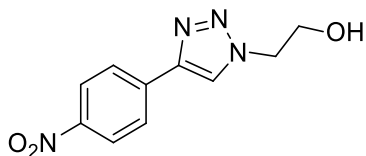
Off white solid, m.p. 108-111 °C; ¹H NMR (CDCl₃ 400 MHz) δ 1.14 (t, 3H, *J* = 7.1 Hz, CH₃), 1.26 (t, 3H, *J* = 7.2 Hz, CH₃), 3.42 (m, 4H, CH₂), 5.25 (s, 2H, CH₂), 7.19-7.23 (m, 1H, Ar-H), 7.74-7.78 (m, 1H, Ar-H), 8.14 (d, 1H, *J* = 7.9 Hz, Ar-H), 8.35 (s, 1H, CH), 8.57 (m, 1H, Ar-H); ¹³C NMR (CDCl₃ 100 MHz) δ 13.0, 14.6, 41.2, 42.1, 51.2, 120.5, 123.0, 124.1, 137.0, 148.8, 149.6, 150.4, 163.9; HRMS (ESI-orbi): *m/z* calculated for C₁₃H₁₇N₅O₂Na [M+Na]⁺ 282.1331; found *m/z* 282.1320; IR (film) ν_{max}/cm⁻¹ = 3084w, 2975w, 2932w, 1663s, 1454m.

1-Ethyl-4-(4-nitrophenyl)-1H-1,2,3-triazole (43)



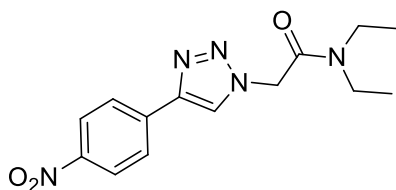
Yellow solid, m.p. 134-136 °C; ¹H NMR (CDCl₃ 400 MHz) δ 1.64 (t, 3H, *J* = 7.4 Hz, CH₃), 4.51 (q, 2H, *J* = 7.4 Hz, CH₂), 7.91 (s, 1H, CH), 8.01 (d, 2H, *J* = 8.9 Hz, Ar-H), 8.30 (d, 2H, *J* = 8.9 Hz, Ar-H); ¹³C NMR (CDCl₃ 100 MHz) δ 15.7, 45.8, 120.6, 124.5, 126.3, 137.2, 145.9, 147.5; HRMS (ESI-orbi): *m/z* calculated for C₁₀H₁₁N₄O₂ [M+H]⁺ 219.0877; found *m/z* 219.0876; IR (film) ν_{max}/cm⁻¹ = 2922m, 1605m, 1512s, 1349m, 1337m.

2-(4-(4-Nitrophenyl)-1H-1,2,3-triazol-1-yl)ethan-1-ol (44)



Yellow solid, m.p. 150-151 °C; ¹H NMR ((CD₃)₂SO, 400 MHz) δ 3.86 (t, 2H, *J* = 5.4 Hz, CH₂), 4.50 (t, 2H, *J* = 5.2 Hz, CH₂), 5.14 (s, br, 1H, OH), 8.16 (d, 1H, *J* = 9.0 Hz, Ar-H), 8.34 (d, 1H, *J* = 9.0 Hz), 8.90 (s, 1H, CH); ¹³C NMR ((CD₃)₂SO 100 MHz) δ 52.7, 59.7, 124.0, 124.4, 125.9, 137.4, 144.2, 146.5; HRMS (ESI-orbi): *m/z* calculated for C₁₀H₁₁N₄O₃ [M+H]⁺ 235.0826; found *m/z* 235.0824; IR (film) ν_{max}/cm⁻¹ = 1643m, 1512m, 1346m.

N, N-diethyl-2-(4-(4-nitrophenyl)-1H-1,2,3-triazol-1-yl)acetamide (45)



Yellow Solid, m.p. 167-169 °C; ¹H NMR (CDCl₃, 400 MHz) δ 1.17 (t, 3H, *J* = 7.1 Hz, CH₃), 1.31 (t, 3H, *J* = 7.2 Hz, CH₃), 3.41-3.50 (m, 4H, CH₂), 8.02 (d, 2H, *J* = 9.0 Hz, Ar-H), 8.21 (s, 1H, CH), 8.29 (d, 2H, *J* = 9.0 Hz, Ar-H); ¹³C NMR (CDCl₃, 100 MHz) δ 12.8, 14.4, 41.2, 42.0, 50.8, 123.1, 124.3, 126.2, 136.9, 145.8, 147.3, 163.6; HRMS (ESI-orbi): *m/z* calculated for C₁₄H₁₇N₅O₃Na [M+Na]⁺ 326.1229; found *m/z* 326.1219; IR (film) $\nu_{\max}/\text{cm}^{-1}$ = 2922m, 1642s, 1608m, 1518s, 1352m.

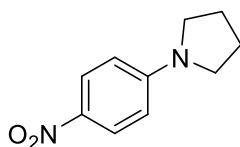
6.2.10 Synthesis of N-benzylaniline through a modified Ullmann coupling

Iodobenzene (5 mmol), benzylamine (6 mmol) and tetrabutylammonium acetate (5.5 mmol) were dissolved in 10 mL of acetonitrile. The UAM copper reactor (R3) was mounted to the chip heater of the Uniqsis flowsyn and pre heated to 75 °C with acetonitrile flowing through. The reagent solution was pumped at 0.01 mL/min for a residence time of 100 minutes. The reactor output was collected and evaporated to dryness *in vacuo* before 10 mL of dichloromethane was added. The organic was washed with 2 x 10 mL water; aqueous layers were combined and washed with 10 mL of dichloromethane. The organic layers were combined and washed with 10 mL brine and dried over MgSO₄ before filtration. The crude mixture was analysed by NMR to estimate the conversion, the final product was not isolated.

6.2.11 Synthesis of 1-(4-Nitrophenyl)pyrrolidine through a modified Ullmann coupling

4-Nitro-iodobenzene (5 mmol), pyrrolidine (6 mmol) and tetrabutylammonium acetate (5.5 mmol) were dissolved in 10 mL DMF. The UAM copper reactor (R3) was mounted to the chip heater of the Uniqsis flowsyn and pre heated to 145 °C with DMF flowing through. The reagent solution was pumped at 0.022 mL/min for a residence time of 45 minutes. The reactor output was collected and evaporated to dryness *in vacuo* before 10 mL of dichloromethane was added. The organic was washed with 2 x 10 mL water; aqueous layers were combined and washed with 10 mL of dichloromethane. The organic layers were combined and washed with 10 mL brine and dried over MgSO₄ before filtration, evaporated *in vacuo* and purified by column chromatography with 9 % ethyl acetate in hexane. The characterisation data are in agreement with the published literature.¹⁸³

1-(4-Nitrophenyl)pyrrolidine (26)

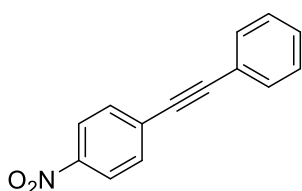


Yellow solid; m.p. 159-162 °C (lit. 165-167 °C)¹⁸³; ¹H NMR (CDCl₃, 400 MHz) δ 2.05-2.10 (m, 4H, CH₂), 3.38-3.43 (m, 4H, CH₂), 6.47 (d, 2H, *J* = 9.0 Hz, Ar-H) 8.12 (d, 2H, *J* = 9.0 Hz, Ar-H); ¹³C NMR (CDCl₃, 100 MHz) δ 25.4, 47.9, 110.4, 126.3, 136.5, 151.8; HRMS (ESI-orbi): *m/z* calculated for C₁₀H₁₂N₂O₂Na [M+Na]⁺ 215.0796; found *m/z* 215.0790; IR (film) $\nu_{\max}/\text{cm}^{-1}$ = 2921w, 2859w, 1609m, 1466m, 1323s.

6.2.12 Synthesis of 1-Nitro-4-(phenylethynyl)-benzene through a Castro-Stephens coupling

4-Nitro-iodobenzene (5 mmol), phenylacetylene (6 mmol) and tetrabutylammonium acetate (5.5 mmol) were dissolved in 10 mL DMF. The UAM copper reactor (R3) was mounted to the chip heater of the Uniqsis flowsyn and pre heated to 145 °C with DMF flowing through. The reagent solution was pumped at 0.022 mL/min for a residence time of 45 minutes. The reactor output was collected and evaporated to dryness *in vacuo* before 10 mL of dichloromethane was added. The organic portion was washed with 2 x 10 mL water; aqueous layers were combined and washed with 10 mL of dichloromethane. The organic layers were combined and washed with 10 mL brine and dried over MgSO₄ before filtration, evaporated *in vacuo* and purified by column chromatography with 9 % ethyl acetate in hexane. The characterisation data are in agreement with the published literature.¹⁸⁴

1-Nitro-4-(phenylethynyl)-benzene (47)



Yellow solid, m.p. 109-113 °C (lit. 121-122 °C)¹⁸⁴; ¹H NMR (CDCl₃, 400 MHz) δ 7.38-7.41 (m, 3H, Ar-H), 7.55-7.58 (m, 2H, Ar-H), 7.66 (d, 2H, *J* = 8.0 Hz, Ar-H), 8.23 (d, 2H, *J* = 8.0 Hz, Ar-H); ¹³C NMR (CDCl₃, 100 MHz) δ 87.5, 94.7, 122.1, 123.6, 128.5, 129.3, 130.2, 131.8, 132.2, 146.9; MS (EI) *m/z*, 223 (M⁺, 100 %), 193 (74), 176 (96); IR (film) $\nu_{\max}/\text{cm}^{-1}$ = 2217w, 1593w, 1510s, 1346s;

6.2.13 Procedure for the synthesis of 1-(tert-butyl) 3-methyl 4-(trifluoromethyl)-1H-pyrrole-1,3-dicarboxylate through flow photochemistry - automated DOE

Solutions were prepared in acetonitrile that had been dried over molecular sieves (4Å) and degassed *via* sonication and N₂ sparging. Solution A was prepared to contain 1-(tert-butyl)-3-methyl-1H-pyrrole-1,3-dicarboxylate (0.4 M), Ru(bpy)₃Cl₂·6H₂O (0.004 M), pyridine-N-oxide (0.4 M) and α,α,α -trifluorotoluene (0.2 M). Solution B contained trifluoroacetic anhydride (0.44 M) and α,α,α -trifluorotoluene (0.2 M).

Solutions A and B were pumped via individual syringe pumps, meeting at a T-piece immediately before the reactor coil (0.8 mm I.D. PTFE, 0.5 mL). The LED source was a Kessil A160 WE set to maximum intensity and maximum 'blue', and positioned approximately 2" from the reactor coil. The reactor coil was arranged in a flat coil of increasing diameter to maximise the irradiated area, and was connected to a glass flow cell carefully aligned within the benchtop NMR spectrometer, filling from the bottom of the flow cell.

The automated DOE was started in MATLAB using a custom function, running a series of experiments in a random order to complete a full factorial DOE list (Table 19). NMR spectra were matched to automatically recorded times that matched the end of each experiment. The function text is in the Appendix. Combined solutions were evaporated to dryness *in vacuo* and purified by column chromatography using 20 % ethyl acetate in hexane. The characterisation data are in agreement with published literature.¹⁶⁸

Table 19. Full factorial experiments performed to optimise the trifluoromethylation of 1-(tert-butyl)-3-methyl-1H-pyrrole-1,3-dicarboxylate - 2 pump system. Experiments marked with '*' were not included in the final model.

Experiment name	Run order	TFAA equivalents	Residence time (minutes)	% Yield
1	2	2.98	2.99	44.6
2	7	1	1	35.1
3	4	0.99	2.99	42.3
4	9	3	1	66.9
5	6	3.03	2	57.8
6	5	2.01	2	45.9
7	3	1.99	1	48.7
8*	8	1.98	2.99	54.8
9	1	1	2	35.2

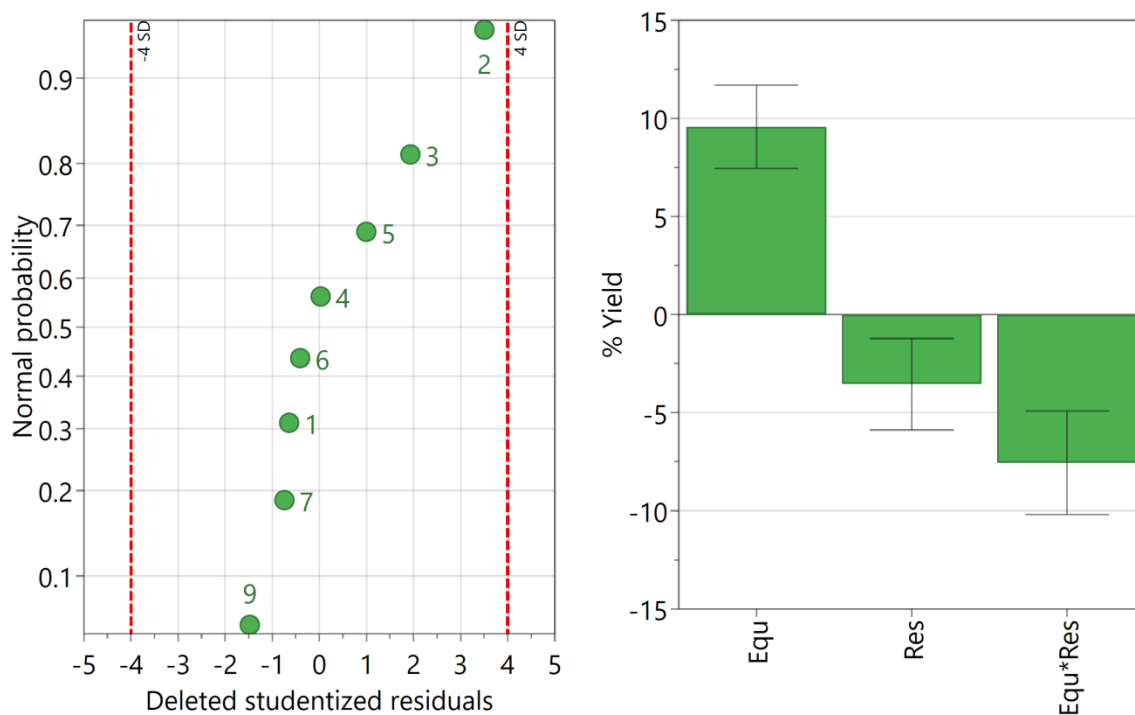
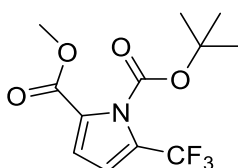


Figure 86. (Left) Residual normal probability plot for trifluoromethylation MLR model (Right) Coefficient plot.

1-(Tert-butyl) 3-methyl 4-(trifluoromethyl)-1H-pyrrole-1,3-dicarboxylate (52)



Pale coloured oil, ^1H NMR (CDCl_3 , 400 MHz), δ 1.61 (s, 9H, CH_3), 3.87 (s, 3H, CH_3), 6.61 (d, 1H, $J = 3.7$ Hz, Ar-H), 6.80 (d, 1H, $J = 3.7$ Hz, Ar-H); ^{13}C NMR (CDCl_3 , 100 MHz), 27.2, 52.2, 86.9, 112.9 (m), 116.2, 119.9 (q, $J = 268.4$ Hz), 125.7 (q, $J = 40.3$ Hz), 127.8, 147.2, 160.2; ^{19}F NMR (CDCl_3 , $\text{C}_6\text{H}_5\text{CF}_3$, 376 MHz), δ -59.6; MS (EI) m/z 57 (100 %), 162 (12), 193 (31) 220 (13, $[\text{M}-(\text{OtBu})]^+$); IR (film) $\nu_{\text{max}}/\text{cm}^{-1} = 2987\text{m}$, 1780s, 1732s, 1557m, 1437m, 1374s, 1256s, 1140s.

6.2.14 General procedure for the synthesis of 2-fluoro-N-phenylaniline through flow photochemistry

Solutions were prepared in acetonitrile that had been dried over molecular sieves (4\AA), degassed *via* sonication and N_2 sparging. Solution A was prepared by dissolving 2-fluoro-iodobenzene (0.2 M), triethylamine (0.4 M), aniline (0.3 M), $\text{NiCl}_2\cdot\text{dme}$ (0.02 M), dtbpy (0.02 M) and α,α,α -trifluorotoluene (0.06 M) in acetonitrile. Solution B was prepared by dissolving 4CzIPN (0.004 M) and α,α,α -trifluorotoluene (0.06 M) in acetonitrile.

The solutions were pumped via syringe pumps, meeting at a mixing tee immediately before a 2 mL PTFE reactor coil of 0.8 mm I.D. The LED source was a Kessil A160 WE set to maximum intensity, and maximum ‘blue’, and positioned approximately 2 inches from the reactor coil. The reactor coil was arranged in a flat coil of increasing diameter to maximise the irradiated area. Reaction sample for each set of experiment conditions (Table 20) was collected at 1.5 reactor volumes and analysed by ¹⁹F NMR, peak areas were normalised to the internal standard which was set to have a value of 1 in all spectra. The list of experiments was generated through the MATLAB function ‘fullfact’.

Table 20. Automated DOE experiments performed to optimise the C-N coupling of aniline to 2-fluoro-iodobenzene - 3 pump system.

Experiment name	Run order	Residence time	4CzIPN mol. %	Product peak area %
1	7	30	1.5	28.5
2	5	60	1.5	35.1
3	8	30	2.5	30.4
4	4	60	2.5	32.5
5	1	30	2	35.6
6	2	60	2	40.6
7	10	45	1.5	32.5
8	9	45	2.5	28.8
9	3	45	2	37.5
10	6	45	2	35.9
11	11	45	2	29.8

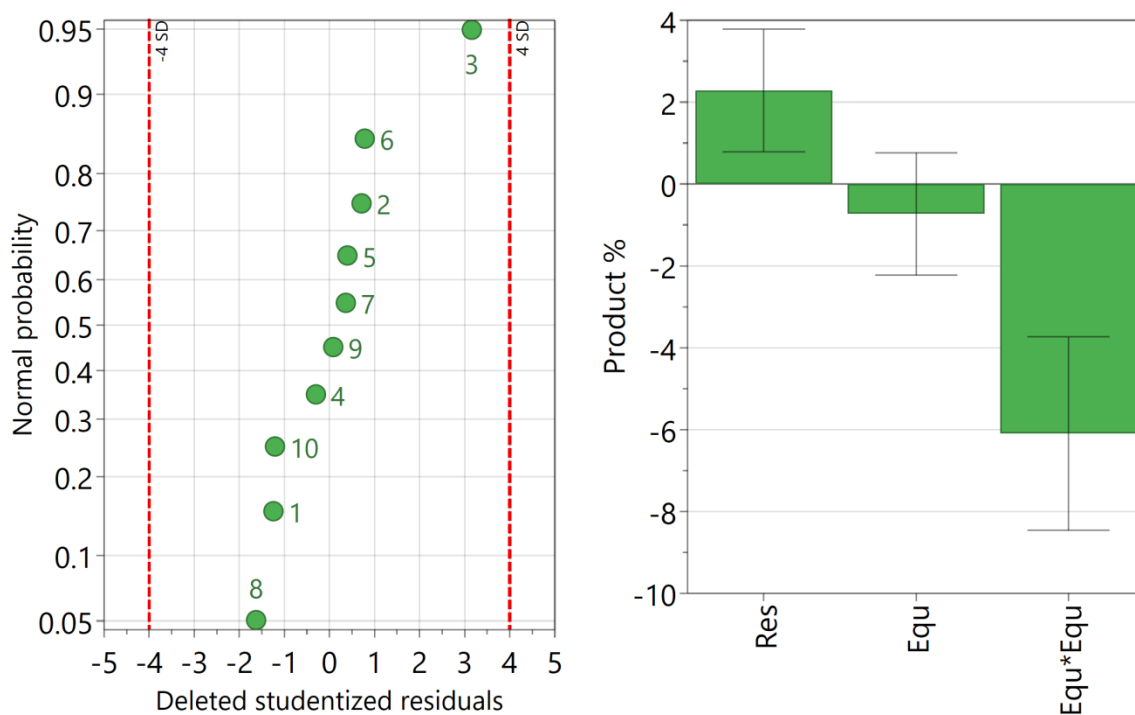
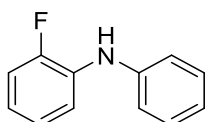


Figure 87. (Left) Residual normal probability plot for C-N MLR model investigating photosensitiser and residence time (Right) Coefficient plot.

Combined experiments were evaporated *in vacuo* and purified through column chromatography using a 9 % solution of ethyl acetate in hexane. Characterisation data are in agreement with the published literature.¹⁸⁵

2-Fluoro-N-phenylaniline (54)



Orange oil; ¹H NMR (CDCl₃, 400 MHz) δ 5.82 (s, br, 1H, NH), 6.82-6.89 (m, 1H, Ar-H), 6.98-7.11 (m, 3H, Ar-H), 7.11-7.16 (m, 2H, Ar-H), 7.29-7.35 (m, 3H, Ar-H); ¹³C NMR (CDCl₃, 100 MHz) δ 115.4, 117.1, 118.6, 120.4, 121.8, 124.2, 129.4, 131.7, 142.0, 153.0; ¹⁹F (CDCl₃, 376 MHz) δ -133.6 (m); MS (EI) *m/z* 187 (M⁺, 100 %), 186 (37.6); IR (film) $\nu_{\max}/\text{cm}^{-1}$ = 3416m, 3050w, 1620s, 1601s, 1517s, 1324s.

6.2.15 Automated optimisation of the flow photochemical synthesis of N-phenyl-4-(trifluoromethyl)aniline; residence time and nickel concentration as factors

Solutions were prepared in acetonitrile that had been dried over molecular sieves (4Å), degassed *via* sonication and N₂ sparging. Solution A was prepared by dissolving 4-bromobenzotrifluoride (0.135 M),

triethylamine (0.32 M), aniline (0.24 M), 4CzIPN (0.0016 M), NiCl₂.dme (0.008 M) and dtbpy (0.008 M) in acetonitrile. Solution B was prepared by dissolving 4-bromobenzotrifluoride (0.135 M), triethylamine (0.32 M), aniline (0.24 M), 4CzIPN (0.0016 M), NiCl₂.dme (0.012 M) and dtbpy (0.012 M) in acetonitrile. Solution C was prepared by dissolving 4-bromobenzotrifluoride (0.135 M), triethylamine (0.32 M), aniline (0.24 M), 4CzIPN (0.0016 M), NiCl₂.dme (0.016 M) and dtbpy (0.016 M) in acetonitrile.

Solutions were pumped via syringe pump, meeting at a mixing cross installed immediately before the reactor coil. The reactor coil had a volume of 2.0 mL and was made from 0.8 mm I.D. PTFE tubing. The coil was connected to a glass flow cell carefully aligned in the NMR spectrometer and filling from the bottom. The LED source was a Kessil A160 WE set to maximum intensity, and maximum 'blue', and positioned approximately 2 inches from the reactor coil. The reactor coil was arranged in a flat coil of increasing diameter to maximise the irradiated area.

The automated DOE was started in MATLAB using a custom function, running a series of experiments in a random order to complete a full factorial DOE list. NMR spectra were continuously acquired by use of a Spinsolve script and were correlated to times logged by the MATLAB function, matching the end of each experiment. The function is located in the Appendix. The product and starting material peaks were integrated and the total of their peak areas normalised to equal 1.

3 automated optimisations were performed in this manner, requiring the preparation of further reaction solutions with nickel and dtbpy concentrations of 0.004 M and 0.00016 M. A total of 21 experiments were performed (Table 21) and were analysed as separate symmetrical designs and as a large design utilising all experiments. Experiment set 1 therefore comprised 11 solutions ranging from approximately 6 to 12 mol. % nickel catalyst, experiment set 2 comprised solutions of approximately 8 to 3 mol. % nickel catalyst and experiment set 3 had solutions from approximately 6 to 0.1 mol. % nickel catalyst.

Table 21. Automated DOE experiments performed to optimise the C-N coupling of aniline to 4-bromo-benzotrifluoride - 3 pump system.

Experiment name	Run order	Residence time	Nickel mol. %	Product peak area %	Experiment set
1	3	15	6.14	28	1, 2, 3
2	10	60	6.14	97	1, 2, 3
3	11	15	12.15	40	1
4	6	60	12.15	97	1
5	1	15	8.85	22	1, 2
6	4	60	8.85	92	1, 2
7	5	37.5	6.14	55	1
8	2	37.5	12.15	59	1
9	7	37.5	8.85	65	1
10	8	37.5	8.85	55	1
11	9	37.5	8.85	55	1, 2, 3
12	15	15	3.07	63	2, 3
13	13	37.5	3.07	87	2, 3
14	14	60	3.07	96	2, 3
15	12	37.5	6.02	58	2
16	16	37.5	6.02	62	2
17	17	37.5	2.95	93	3
18	18	37.5	0.12	9	3
19	19	60	0.12	0	3
20	20	15	0.12	0	3
21	21	37.5	2.95	93	3

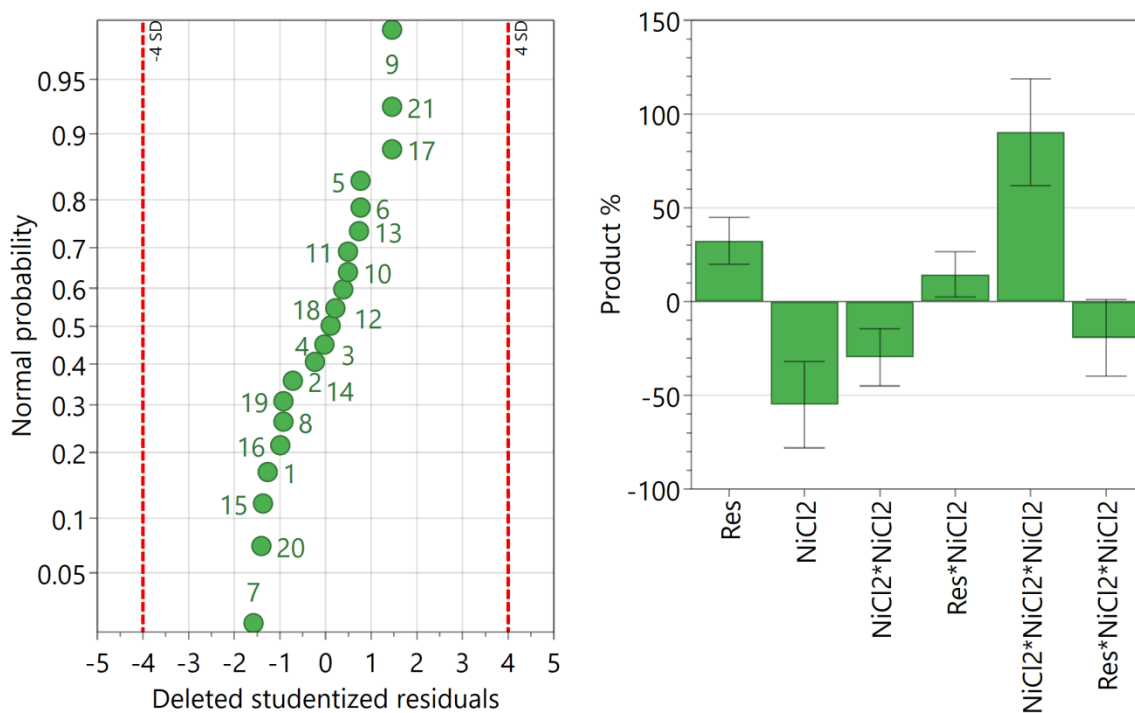


Figure 88. (Left) Residual normal probability plot for C-N MLR model investigating nickel concentration and residence time, combined from 3 data sets (Right) Coefficient plot.

6.2.16 Automated optimisation of the flow photochemical synthesis of N-phenyl-4-(trifluoromethyl); residence time, nickel concentration and photo initiator concentration as factors

Solutions were prepared in acetonitrile that had been dried over molecular sieves (4Å), degassed *via* sonication and N₂ sparging. Solution A was prepared by dissolving 4-bromobenzotrifluoride (0.135 M), triethylamine (0.32 M), aniline (0.24 M), NiCl₂.dme (0.00064 M) and dtbpy (0.00064 M) in acetonitrile. Solution B was prepared by dissolving 4-bromobenzotrifluoride (0.135 M), triethylamine (0.32 M), aniline (0.24 M), NiCl₂.dme (0.016 M) and dtbpy (0.016 M) in acetonitrile. Solution C was prepared by dissolving 4-bromobenzotrifluoride (0.135 M), triethylamine (0.32 M), aniline (0.24 M) and 4CzIPN (0.0016 M) in acetonitrile. Solution D was prepared by dissolving 4-bromobenzotrifluoride (0.135 M), triethylamine (0.32 M), aniline (0.24 M) and 4CzIPN (0.008 M) in acetonitrile.

Solutions were pumped via syringe pump, the solutions corresponding to the high and low nickel concentrations met at a mixing tee. Similarly, the low and high levels of the photo initiator met at a mixing tee, finally the nickel and photo initiator met at a final mixing tee immediately before the reactor coil. The reactor coil had a volume of 0.5 mL and was made from 0.8 mm I.D. PTFE tubing. The coil was connected to a glass flow cell carefully aligned in the NMR spectrometer, filling from the bottom. The LED source was a Kessil A160 WE set to maximum intensity, and maximum 'blue', and positioned

approximately 2 inches from the reactor coil. The reactor coil was arranged in a flat coil of increasing diameter to maximise the irradiated area.

The automated DOE was started in MATLAB using a custom function, running a series of experiments in a random order to complete a full factorial DOE list (Table 22). NMR spectra were continuously acquired by use of a Spinsolve script and were correlated to times logged by the MATLAB function, matching the end of each experiment. The function is located in the Appendix. The product and starting material peaks were integrated and the total of their peak areas normalised to equal 1.

Table 22. Automated DOE experiments performed to optimise the C-N coupling of aniline to 4-bromo-benzotrifluoride - 4 pump system.

Experiment name	Run order	Nickel mol. %	4CzIPN mol. %	Residence time (minutes)	Peak area %
1	19	0.24	0.6	20	3
2	5	3.06	0.6	20	87
3	29	5.87	0.6	20	52
4	16	0.28	3.46	20	47
5	12	3.53	3.46	20	15
6	25	6.78	3.46	20	19
7	14	0.33	6.33	20	54
8	17	4.17	6.33	20	6
9	10	8.02	6.33	20	63
10	2	0.24	0.6	30	0
11	21	3.06	0.6	30	0
12	24	5.87	0.6	30	68
13	1	0.28	3.46	30	0
14	13	3.53	3.46	30	75
15	27	3.53	3.46	30	34
16	28	3.53	3.46	30	68
17	15	6.78	3.46	30	8
18	20	0.33	6.33	30	0
19	23	4.17	6.33	30	6
20	7	8.02	6.33	30	80
21	22	0.24	0.6	40	37
22	8	3.06	0.6	40	90
23	26	5.87	0.6	40	63
24	18	0.28	3.46	40	19
25	9	3.53	3.46	40	50
26	6	6.78	3.46	40	47
27	11	0.33	6.33	40	95
28	3	4.17	6.33	40	0
29	4	8.02	6.33	40	77

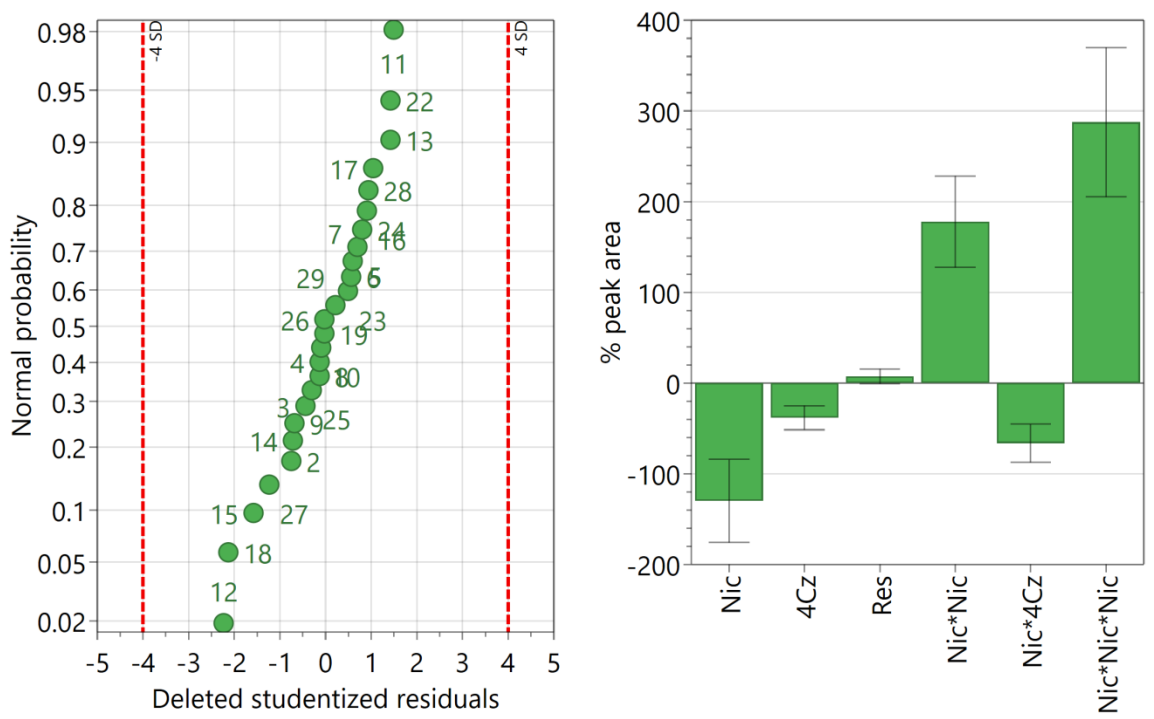
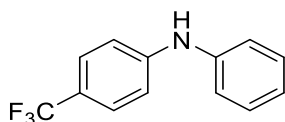


Figure 89. (Left) Residual normal probability plot for C-N MLR model investigating photosensitiser, residence time, and nickel concentration (Right) Coefficient plot.

Combined experiments were evaporated *in vacuo* and purified through column chromatography using a 9 % solution of ethyl acetate in hexane. Characterisation data are in agreement with the published literature.¹⁸⁶

N-phenyl-4-(trifluoromethyl)aniline (50)



Off white solid; m.p. 62-63 °C (lit. 61-62 °C)¹⁸⁶; ¹H NMR (CDCl₃, 400 MHz), δ 7.03 - 7.09 (m, 3H, Ar-H), 7.13 - 7.18 (m, 2H, Ar-H), 7.31 - 7.37 (t, 2H, *J* = 8.0 Hz, Ar-H), 7.45 - 7.50 (d, 2H, *J* = 8.4 Hz, Ar-H); ¹³C NMR (CDCl₃, 100 MHz), δ 115.3, 120.0, 121.7 (q, *J* = 32.4 Hz), 122.9, 124.6 (d, *J* = 270.3 Hz), 126.7 (q, *J* = 3.7 Hz), 129.5, 141.1, 146.7; ¹⁹F NMR (CDCl₃, 376 MHz), δ -62.4 (s); MS (EI) *m/z*, 237 (M⁺, 100 %), 167 (28); IR (film) $\nu_{\max}/\text{cm}^{-1}$ = 3063w, 1616s, 1595s, 1523s, 1501s, 1449m, sh.

7. References

- 1 J. S. L. Philpot, *Trans. Faraday Soc.*, 1940, **35**, 38–46.
- 2 J. H. Bannock, S. H. Krishnadasan, M. Heeney and J. C. de Mello, *Mater. Horizons*, 2014, **1**, 373–378.
- 3 L. Malet-Sanz and F. Susanne, *J. Med. Chem.*, 2012, **55**, 4062–4098.
- 4 G. Pennycook, J. A. Cheyne, N. Barr, D. J. Koehler and J. A. Fugelsang, *Judgm. Decis. Mak.*, 2015, **10**, 549–563.
- 5 R. L. Hartman, J. P. McMullen and K. F. Jensen, *Angew. Chemie Int. Ed.*, 2011, **50**, 7502–7519.
- 6 T. Razzaq, T. N. Glasnov and C. O. Kappe, *European J. Org. Chem.*, 2009, **2009**, 1321–1325.
- 7 A. Nagaki, M. Togai, S. Suga, N. Aoki, K. Mae and J. Yoshida, *J. Am. Chem. Soc.*, 2005, **127**, 11666–11675.
- 8 D. M. Ratner, E. R. Murphy, M. Jhunjhunwala, D. A. Snyder, K. F. Jensen and P. H. Seeberger, *Chem. Commun.*, 2005, 578–580.
- 9 J. A. Newby, D. W. Blaylock, P. M. Witt, J. C. Pastre, M. K. Zacharova, S. V. Ley and D. L. Browne, *Org. Process Res. Dev.*, 2014, **18**, 1211–1220.
- 10 W. J. Middleton, *J. Fluor. Chem.*, 1989, **42**, 137–143.
- 11 M. Baumann, I. Baxendale and S. V. Ley, *Synlett*, 2008, **2008**, 2111–2114.
- 12 H. Lehmann, J. Guerra, P. Poehlauer, B. Gutmann, C. O. Kappe, M. McKerverey, J.-P. Sherlock and A. J. Florence, *Green Chem.*, 2017, **19**, 1449–1453.
- 13 A. M. Nightingale, T. W. Phillips, J. H. Bannock and J. C. de Mello, *Nat. Commun.*, 2014, **5**, 3777–3782.
- 14 A. Palmieri, S. V. Ley, K. Hammond, A. Polyzos and I. R. Baxendale, *Tetrahedron Lett.*, 2009, **50**, 3287–3289.
- 15 C. Yan, J. Fraga-Dubreuil, E. Garcia-Verdugo, P. A. Hamley, M. Poliakoff, I. Pearson and A. Coote, *Green Chem.*, 2008, **10**, 98–103.
- 16 D. Webb and T. F. Jamison, *Chem. Sci.*, 2010, **1**, 675–680.

- 17 R. L. Hartman, H. R. Sahoo, B. C. Yen and K. F. Jensen, *Lab Chip*, 2009, **9**, 1843–1849.
- 18 H. R. Sahoo, J. G. Kralj and K. F. Jensen, *Angew. Chemie Int. Ed.*, 2007, **46**, 5704–5708.
- 19 M. D. Hopkin, I. R. Baxendale and S. V Ley, *Chem. Commun.*, 2010, **46**, 2450–2452.
- 20 J. Yoshida, A. Nagaki and T. Yamada, *Chem. - A Eur. J.*, 2008, **14**, 7450–7459.
- 21 A. Nagaki, Y. Tomida, H. Usutani, H. Kim, N. Takabayashi, T. Nokami, H. Okamoto and J. Yoshida, *Chem. Asian J.*, 2007, **2**, 1513–1523.
- 22 F. Lévesque and P. H. Seeberger, *Angew. Chemie Int. Ed.*, 2012, **51**, 1706–1709.
- 23 J. C. Pastre, D. L. Browne and S. V Ley, *Chem. Soc. Rev.*, 2013, **42**, 8849–8869.
- 24 I. R. Baxendale, J. Deeley, C. M. Griffiths-Jones, S. V Ley, S. Saaby and G. K. Tranmer, *Chem. Commun.*, 2006, 2566–2568.
- 25 P. Zhang, M. G. Russell and T. F. Jamison, *Org. Process Res. Dev.*, 2014, **18**, 1567–1570.
- 26 B. D. A. Hook, W. Dohle, P. R. Hirst, M. Pickworth, M. B. Berry and K. I. Booker-Milburn, *J. Org. Chem.*, 2005, **70**, 7558–7564.
- 27 B. G. Anderson, W. E. Bauta and W. R. Cantrell, *Org. Process Res. Dev.*, 2012, **16**, 967–975.
- 28 J. A. Banister, P. D. Lee and M. Poliakoff, *Organometallics*, 1995, **1995**, 3876–3885.
- 29 J. A. Banister, S. M. Howdle and M. Poliakoff, *J. Chem. Soc. Chem. Commun.*, 1993, **1993**, 1814–1815.
- 30 R. A. Bourne, X. Han, M. Poliakoff and M. W. George, *Angew. Chemie Int. Ed.*, 2009, **48**, 5322–5325.
- 31 D. S. Lee, Z. Amara, C. A. Clark, Z. Xu, B. Kakimpa, H. P. Morvan, S. J. Pickering, M. Poliakoff and M. W. George, *Org. Process Res. Dev.*, 2017, **21**, 1042–1050.
- 32 E. N. DeLaney, D. S. Lee, L. D. Elliott, J. Jin, K. I. Booker-Milburn, M. Poliakoff and M. W. George, *Green Chem.*, 2017, **19**, 1431–1438.
- 33 C. A. Clark, D. S. Lee, S. J. Pickering, M. Poliakoff and M. W. George, *Org. Process Res. Dev.*, 2016, **20**, 1792–1798.
- 34 A. Caron, A. C. Hernandez-Perez and S. K. Collins, *Org. Process Res. Dev.*, 2014, **18**, 1571–1574.

- 35 D. Cantillo, O. de Frutos, J. A. Rincon, C. Mateos and C. O. Kappe, *J. Org. Chem.*, 2014, **79**, 223–229.
- 36 R. C. R. Wootton, R. Fortt and A. J. De Mello, *Org. Process Res. Dev.*, 2002, **6**, 187–189.
- 37 K. G. Maskill, J. P. Knowles, L. D. Elliott, R. W. Alder and K. I. Booker-Milburn, *Angew. Chemie Int. Ed.*, 2013, **52**, 1499–1502.
- 38 J. P. Knowles, L. D. Elliott and K. I. Booker-Milburn, *Beilstein J. Org. Chem.*, 2012, **8**, 2025–2052.
- 39 N. J. W. Straathof, B. J. P. Tegelbeckers, V. Hessel, X. Wang and T. Noël, *Chem. Sci.*, 2014, **5**, 4768–4773.
- 40 C. ‘Chip’ Le, M. K. Wismer, Z. C. Shi, R. Zhang, D. V. Conway, G. Li, P. Vachal, I. W. Davies and D. W. C. MacMillan, *ACS Cent. Sci.*, 2017, **3**, 647–653.
- 41 J. W. Beatty, J. J. Douglas, R. Miller, R. C. McAtee, K. P. Cole and C. R. J. Stephenson, *Chem*, 2016, **1**, 456–472.
- 42 X. Zhang and D. W. C. MacMillan, *J. Am. Chem. Soc.*, 2017, jacs.7b07078.
- 43 H. Uoyama, K. Goushi, K. Shizu, H. Nomura and C. Adachi, *Nature*, 2012, **492**, 234–238.
- 44 C. Lévêque, L. Chenneberg, V. Corcé, C. Ollivier and L. Fensterbank, *Chem. Commun.*, 2016, **52**, 9877–9880.
- 45 M. D. Lainchbury, M. I. Medley, P. M. Taylor, P. Hirst, W. Dohle and K. I. Booker-Milburn, *J. Org. Chem.*, 2008, **73**, 6497–6505.
- 46 L. D. Elliott, J. P. Knowles, P. J. Koovits, K. G. Maskill, M. J. Ralph, G. Lejeune, L. J. Edwards, R. I. Robinson, I. R. Clemens, B. Cox, D. D. Pascoe, G. Koch, M. Eberle, M. B. Berry and K. I. Booker-Milburn, *Chem. - A Eur. J.*, 2014, **20**, 15226–15232.
- 47 W. Ehrfeld, K. Golbig, V. Hessel, H. Lo and T. Richter, *Ind. Eng. Chem. Res.*, 1999, **38**, 1075–1082.
- 48 J. Burns and C. Ramshaw, *Chem. Eng. Res. Des.*, 1999, **77**, 2–7.
- 49 K. F. Jensen, *Chem. Eng. Sci.*, 2001, **56**, 293–303.
- 50 K. Jähnisch, M. Baerns, V. Hessel, W. Ehrfeld, V. Haverkamp, H. Löwe, C. Wille and a. Guber, *J. Fluor. Chem.*, 2000, **105**, 117–128.

- 51 V. Hessel and H. Lowe, *Chem. Eng. Sci.*, 2003, **26**, 13–24.
- 52 J. J. Chen, X. C. Qiu, C. M. Shen, S. J. Chen and Y. W. Ko, *Trans. Can. Soc. Mech. Eng.*, 2012, **37**, 655–664.
- 53 Chemtrix, <http://www.chemtrix.com/flow-chemistry>, accessed 13 September 2017.
- 54 Uniqsis, <http://www.Uniqsis.com>, accessed 13 September 2017
- 55 Vapourtec, <http://www.vapourtec.com>, accessed 13 September 2017.
- 56 A. R. Bogdan, M. Charaschanya, A. W. Dombrowski, Y. Wang and S. W. Djuric, *Org. Lett.*, 2016, **18**, 1732–1735.
- 57 A. Adeyemi, J. Bergman, J. Brånalt, J. Sävmarker and M. Larhed, *Org. Process Res. Dev.*, 2017, **21**, 947–955.
- 58 P. D. I. Fletcher, S. J. Haswell, E. Pombo-Villar, B. H. Warrington, P. Watts, S. Y. F. Wong and X. Zhang, *Tetrahedron*, 2002, **58**, 4735–4757.
- 59 X. Yan and P. Gu, *CAD Comput. Aided Des.*, 1996, **28**, 307–318.
- 60 R. Hague, S. Mansour, N. Saleh and R. Harris, *J. Mater. Sci.*, 2004, **39**, 2457–2464.
- 61 B. C. Gross, J. L. Erkal, S. Y. Lockwood, C. Chen and D. M. Spence, *Anal. Chem.*, 2014, **86**, 3240–3253.
- 62 X. Zhang, X. Jiang and C. Sun, *Sensors Actuators A Phys.*, 1999, **77**, 149–156.
- 63 T. Cheng, W., Fuh, J.Y.H., Nee, A.Y.C., Wong, Y.S., Loh, H.T., Miyazama, *Rapid Prototyp. J.*, 2002, **1**, 12–23.
- 64 S. Kumar, *J. Mech.*, 2003, **55**, 43–47.
- 65 M. Rombouts, L. Froyen, P. Mercelis and J. P. Kruth, *CIRP Ann.*, 2006, **55**, 187–192.
- 66 E. Louvis, P. Fox and C. J. Sutcliffe, *J. Mater. Process. Technol.*, 2011, **211**, 275–284.
- 67 S. Sandron, B. Heery, V. Gupta, D. A. Collins, E. P. Nesterenko, P. N. Nesterenko, M. Talebi, S. Beirne, F. Thompson, G. G. Wallace, D. Brabazon, F. Regan and B. Paull, *Analyst*, 2014, **139**, 6343–6347.
- 68 R. J. Friel and R. A. Harris, *Procedia CIRP*, 2013, **6**, 35–40.
- 69 T. Monaghan, A. J. Capel, S. D. Christie, R. A. Harris and R. J. Friel, *Compos. Part A Appl.*

- Sci. Manuf.*, 2015, **76**, 181–193.
- 70 Fabrisonic LLC, Fabrisonic - Sound 3D Printing, <https://fabrisonic.com/unique-geometry/>, accessed 7 September 2017.
- 71 K. Kadimisetty, S. Malla and J. F. Rusling, *ACS Sensors*, 2017, **2**, 670–678.
- 72 S. K. Anciaux, M. Geiger and M. T. Bowser, *Anal. Chem.*, 2016, **88**, 7675–7682.
- 73 W. Lee, D. Kwon, W. Choi, G. Y. Jung, A. K. Au, A. Folch and S. Jeon, *Sci. Rep.*, 2015, **5**, 7717–7722.
- 74 M. R. Penny, Z. J. Cao, B. Patel, B. Sil dos Santos, C. R. M. Asquith, B. R. Szulc, Z. X. Rao, Z. Muwaffak, J. P. Malkinson and S. T. Hilton, *J. Chem. Educ.*, 2017, **94**, 1265–1271.
- 75 P. J. Kitson, M. H. Rosnes, V. Sans, V. Dragone and L. Cronin, *Lab Chip*, 2012, **12**, 3267–3271.
- 76 M. D. Symes, P. J. Kitson, J. Yan, C. Richmond, G. J. T. Cooper, R. W. Bowman, T. Vilbrandt and L. Cronin, *Nat. Chem.*, 2012, **4**, 349–354.
- 77 A. J. Capel, S. Edmondson, S. D. R. Christie, R. D. Goodridge, R. J. Bibb and M. Thurstans, *Lab Chip*, 2013, **13**, 4583–4590.
- 78 A. B. Leduc and T. F. Jamison, *Org. Process Res. Dev.*, 2012, **16**, 1082–1089.
- 79 Z. X. Rao, B. Patel, A. Monaco, Z. Jing Cao, M. Barniol-Xicotá, E. Pichon, M. Ladlow and S. Hilton, *European J. Org. Chem.*, 2017, 6499–6504.
- 80 K. C. Bhargava, B. Thompson and N. Malmstadt, *Proc. Natl. Acad. Sci. U. S. A.*, 2014, **111**, 15013–15018.
- 81 O. Okafor, A. Weilhard, J. A. Fernandes, E. Karjalainen, R. Goodridge and V. Sans, *React. Chem. Eng.*, 2017, **2**, 129–136.
- 82 V. Sans and L. Cronin, *Chem. Soc. Rev.*, 2016, **45**, 2032–2043.
- 83 H. S. Ewan, K. Iyer, S.-H. Hyun, M. Wleklinski, R. G. Cooks and D. H. Thompson, *Org. Process Res. Dev.*, 2017, **21**, 1566–1570.
- 84 C.-H. Hsieh, C.-S. Chao, K.-K. T. Mong and Y.-C. Chen, *J. Mass Spectrom.*, 2012, **47**, 586–590.
- 85 L. Zhu, G. Gamez, H. W. Chen, H. X. Huang, K. Chingin and R. Zenobi, *Rapid Commun.*

- Mass Spectrom.*, 2008, **22**, 2993–2998.
- 86 X. Yan, R. M. Bain, Y. Li, R. Qiu, T. G. Flick and R. G. Cooks, *Org. Process Res. Dev.*, 2016, **20**, 940–947.
- 87 B. J. McCullough, T. Bristow, G. O’Connor and C. Hopley, *Rapid Commun. Mass Spectrom.*, 2011, **25**, 1445–1451.
- 88 C. J. Pulliam, R. M. Bain, H. L. Osswald, D. T. Snyder, P. W. Fedick, S. T. Ayrton, T. G. Flick and R. G. Cooks, *Anal. Chem.*, 2017, **89**, 6969–6975.
- 89 P. Dell’Orco, J. Brum, R. Matsuoka, M. Badlani and K. Muske, *Anal. Chem.*, 1999, **71**, 5165–5170.
- 90 D. L. Browne, S. Wright, B. J. Deadman, S. Dunnage, I. R. Baxendale, R. M. Turner and S. V. Ley, *Rapid Commun. Mass Spectrom.*, 2012, **26**, 1999–2010.
- 91 N. Holmes, G. R. Akien, R. J. D. Savage, C. Stanetty, I. R. Baxendale, A. J. Blacker, B. A. Taylor, R. L. Woodward, R. E. Meadows and R. A. Bourne, *React. Chem. Eng.*, 2016, **1**, 96–100.
- 92 T. W. T. Bristow, A. D. Ray, A. O’Kearney-McMullan, L. Lim, B. McCullough and A. Zammataro, *J. Am. Soc. Mass Spectrom.*, 2014, **25**, 1794–802.
- 93 S. Kittiwachana, D. L. S. Ferreira, L. A. Fido, D. R. Thompson, R. E. A. Escott and R. G. Brereton, *J. Chromatogr. A*, 2008, **1213**, 130–144.
- 94 S. Wold and M. Sjostrom, *Chemom. Intell. Lab. Syst.*, 2001, **58**, 109–130.
- 95 T. Kourti, *Crit. Rev. Anal. Chem.*, 2006, **36**, 257–278.
- 96 R. Schindler and B. Lendl, *Anal. Commun.*, 1999, **36**, 123–126.
- 97 E. Venardou, E. Garcia-Verdugo, S. J. Barlow, Y. E. Gorbaty and M. Poliakoff, *Vib. Spectrosc.*, 2004, **35**, 103–109.
- 98 S. M. Mennen, M. L. Mak-Jurkaskas, M. M. Bio, L. S. Hollis, K. A. Nadeau, A. M. Clausen and K. B. Hansen, *Org. Process Res. Dev.*, 2015, **1**, 150625083324004.
- 99 C. F. Carter, H. Lange, S. V. Ley, I. R. Baxendale, B. Wittkamp, J. G. Goode and N. L. Gaunt, *Org. Process Res. Dev.*, 2010, **393**, 393–404.
- 100 T. Brodmann, P. Koos, A. Metzger, P. Knochel and S. V. Ley, *Org. Process Res. Dev.*, 2012, **16**, 1102–1113.

- 101 M. Tjahjono, X. Li, F. Tang, K. Sa-ei and M. Garland, *Talanta*, 2011, **85**, 2534–2541.
- 102 M. Tjahjono, C. Huiheng, E. Widjaja, K. Sa-ei and M. Garland, *Talanta*, 2009, **79**, 856–862.
- 103 K. L. A. Chan, S. Gulati, J. B. Edel, A. J. de Mello and S. G. Kazarian, *Lab Chip*, 2009, **9**, 2909–2913.
- 104 J. Yue, F. H. Falke, J. C. Schouten and T. A. Nijhuis, *Lab Chip*, 2013, **13**, 4855–4863.
- 105 C. Y. Kong, R. C. Soar and P. M. Dickens, *Compos. Struct.*, 2004, **66**, 421–427.
- 106 C. Y. Kong and R. Soar, *Appl. Opt.*, 2005, **44**, 6325–6333.
- 107 T. Monaghan, M. J. Harding, R. A. Harris, R. J. Friel and S. D. R. Christie, *Lab Chip*, 2016, **16**, 3362–3373.
- 108 W. Ferstl, T. Klahn, W. Schweikert, G. Billeb, M. Schwarzer and S. Loebbecke, *Chem. Eng. Technol.*, 2007, **30**, 370–378.
- 109 S. Löbbecke, W. Ferstl, S. Panić and T. Türcke, *Chem. Eng. Technol.*, 2005, **28**, 484–493.
- 110 F. Benito-Lopez, W. Verboom, M. Kakuta, J. H. G. E. Gardeniers, R. J. M. Egberink, E. R. Oosterbroek, A. van den Berg and D. N. Reinhoudt, *Chem. Commun.*, 2005, 2857–2859.
- 111 T. Ibata, Y. Isogami and J. Toyoda, *Bull. Chem. Soc. Jpn.*, 1991, **64**, 42–49.
- 112 C. A. McGill, A. Nordon and D. Littlejohn, *Analyst*, 2002, **127**, 287–292.
- 113 J. F. Haw, T. E. Glass, D. W. Hausler, E. Motell and H. C. Dorn, *Anal. Chem.*, 1980, **52**, 1135–1140.
- 114 M. V. Gomez and A. De La Hoz, *Beilstein J. Org. Chem.*, 2017, **13**, 285–300.
- 115 P. A. Keifer, S. H. Smallcombe, E. H. Williams, K. E. Salomon, G. Mendez, J. L. Belletire and C. D. Moore, *J. Comb. Chem.*, 1999, **2**, 151–171.
- 116 V. Sans, L. Porwol, V. Dragone and L. Cronin, *Chem. Sci.*, 2015, **6**, 1258–1264.
- 117 B. Ahmed-Omer, E. Sliwinski, J. P. Cerroti and S. V. Ley, *Org. Process Res. Dev.*, 2016, **20**, 1603–1614.
- 118 F. Dalitz, M. Cudaj, M. Maiwald and G. Guthausen, *Prog. Nucl. Magn. Reson. Spectrosc.*, 2012, **60**, 52–70.
- 119 E. Seifert, L. Abramo, B. Thelin, T. Lundstedt, A. Nystrom, J. Petteresen and R. Bergman,

- Chemom. Intell. Lab. Syst.*, 1998, **42**, 3–40.
- 120 F. Yates, *J. Agric. Sci.*, 1936, **26**, 424–55.
- 121 F. Yates, *Ann. Eugen.*, 1936, **7**, 121–140.
- 122 F. Yates, *Suppl. to J. R. Stat. Soc.*, 1935, **2**, 181–247.
- 123 S. A. Weissman and N. G. Anderson, *Org. Process Res. Dev.*, 2015, **19**, 1605–1633.
- 124 R. Carlson, T. Lundstedt and R. Shabana, *Acta Chem. Scand. B*, 1986, **40**, 534–544.
- 125 D. M. Roberge, *Org. Process Res. Dev.*, 2004, **8**, 1049–1053.
- 126 P. Plou, A. Macchi and D. M. Roberge, *Org. Process Res. Dev.*, 2014, **18**, 1286–1294.
- 127 B. J. Reizman and K. F. Jensen, *Org. Process Res. Dev.*, 2012, **16**, 1770–1782.
- 128 K. Koch, B. J. A. van Weerdenburg, J. M. M. Verkade, P. J. Nieuwland, F. P. J. T. Rutjes and J. C. M. van Hest, *Org. Process Res. Dev.*, 2009, **13**, 1003–1006.
- 129 S. Silvestrini, T. Carofiglio and M. Maggini, *Chem. Commun.*, 2013, **49**, 84–86.
- 130 S. Krishnadasan, R. J. C. Brown, A. J. DeMello and J. C. DeMello, *Lab Chip*, 2007, **7**, 1434–1441.
- 131 S. G. Pedro, C. S. Martínez-Cisneros, M. Puyol and J. Alonso-Chamarro, *Lab Chip*, 2012, **12**, 1979–1986.
- 132 J. P. McMullen, M. T. Stone, S. L. Buchwald and K. F. Jensen, *Angew. Chemie Int. Ed.*, 2010, **49**, 7076–7080.
- 133 J. R. Hyde, R. A. Bourne, I. Noda, P. Stephenson and M. Poliakoff, *Anal. Chem.*, 2004, **76**, 6197–6206.
- 134 R. A. Bourne, R. A. Skilton, A. J. Parrott, D. J. Irvine and M. Poliakoff, *Org. Process Res. Dev.*, 2011, **15**, 932–938.
- 135 A. J. Parrott, R. A. Bourne, G. R. Akien, D. J. Irvine and M. Poliakoff, *Angew. Chemie Int. Ed.*, 2011, **50**, 3788–3792.
- 136 R. A. Skilton, R. A. Bourne, Z. Amara, R. Horvath, J. Jin, M. J. Scully, E. Streng, S. L. Y. Tang, P. A. Summers, J. Wang, E. Pérez, N. Asfaw, G. L. P. Aydos, J. Dupont, G. Comak, M. W. George and M. Poliakoff, *Nat. Chem.*, 2014, **7**, 1–5.

- 137 R. A. Skilton, A. J. Parrott, M. W. George, M. Poliakoff and R. A. Bourne, *Appl. Spectrosc.*, 2013, **67**, 1127–1131.
- 138 A. Kandelbauer, W. Kessler and R. W. Kessler, *Anal. Bioanal. Chem.*, 2008, **390**, 1303–1315.
- 139 S. J. Kok, C. A. Wold, T. Hankemeier and P. J. Schoenmakers, *J. Chromatogr. A*, 2003, **1017**, 83–96.
- 140 H. Knözinger, *Top. Catal.*, 1998, **6**, 107–110.
- 141 M. H. M. Killner, J. J. R. Rohwedder and C. Pasquini, *Fuel*, 2011, **90**, 3268–3273.
- 142 D. Šahnić, E. Meštrović, T. Jednačak, I. Habinovec, J. Parlov Vuković and P. Novak, *Org. Process Res. Dev.*, 2016, **20**, 2092–2099.
- 143 G. Zhou, S. Grosser, L. Sun, G. Graffius, G. Prasad, A. Moment, A. Spartalis, P. Fernandez, J. Higgins, B. Wabuyele and C. Starbuck, *Org. Process Res. Dev.*, 2016, **20**, 653–660.
- 144 M. Tian, L. Bakovic and A. Chen, *Electrochim. Acta*, 2007, **52**, 6517–6524.
- 145 T. J. Thurston, R. G. Brereton, D. J. Foord and R. E. A. Escott, *Talanta*, 2004, **63**, 757–769.
- 146 A. C. Quinn, P. J. Gemperline, B. Baker, M. Zhu and D. S. Walker, *Chemom. Intell. Lab. Syst.*, 1999, **45**, 199–214.
- 147 J. Grznar, D. E. Booth and P. Sebastian, *J. Chem. Inf. Model.*, 1997, **37**, 241–248.
- 148 M. C. Carreño, J. L. G. Ruano, G. Sanz, M. A. Toledo and A. Urbano, *J. Org. Chem.*, 1995, **60**, 5328–5331.
- 149 R. K. Lade, E. J. Hippchen, C. W. Macosko and L. F. Francis, *Langmuir*, 2017, **33**, 2949–2964.
- 150 R. Ballal, A. Cheema, W. Ahmad, E. M. Rosen and T. Saha, *J. Biomol. Tech.*, 2009, **20**, 190–194.
- 151 C. A. Hone, N. Holmes, G. R. Akien, R. A. Bourne and F. L. Muller, *React. Chem. Eng.*, 2017, **352**, 61–67.
- 152 Y. R. Lee, H. C. Jung and H. Y. Sang, *Tetrahedron Lett.*, 2005, **46**, 7539–7543.
- 153 A. J. Capel, Loughborough University, 2016.
- 154 A. J. Capel, A. Wright, M. J. Harding, G. W. Weaver, Y. Li, R. A. Harris, S. Edmondson, R. D. Goodridge and S. D. R. Christie, *Beilstein J. Org. Chem.*, 2017, **13**, 111–119.

- 155 G. W. Bishop, J. E. Satterwhite, S. Bhakta, K. Kadimisetty, K. M. Gillette, E. Chen and J. F. Rusling, *Anal. Chem.*, 2015, **87**, 5437–5443.
- 156 H. Lu, M. A. Schmidt and K. F. Jensen, *Lab Chip*, 2001, **1**, 22–28.
- 157 A. S. Bhambra, M. Edgar, M. R. J. Elsegood, Y. Li, G. W. Weaver, R. R. J. Arroo, V. Yardley, H. Burrell-Saward and V. Krystof, *Eur. J. Med. Chem.*, 2016, **108**, 347–353.
- 158 K. Kaupmees, A. Trummal and I. Leito, *Croat. Chem. Acta*, 2014, **87**, 385–395.
- 159 S. Ceylan, T. Klande, C. Vogt, C. Friese and A. Kirschning, *Synlett*, 2010, 2009–2013.
- 160 M. Fuchs, W. Goessler, C. Pilger and C. O. Kappea, *Adv. Synth. Catal.*, 2010, **352**, 323–328.
- 161 E. Haldón, M. C. Nicasio and P. J. Pérez, *Org. Biomol. Chem.*, 2015, **13**, 9528–9550.
- 162 Kessil A160WE, http://www.kessil.com/aquarium/Saltwater_A160_Tuna_Blue.php, accessed 12 June 2018.
- 163 Magritek Spinsolve, <http://www.magritek.com/products/spinsolve/>, accessed 10 September 2017.
- 164 Thermo Fisher picoSpin, <https://www.thermofisher.com/order/catalog/product/912A0813>, accessed 10 September 2017.
- 165 Oxford Instruments Pulsar, <https://www.oxford-instruments.com/products/spectrometers/nuclear-magnetic-resonance-nmr/pulsar>, accessed 10 September 2017.
- 166 Nanalysis NMReady-60, NMReady-60, <http://www.nanalysis.com/>, accessed 10 September 2017.
- 167 E. Letot, G. Koch, R. Falchetto, G. Bovermann, L. Oberer and H. J. Roth, *J. Comb. Chem.*, 2005, **7**, 364–371.
- 168 J. W. Beatty, J. J. Douglas, K. P. Cole and C. R. J. Stephenson, *Nat. Commun.*, 2015, **6**, 7919–7625.
- 169 C. H. Basch, J. Liao, J. Xu, J. J. Piane and M. P. Watson, *J. Am. Chem. Soc.*, 2017, **139**, 5313–5316.
- 170 E. B. Corcoran, M. T. Pirnot, S. Lin, S. D. Dreher, D. A. DiRocco, I. W. Davies, S. L. Buchwald and D. W. C. MacMillan, *Science*, 2016, **353**, 279–283.

- 171 D. Petzold and B. König, *Adv. Synth. Catal.*, 2018, **2018**, 626–630.
- 172 E. Kiehlmann and R. W. Lauener, *Can. J. Chem.*, 1989, **67**, 335–344.
- 173 M. Kumar, A. Renu, S. Ajay and S. Veena, *J. Sol-Gel Sci. Technol.*, 2016, **79**, 114–121.
- 174 A. Ying, L. Liu, G. Wu, G. Chen, X. Chen and W. Ye, *Tetrahedron Lett.*, 2009, **50**, 1653–1657.
- 175 K. Katakawa, M. Kainuma, K. Suzuki, S. Tanaka and T. Kumamoto, *Tetrahedron*, 2017, **73**, 5063–5071.
- 176 G.-Y. Luo, H. Wu, Y. Tang, H. Li, H.-S. Yeom, K. Yang and R. P. Hsung, *Synthesis*, 2015, **47**, 2713–2720.
- 177 P. Mathew, A. Neels and M. Albrecht, *J. Am. Chem. Soc.*, 2008, **130**, 13534–13535.
- 178 R. Romeo, S. V Giofrè, C. Carnovale, A. Campisi, R. Parenti, L. Bandini and M. A. Chiacchio, *Bioorg. Med. Chem.*, 2013, **21**, 7929–7937.
- 179 D. Kumar, G. Patel and V. B. Reddy, *Synlett*, 2008, **2008**, 399–402.
- 180 L. Bernet, R. Lalrempuia, W. Ghattas, H. Mueller-bunz, L. Vigara, A. Llobet and M. Albrecht, *Chem. Commun.*, 2011, **47**, 8058–8060.
- 181 N. Pentela, P. Murugan, S. N. Jaisankar, D. Samanta and A. Baran, *J. Organomet. Chem.*, 2015, **778**, 42–46.
- 182 L. Oreste, G. Biagi, M. Ferretti, A. Lucacchini and P. L. Barili, *Eur. J. Med. Chem.*, 1983, **18**, 471–475.
- 183 K. Yang, Y. Qiu, Z. Li, Z. Wang and S. Jiang, *J. Org. Chem.*, 2011, **76**, 3151–3159.
- 184 J. Mao, M. Wu, G. Xie and S. Ji, *Adv. Synth. Catal.*, 2009, **2009**, 2101–2106.
- 185 X. Zhu, Q. Zhang and W. Su, *RSC Adv.*, 2014, **3**, 22775–22778.
- 186 Y. Yu, J. Srogl and L. S. Liebeskind, *Org. Lett.*, 2004, **15**, 2631–2634.

8. Appendix 1

8.1 MATLAB code written for instrument control and optimisations

The code shown below can be copied into MATLAB for operation. Comments in the code are shown following '%' and are coloured in blue to distinguish them from active commands. The pumps referred to in all the following are AL-1000 syringe pumps.

8.1.1 Code for creating serial objects to connect RS-232 controlled syringe pumps

Serial objects are created using a custom MATLAB function. The COM port and baudrate are specified by the user, the terminator characters are dependent on the hardware type being used. The code below connects simultaneously to four AL-1000 syringe pumps and can be modified as required by deleting or adding lines if a different number are required.

```
function
[Pump1,Pump2,Pump3,Pump4,response1,response2,response3,response4]=Feelthepain4(Port1,Port2,Port3,P
ort4,Baud) %type COM port pump is attached to, baud rate determined by the hardware

Pump1=serial(Port1,'Baudrate',Baud,'Terminator',{3,13});
Pump2=serial(Port2,'Baudrate',Baud,'Terminator',{3,13});
Pump3=serial(Port3,'Baudrate',Baud,'Terminator',{3,13});
Pump4=serial(Port4,'Baudrate',Baud,'Terminator',{3,13});

fopen(Pump1); % open communication
fprintf(Pump1,'VER'); % send firmware query as test
response1=fscanf(Pump1); % should give 00SNE1000V3.921 if communication worked

fopen(Pump2); % open communication
fprintf(Pump2,'VER'); % send firmware query as test
response2=fscanf(Pump2); % should give 00SNE1000V3.921 if communication worked

fopen(Pump3); % open communication
fprintf(Pump3,'VER'); % send firmware query as test
response3=fscanf(Pump3); % should give 00SNE1000V3.921 if communication worked

fopen(Pump4); % open communication
fprintf(Pump4,'VER'); % send firmware query as test
response4=fscanf(Pump4); % should give 00SNE1000V3.921 if communication worked
```

```
end
```

8.1.2 Code for the optimisation of one reagent factor and residence time - two pumps.

The inputs hardware1 and hardware2 should be serial objects previously created and opened for communication. The input DOE can be any list of experiments as long as the residence time is in column 2 and the reagent equivalents is in column 1. The output 't' is the timestamp vector and allows identification of the analysis to match the experiment.

```
% Controls two syringe pumps
% DOE_list is your experiment matrix in Row x Column format
% hardware1 & 2 are serial objects, units are 'MM','MH','UM' or 'UH' for the
% Al 1000 syringe pumps
% coil volume is in mL
% Equiv should be in column 1, residence time in column 2

function [Random_list,Command_list1,Command_list2,t]=Dual_pump_run_NMR(DOE_list, units,
coil_volume,hardware1,hardware2)
[X,~]=size(DOE_list);

Flowrate_true=zeros(X,2);

for m=1:X;
    Flowrate_true(m,1)=round((DOE_list(m,1)/((DOE_list(m,1))+1))*coil_volume/DOE_list(m,2),3);
    Flowrate_true(m,2)=round(coil_volume/DOE_list(m,2)-Flowrate_true(m,1),3);
end

% determines the number of experiments to run from the no. of rows
% toot(n) are strings containing a numerical value of the parameter from your
% experiment matrix. honk(n) concatenates 'toot' along with the appropriate
% command structure for your hardware

for k=1:X;
toot1=num2str(Flowrate_true(1:k,1));
honk1=strcat('RAT',toot1,units);
toot2=num2str(Flowrate_true(1:k,2));
honk2=strcat('RAT',toot2,units);
end

% Command_list creates a cell array each containing the individual commands
% for the experiments
% Random_list generates a random permutation of 1 to X returning each value
% only once

Command_list1=cellstr(honk1);
Command_list2=cellstr(honk2);
Random_list=randperm(X,X);

% The experiments will run for 1.5 times the residence time, which is
% generated from the combined flow rates of both pumps (in minutes)
% to ensure steady state; this can be altered if 1.5 is too short for
% by simply altering the 1.5 in the 'pause' command
% the final fscanf is to clear the read buffer

for j=1:X;
    A=Random_list(j,1);
    res_time=DOE_list(A,2);
```

```

fprintf(hardware1,Command_list1{A,1});
fprintf(hardware2,Command_list2{A,1});
fprintf(hardware1,'RUN');
fprintf(hardware2,'RUN');
fscanf(hardware1);
fscanf(hardware2);
pause(res_time*60*1.5)
fprintf(hardware1,'STP');
fprintf(hardware2,'STP');
t(j,1)=datetime;
fscanf(hardware1);
fscanf(hardware2);
end
end

```

8.1.3 Code for the optimisation of one reagent factor and residence time - three pumps

```

function [Pump_order,Random_list,run_list,FlowuL,honk1,t]=run_optim4(DOE, coil, Syringe1,
Syringe2, Syringe3)

[X,~]=size(DOE);
FlowuL=zeros(X,1); % pre allocate matrix

Random_list=randperm(X,X)'; % random number list

for m=1:X;
run_list(m,1)=DOE(Random_list(m,1),1);
run_list(m,2)=DOE(Random_list(m,1),2); % randomise experiments
end

for k=1:X;
FlowuL(k,:)=round(1000*coil/run_list(k,2),1); % convert to flow rates
end

Pump_order=cell(X,1); % preallocate cell for pump identity

% returns a pump identity based on a logical test using the maximum, centre
% and minimum values obtained earlier. Puts the pump name into a cell

for n=1:X;
toot1=num2str(FlowuL(1:n,1));
honk1=strcat('RAT',toot1,'UM');
end
Command_list1=cellstr(honk1);

% need to generate strings with flow rate, units and pump identity.
% alter the number in the if else to account for equivalents changes

for j=1:X;
if (5.1>run_list(j,1) && 4.9<run_list(j,1))
Pump_ID=Syringe1;
elseif (10.1>run_list(j,1) && 9.9<run_list(j,1))
Pump_ID=Syringe2;
else
Pump_ID=Syringe3;
end
Pump_order{j,1}=Pump_ID;

```

```

end
for p=1:X;
fprintf(Pump_order{p,1},Command_list1{p,1});
fprintf(Pump_order{p,1},'RUN');
fscanf(Pump_order{p,1});
pause(run_list(p,2)*60*1.5)
fprintf(Pump_order{p,1},'STP');
t(p,1)=datetime;
fscanf(Pump_order{p,1});
end
end

```

8.1.4 Code for the control of four pumps for optimisation of residence time and two stoichiometry factors.

The inputs hardware1 - 4 should be serial objects previously created and opened for communication. The stoichiometry factors are input as low1, high1; low2, high2 and will form columns 1 and 2 of the generated DOE list. A default steady state factor of 1.5 has been entered, this can be altered as required.

```

function [ExperimentsFF,run_list,A,B,t]=DOEff3fac_cp_optim(levels1,levels2,levels3,low1, high1,
low2, high2,low3,high3,responses,coil,Hardware1,Hardware2,Hardware3,Hardware4)

```

```

% Generates a full factorial design for 3 factors only
% levels is the number of levels for your 3 factors
% low(n) high(n) are the lower and upper bounds for your levels, a
% centrepoint will be automatically generated
% put residence time as the third factor

```

```

Explist=fullfact([levels1,levels2,levels3]); % creates coded matrix values
[howbigx,howbigy]=size(Explist);
Explist_cp=zeros(howbigx+2,howbigy);
for j=1:howbigx;
Explist_cp(j,1:3)=Explist(j,1:3);
end

```

```

bounds = [low1 high1;low2 high2;low3 high3]; % Min and max values for each factor
RealValue = zeros(size(Explist_cp)); % pre-allocates matrix with 2 additional centre points
Explist_cp(howbigx+1:howbigx+2,1:howbigy)=2;

```

```

for i = 1:size(Explist_cp,2) % Convert coded values to real-world units
zmax = max(Explist_cp(:,i));
zmin = min(Explist_cp(:,i));
RealValue(:,i) = interp1([zmin zmax],bounds(i,:),Explist_cp(:,i));
end

```

```

Number_of_columns=size(RealValue); % determines the size of the DOE list
Dummy_response_column=zeros(Number_of_columns(1,1),responses); % generates a column of
%zeros for the responses
ExperimentsFF=[RealValue,Dummy_response_column]; % adds the responses columns to the DOE
%table

```

```

[X,~]=size(ExperimentsFF);
FlowuL=zeros(X,1); % pre allocate matrix %possibly redundant!%

```

```

Random_list=randperm(X,X)'; % random number list

```

```

for m=1:X;
run_list(m,1)=ExperimentsFF(Random_list(m,1),1);
run_list(m,2)=ExperimentsFF(Random_list(m,1),2);run_list(m,3)=ExperimentsFF(Random_list(m,1),3);
end

for k=1:X;
FlowuL(k,:)=round(1000*coil/run_list(k,3),1); % convert to flow rates %possibly redundant!%
end

for j=1:X;

    if (low1+0.01>run_list(j,1) && low1-0.01<run_list(j,1))
        Pump_ID1=1;Pump_ID2=0;
    elseif (high1+0.01>run_list(j,1) && high1-0.01<run_list(j,1))
        Pump_ID1=0;Pump_ID2=1;
    else
        Pump_ID1=1;Pump_ID2=1;
    end
NiPump_order{j,1}=Pump_ID1;
NiPump_order{j,2}=Pump_ID2;

    if (low2+0.01>run_list(j,2) && low2-0.01<run_list(j,2))
        Pump_ID3=1;Pump_ID4=0;
    elseif (high2+0.01>run_list(j,2) && high2-0.01<run_list(j,2))
        Pump_ID3=0;Pump_ID4=1;
    else
        Pump_ID3=1;Pump_ID4=1;
    end

CzIPNPump_order{j,1}=Pump_ID3;
CzIPNPump_order{j,2}=Pump_ID4;

end

A=cell2mat(NiPump_order);
B=cell2mat(CzIPNPump_order);

for n=1:29;
Pump(n,1)=0.5*(coil/run_list(n,3))*A(n,1)/(A(n,1)+A(n,2));
Pump(n,2)=0.5*(coil/run_list(n,3))*A(n,2)/(A(n,1)+A(n,2));
Pump(n,3)=0.5*(coil/run_list(n,3))*B(n,1)/(B(n,1)+B(n,2));
Pump(n,4)=0.5*(coil/run_list(n,3))*B(n,2)/(B(n,1)+B(n,2));
end

for n=1:X;
for m=1:4;
MicroL(n,m)=1000*Pump(n,m);
MicroL_round(n,m)=round(MicroL(n,m),1);
toot1=num2str(MicroL_round(n,m));
honk1=strcat('RAT',toot1,'UM');
Commandlist(n,m)=cellstr(honk1);
end;
end

for p=1:X;
fprintf(Hardware1,Commandlist{p,1});
fprintf(Hardware2,Commandlist{p,2});
fprintf(Hardware3,Commandlist{p,3});
fprintf(Hardware4,Commandlist{p,4});

```

```

fprintf(Hardware1,'RUN');
fprintf(Hardware2,'RUN');
fprintf(Hardware3,'RUN');
fprintf(Hardware4,'RUN');
fscanf(Hardware1);
fscanf(Hardware2);
fscanf(Hardware3);
fscanf(Hardware4);
pause(run_list(p,3)*60*1.5)
fprintf(Hardware1,'STP');
fprintf(Hardware2,'STP');
fprintf(Hardware3,'STP');
fprintf(Hardware4,'STP');
t(p,1)=datetime;
fscanf(Hardware1);
fscanf(Hardware2);
fscanf(Hardware3);
fscanf(Hardware4);
end

```

8.1.5 Code for automated NMR acquisition scripts executable in Spinsolve

The intended name for the script, the list of experiments with residence time as the third column, and the steady state factor are the input values. The output is a script with all experiment timings that will acquire three spectra at 1.5 reactor volumes for all experiments. The characters required for the script to be recognised by the Spinsolve software are contained within a cell array.

```

function [Auto_acq]=Auto_NMR_acq(Script_name,DOE,steady_state_factor)

Acq_lines={ 'TimeStampFolder      = "c:/ReactionMonitor/19F";'FluorinePhase      =
'FirstScan";#FluorinePhase      = "ManualPhase(-100,360)" # manually set the phase to be used
for all scans';# Loop ';loop(3, 00:03:00:000); 'RunProtocol("1D FLUORINE+", ["Number=64",
'RepetitionTime=2", "PulseAngle=90", "AcquisitionTime=1.64"])' ;'endloop'};
[X,~]=size(DOE);

for p=1:X;
acq_delays(p,1)=(DOE(p,3));
end

for q=1:29;
acq_wait{q,1}=datestr((9+steady_state_factor*acq_delays(q,1)/1440), 'HH:MM:SS:FFF'); % 9 adds
%the acquisition time on
end

ZA='(';
ZB=')';

for r=1:29;
acq_wait_full{r,1}=strcat('wait',ZA,acq_wait{r,1},ZB);
end

Auto_acq(1:3,1)=Acq_lines(1:3,1);
for i=1:29;
Auto_acq(5*i-1,1)=acq_wait_full(i,1);
Auto_acq(5*i:3+5*i,1)=Acq_lines(4:7,1);
end

```



```
fileID = fopen(Script_name,'wt');
formatSpec = '%s\r\n%d%2.1f%s\r\n';
[nrows,~] = size(Auto_acq);
for row = 1:nrows
    fprintf(fileID,formatSpec,Auto_acq{row,:});
end
fclose(fileID);
```

9 Appendix 2. Publication list

[1] T. Monaghan, M. J. Harding, R. A. Harris, R. J. Friel and S. D. R. Christie, *Lab Chip*, 2016, **16**, 3362–3373.

[2] A. J. Capel, A. Wright, M. J. Harding, G. W. Weaver, Y. Li, R. A. Harris, S. Edmondson, R. D. Goodridge and S. D. R. Christie, *Beilstein J. Org. Chem.*, 2017, **13**, 111–119.